The Synthesis and Functionalization of Nanostructured Carbon Black by Thermal Plasma for Use in PEM Fuel Cells

Ramona Pristavita

Department of Chemical Engineering
McGill University

A thesis submitted to McGill University in partial fulfillment of the requirements of the degree of Doctor of Philosophy.

June 2011

I dedicate this thesis to my family, especially to my husband Ciprian.

“As we advance in life it becomes more and more difficult, but in fighting the difficulties the inmost strength of the heart is developed.”

- Vincent van Gogh

“Patience and perseverance have a magical effect before which difficulties disappear and obstacles vanish.”

- John Quincy Adams

Abstract

The Polymer Electrolyte Membrane (PEM, also called Proton Exchange Membrane) fuel cell constitutes a clean and efficient alternative energy source, however the production cost of these systems must be reduced substantially in order to be economically viable on a large production scale. One method to reduce this cost is to develop an alternative, low cost non-noble metal catalyst replacing platinum which would ideally be dispersed at the atomic level. The proposed material studied in this thesis consists of a carbon black (CB) powder which contains nitrogen atoms bonded to the graphitic support and iron atoms bounded to the nitrogen atoms, the iron atoms creating the active centers of the catalyst. The scope of the project was to produce CB materials with or without nitrogen attached to the graphitic support.

CB nanopowders were obtained by plasma decomposition of a carbon-containing feedstock. Two types of plasma sources were tested: a DC thermal plasma torch system of 100 kW in which benzene is used as the carbon precursor, and an inductively coupled thermal plasma (ICP) torch system of 35 kW using methane as the carbon precursor.

The carbon nanopowders obtained using the DC plasma system showed non uniformity in the collected particles morphologies and metal particle contamination generated by the erosion of internal parts of the system. Such contamination is incompatible with the PEM catalyst application and disables such system for generating the catalyst support material. A similar cylindrical geometry of the ICP reactor also generated non uniform particles morphology; for both DC and ICP systems this was attributed to the presence of recirculation areas in the reactor. The ICP however generated powders that were free of metal contamination.

Modeling the fluid dynamics and the plasma evolution in the ICP reactor enabled to verify that a conical geometry permitted to eliminate the recirculation zones, providing a better control of the conditions for nanoparticle nucleation. The product obtained with the ICP plasma system and the new conical reactor showed

effectively a very uniform morphology throughout the collection zones and a crystalline graphitic structure can be obtained, with production results that are highly reproducible even under some variations of the system control parameters. The highly crystalline carbon material shows graphene planes stacking with a nano-flake morphology having between 6 and 16 atomic planes (5 nm thickness) and with in-plane dimensions of approximately 100 nm long and 50 nm wide. Nitrogen was also introduced along with the methane precursor using flow rates of 0.1 and 0.2 slpm N_2. The resulting carbon product containing nitrogen has the same nano-flake structural properties, and some of the nitrogen is observed using XPS to be incorporated into the graphitic structure through pyridinic bonds. Such bonding structure effectively corresponds to what is believed to be the required chemical functionalization needed for incorporating iron atoms capable of acting as a non noble catalyst in the PEM fuel cells.

The surface area of the particles evaluated using a BET technique was surprisingly very small for most of the produced materials. This indicated the presence of contaminants in the experimental powders, as confirmed by Raman spectroscopy, TGA, and GC-MS extraction and indentification. The two families of volatile organic compounds (VOC's) were observed: low and high boiling point VOC's. The DC samples contained the highest amounts of organic compounds and the majority of these were in the form of aromatic compounds containing one or more benzene rings. For the ICP reactor, a close correlation between the amount of organic compounds present in the CB samples and the collection position within the cylindrical reactor was observed. The samples collected where the presence of recirculation areas was observed contained a higher concentration of VOC's. Also, long chain hydrocarbons containing nitrogen were observed when nitrogen was introduced in the system along with the methane. Few VOC's were present in the carbon nano-flakes samples produced using the ICP system with the conical shape reactor and methane flow rates above 5 slpm, while no VOC's were observed at lower flow rates.

All the powders were analyzed using SEM, TEM, XRD and Raman Spectroscopy before and after the thermal treatment in order to determine the effect of the heat treatment on the powder structural properties.

Résumé

Les piles à combustible à base de membrane électrolyte en matériau polymérique (PEM, également appelée membrane d'échange de proton) constituent une source d'énergie propre et efficace, cependant leur coût de production doit être substantiellement réduit pour pouvoir former une solution énergétique économiquement viable. Une solution pour réduire le coût est de développer un catalyseur alternatif remplaçant le platine, idéalement à partir d'un métal non-noble et dispersé à l'échelle atomique. Un catalyseur alternatif est proposé dans ce projet, celui-ci est composé d'une poudre de noir de carbone (NC) contenant des atomes d'azote liés aux atomes de carbone en bordure de zones cristallines nanométriques. Des atomes de fer sont ensuite liés aux atomes d'azote afin de créer les centres actifs.

Dans ce projet les nanopoudres de carbone ont été obtenus par décomposition par plasma d'une source à base de carbone. Deux types de systèmes plasma sont utilisés: une source de plasma thermique à courant continu (CC) de 100 kW utilisant benzène comme précurseur de carbone, et une source de plasma thermique inductif (ICP) de 35 kW utilisant le méthane comme précurseur de carbone.

Les nanopoudres de carbone obtenus en utilisant la source de plasma CC ont montré une morphologie non uniforme de particules et la présence de contaminants métalliques liés à l'érosion des électrodes. Ceci rend les poudres produites inaptes à un usage comme matériel support de catalyseur. Le système à plasma thermique ICP et un réacteur semblable de forme cylindrique ont également montré une morphologie non uniforme de particules mais ne contiennent cependant aucun contaminant métallique. Dans les deux cas la non-uniformité du produit est attribuée à la présence de vortex de recirculation dans le réacteur.

Une modélisation de la dynamique des fluides et du plasma dans le réacteur ICP a montré qu'une géométrie conique permettait d'éliminer les problèmes de recirculation et de mieux contrôler les conditions nécessaires à la nucléation de nanoparticules. Les poudres de carbone produites en utilisant un système de

plasma thermique ICP de 35 kW et une géométrie de réacteur de forme conique montrent effectivement qu'une morphologie uniforme est obtenue dans tout le réacteur et qu'une structure graphitique cristalline est générée. Ces résultats montrent également une grande reproductibilité des résultats même avec des variations des paramètres de contrôles du réacteur. La structure de carbone obtenue est hautement cristalline et montre un empilement de plans de graphènes en nano-flocons avec un empilement de 6 à 16 plans atomiques (5 nm d'épaisseur) et des dimensions approximatives dans le plan de 100 nm de longueur et 50 nm de largeur. L'azote a également été injecté avec le méthane en utilisant des débits de 0.1 and 0.2 slpm N_2. Les poudres de carbone obtenues avec l'azote conserve les mêmes propriétés structurales en nano-flocons, et une partie de l'azote est incorporé dans la structure graphitique par des liaisons de type pyridinique tel qu'observé par mesures XPS. Cette structure correspond effectivement à la fonctionnalisation chimique nécessaire à l'attachement d'atomes de fer aptes à agir comme catalyseurs non-nobles dans les piles à combustibles de type PEM.

Les valeurs obtenues pour la surface spécifique des particules en utilisant une technique BET sont faibles pour la plupart des matériaux produits. Ceci révèle la présence de contaminants dans les poudres expérimentales, présence confirmée par spectroscopie de Raman, thermo-gravimétrie (TGA), et par une identification chromatographique (GC-MS). Les résultats de GC-MS montrent la présence dans les échantillons de NC de deux familles de composés organiques volatiles (COV), soit des composés à bas et à haut point d'ébullition. Les échantillons de NC produits en utilisant le système CC a les quantités les plus élevés de composés organiques. La majorité était sous forme de composés aromatiques contenant un ou plusieurs anneaux de benzène. Une corrélation directe entre la quantité de composés organiques présentes et la position de leur collection dans le réacteur cylindrique ICP a été observée. Les échantillons collectés dans les zones de vortex de recirculations contiennent une concentration plus élevée de COV. En outre dans les échantillons pour lesquels l'azote a été ajouté au méthane, la présence d'hydrocarbures à longue chaîne contenant de l'azote a été observée. Peu de COV

étaient présents dans les échantillons de nano-flocons produits en utilisant le système ICP et le réacteur de forme conique en employant des débits de méthane au-dessus du 5 slpm, alors qu'on n'observait aucun COV aux débits inférieurs.

Les poudres expérimentales ont été analysées utilisant les techniques SEM, TEM, XRD et la spectroscopie Raman avant et après le traitement thermique afin de déterminer l'effet de ce traitement sur les propriétés structurales des poudres.

Acknowledgments

I would like to express my most sincere gratitude to Professors Jean-Luc Meunier and Dimitrios Berk for their support, thoughtful guidance and edifying discussions, without which this thesis would never have been written.

A special thank to Professor Richard Munz for allowing me to use the conical reactor and for all his advises and the confidence he showed me.

I would like to thank Professors Jean-Pol Dodelet and Barry L. Stansfield and all other members of the INRS-EMT Varennes for their advices and collaboration.

Many thanks to the non-academic staff that help me carrying out my research activities: Mr. Frank Caporuscio and Mr. Csaba Szalacsi for their help with the construction and installation of the reactor, Mr. Ranjan Roy for his excellent collaboration regarding the GC-MS analysis, Ms. Monique Riendeau for the X-ray diffraction tests, Ms. Helen Campbell and Ms. Line Mongeon for the SEM training. Special thanks to Ms. Emily Musgrave for the encouragements and all the advices.

I thank the past and present members of the CRTP McGill: L. N. Rao, Ian Castillo, Frederic Marion, Jason Tavares, Carole Baddour and Norma Mendoza for their company, advice and support. Special thanks to the summer students Blain Moran and Pierre-Alexander Pascone for their help in different stages of this project.

Finally, I wish to acknowledge the financial support provided by the Natural Science and Engineering Research Council of Canada (NSERC), Fonds de Recherche sur la Nature et Technologies (FQRNT), Plasma Quebec and GM Canada.

Table of contents

List of figures

List of tables

Nomenclature

L_a Average lengths of the parallel layers in the ab plane.

L_c Average stacking height in the c direction.

L_{eq} Average crystallites lengths.

G Graphitic band.

$G^{'}$ Second order disorder band.

D Disorder band.

w_D Band D halfway width.

w_{2D} Band 2D ($G^{'}$) halfway width.

I_D Intensity of the D band/peak.

I_G Intensity of the G band/peak.

$I_{G'}$ Intensity of the $G^{'}$ band/peak.

$\underline{k}$ Specific wave vector for a given Bravais lattice.

K Ewald sphere radius.

θ_B Bragg angle.

g_{hkl} Reciprocal lattice vector.

p_o Saturation or vapor pressure.

v_m Volume of one monomolecular layer of gas.

c Constant for the particular temperature and gas-solid system.

N_o Avogadro's number, 6.02×10^{23} molecules/mol.

V Volume per mole of gas at conditions of v_m (V=22.414 l/g mol).

M Molecular weight.

ρ Density of the adsorbed molecules.

2Θ XRD diffraction angle.

Chapter 1 – Introduction

1.1 Problem definition and project scope

Energy is an essential part of our society. We use a large amount of energy that comes from different sources, most of which are non-renewable sources. Energy production leads to huge emissions of carbon dioxide (CO_2) into the atmosphere, a direct cause of the enhanced greenhouse effect that is responsible for the global warming and climate change.

As a solution to the energy problem, the attention is now directed to renewable energy sources such as wind and solar power, biomass, hydroelectric and hydrogen fuel cells. This research project focuses on this last sector, more particular on improving the catalyst that should help a wider implementation of fuel cells.

Hydrogen fuel cells are seen as one of the solutions to the future energy needs. Sources of hydrogen are methane, petroleum, biomass and coal. Gaseous hydrogen can be also obtained by separation of the oxygen atoms from water using an electrolysis process.

There is an ongoing effort to develop and increase the use of hydrogen fuel cells, particularly the Polymer Electrolyte Membrane (also called Proton Exchange Membrane (PEM)) fuel cells, presently being implemented in transportation applications. The reactants in such a fuel cell are gaseous hydrogen and air. The hydrogen atoms are split into protons and electrons by a catalyst and they pair up again on the other side of the membrane in the presence of air, forming water molecules.

Even if the PEM fuel cells represent a clean and efficient alternative energy source, their production cost must be reduced substantially in order for them to be economically viable. In a cost study conducted by Directed Technologies Inc. [James, 2010] it was shown that three components of the PEM fuel cells: the gas diffusion layer, the membrane and the catalyst (exclusively platinum on a carbon support at present) account for 80% of the production cost. In a large scale production scenario (500 000 systems/year), the price of the gas diffusion layer

and the membranes is decreased to about 10% each from the total production cost [James, 2010]. While the price of these two components decreases, the price of the catalyst is however constantly increasing because of an unbalanced supply/demand. One possible way to reduce this cost is to develop an alternative, low cost catalyst. This thesis concentrates on the development of a low cost alternative catalyst.

Platinum-based catalysts are typically structured as nanoparticles supported by a carbon black (CB) powder. The proposed catalyst material in the present project consists of making available the iron replacement metal as active catalyst site at the atomic level. For this purpose, a CB powder is produced with a specific structure which can be functionalized with nitrogen atoms bonded to the graphitic support. The iron atoms are then bounded to specific nitrogen atoms sites to create the active centers of the catalyst. In this atomic architecture, the iron needs a specific coordination with the nitrogen, this requirement imposing a specific structure of the CB material and pyridinic type of bonds for the nitrogen functionalization. CB is also chosen because of its electrical conductivity, its high surface area and its ability to function in the highly acidic medium of the PEM fuel cells. The objective is to produce CB nanopowders having a high catalytic activity and good stability in time. This implies that there is a need for a high density of catalytic sites on the surface of the carbon particles. In terms of chemical structure, this increase in the number of catalytic sites requires an increase in quantity of nitrogen incorporated in the nanostructure through the pyridinic bonds.

The CB nanopowders were obtained by plasma decomposition of a carbon-containing feedstock. The plasma process was chosen because of its many advantages. The plasma process does not generate CO_2 and the resulting carbon black does not contain large amounts of impurities as in the flame process. The high temperature of thermal plasma systems means the possibility to attain a high degree of crystallinity of the product. The decoupling of the carbon material production from the energy requirements (no fuel control but electrical control of temperature and relatively independent supply of carbon) leads to a better control

of temperature, velocity profiles and residence times in the synthesis reactor. Another advantage of plasma technology is the ability to work at different pressures without affecting too much the energy input. Also, with plasma technology different reactor designs and any carbon feedstock, in gaseous, liquid or solid state can be used.

The work carried out in this project aimed to complement and extend the work done by Professor Dodelet's group (INRS-EMT, Varennes). It was a team effort (Prof. Jean-Pol Dodelet, Prof. Barry Stansfield, Mr. Nicholas Larouche, Mr. Juan Herranz, Mr. Michel Lefevre) concentrating on alternative methods to generate CB support powders and to functionalize them for non-noble catalyst materials for PEM fuel cells applications.

1.2 Thesis objectives

The carbon black was produced by the plasma decomposition of a carbon-containing feedstock. The objectives of the project are:

1) To optimize the carbon black nanostructure (the size of the crystallites and the dimensions of the micropores) for non noble catalysts synthesis.
2) To incorporate nitrogen, via in situ functionalization, into the carbon black in order to affix the iron catalyst.
3) To optimize the catalytic activity of the non noble catalysts for fuel cells and verify its stability. This objective will be fulfilled thru work in collaboration with INR-EMT Varennes.

Two plasma reactors were used, the plasma being generated in the first case by a DC plasma torch with a nominal power of 100 kW and, in the second case, by an inductively coupled plasma (ICP) torch of 35 kW. The main challenge of the project was to optimize the microporous structure of the carbon black and to include nitrogen into the pyridinic structure.

1.3 Thesis outline

This thesis is a paper-based thesis and is divided into 11 chapters and the appendices. The thesis covers the work done on both the DC system and the ICP

system, focusing on results from the experimental work done using the ICP thermal system.

A literature review is presented in a concise form in the three chapters including the published and submitted papers and a more complete literature review has been added (Chapter 3) for a clear understanding of the project and to introduce the reader to notions such as thermal plasmas, fuel cells, catalyst and carbon blacks. Care has been taken to minimize the repetition, but some information overlap between this chapter and the chapters including the published and submitted papers should be expected.

The experimental work done using the DC reactor is presented first. These results are presented (Chapter 5) to show the non compatibility of the materials produced with the scope of the project and explain the choice to focus only on the ICP system for the production of carbon black materials.

The Chapters 6, 7, 8 and 9 include the published and submitted papers resulting from this work; each paper constitutes a chapter.

Computational Fluid Dynamic (CFD) modeling complements the experimental work made on the ICP system. This modeling work was carried out by Dr. Norma Mendoza as the early work on the DC reactor (Chapter 5) and the initial ICP reactor (Chapter 6) proved that changes in the reactor design were necessary. These changes follow from the requirement to achieve a uniform flow pattern inside the reactor body creating conditions for the production of uniform morphologies and narrow particle size distributions of the product. It was taking into consideration the formation of recirculation areas and the temperature profiles inside the reactor. These modeling results are important in the context of the present work, they are presented in detail in Chapter 8.

The references included in each paper are listed in numerical format at the end of the chapter and any other references used in this thesis are listed alphabetically at the end of the thesis under “References”.

Chapter 1 - Introduction

This chapter includes the problem definition and the scope of the project, a statement of the project objectives and the thesis outline.

Chapter 2 - Contributions of authors

A description of the work carried out by the authors of the papers is presented and the contribution of each person involved in the work is stated.

Chapter 3 - Literature review

The literature review includes a brief presentation of thermal plasmas, a description of the fuel cells types and theory, and of the catalyst used presently in PEM fuel cells. Then, a detailed presentation of carbon black is included. The chapter ends with the description of the analytical methods used for the characterization of the carbon black materials.

Chapter 4 - Experimental equipments and methodology

The DC and the ICP plasma systems are described and the methodology used is discussed.

Chapter 5 - Experimental results: DC thermal plasma system

This chapter summarizes the experimental results of the DC thermal plasma system and states the conclusion regarding the use of the obtained material as a catalyst support in PEM fuel cells.

Chapter 6 - Carbon blacks produced by thermal plasma: The influence of the reactor geometry on the product morphology (Peer reviewed paper published in Plasma Processing & Plasma Chemistry Journal)

This chapter includes a published paper presenting different carbon black materials produced using the ICP plasma system. A comparison between two reactor geometries is also presented.

Chapter 7 - Carbon nano-flakes produced by an inductively coupled thermal plasma system (Peer reviewed paper published in Plasma Processing & Plasma Chemistry Journal)

The paper on carbon nano-flakes is included in this chapter. The material was obtained using the ICP thermal system and the conical shape reactor. An in dept characterization of the nano-flakes is also presented.

Chapter 8 – Carbon nanoparticles production by inductively coupled thermal plasmas: Controlling the thermal history of particle nucleation (Peer reviewed paper accepted for publication in Plasma Processing & Plasma Chemistry Journal)

Flow patterns, temperature profiles and particles residence times were calculated for the case of the ICP system and conical shape reactor at different reactor pressures. The results are presented and discussed.

Chapter 9 - Volatile compounds present in carbon blacks produced by thermal plasmas (Peer reviewed paper accepted for publication in Plasma Processing & Plasma Chemistry Journal)

A thermal treatment of the carbon material obtained using both DC and ICP plasma systems is presented in this chapter. The collection and characterization methods of organic contaminants are also presented and the results are discussed.

Chapter 10 - Discussion

The work derived from this project is presented and recommendations for future research are discussed.

Chapter 11 - Original contributions and recommendations for future work

This chapter summarizes the original contributions of this project and gives recommendations for future work.

Chapter 2 – Contributions of authors

This chapter describes the author's contributions to the papers incorporated in this thesis. The first paper includes the computer simulation and experimental results of the work done on the ICP system and two reactor geometries, the second paper presents experimental results obtained using the ICP system and the conical shape reactor. The third paper presents the flow and temperature modeling results for the case of the ICP system and conical shape reactor at different reactor operating pressures. The fourth paper presents the experimental results of a thermal treatment and characterization of carbon blacks produced using both DC and ICP systems.

1. **Pristavita R**, Mendoza-Gonzales N Y, Meunier J L and Berk D, Carbon Blacks Produced by Thermal Plasma: The Influence of the Reactor Geometry on the Product Morphology, *Plasma Chemistry and Plasma Processing* **30,** No 2, 267, 2010 (Chapter 6)

I carried out all the experimental and analytical work shown in this paper. I am also the first author of the article. The computer simulation work was carried out by Dr. Norma Mendoza, who is a co-author of this paper. Professor Jean-Luc Meunier and Professor Dimitrios Berk provided oversight and suggested corrections to the manuscript.

2. **Pristavita R**, Meunier J L and Berk D, Carbon nano-flakes produced by an inductively coupled plasma system, *Plasma Chemistry and Plasma Processing* **31,** No 2, 393, 2011 (Chapter 7)

I carried out all the experimental and analytical work shown in this paper. I am also the first author of the article. Professor Jean-Luc Meunier and Professor Dimitrios Berk provided oversight and suggested corrections to the manuscript.

3. **Pristavita R,** Mendoza-Gonzales N Y, Meunier J L and Berk D, Carbon Nanoparticles Production by Inductively Coupled Thermal Plasmas:

Controlling the Thermal History of Particle Nucleation, *Plasma Chemistry and Plasma Processing*, DOI : 10.1007/s11090-011-9319-y (Chapter 8)

I am the first author of the article. The computer simulation work was carried out by Dr. Norma Mendoza, who is a co-author of this paper. Professor Jean-Luc Meunier and Professor Dimitrios Berk provided oversight and suggested corrections to the manuscript.

4. **Pristavita R**, Roy R, Moran B, Meunier J L and Berk D, Volatile Compounds Present in Carbon Blacks Produced by Thermal Plasmas, *Plasma Chemistry and Plasma Processing*, DOI : 10.1007/s11090-011-9321-4 (Chapter 9)

I carried out all the experimental work shown in this paper. I am also the first author of the article. The analytical work was done in collaboration with Mr. Ranjan Roy, who is co-author of this paper. The heat treatment work was carried out by Mr. Blain Moran as an undergraduate summer student under my supervision; he is also co-author of the paper. Professor Jean-Luc Meunier and Professor Dimitrios Berk provided oversight and suggested corrections to the manuscript.

Chapter 3 – Literature review

3.1 Thermal plasmas

More than 99% of the known universe is in the plasma state. The plasmas consist of a mixture of electrons, ions, neutral particles, photons and exited species [Boulos, 1994]. Thermal plasmas are a type of plasma that can reach temperatures around 10 000 K and are characterized by high energy density and equality between the temperature of heavy particles and electrons temperature ($T_h = T_e$). This means that they are in or close to local thermodynamic equilibrium (LTE) state [Boulos, 1991]. Thermal plasmas can be generated by passing an electrical current through a gas. For this, the gas is forced to be electrically conductive by generating a certain number of charge carriers, a process known as "electrical breakdown".

Thermal plasma technology evolved from the 1980s to today into a well-established interdisciplinary science with many applications in materials processing. Typical examples of industrially used thermal plasmas include DC transferred arcs and RF inductively coupled discharges.

The DC plasma torches produce a high temperature plasma jet in which the material to be processed can be injected for in-flight melting and vaporization, or chemical dissociation. Commonly used gases for this type of systems include argon, helium, nitrogen and hydrogen. No oxidizing gases are used since these can damage the tungsten cathode. Typically power levels of the systems are below 100 kW. Higher power systems also exist up to the MW level. In this case however the tungsten-based cathode can no longer sustain the larger thermal loads; a water-cooled cylindrical cathode is used in these systems along with a gas vortex and possibly magnetic fields to move the arc root and distribute the heat load on the electrode.

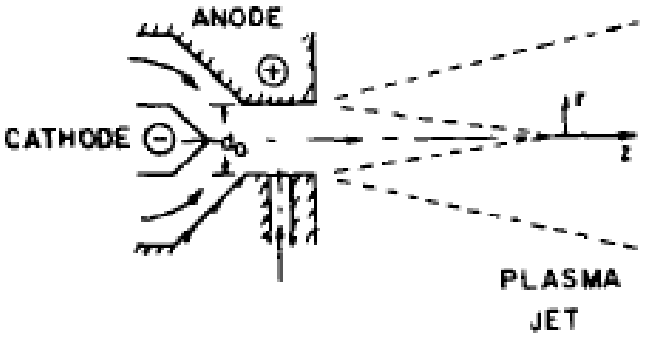

Figure 3.1 Schematic diagram of DC torches with thoriated tungsten cathode and annular copper anode [Boulos, 1991]

In the RF systems, energy coupling to the plasma is accomplished through the electromagnetic field generated by an induction coil. In this type of system the plasma is not in contact with the electrodes, thus eliminating possible sources of contamination and enabling the operation using a wide range of gases including inert, reducing, oxidizing and other corrosive systems. Typically power levels for laboratory systems are between 30 kW and 50 kW but industrial systems presently reach power levels up to 1 MW [Boulos, 1991].

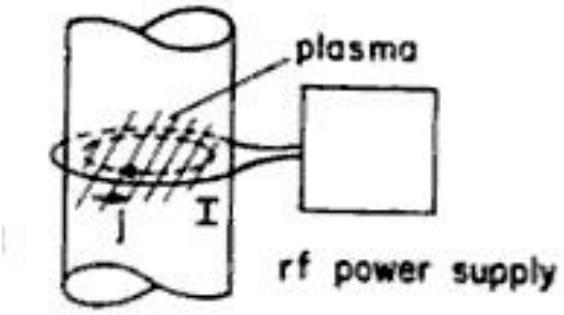

Figure 3.2 Schematic of an inductively coupled RF discharge [Boulos, 1994]

3.2 Fuel cells

Fuel cells are a very promising energy technology with many possible applications. They have a high efficiency compared to the internal combustion engines (~ 50% for the PEM fuel cells comparing with 15% for the internal combustion engines). The fuel cells have also a low or zero emission and they are very quiet (makes them very attractive for transportation applications) [Barbir, 2005].

A fuel cell is an electrochemical system which converts chemical energy into direct current (DC) electricity. The discovery of the operating principle of fuel cells is attributed to Sir William Grove in 1839, although it seems that the Swiss scientist Christian F. Shoenbein discovered the same process about one year earlier. In 1937, Francis T. Bacon started working on practical fuel cells and he developed a 6 kW fuel cell at the end of the 1950s. The fuel cells found their first practical application at the beginning of the 1960s, in the NASA's Gemini Space Flights, when a 1 kW PEM fuel cell was constructed to provide auxiliary power requirements in the space vehicles and drinking water for the astronauts. The application of fuel cells as a power source for the automobiles and buses started in the late 1970s, and received a major boost in the late 1980s and early 1990s, because of the new legislation to develop ultra low and zero emission vehicles. Another high potential application for the PEM fuel cell technology is in the field of portable power sources where it may be able to compete with the lithium ion or nickel/metal hydride batteries for higher efficiency energy sources [Costamagna et al, 2001].

3.2.1 Fuel cell types

Depending on the type of electrolyte used, the fuel cells can be grouped in: alkaline fuel cells (AFCs), polymer electrolyte membrane fuel cells (PEMFCs), phosphoric acid fuel cells (PAFCs), molten carbonate fuel cells (MCFCs) and solid oxide fuel cells (SOFCs) [Barbir, 2005].

Alkaline fuel cells (AFCs)

These fuel cells have been used in the space program since 1960s. The electrolyte (KOH) is retained in an asbestos matrix and the electrocatalysts that have been used include Ni, Ag, metal oxides and noble metals. There are two types of AFCs: for high temperature operation (~250^{o}C), in which concentrated KOH solution is used (85 wt%) and for lower temperature operation (<120^{o}C), in which a less concentrated KOH solution is used (53-50 wt%). It uses sintered nickel electrodes with Pt metal catalyst (40 mg/cm^2 Pt loading). These types of fuel cells are attractive because the alkaline electrolyte is much less corrosive than a strong acidic electrolyte (such as phosphoric acid for the case of the PAFC) and the oxygen reduction in alkaline environment is more favorable than in acid environment (i.e. the voltage drop is lower). This type of systems yields the highest voltage at comparable current densities, leading to a higher efficiency of the system compared to other fuel cell systems. It operates well at room temperature and has a good cold start capability. The disadvantage of this type of fuel cell consists in the fact that not many organic fuels and no air (this fuel cell is intolerant to CO_2) can be used in this type of systems. Also, given the strong alkaline environment, the solubility of carbonate crystal is poor, leading to the blocking of the electrolyte pathways and electrolyte pores and to a poor long-term stability of AFCs [Vielstich et al, 2003].

Phosphoric acid fuel cells (PAFCs)

PAFCs are used for stationary electricity generators (200 kW units). The electrolyte used is concentrated phosphoric acid (~100%) retained usually on a SiC matrix. The electrocatalyst is Pt for both the anode (Pt loading of 0.50 mg/cm^2) and the cathode (Pt loading of 0.25 mg/cm^2). As a catalyst carrier, conductive oil furnace black (Vulcan XC-72 from Cabot Corp.) is used. These fuel cells can operate at temperatures between 150^{o}C and 220^{o}C. This type of fuel cells has the advantage (comparing with AFCs) that it does not need to deal with the CO_2 (from air, organic fuel materials or resulting from the electrochemical conversion of organic fuels). The disadvantages of these systems include cathode

catalyst degradation, electrolyte migration, cell contamination and material corrosion. The Pt cathode catalyst loses activity by dissolution (Pt solubility increases with potential) into the electrolyte and loss of surface area per unit mass (by sintering, dissolution-precipitation and crystallite migration). The electrolyte migration results into decay due to evaporation of electrolyte from the cell, migration from the cathode side to the anode side of the cell due to potential profile across an operating cell (anode flooding) and migration of electrolyte through the bipolar plates. Very important is the fact that harmful contaminants can enter the cell in the reactant gas streams poisoning the catalyst or reacting with the electrolyte and changing its properties [Vielstich et al, 2003].

Molten carbonate fuel cells (MCFC)

These types of fuel cells are not yet commercialized. The electrolyte is a combination of alkali (Li, Na, K) carbonates retained on a $LiAlO_2$ matrix. NiO is used as cathode material and Ni, Cr and Al alloy is used as anode material. The operating temperatures are between 600^{o}C and 700^{o}C. The MCFCs have the advantage of high open-circuit potential (OCV) value, but the current density is limited to low values. Important issues with these types of fuel cells are the heat management and high-pressure operation, which are important to reach high efficiencies. This requires the addition of a gas circulation system which increases the final production cost. Also, an important issue of the MCFCs consists in reducing the NiO dissolution (cathode dissolution) [Vielstich et al, 2003].

Solid oxide fuel cells (SOFCs)

Small units of SOFCs are commercialized for portable power and auxiliary power in automobiles but these systems are mainly targeted for moderate to high electrical power generation, supplying the demand for example for buildings or small industries. The electrolyte is a solid, nonporous metal oxide, usually Y_2O_3 stabilized with ZrO_2 (YSZ). The cathode material is a Pr-ZrO_2/SnO/In_2O_3 alloy and the anode is made of YSZ material. In order to provide ion conductivity of the solid electrolyte, the operation temperature ranges in SOFCs are higher than for

the other types of fuel cells, with temperature values typically between 800^{o}C and 1000^{o}C. The SOFCs are superior to the MCFCs because of the lower corrosion rates. The main drawback of these systems (SOFCs stacks) consists in the use of metal interconnects due to materials different thermal expansion properties and durability against frequent thermal cycles. To increase the durability of materials, a coating can be applied to the components, but this increases the fabrication cost. [Vielstich et al, 2003].

Polymer electrolyte membrane fuel cells (PEMFCs)

PEM stands for polymer electrolyte membrane or proton exchange membrane. This type of fuel cell technology has drawn a lot of attention because of its simplicity, viability, quick start-up and because it was demonstrated that it can be used for almost any type of applications. PEMFCs are ideal for automotive applications, but also for stationary power generators and portable power applications. The electrolyte is a thin (20-200μm) polymer membrane, such as perfluorosulfonated acid polymer (Nafion^{TM}). The operating temperature is between 60^{o}C and 80^{o}C [Barbir, 2005].

3.2.2 PEM fuel cell theory

The heart of a PEM fuel cell is a polymer membrane (Figure 3.3) that is impermeable to gases but it conducts protons. The membrane is squeezed between two porous, electrically conductive electrodes. The electrodes are usually made out of carbon cloth or carbon fiber paper. Between the porous electrode and the polymer membrane is a layer of catalyst, typically platinum supported on carbon.

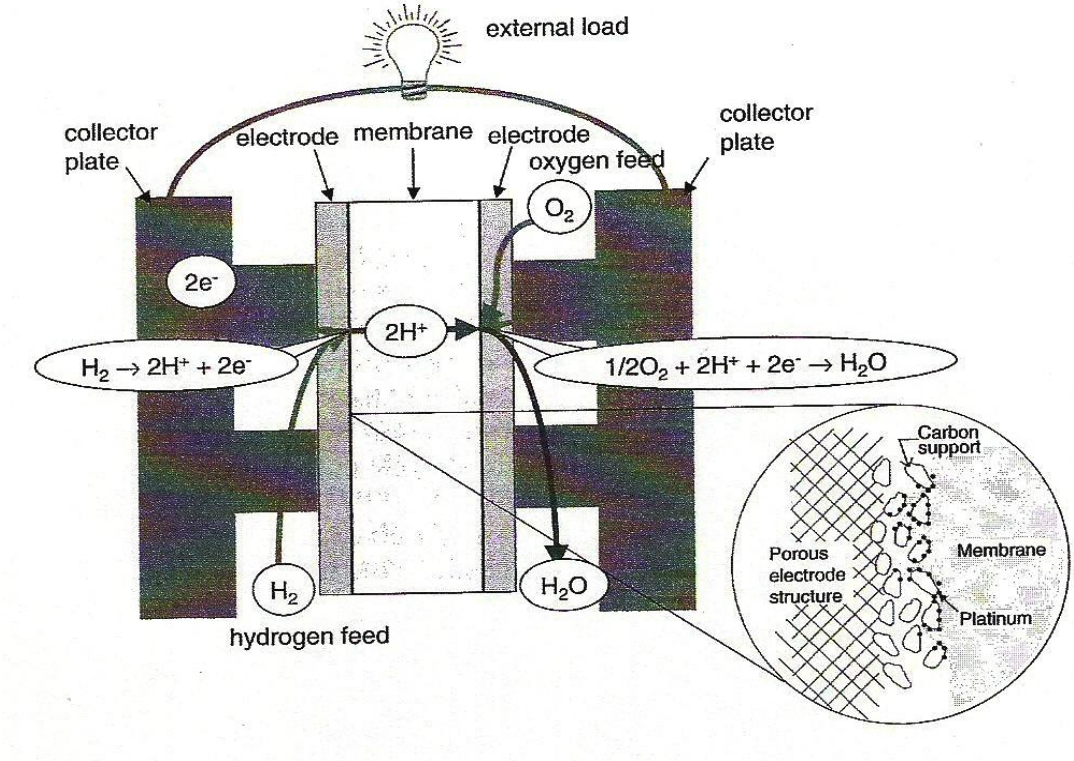

Figure 3.3 Schematic of a PEM fuel cell [Barbir, 2005]

The hydrogen molecules give up electrons at the anode and form hydrogen ions. This process is made possible because of the presence of the platinum catalyst. The electrons travel through an external circuit, producing electrical work and then they reach the cathode. The hydrogen ions pass through the proton exchange membrane, where they combine with the oxygen molecules and the electrons at the cathode and form water molecules. No pollution is produced and the only products are electricity, water and heat.

The electrochemical reactions take place at the surface of the catalyst, at the interface between the electrolyte and the membrane.

Anode: $H_2 \rightarrow 2H^+ + 2e^-$ (3.1)

Cathode: $\frac{1}{2} O_2 + 2H^+ + 2e^- \rightarrow H_2O$ (3.2)

Overall: $H_2 + \frac{1}{2} O_2 \rightarrow H_2O$ (3.3)

There are three kinds of species that participate in the electrochemical reactions: gases, electrons and protons. The reactions can take place only on specific spots

of the catalyst surface where all these three species have access. The electrons travel through the electrically conductive solids, including the catalyst. To make this possible, it is important that the catalyst is electrically connected to the substrate. Protons travel through ionomer (Nafion®), so the catalyst has to be in contact with the ionomer. The gases travel through voids, so the electrodes must be porous. The reactions here take place at a three-phase boundary, as can be seen in Figure 3.4a. This reaction surface area can be enlarged by incorporating ionomer in the catalyst layer (Figure 3.4b) or by covering the entire catalyst surface with a thin ionomer layer (Figure 3.4c) [Barbir, 2005].

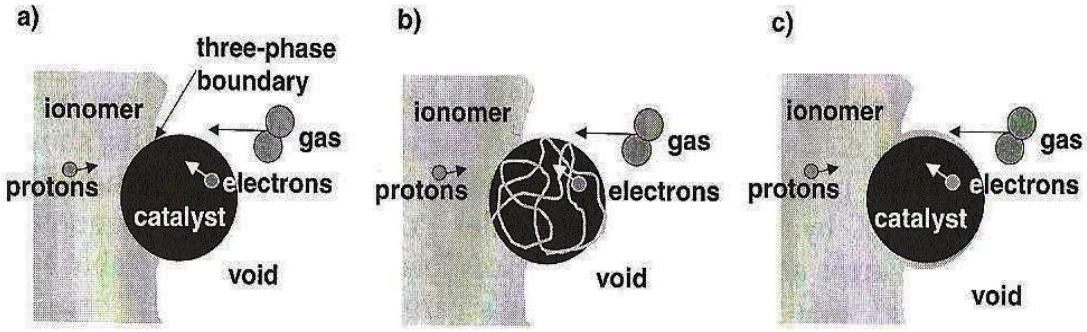

Figure 3.4 Graphical representation of reaction sites [Barbir, 2005]

3.2.3 The catalyst

The most common catalyst in PEM fuel cells for both hydrogen oxidation and oxygen reduction reactions is platinum. The amount of Pt catalyst used in a fuel cell is around 0.3-0.4 mg/cm^2. The most important factor is not the amount of the catalyst, but its surface area, so it is very important to have small Pt particles (4 nm or smaller) dispersed on the surface of the catalyst support (Figure 3.5). The high surface area to volume ratio of supported catalysts maximizes the area of catalytic surface available for reactions.

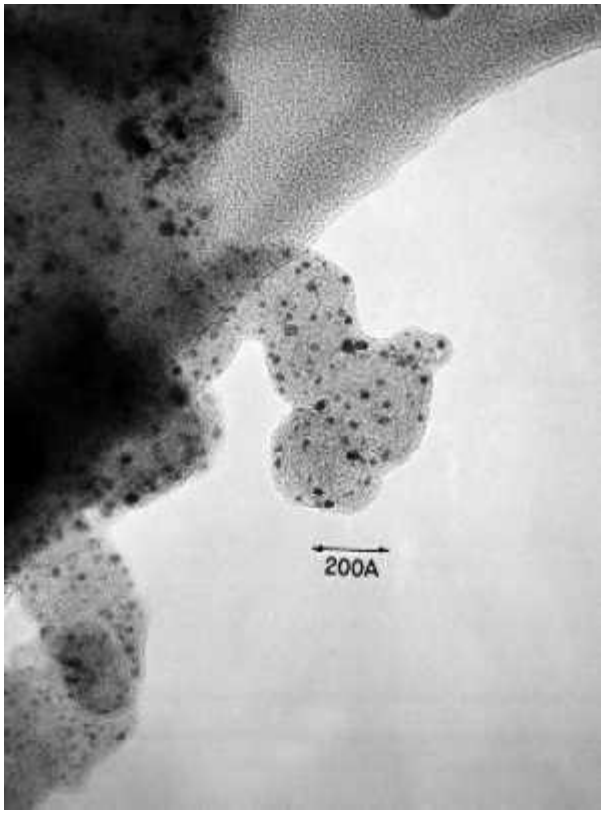

Figure 3.5 High-resolution transmission electron micrograph platinum particles dispersed on carbon [Kinoshita, 2001]

High dispersion of Pt nanoparticles on the carbon support is very important in order to minimize the loss in activity due to agglomeration of the nanoparticles. The catalyst can be deposited on the support using different methods, such as spreading, spraying, sputtering, painting, screen printing, decaling, electrodeposition, evaporative deposition and impregnation reduction. Carbon powders with high mesoporous area (>75 m^2/g) are used as catalyst support. A typical support material is Vulcan XC72R by Cabot, but other carbon black materials are also used, materials such as Black Pearls BP 2000 (by Cabot), Ketjenblack EC-600JD (by Akza Nobel) and Printex XE-2 (by Degussa Huls).

There are two ways of preparing the catalyst layer and to attach it to the ionomer membrane (to form the membrane electrode assembly). The first way consists in depositing the catalyst layer to the porous gas diffusion layer (usually carbon fiber paper or carbon cloth) and then hot-press it to the membrane. The

second way is to apply the catalyst layer directly to the membrane and add in a later stage the gas diffusion layer [Barbir, 2005].

Alternative catalysts for the oxygen oxidation reaction taking place in the fuel cell have been studied. Some Pt-based alloy materials were proposed as a Pt replacement. Materials like Pt_3Co and Pt_3Cr alloy nanoparticles exhibit better performance than Pt under fuel cell conditions [Rao et al, 2011].

Due to increasing cost of Pt, intense research work is conducted for the development of materials with the required stability and greater activity by replacing completely Pt with non-noble materials. Many non-platinum materials, such as transition metal oxides, chalcogenides and carbides were investigated as electrocatalysts for PEM fuel cells applications. Transition metal carbides, such as tungsten carbide were used as anode material due to their corrosion resistance, electrical conductivity, good resistance to CO poisoning and a Pt-like behavior for the chemisorptions of hydrogen and oxygen. But these materials exhibited a very poor activity. Similar properties to the transition metal carbides can be seen with transition metal nitrides, however the nitrides exhibit a charge transfer because of the difference in electronegativity between the metal and the nitrogen atoms. This charge transfer results in the creation of base/acid sites leading to a catalytic activity of the material [Zhong et al, 2006].

Nitrides catalyst materials were obtained by adsorbing Fe-N_4 and Co-N_4 macrocycles on a carbon support and pyrolizing the resulted material in an inert atmosphere [Zagal et al, 2006]. An important step in this direction was obtained when these expensive macrocycles showed they could be replaced by individual N and Co precursors [Gupta et al, 1989]. In 1964, Jasinski [23] discovered that cobalt phthalocyanines display a high activity for the ORR in alkaline electrolytes. Later on, it was revealed that a heat treatment of these metal chelates improves the stability and activity of the catalyst. In 1989, Yeager and his team showed that Co^{II} or Fe^{II} salts can be pyrolyzed with polyacrylonitrile at 800 ^{0}C in argon to obtain catalysts for the ORR.

Alternative catalysts can be also obtained when iron, nitrogen and carbon are pyrolyzed together at high temperature in an inert or reductive atmosphere. In the latest studies [Jaouen et al, 2006; Médard et al, 2006] alternative catalysts were obtained from the high temperature treatment of a carbon black powder and iron acetate in an ammonia-rich atmosphere. The reaction of ammonia with the disordered carbon leads to the N-bearing functionalities which are necessary to bind iron cations to the carbon support. It was found that the density of active sites on the carbon is limited by the maximum loading of metal. Using a loading greater then 0.2-0.5 wt% of metal on the carbon, the activity of the catalyst decreases because of the small amount of nitrogen on the carbon (1-2 at.%) that bonds the metal atoms and form these active sites. The quantity of nitrogen which can be incorporated in the catalyst structure is directly related to the nanostructure of the surface of the carbon black particles. The nitrogen has to be bonded to the edges of the graphene crystallites throughout a pyridinic type bond to be able to coordinate the iron in the catalytic site [Lefèvre, 2002].

The graphene sheets can present two types of edges: a ”zig-zag” edge and an “armchair” edge. There are also three types of surface-bonded nitrogen: the pyridinic type, the pyrrole type and the substituted quaternary type, but only the pyridine type can form an active site. Taking in account all these structural constrains, two geometries of the active sites are seen possible, as presented in Figures 3.6a and 3.6b. The coordination number of iron can vary between 4 and 6, but the coordination number of iron in the carbon black catalytic site is unknown.

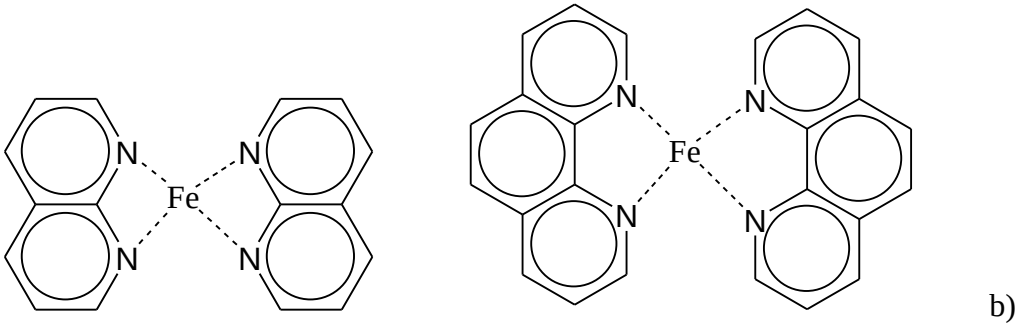

Figure 3.6 Possible structures of active sites: a) “zig-zag” structure and b) “armchair” structure

The activity of the created active sites is determined by the type of nitrogen-carbon bonds and possibly the geometry of the carbon surrounding these bonds.

In nature, a similar structure occurs in iron porphyrin (heme) where the metal atom (i.e. iron) is coordinated into the porphyrin active site via coordinate-covalent bonds (see Figure 3.7). In this type of bonds, both shared electrons come from the same atom, called the donor atom (i.e. nitrogen). The coordination number of the central metal (i.e. iron) atom is given by the total number of occupied coordination sites around the central iron atom. In heme, the iron coordination number is five (four in plane of donor atoms and one axial ligand which is out of plane in the figure) or six (four in plane of donor atoms and two axial ligands out of plane in the top, respectively the bottom direction), but never four (no axial ligands only, as shown on the in-plane structure of Figure 3.7). Depending on the coordination number, the iron cation can be located at the center (planar structure) or above (out-of-plane structure) the porphyrin tetradentate site. Iron II has six valence electrons of d type. In the case of the five-coordinate complex, there are six d-electrons distributed over five d-orbitals resulting in four unpaired electrons (spin state S=2) and a "high-spin" complex (Figure 3.8). In this state, the orbitals d_{x2-y2} and d_{z2} are partially occupied, the iron-ligand bond distances are increased and a weaker bond is formed. Because of these longer bonds and the minimization of steric interactions the iron(II) cation is located out-of-plane. When a six-coordinate complex is formed, all six d-electrons are distributed over the d_{xz}, d_{yz} and d_{xy} orbitals. This results into a "low-spin" complex (spin state S=0) and a shortening of bonds, leading to a planar structure of the active site.

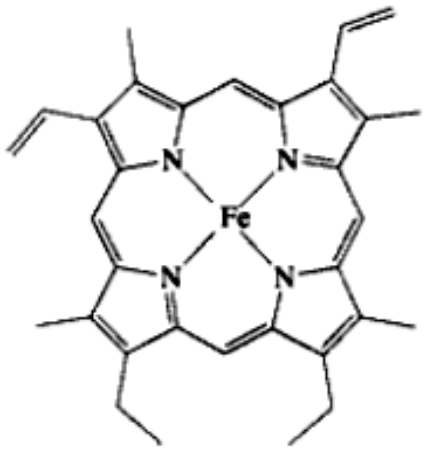

Figure 3.7 Iron porphyrin chemical structure [Atwood *et al*, 1996]

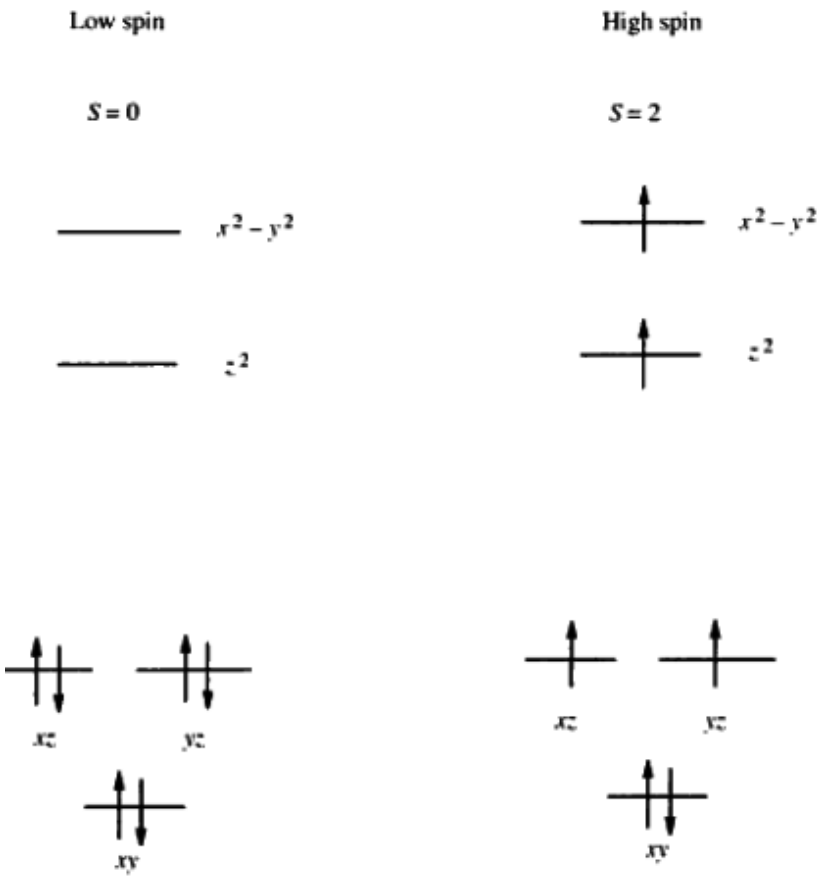

Six-coordinated complex **Five-coordinated complex**

Figure 3.8 Iron (II) d^6 configuration [Atwood *et al*, 1996]

From the analogy between the heme structure and the zig-zag & armchair structures of Fe-N and C we can conclude that both structures are probably incomplete, requiring one or two additional N pyridinic bond(s) out of plane, and the requirement of specific availability of such out-of-plane sites in the carbon structure.

Another very important aspect is the stability of the non-noble catalyst materials. It was showed that even if the activity of the non-noble catalyst materials was greatly increased by increasing the number of active sites formed, these catalysts are not stable (< 20h in PEM fuel cell medium). The stability of the catalyst materials was related to the degree of crystallinity of CB support used. The fuel cell is a very corrosive environment. Carbon black structures presenting a large amount of defects in their graphitic structure are expected to induce corrosion sites and a more rapid local deterioration of the support. Highly graphitized structures are expected to reduce the onset of such corrosion phenomena. It was found that the higher the degree of crystallinity (higher L_{eq} values) the more stable is the catalyst [Larouche, 2010].

3.3 Carbon black

3.3.1 Carbon black production

Carbon black is elemental carbon in the form of colloidal particles that are produced by the incomplete combustion or thermal decomposition of solid, liquid or gaseous hydrocarbons under controlled conditions. The current world CB production is estimated at more than 8 million tons per year [Moreno-Couranjou, 2009].

Two types of manufacturing processes are known: the furnace process and the thermal process. The “furnace” process uses heavy aromatic oils as feedstock and a closed reactor to atomize the feedstock. The reaction rate is controlled by steam or water spraying. The “thermal” process uses natural gas as feedstock and a pair of furnaces that alternate approximately every five minutes between preheating and carbon black production.

More than 95% of the total CB production comes from the furnace process [Moreno-Couranjou, 2009]. The disadvantages of this process are the incomplete combustion of the carbon precursor and a limited reaction temperature (this being a function of the carbon source/air ratio). Also, both processes emit large amounts of polluting gases, such as CO, CO_2, SO_2 and NO_x.

3.3.2 Carbon black properties

There are many types of carbon black powders, all of them containing more than 97% elemental carbon arranged as aciniform (grape-like cluster) particulates. Some of the carbon black properties are presented in the table below.

Tabel 3.1 Properties and characteristics of carbon black

Formula weight	12
Physical state	Solid: powder or pellet
Particle size	13-95 nm
Particle shape	Spherical, irregular, flake, shot, needle, crystal
Surface area	90-460 m^2/g

During the production process, nearly spherical nodules (primary particles) fuse and form aggregates. Strong electrical forces bond the aggregates and promote the formation of agglomerates (see Figure 3.9). From the physical point of view, carbon black is an intermediate structural form between graphite and an amorphous structure. In *graphite*, the carbon atoms form layers (planes of symmetrical hexagons). Each layer is horizontally displaced relative to the next one. Starting with this perfect arrangement, degenerated structures can be constructed based on lower degrees of symmetry. In a *turbostratic structure* the layers are disorientated by a series of rotations of the planes. In a *lubricostratic structure* the planes show an arbitrary displacement. These two structural forms are nearly identical. Another structural form can contain only isolated planes (*single layer structure*), disorientated with respect to one another. And finally, in an *amorphous structure*, the carbon atoms are not located in planes. In carbon

black particles, all these forms coexist. There are many types of carbon black powders, depending on the type and amount of organized and unorganized materials present in the particles [Donnet, 1976].

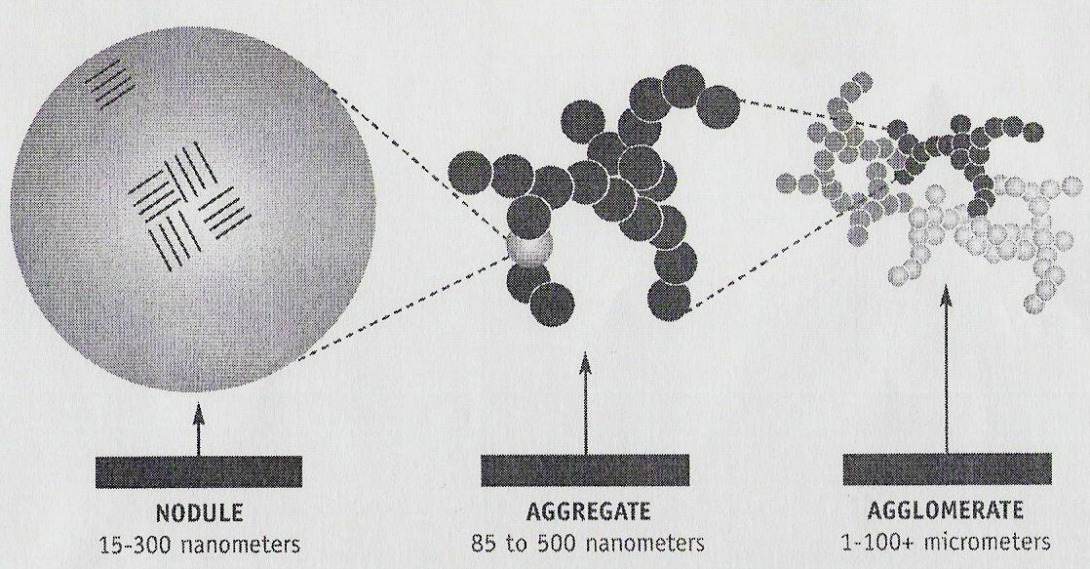

Figure 3.9 Carbon black structure development [Carbon Black User's Guide]

In Table 3.2 are presented the microstructural properties of different carbon blacks, according to Austin, (1958). In the Table 3.2, L_a and L_c are the average lengths of the parallel layers in the ab plane, respectively, and the average stacking height in the c direction (a,b and c are vectors defined for the graphite structure). As observed in the same table, carbon black particles can be considered to consist in parts of crystallites consisting in average of three to four layers. These layers are orientated around multiple centers, randomly distributed in the particle (growth centers) and are connected between them by poorly organized carbon. The differences in L_a are attributed by Austin [Austin, 1958] to the distortion of the planes, due to the presence of the impurities or lattice imperfections. As a consequence of the particles structure, the carbon black presents heterogeneity of the physical-chemical properties. The same author

showed that the carbon microstructure depends on the initial hydrocarbon feedstock and on the method of production.

Table 3.2 Microstructural properties of carbon blacks

Carbon Black	Code	Dimensions (nm)			Carbon (%)			Probability of number of parallel planes	
		L_a		L_c	Unorganized	Parallel planes	Single planes	3	4
		(10)	(11)	(002)					
Acetylene	ACET	2.6	2.6	2.5	4	96	0	--	--
Vulcan SC	SCF	2.0	1.6	1.06	8	90	2	1.0	0
Sterling SO	N 550	1.6	1.4	1.13	11	83	5	0.8	0.2
Philblack A	N 550	2.0	1.5	1.24	5	70	25	0.5	0.5
Kosmos 50	N 440	1.8	1.4	1.24	11	79	10	0.5	0.5
Philblack O	N 330	2.0	1.6	1.17	15	83	2	0.7	0.3
Philblack I	N 220	1.4	1.6	1.13	16	80	4	0.8	0.2
Philblack E	N 110	1.7	1.6	1.13	15	74	6	0.8	0.2
Sterling V	N 660	2.0	1.5	1.24	13	74	13	0.5	0.5
Statex B	N 326	2.0	1.6	1.17	5	89	6	0.7	0.3
Kosmos 40	N 601	2.2	2.2	1.34	7	63	30	0.2	0.8
Pelletex	N 770	2.0	1.6	1.34	8	83	9	0.2	0.8
Thermax	N 990	2.4	1.7	1.38	4	40	6	0.1	0.9
P-33	N 880	2.8	1.9	1.39	8	82	10	0.2	0.8
Spheron 4	S 302	1.6	1.6	1.12	9	67	24	0.9	0.1
Spheron 6	S 301	2.0	1.6	1.12	6	80	14	0.7	0.7
Spheron 9	S 300	1.6	1.4	1.12	15	81	4	0.7	0.3
Carbolac	HCC	1.6	1.5	1.12	26	74	0	0.85	0.15

By heating carbon black at high temperatures (up to 3000^{o}C), an increase in the degree of crystallization is observed due to an ordering and limited growth of crystallites. This growth is inhibited by the presence of unorganized carbon.

Another important physical property of carbon black powders is the surface area. The carbon black particles are very small; therefore the specific surface area is large (see Table 3.1). The carbon black surface and its porosity are the key parameters in using these materials as catalyst support in the fuel cells, because these two properties are considered to influence the dispersion of the metal nano-particles at the carbon black surface as well as the segregation effects of these metal particles during catalyst preparation and fuel cell operation. Good metal particles dispersion is important for the high activity and for the stability of the catalyst. The stability of the catalyst ensures a good cycling stability and a long life of the fuel cell.

3.3.3 New carbon black grades

New carbon black structures were synthesized recently using plasma technology. Girshick *et al* [1988] conducted a general modeling investigation on the physical requirements for homogeneous nucleation of particles from the vapor phase of some arbitrary material in a thermal plasma reactor. They reported that the particle size and the number of nucleated particles are affected essentially by two factors: the cooling rate at the location of the nucleation and the monomer concentration. High monomer concentration and low cooling rates are favoring the nucleation of larger and fewer particles. There are possibly three routes for the conversion from the gas phase to a condensed phase [Girshick, 1989]: homogeneous nucleation, condensation on an existing particle and heterogeneous nucleation at a particle surface. The homogeneous nucleation is favored by high temperature chemistry and rapid cooling.

Fulcheri *et al* [1997] used an AC thermal plasma reactor to produce carbon black, and they concluded that temperature is one of the most important process parameters that influence the properties of the product. In their experiments, they observed the formation of three families of carbon blacks. They injected the hydrocarbon source in the arc zone (T~5000 K for the case of a nitrogen plasma and ~10000 K for an argon plasma), and the obtained product was a highly organized carbon black. The second family of carbon black was an amorphous product, with spherical particles, a structure corresponding to a low temperature carbon black. This was attributed to a growth of the particles in a low temperature region of the reactor ($T<1600^{o}C$). In the last family of products, the carbon black particles were highly crystallized and showed a clear polygonal shape. They assumed that these particles initially belonged to the second family of carbon black which was recirculated in the arc zone.

Fabry *et al* [2001] developed a 100 kW 3-phase AC plasma torch with an open circuit voltage of 760 V, a maximum current of 266A and a frequency of 50 Hz. Using Transmission Electron Microscopy to analyze the product, they also observed the presence of three families of carbon black. The first one was composed of particles with a high degree of organization and poorly aggregated

molecules. The second family was ***c***omposed of nearly spherical amorphous particles, which indicated a formation mechanism at low temperatures. The last family looked like acetylene black (refer to Appendix I for structure) aggregated, suggesting a formation at high temperature. The authors concluded that the nature of the feedstock does not influence the size distribution of carbon black aggregated but an important role is played by the zone where the carbon source is injected. The injection of the carbon source in the annular zone between the electrode and the sleeve gives smaller aggregates composed of more than 40% of the particles with 50 nm diameter.

In a review of some plasma produced carbon blacks, Probst *et al* [2002] concluded that a part of these powders have a high degree of crystallinity, the carbon layers are very large and practically the layer edges do not exist. This type of growth suggests a molecular growth in the homogeneous phase.

Juan *et al* [2003] showed a new route to produce carbon black in which natural gas was cracked in the absence of oxygen using electric energy supply given by a plasma jet. The obtained carbon black particles had a narrow size distribution, a small average diameter (38 nm) and a highly branched aggregate structure. The experiments were carried out in atmospheric pressure using electric powers between 90 kW and 200 kW. Nitrogen was used as plasma gas and no quench was used in all the experiments. Using Fourier Transform Infrared (FTIR) Spectroscopy to analyze the product, they observed aromatic C-C bonds, as well as a large amount of nitrogen-containing functional groups, such as –NH and –CN.

A DC-RF hybrid thermal plasma reactor [Kim *et al*, 2005] was developed by Kim *et al* [2005]. The carbon source was methane. The produced carbon black presented a large surface area and also a high degree of crystallization.

In 2009, a non-thermal plasma reactor was used by Moreno-Couranjou *et al* [2009] for the continuous gas phase synthesis of carbon nanoparticles at atmospheric pressure. A large range of carbon morphologies were synthesized, including concentric texture nanocarbons similar to furnace-type CB, acetylene-

type CB, carbon shells filled with metal, “crumpled paper sheet” isotropic texture nanoparticles and carbon rods.

More recently, graphene flakes were produced in a high-current arc discharge setup [Levchenko *et al*, 2010]. The setup contained carbon anode and cathode, installed in a non-magnetic vacuum chamber. A Y-Ni catalyst powder was used to promote the graphene flakes growth. The estimated size of the flakes was approximately 500 – 2500 nm, typically with up to 10 graphene layers.

Please refer to Appendixes I for different types of carbon black structure.

3.3.4 Formation mechanism

Fabry *et al* [2001] used a 3-phase AC plasma torch with a nominal power of 100 kW and a 2 meters high, water-cooled stainless steel reactor to obtain new carbon black grades from hydrocarbon cracking. They indicate that the internal fluid flow has a strong influence in the resulting structure of carbon particles. In their work it was concluded that most of carbon black particles grow at temperatures in the range 1300-1600 K and are then annealed in the region of electric arcs due to fluid recirculation. TEM analysis indicated the existence of three types of plasma-generated carbon black particles and the existence of a dominant type consisting of partially graphitized spherical particles with mean diameter in the range 150-200 nm. A three-step mechanism was assumed. The first step consists in the primary growth of the particles at low temperature (~ 1500 K). The second step consists in the recirculation of the particles in the high temperature regions of the reactor (arc jet zone) causing partial graphitization of the carbon surface layer. The last step of the process is a secondary growth of the particle in the low temperature region, the particles forming an amorphous surface layer.

Graphene type carbons formation mechanism was proposed by Levchenko *et al* [2010]. The following growth scenario was assumed. First a base graphene layer nucleates and then it grows to a critical size. Then, a second graphene layer nucleates on top of the first one and the process continues till the flake is deposited in the collection area. The flake size is determined by the first-nucleated graphene layer.

3.4 Characterization techniques

The obtained material is characterized using different techniques, such as: Scanning and Transmission Electron Microscopy (SEM and TEM), X-Ray Diffraction (XRD), X-Ray Photoelectron Spectroscopy (XPS), BET for surface area measurements, thermo gravimetric analysis (TGA), and Raman Spectroscopy. The material was also tested for the catalytic activity (fuel cell tests done at INRS).

Raman Spectroscopy

When monochromatic radiation is sent to a sample, this light will interact with the sample. It may be reflected, absorbed or scattered. A small fraction of light (approximately 1 in 10^7 photons) is scattered at optical frequencies different from, and usually lower than, the frequency of the incident photons. The difference in the energy between the incident photon and the Raman scattered photon is equal to the energy of vibration of the scattering molecule. By plotting the intensity of scattered light versus the energy difference, a Raman spectrum is obtained. The Raman spectrum provides information on molecular bond energies and orientations, in other words it provides a tool to identify the type of bonds present at the surface of the sample. The Raman spectrum of a carbon sample shows different vibration modes visible as independent peaks or broader bands. Two of these peaks are important for the characterization of carbon black powders: the graphitic mode (G) located in the 1500 cm^{-1} – 1600 cm^{-1} range and the disorder mode (D) situated from 1250 cm^{-1} to 1350 cm^{-1}. The G mode informs about the graphitic content of the sample and the D mode about the presence of non-graphitized species, such as carbon impurities, amorphous carbon and pentagon rings. Typical spectra of different allotropic forms of carbon are presented in Figure 3.10.

Graphitic indices are used for nanocarbon materials characterization. These parameters are calculated by using the areas of the D and G bands. The most important index used in the literature is the crystallite size $L_{a,}$ which corresponds to the in-plane dimension of the single microcrystalline domain in graphite. This

index is inversely proportional to the integrated intensity ratio I_D/I_G [Jawhari et al, 1995]. Other important lattice parameters are the D band width at half maximum w_D, the crystallites length L_{eq} and the 2D band (also named D' band) position w_{2D}.

An assessment of the purity of the product can be made from Raman spectra by using the relative ratios of the Raman peaks. The most suitable Raman ratio was found to be $I_{G'}/I_D$ [DiLeo et al, 200]. This follows from the fact that the G' band results from a two-phonon process and shows an intensity decreasing as the sample becomes less ordered. The impurities present in the sample does not allow the coupling effect necessary for the two-phonon process, yielding a better discrimination between well graphitized and disordered samples [DiLeo et al, 2007].

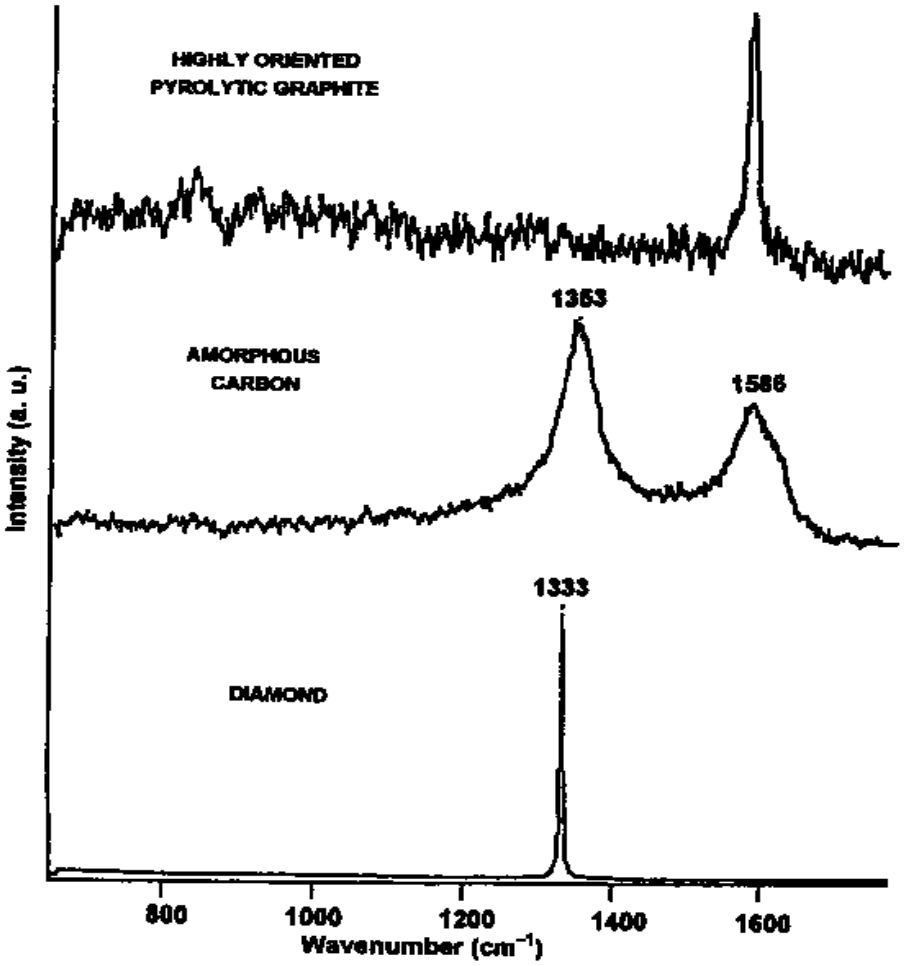

Figure 3.10 Raman spectra of allotropic form of carbon

Raman spectroscopy gives information about the carbon powder structure. Raman spectra of natural graphite reveals a sharp and intense G band while the G' band is broader and less intense (see Figure 3.11a). The G' band changes in intensity and shape for carbon powders having a crystalline morphology composed of a small number of graphene layers (1 to 5 layers), becoming a single sharp and intense peak, more intense than the G band. By increasing the number of grapheme layers a broadening of the G' band can be observed, as presented in Figure 3.11b [Ferrari et al, 2006].

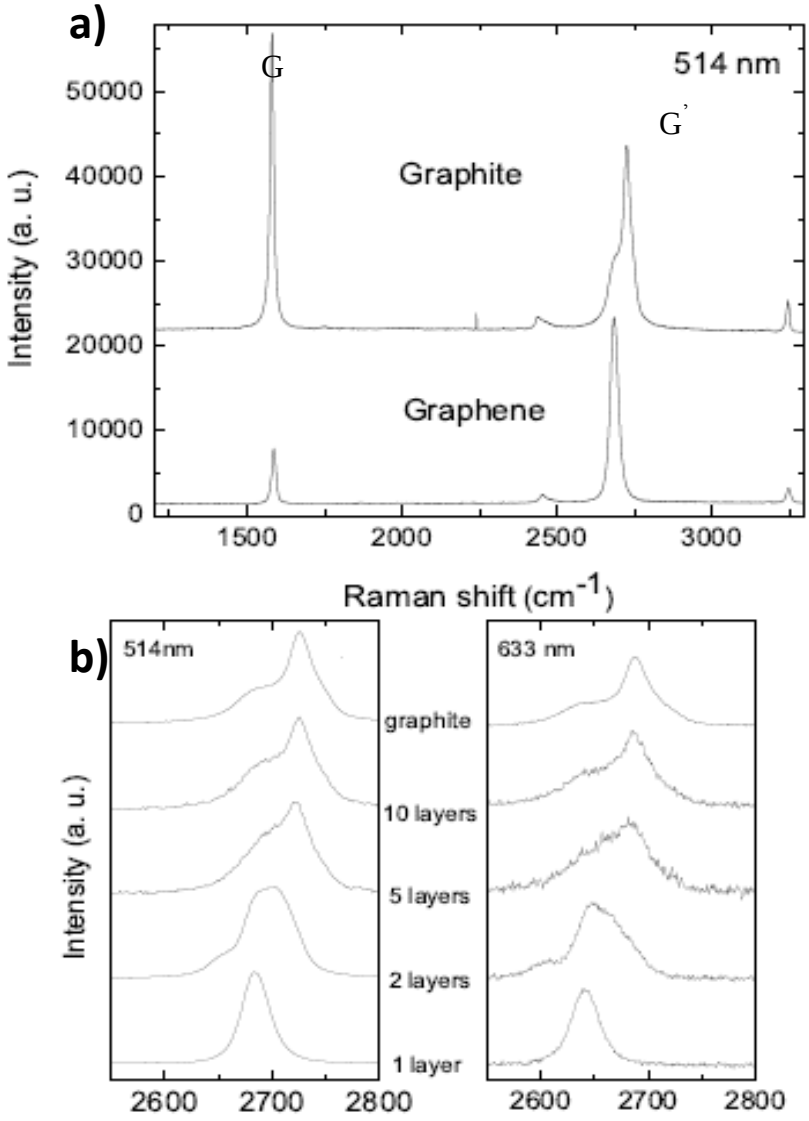

Figure 3.11 a) Comparition of Raman spectra of graphite and graphene; b) evolution of spectra with number of layers [Ferrari et al, 2006]

All the spectra presented in this thesis were recorded by using an inVia Reflex confocal micro-Raman from Renishaw. The equipment uses a Leica microscope with a 50x objective, with a grating of 1800 l/mm and a CCD camera. There is a choice of four lasers, with different wavelength: 488 nm, 514.5 nm, 632 nm and 780 nm, but only the 514.5 nm laser was used for our measurements. The main disadvantage of this technique is the fact that with the use of this wavelength, the depth of analysis is < 100 nm. The system was calibrated using silicium reference (peak at 520 cm^{-1}). The equipment final resolution is ±1 cm^{-1} on the peak position and ±5 cm^{-1} for the peak/band width. All the spectra were recorded in the 150 cm^{-1} to 3500 cm^{-1} range. Wire 2.0 software was used for the spectra analysis.

X-ray Diffraction (XRD)

XRD is a powerful non-destructive technique used to characterize crystalline materials. It provides information on structures, phases, preferred crystal orientations and other structural parameters such as average grain size and crystal defects. The spectrum presents the X-ray diffraction peaks, produced by constructive interference of the beam scattered from each set of planes at specific angles. In a XRD spectrum the presence of sharp peaks (Figure 3.12a) indicates a highly graphitized structure. The broadening of the peaks (Figure 3.12b) is due to the presence of crystallites having a small size and to the presence of strain in the structure.

From the peak position in the XRD diffraction patterns and using Bragg's law, the lattice parameters, such as crystallites size L_a, crystallites dimension L_c and the interlayer spacing d_{002} can be calculated.

The main advantage of using XRD is the use of a relatively large amount of sample (if compared with other techniques such as TEM and Raman spectroscopy) and a depth of analysis of a few micrometers.

The system used in this project is a PHILIPS PW1710 powder X-ray diffraction system equipped with a copper X-ray source operated at 800 W. Philips PC APD and Philips PC Identify software were used for the diffraction patter analysis and peak identification.

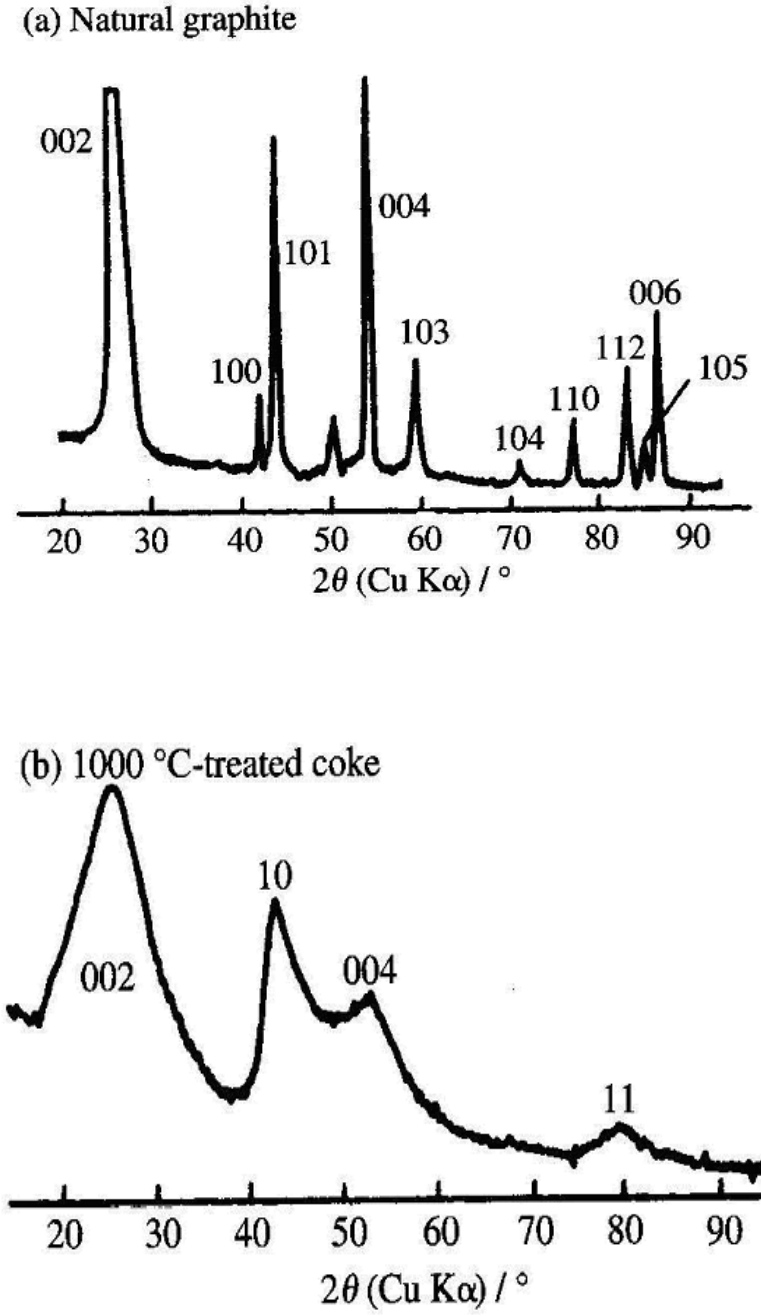

Figure 3.12 XRD diffraction patterns of different carbons: a) natural graphite; b) thermal treated coke [Inagaki, 2000]

X-ray Photoelectron Spectroscopy (XPS)

This type of spectroscopy performs a surface analysis and gives information about elemental composition and chemical state of the sample. Monoenergetic x-rays (Mg Kα or Al Kα) are irradiating the sample in vacuum. After their interactions with the atoms from the surface region (the penetrating power is 1-10 micrometers) electrons are emitted by the photoelectric effect. The energy of the emitted electrons is analyzed and a spectrum is obtained by plotting the number of detected electrons versus their kinetic energy. Each element has a unique spectrum and from the position of the peaks the chemical structure (type of bonds) of the sample is determined. A quantitative analysis can be performed from the area of the peaks.

The carbon (sp^2 hybridization) has the C1s bonding energy has a value around 284.5 eV, while the N1s bonding energy of a nitrogen atom replacing a carbon atom in the graphene structure has a value around 398.9 eV [Nist database]. An important characteristic of the XPS peaks is the fact that their position present chemical shifting, which means they change position depending on the chemical group present in the molecule. For example, the pure C-C sp^2 bonding gives a peak with a width equivalent to the equipment experimental resolution. The enlargement of a peak leads to the conclusion that there is more than one type of bonding present (i.e. C-C sp^3, C-O, C-N etc) [Darmstadt et al, 2003]. An example of different nitrogen groups present in carbon materials is given in Figure 3.13.

The XPS system used is an ESCALAB MKII with a X-ray source operating at 15 kW and 100 mA. The radiation source is Mg/Al which can produce two independent X-rays at 1253.6 eV (Mg) and 1486.6 eV (Al). The depth profiling of analysis is 1μm. Avantage software was used for spectra manipulation and NIST database (srdata.nist.gov) was used for the identification of peaks.

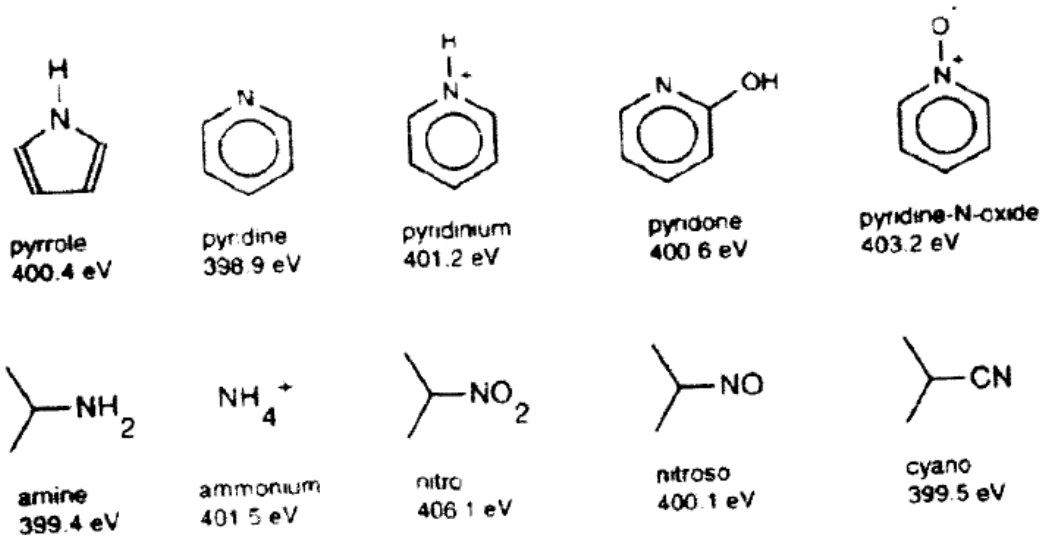

Figure 3.13 Nitrogen chemical groups present in carbon materials [Pels et al, 1995]

Scanning Electron Microscopy (SEM)

Scanning electron microscopy (SEM) is a method for high-resolution imaging of surfaces. SEM uses an energetically well-defined, highly focused beam of electrons scanned across a sample. The incident electron beam is raster-scanned across the sample's surface, and the resulting electrons emitted from the sample are collected to form an image of the surface. Imaging is typically obtained using secondary electrons for the best resolution of fine surface topographical features. Alternatively, imaging with backscattered electrons gives contrast based on atomic number to resolve microscopic composition variations, as well as topographical information. Using carbon black samples, information such as morphology and particles size is obtained.

A Hitachi 4700 Field Emission Scanning Electron Microscope (FE-SEM) in ultrahigh resolution mode was used during this project. Each sample was carbon taped to an SEM aluminum stub and coated with a gold-palladium alloy for 2 minutes, using a plasma coating system. The images were obtained using the following operation conditions: 5 kV, 10 μA, Ultra High Resolution (UHR) mode and 6 mm working distance (WD).

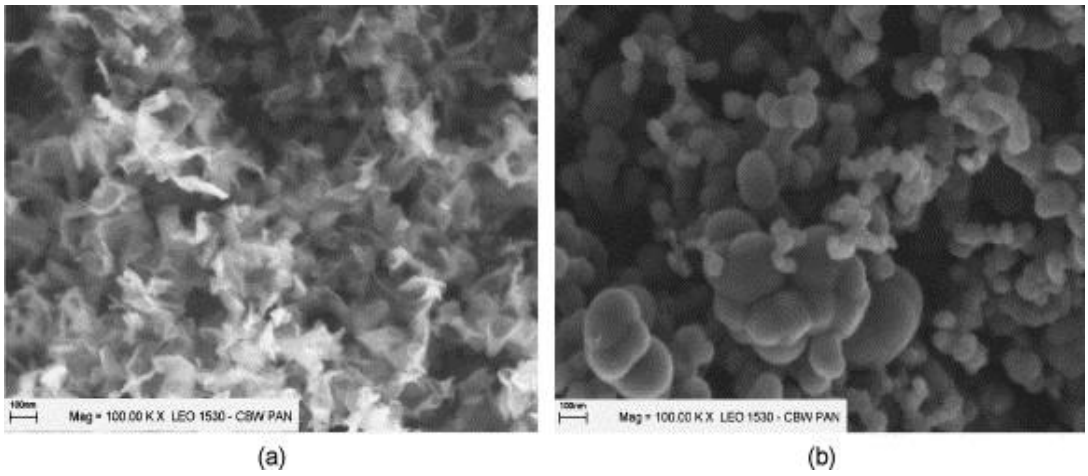

Figure 3.14 SEM images of (a) plasma produced carbon black; (b) traditional furnace carbon black [Donnet, 1976]

Transmission Electron Microscopy (TEM)

TEM is used in order to provide information about the primary particles shape and size and also about the aggregate structure. The contrast of the TEM images is strongly related to the electron diffraction and this allows us to image the defects (dislocation, grain boundaries, stacking faults, twins, etc). From the interaction of the incident beam with the specimen, different signals are generated (Figure 3.15). Only the transmitted and the diffracted electrons form the basic signals in TEM.

TEM uses a high voltage electron beam emitted by a cathode and formed by magnetic lenses. The electron beam is partially transmitted through the very thin specimen and carries information about the inner structure of the specimen. The obtained image is then magnified by a series of magnetic lenses until it is recorded by hitting a fluorescent screen, photographic plate, or light sensitive sensor such as a CCD camera (see Figure 3.16).

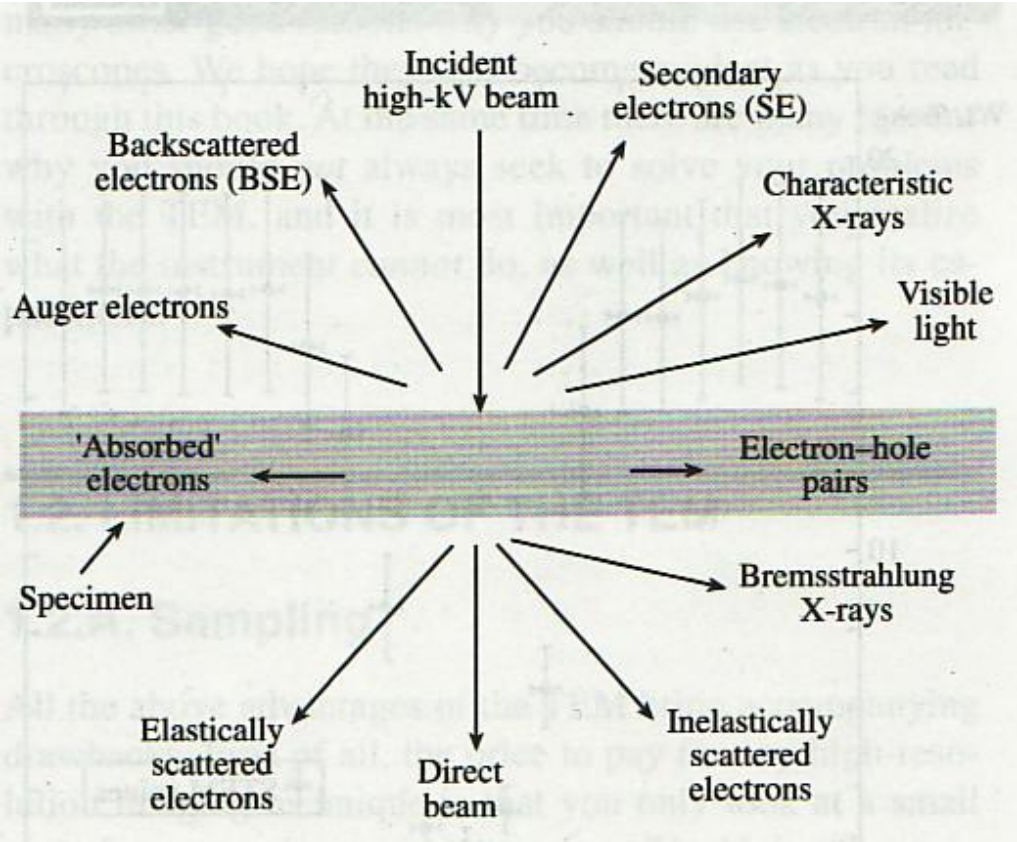

Figure 3.15 Signals generated in TEM [Williams, 1996]

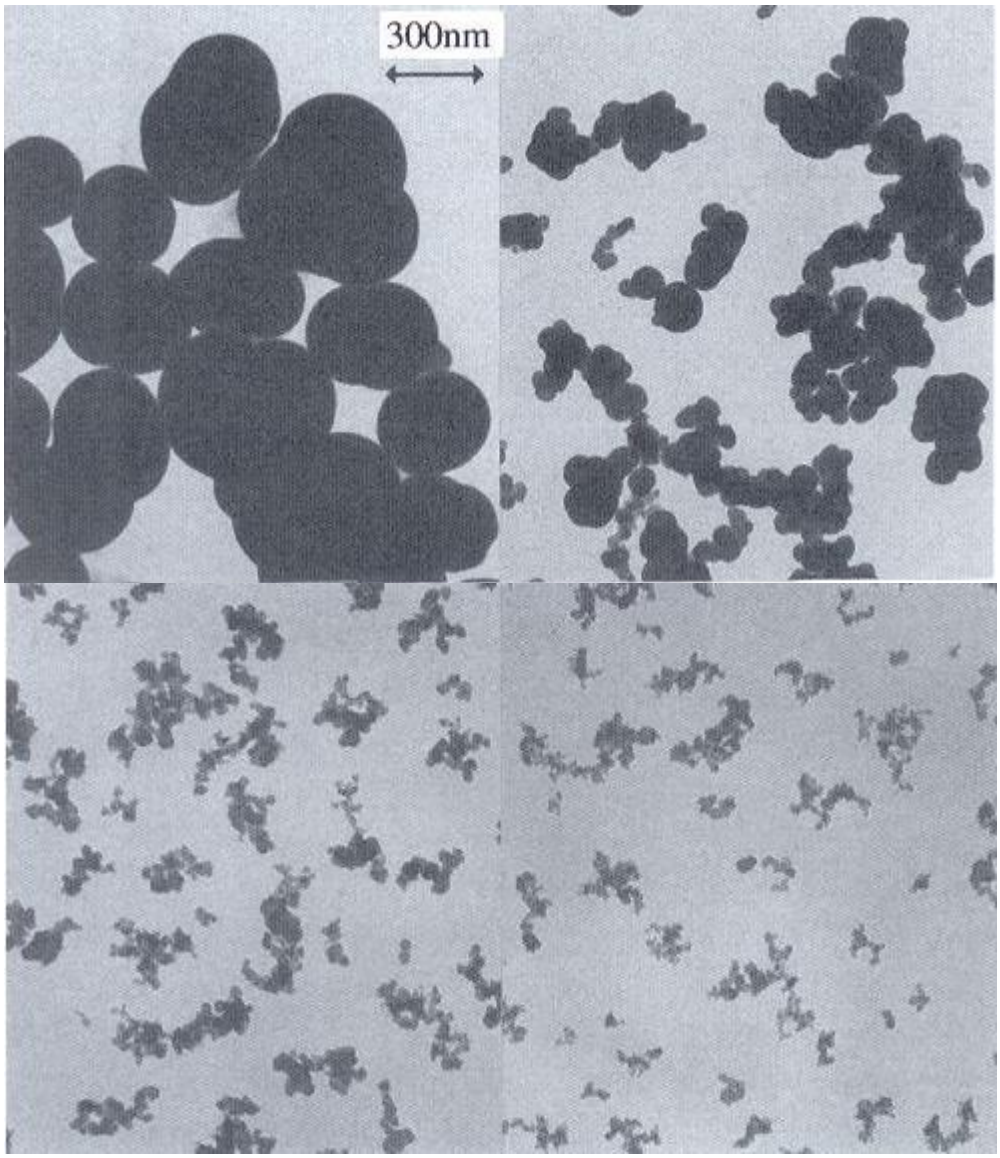

Figure 3.16 TEM images of carbon blacks of different sizes (the scale bar is the same for all four figures) [Inagaki, 2000]

The electron diffraction is graphically represented using the reciprocal lattice, a lattice representing a specific set of wave vectors **k** for a given Bravais lattice. In a simplified view of the reciprocal lattice, the set of parallel atomic planes having Miller indices (hkl) are represented by a single point located at a distance $1/d_{hkl}$ from the origin of the lattice. In other words, the reciprocal lattice is a way of representation of the periodicity of the crystal structure interacting with the

electromagnetic wave, and facilitating the interpretation of the diffraction condition in the TEM.

The diffraction occurs in TEM when the electron beam is at a relatively small angle to the atomic plane (hkl); it is visualized by using Bragg's law:

$$2K\sin\theta_B = g_{hkl} \qquad (3.4)$$

where θ_B is the Bragg angle between the (hkl) plane and the incident electrons, g_{hkl} is the reciprocal lattice vector and $K=1/\lambda$.

We can interpret this equation graphically as drawing a sphere or radius K in the reciprocal lattice. This sphere is called the Ewald sphere and the diffraction pattern includes all the reciprocal lattice points which are cut by the sphere (Figure 3.17).

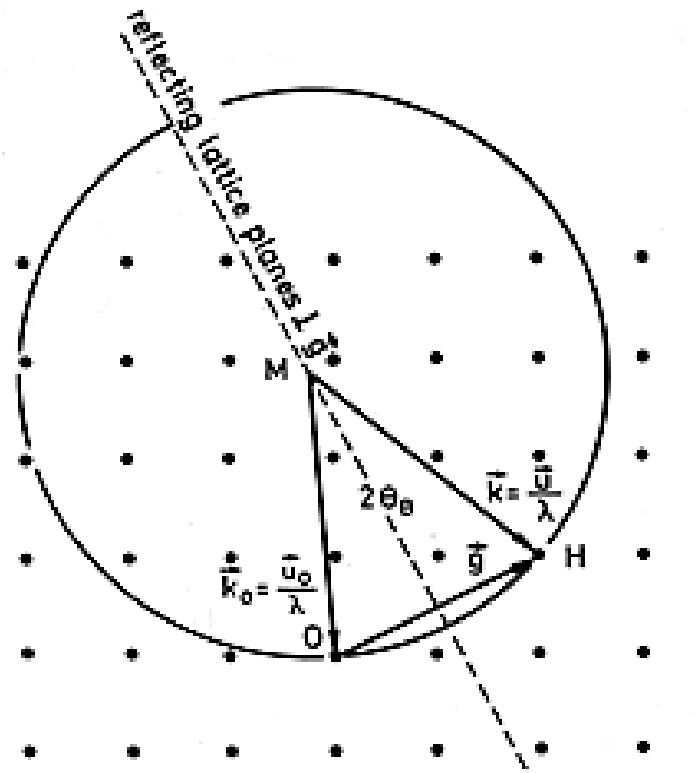

Figure 3.17 Ewald sphere [Williams, 1996]

The intensity of the diffraction spots depends on the crystal structure.

When the specimens in TEM are very thin (<100 nm), the reciprocal space is not made up of points, but of rods of length 1/t, where t is the specimen thickness.

The diffraction is possible when the Ewald sphere cuts the center of the rod and the Bragg condition for diffraction is exactly fulfilled [Williams, 1996].

Figure 3.18 presents examples of diffraction patterns of three different materials: crystalline aluminum, polycrystalline gold and amorphous carbon. Depending on the morphology of the material analyzed, the diffraction pattern looks different. In the case of an amorphous material, the diffraction patter presents bands of different intensities. In the case of a crystalline or polycrystalline material, the diffraction patters will show intense contours of different width or diffraction spots corresponding to the crystal structure.

For the case of carbon materials, when an amorphous material is produced, the diffraction pattern presents diffraction bands of different intensities, but when a crystalline structure is obtained, the diffraction pattern will present intense diffraction lines.

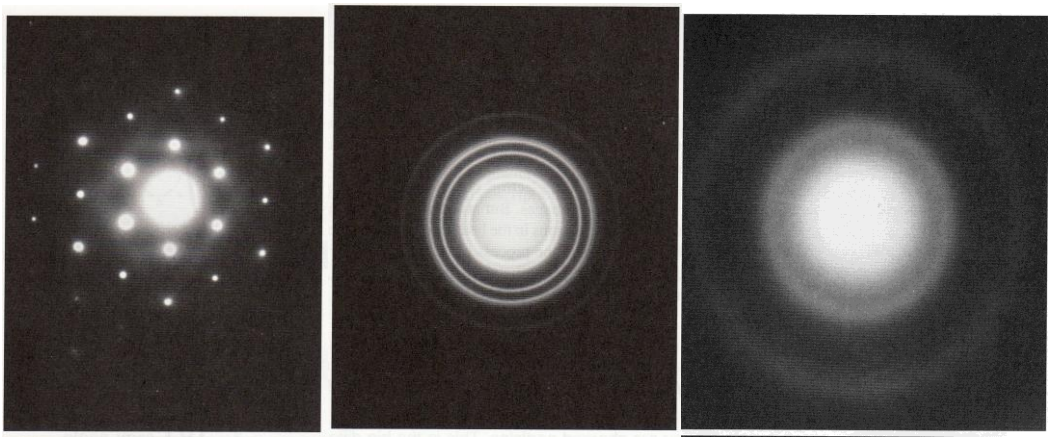

Figure 3.18 Diffraction patterns of: crystalline Al ; b) polycrystalline Au ; c) amorphous C [Williams, 1996]

The equipment used for this project is a Philips CM200 dotted with a field emission gun (FEG-TEM). The majority of functions are controlled via computer interface. The images are obtained in bright field mode and recorded using a CCD camera.

Energy-Dispersive x-Ray Spectroscopie (EDS)

EDS is a technique which allows us to perform qualitative elemental analysis of

a complex structure and also a full quantitative analysis. The spectrum generated (Figure 3.19) is a plot of X-ray counts versus X-ray energy. When atoms are ionized by electrons, they emit characteristic X-ray energy which has a unique value to the ionized atom, permitting in this way the identification of the emitting atom. When the electrons are slowed down by interactions with the nucleus, they also produce a continuum Bremsstrahlung X-ray. The characteristic X-ray spectra appear as a Gaussian-shape peak on a background of Bremsstrahlung X-rays.

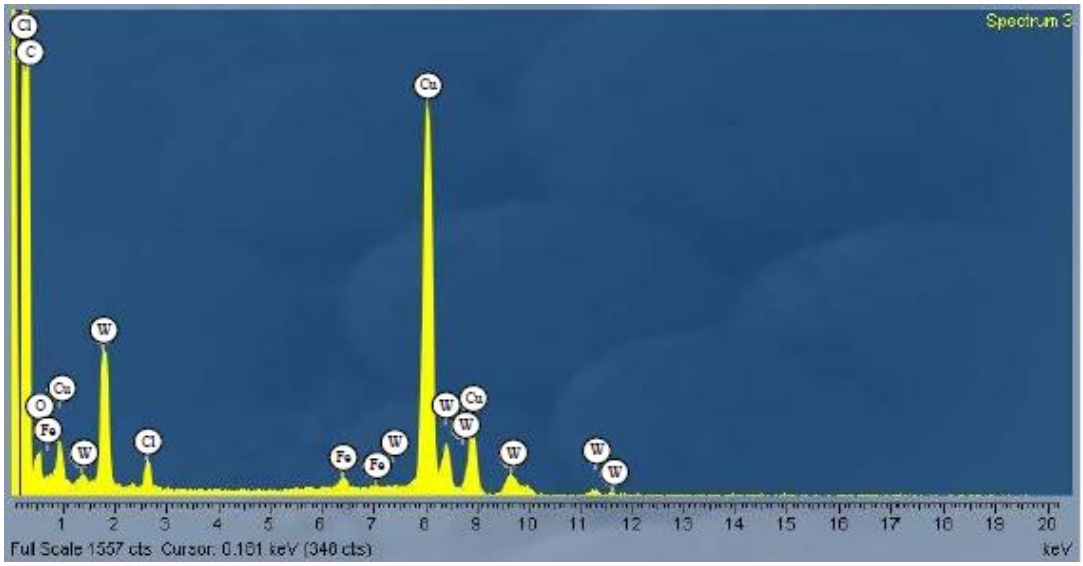

Figure 3.19 EDS spectrum of carbon nanotubes (CNT's) showing the presence of iron metal particles (catalyst used for the growth of the CNT's) and contaminants [Harbec, 2005]

The detector generates a pulse proportional to the X-ray energy, which is converted to a voltage. Then, the signal is amplified through a field effect transistor (FET), is isolated from other pulses and identified electronically as coming from an X-ray of specific energy. The digitized signal is stored in a channel assigned to that energy in the MCA. The detector and the FET must be cooled, to avoid undesirable effects, such as the activation of electron-hole pairs, atoms diffusion, etc. This cooling however gives some undesirable effects, such as deposition of contaminants. This is causing the absorption of lower-energy X-

rays. To avoid this, the detectors are sealed in a prepumped tube with a "window" allowing X-rays through into the detector. To detect the X-rays we need absorption in the crystal detector, and often one also has absorption in the window. For this reason, windows made of light elements (i.e. Be window) or polymeric materials are used [Loretto, 1984; Gauvin, 1997].

A Hitachi 4700 Field Emission Scanning Electron Microscope (FE-SEM) in ultrahigh resolution analysis (UHR-A) mode was used during this project. The operation conditions used are: 15 kV, 40 μA and 12 mm WD. INCA software was used for the spectra analysis.

Specific Surface Area Measurements (BET)

The most reliable method used to determine the specific surface area is the physical adsorption of gases, especially nitrogen. The amount of nitrogen absorbed at equilibrium at the normal boiling point of nitrogen (-195.8 ^{0}C) is measured over a range of pressures from near zero to 1 atm. The procedure consists in passing a gas over a sample until equilibrium is reached. Then the gas is desorbed by heating the sample and the amount of desorbed gas is measured with a thermal-conductivity cell or other detector. This gives one point on the isotherm. Then the process is repeated for different pressures, until the isotherm is constructed.

The nitrogen (N_2) adsorption isotherms are evaluated according to Brunauer, Emmet and Teller (BET). The theory is an extension of the Langmuir theory, which is a theory for monolayer molecular adsorption, to multilayer adsorption with the following hypotheses:

- gas molecules physically adsorb on a solid in layers;
- there is no interaction between each adsorption layer;
- Langmuir theory can be applied to each layer.

For multilayer adsorption, the following equation can be used:

$$\frac{p}{v(p_0-p)} = \frac{1}{v_m c} + \frac{(c-1)p}{c v_m p_0} \quad (3.5)$$

where p_o is the saturation or vapor pressure, v_m is the volume of one monomolecular layer of gas and c is a constant for the particular temperature and gas-solid system.

By ploting $p/v(p_o-p)$ versus p/p_o, a BET plot is obtained, from which, if considering $p/p_o = 0$, the volume of adsorbed gas can be obtained, by using the equation:

$$v_m = \frac{1}{I+s} \quad (3.6)$$

where I is the intercept value $I=1/v_m c$.

If the area covered by one single gas molecule adsorbed is α, then the surface area is given by the equation:

$$S_g = \left[\frac{v_m N_0}{V}\right]\alpha \quad (3.7)$$

Where N_o is Avogadro's number, 6.02×10^{23} molecules/mol, V is the volume per mole of gas at conditions of v_m ($V=22.4$ cm^3/g mol).

The value of α can be calculated using formula:

$$\alpha = 1.09\left[\frac{M}{N_0 \rho}\right]^{2/3} \quad (3.8)$$

Where M is the molecular weight and ρ is the density of the adsorbed molecules [Smith, 1981].

The equipment used during this project is a TriStart 3000 Analyzer from Micromeritics. The instrument has three analysis ports, so up to three samples can be run simultaneously. It measures surface areas as low as 0.01 m^2/g and it performs multipoint measurements using incremental pressure values (range: 0 to

999 mmHg). The instrument resolution is within 0.05 mmHg and the accuracy within 0.5%. The model TriStar V6.07A software allows the data plotting and calculates average pore size values. Before analysis, the CB samples were degassed for 2 hours at 120 ^{0}C.

Thermogravimetric Analysis (TGA)

TGA measures changes in the mass of a sample with increasing temperature in the presence of some specific gas. This technique can be used to identify and measure the distribution of different carbonaceous species.

When the TGA furnace reaches the burning temperature of one species, the TGA balance registers a mass loss. The apparatus software plots the mass loss versus the temperature and the result is the TGA curve. The derivative of this curve with respect to temperature yields various peaks associated to the mass-loss of each carbonaceous species. The surface area under the peak estimates the fraction of the related carbonaceous species present in the sample.

The sample can be heated up to 1000 ^{0}C. Amorphous carbon and other impurities burn at temperatures lower than 450 ^{0}C and well-graphitized materials at temperatures greater than 450 ^{0}C.

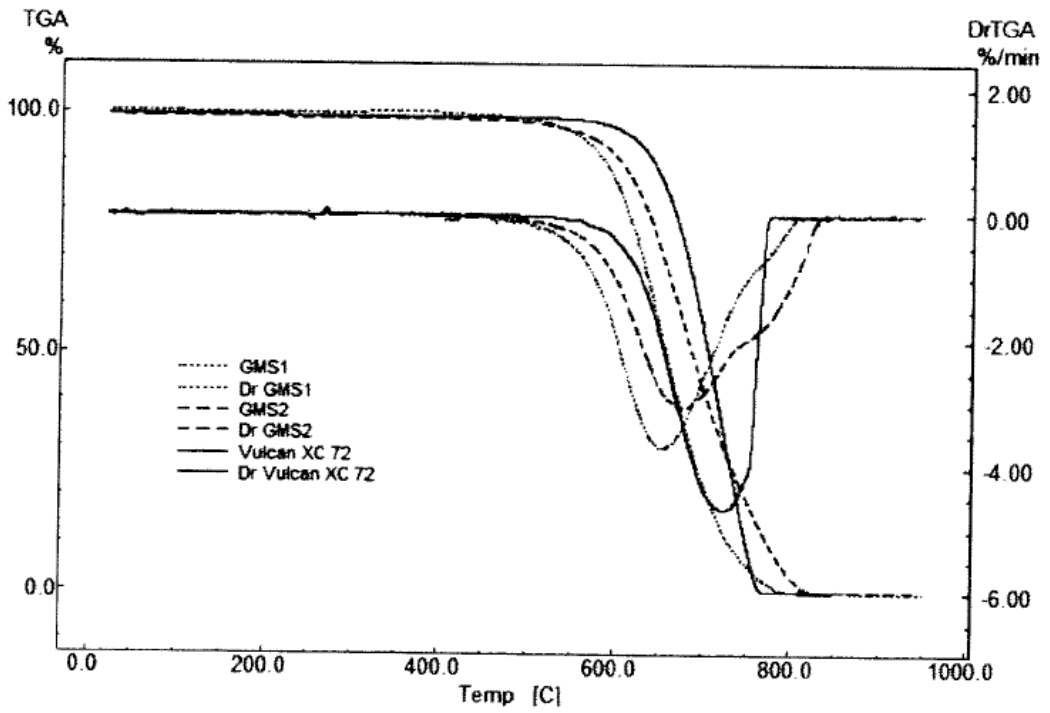

Figure 3.20 TGA graphs of different commercial available and experimental carbons [Larouche, 2010]

The equipment used is a TGA7 from Perkin Elmer with a TAC7/DX Thermal analysis Controller. The tests were done in argon atmosphere, up to 800 ^{0}C using a heating rate of 10 ^{0}C/min. The equipment has the capability to record both mass loss and derivative mass loss and the build in software allows the setting of experimental steps.

Chapter 4 – Experimental equipments and methodology

4.1 Experimental equipment

4.1.1 Non-transferred DC thermal plasma system

The non-transferred DC thermal plasma system (Figure 4.1) includes the following major components: DC plasma torch, reactor, power supply, control console, carbon source injection system and data acquisition system.

The plasma source is a non-transferred DC thermal plasma torch from Pyrogenesis Inc., model RPT2 (Figure 4.2), which uses two copper hollow electrodes covered with a thoriated tungsten internal lining (ThO_2W: 98 wt.% W and 2 wt.% ThO_2). The electrodes have an internal diameter of 0.5 cm, and electrically connected in reverse polarity with the downstream electrode negative. This system has been used in the past by D. Harbec for the synthesis of carbon nanotubes using various carbon precursors [Harbec, 2004; Harbec, 2007]. The torch features a maximum nominal power of 100 kW. The experiments were done using a power of 10 kW and argon as a plasma gas. The carbon source is injected in the torch nozzle attached to the downstream electrode, this nozzle being also made of thoriated tungsten but with an increased internal diameter of 1.0 cm. The torch nozzle possesses six injection ports uniformly distributed around its periphery. The plasma-forming gas is introduced through a vortex generator placed between both electrodes. This vortex generator is made of a perforated annular ring and provides aerodynamic stabilization of the plasma. The torch body, the electrodes and the injection nozzle are all heavily water cooled.

The reactor is a double-wall cylindrical water-cooled vessel made of stainless steel. The internal diameter of the reactor is 40 cm and the overall length is 100 cm. A movable water-cooled disk (which plays the role of collection plate) of 36 cm in diameter provides the means to adjust the length of the reactor up to a possible total internal length of 88 cm. A quartz window mounted on the side of the reactor provides a view of the plasma jet. A quench ring made of stainless steel was used during the experiments. The ring has a circular cross section of 1.94 cm in internal diameter (8.87 cm outer diameter) for the main plasma jet

throughput. A series of 24 axial injection ports are present on the internal side of the ring for a uniform cold gas injection, each injection hole being 0.5 mm in diameter. The quench gas used is argon at flow rates of 15 slpm.

The power supply consists of eight 400 A Miller power supply units connected in series. A control panel from Pyrogenesis Inc. enables the arc ignition in the torch using a high-frequency voltage pulse generator. The operating conditions of the plasma system such as the arc current, the arc voltage, the flow of plasma-forming gas, the reactor pressure, the inlet and outlet temperatures of the cooling-water and the flow of cooling-water are also controlled and monitored from this control panel.

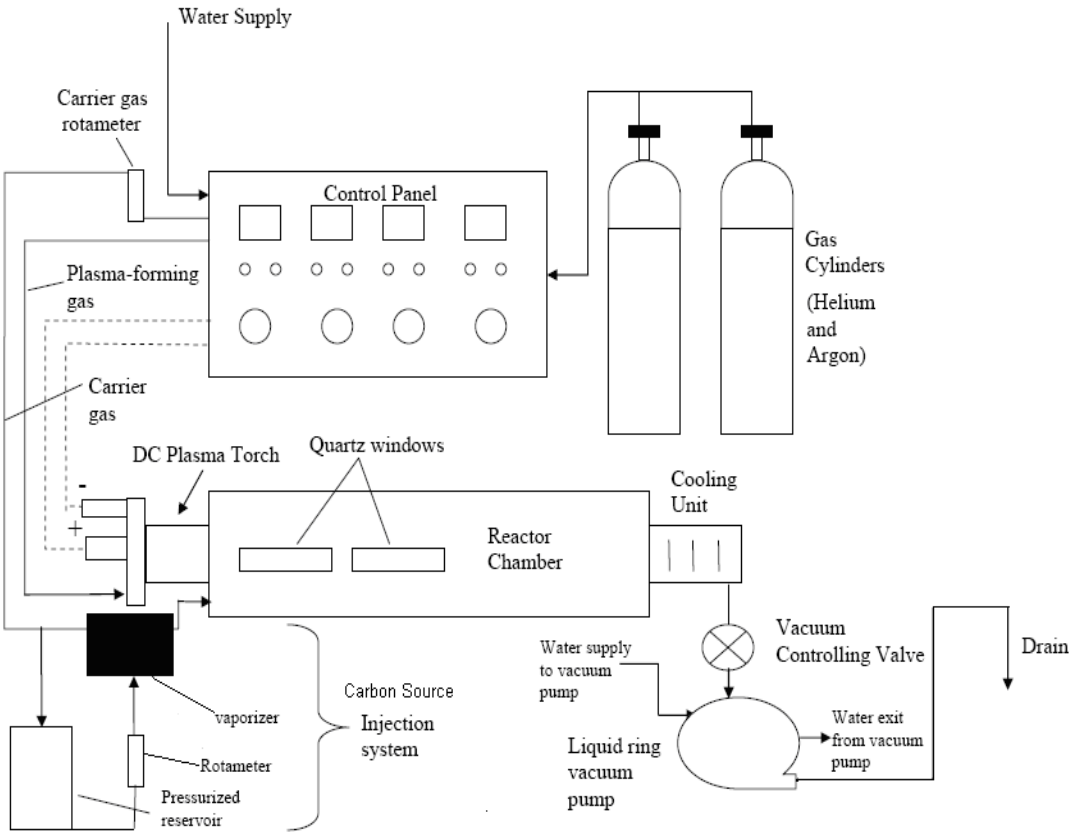

Figure 4.1 Schematic diagram of the non-transferred DC thermal plasma torch system [Harbec, 2005]

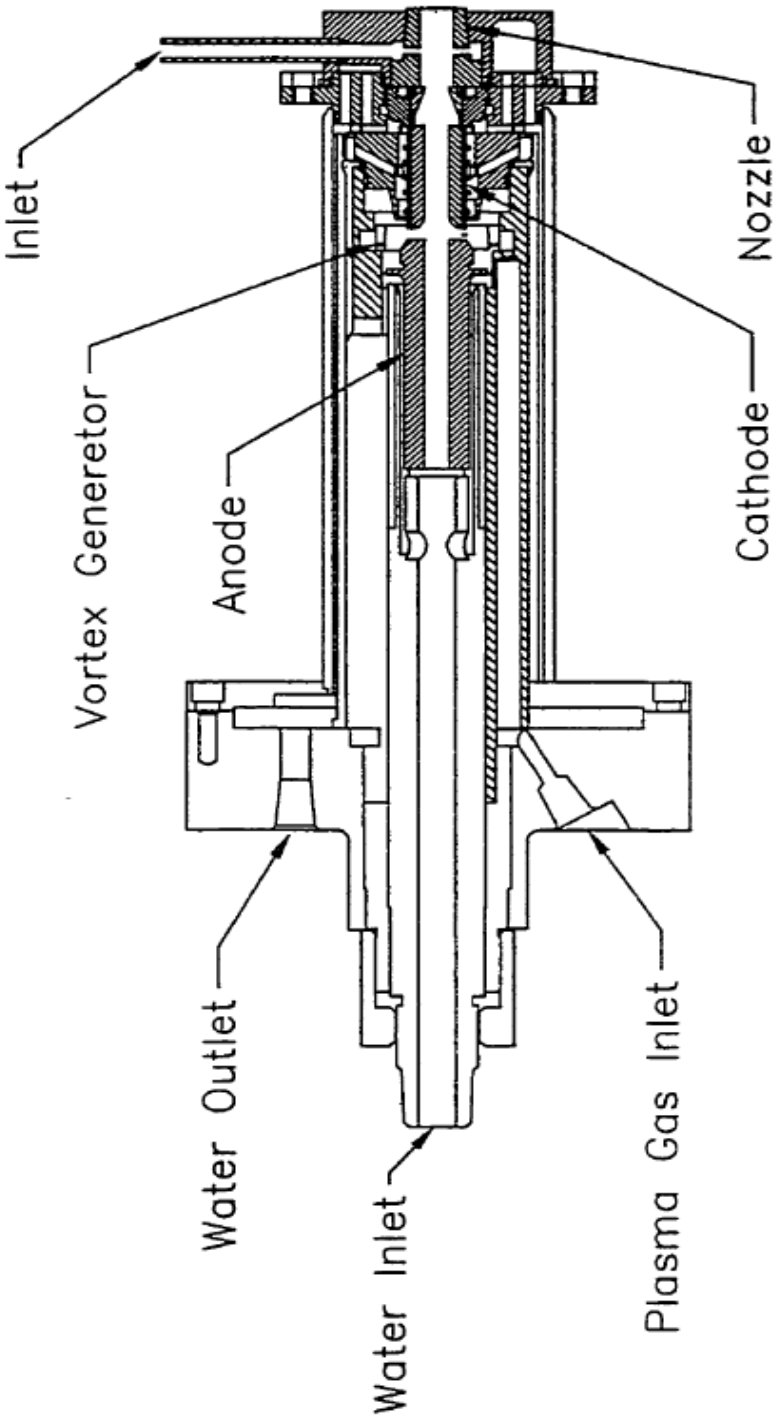

Figure 4.2 Design of the 100 kW dc non-transferred thermal plasma torch. Note that contrary to the present figure, the downstream electrode (cathode in the present case of a reverse polarity mode) used in the present experiments has a straight cylindrical geometry up to the nozzle (injection) section. [Alexakis, 1997]

The carbon source injection system consists of a 2 liters stainless steel pressurized reservoir containing benzene and having an internal diameter of 10 cm. Benzene was used as a carbon source because at the beginning of this project it was proposed to try a complete functionalization of the CB material, which means to add both nitrogen and iron to the CB support. Ferrocene was intended to be used as an iron source. Since ferrocene is completely soluble in benzene, we choose to use benzene as a carbon precursor. Helium, at a pressure of 100 psig (690 kPa) applied at the top of the reservoir allows the pumping of the liquid carbon source towards the vaporizer. The benzene vapors are then injected directly in the DC torch nozzle inlet indicated in Figure 4.2. Previous studies [Harbec, 2005; Guo, 2009] have showed complete dissociation was rapidly attained in the hot zones of the nozzle and in the first cm downstream of the nozzle.

Based on calorimetric studies and depending on the plasma forming gas used and the input power, the torch efficiency varies from 53.9 % to 76.4 % [Harbec, 2005].

A data acquisition system from ComputerBoards is used for temperature readouts and it consists of a DAS-08 card inserted into the motherboard of an Intel Pentium III computer and connected to a CIO EXP-16 multiplexer and a CIO MINI 37 board. The CIO EXP-16 multiplexer reads out thermocouple measurements and the CIO MINI 37 board, output voltage of other meters. The software Software compiles the data as a function of time. Type K thermocouples, connected on the CIO EXP-16 multiplexer are used to measure the temperatures in different parts of the system during the experiments. The flow of cooling water is measured using rotameters placed at the water inlet [Harbec, 2005].

4.1.2 Inductively coupled plasma (ICP) system

An inductively coupled plasma system consists of the following principal components or subsystems: the radio frequency (RF) generator, an induction plasma torch and its control console. The ICP system used in the present project is a PL-35 plasma torch and peripheral equipment produced by Tekna.

The Lepel RF generator in the Tekna system provides a 60 kW maximum RF output (electrical supply: 380 V, 3 phases and 60 Hz). The nominal operating frequency is in the 2 to 5.0 MHz range. The inductively coupled plasma (ICP) torch (Figure 4.3) uses a radio frequency power source to generate a plasma of high temperature and high enthalpy. An induction plasma torch is typically made of a copper coil of several turns wrapping a confinement tube, inside which the induction plasma is generated. One end of the confinement tube is open. The plasma within the torch body is maintained using a continuous flow of gas which forms a high-temperature/high velocity jet at the torch outlet. The plasma is in a recombination regime downstream of the outlet in a way similar to the DC thermal plasma torch. The plasma parameters are however quite different, the ICP system being characterized by larger plasma volumes, lower plasma jet velocities, and possibly lower maximum temperatures that may be attained. During induction plasma operation, the generator supplies a RF current to the torch coil. This induces an alternative magnetic field inside the coil and, provided that a low density pre-ionized gas is present in the torch, an induced current heating this gas and coupling the torch power to this one-turn plasma secondary. The plasma jet generated in an ICP thermal plasma torch gives temperatures typically in the 5000 K to 10000 K range, and enthalpies of 10^3~10^5 kJ/kg depending on the plasma gas species. The internal torch body is molded with a proprietary resin material, while the induction coil itself is integrated inside the torch body. A ceramic plasma confinement tube is centered within the torch body. The Tekna torch model number (PL-35) refers here to the internal diameter, in millimeters, of this ceramic plasma confinement tube. The induction coil is usually cooled by the same water flow used for the power supply, while the torch body and plasma confinement tube are cooled by a separate cooling water circuit. A gas distributor is designed to produce a uniform axial flow of protective sheath gas parallel to the wall of the plasma confinement tube, and a swirl flow of the central gas. Along with the distribution of these gases, the torch head also supports the intermediate quartz tube which separates the sheath gas from the central gas, and the water-cooled axial injection probe which is used to introduce powders and/or gaseous

reactants into the discharge. The length of the intermediate quartz tube is designed so that its downstream edge is at the level of the first turn of the induction coil. The exit nozzle is located at the downstream end of the torch.

The control console monitors all vital system parameters and the operating parameters such as gas flow rate, water flow rate, temperature, gas pressure and water.

Similarly to the DC thermal plasma system, the initial downstream reactor used in the present project is a double-walled water cooled stainless-steel cylindrical vessel having 32 cm in diameter and 100 cm in length. Both the ICP torch and reactor vessel are positioned vertically on the system axis, and a movable water cooled collection plate is inserted inside the reactor through the reactor bottom to enable the collection of the powders at different reactor heights.

Section 6 of the present thesis will indicate important effects induced by the specific flow patterns inside this cylindrical reactor and affecting the morphology of the particles produced. These effects will result in an important modification of the reactor geometry. These developments and the new reactor geometry are discussed in sections 6&7.

Please refer to Appendixes II&III for operation procedures for both DC and ICP plasma systems.

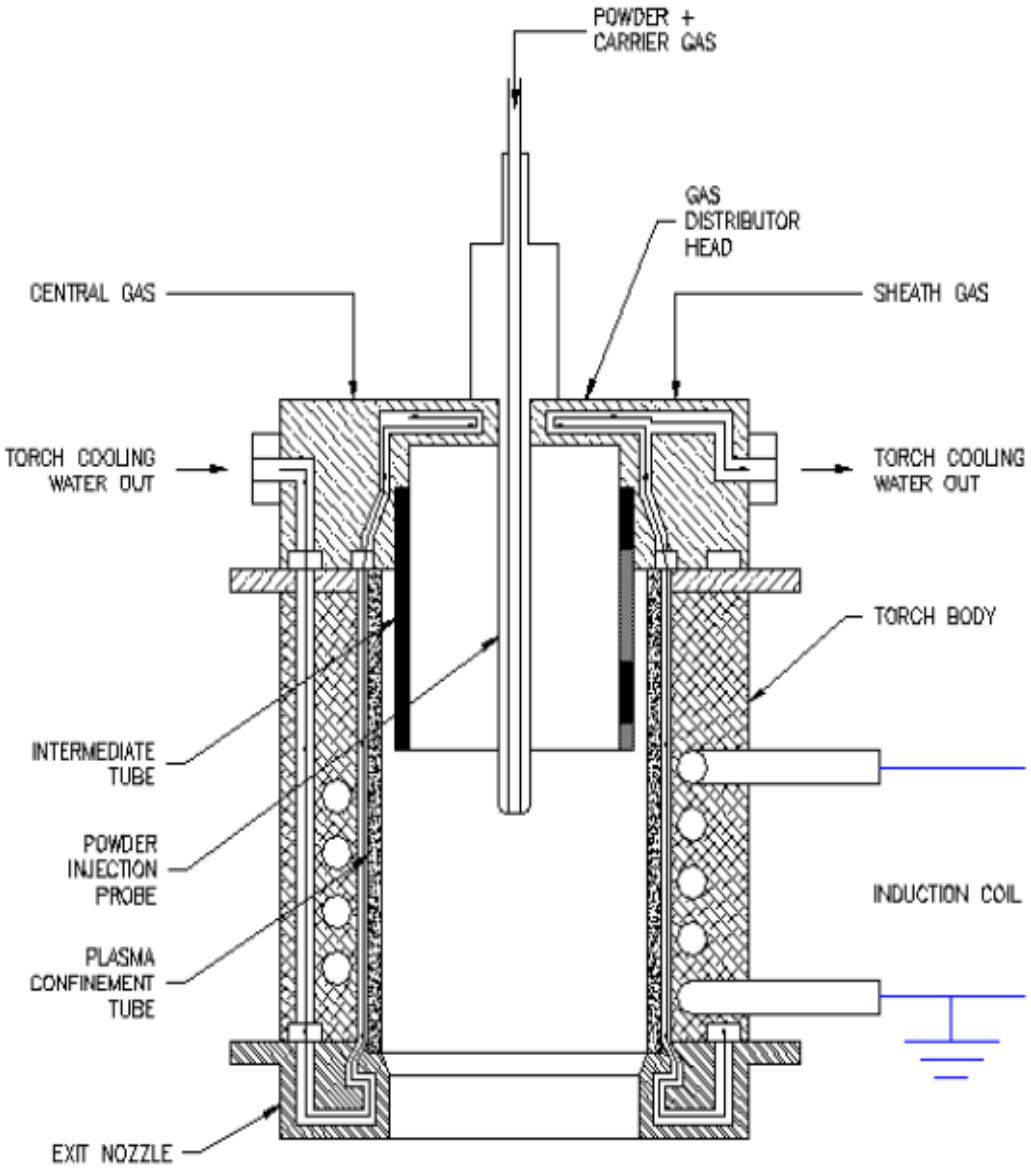

Figure 4.3 Schematic diagram of Induction Plasma Torch [Induction Plasma Torch PL-35 & PL-50, Operation & Service Manual, 2004]

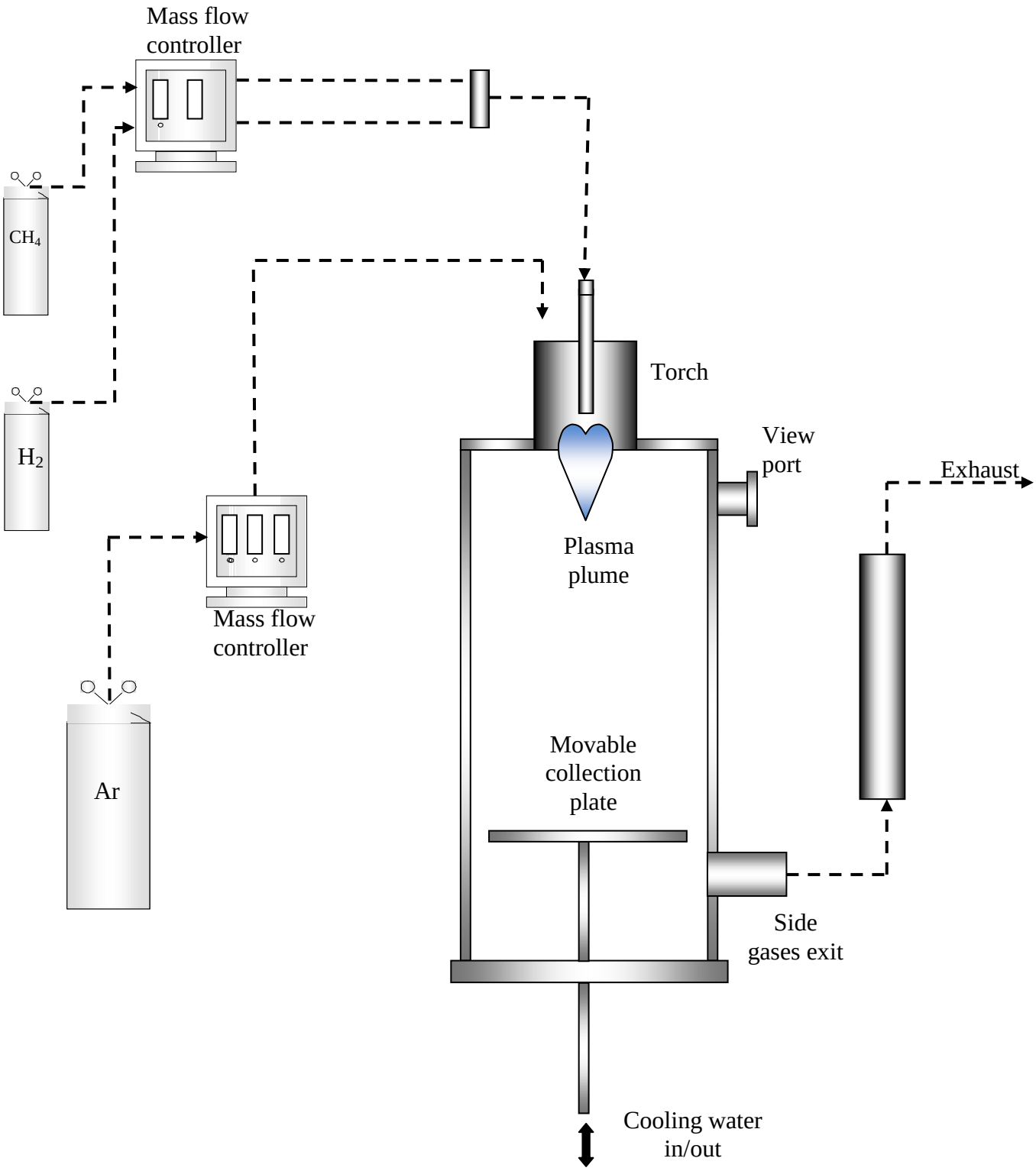

Figure 4.4 Schematic diagram of the ICP thermal plasma system

Chapter 5 – Experimental results: DC thermal plasma system

5.1 Experimental conditions

In the experiments performed using the DC thermal plasma system the carbon source used was benzene at flow rates of 10 smlpm and 15 smlpm. The carbon source was heated at 300^{o}C before injection in each experiment. The carbon source injection time varied between 3 and 12 min. The plasma forming gas used was Ar at a flow rate of 100 slpm and the power was varied between 20 kW and 47 kW. The reactor pressure was kept constant at 26.6 kPa. A hydrogen flow of 20 slpm was added in the system to prevent the formation of carbon material and the blocking of the torch nozzle.

5.2 Powders characterization

The CB powders obtained were analyzed using different techniques: Raman Spectroscopy, X-Ray Diffraction (XRD), BET for surface area measurements, thermo gravimetric analysis (TGA), Scanning and Transmission Electron Microscopy (SEM and TEM) and Energy-Dispersive X-ray Spectroscopy (EDS).

The Raman spectra (Figure 5.1) were obtained using an incident laser wavelength of 488 nm and a grating of 1800 lpmm. In order to assess the uniformity of the powder morphology throughout the entire reactor, the powders were collected from different parts of the reactor such as the reactor wall (over the entire reactor surface), the quench ring (the upstream quench ring surface) located 5 cm downstream of the torch nozzle, and the collection plate positioned in a stagnation point flow geometry 88 cm downstream of the torch. All the recorded spectra show distinct G and D bands characteristic of graphitic materials, on a strong fluorescence background. The presence of this background is indicative of a significant fraction of volatile organic compounds (VOCs) present in the samples. This result is consistent throughout all the CB powders produced, proving a relative low purity of the samples.

According to the modeling of Guo [Guo, 2009] on the flow and energy fields generated during the operation of the DC plasma system, the plasma jet leaving the nozzle is confined close to the reactor axis and does not mix with the surrounding environment until it hits the collection plate. This results in the formation of large recirculation loops (Figure 5.2). Note that the quench ring is not present in this modeling and only the part of the reactor where the recirculation loops are formed is presented in Figure 5.2 (the total reactor length is 100 cm). The collection plate was positioned 57 cm away from the nozzle outlet.

The residence time of the particles captured in this recirculation zone is much longer than the residence time expected in other parts of the reactor. This should translate into a higher degree of graphitization of samples. Because of the lower temperatures prevailing in the recirculation zone compared to the plasma jet itself, some gaseous species present in the stream may form secondary compounds which are mixed with the CB particles and trigger or help an agglomeration process.

BET measurements were performed to determine the surface area of the carbon black powders produced using the DC system. The surface area of these powders is very low, ranging from 10 m^2/g to 30 m^2/g. Usually, carbon blacks have specific surface area values between 90 m^2/g and 460 m^2/g [Donnet, 1976]. Typically, individual CB particles have very small porosity, the large surface area being the result of an agglomeration of the fine particles generating a structure with a very open porosity. The low specific surface area values measured correlate with the possible presence of volatile aromatic hydrocarbons in the sample as suggested by the Raman spectra; these molecules may possibly coat and agglomerate the particles, filling the pores and resulting in a decrease of the specific surface area of the product.

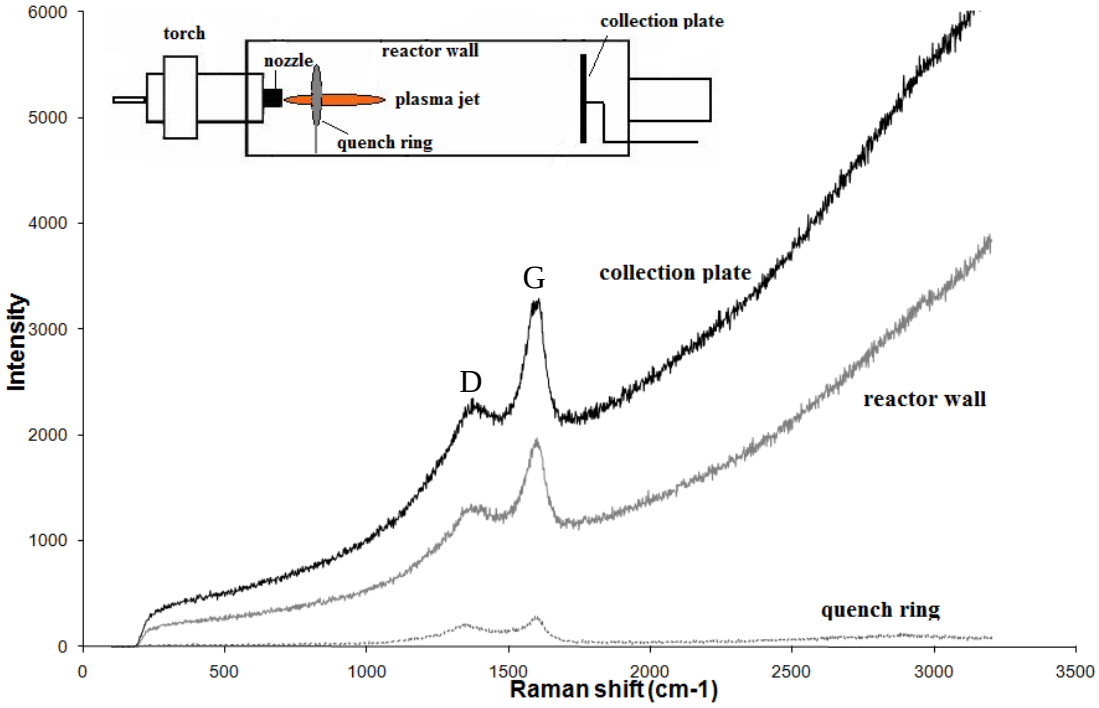

Figure 5.1 Raman spectra of the CB powders produced by the DC torch for three specific collection regions within the reactor

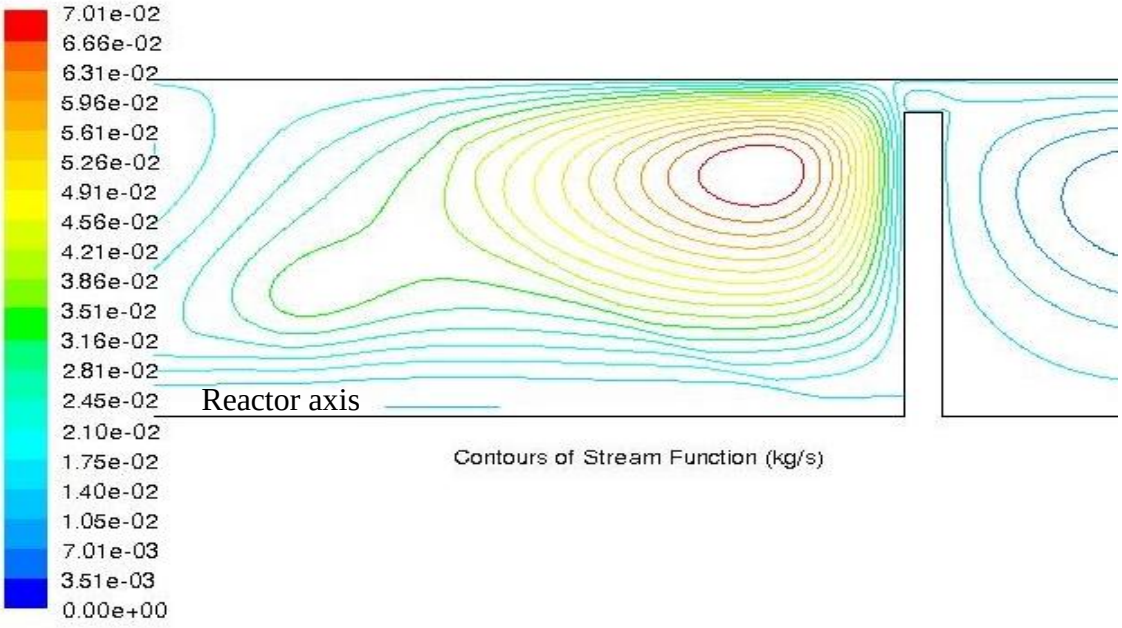

Figure 5.2 Stream function lines in the DC plasma system (reactor not to scale) [Guo, 2009]

The presence of these volatile compounds was also observed in the TGA tests. The TGA measurements were performed in air, using a heating rate of 10°C/min, up to 900°C. The derivatives of the TGA mass loss observed are given in Figure 5.3. The large peak in mass loss located between 350°C - 650°C is a typical result of carbon loss, however the mass loss observed in the lower temperature range (peaks in the interval 100°C - 300°C) is related to the elimination of volatile contaminants from the carbon black samples. The peak around 80°C is due to moisture elimination from the sample.

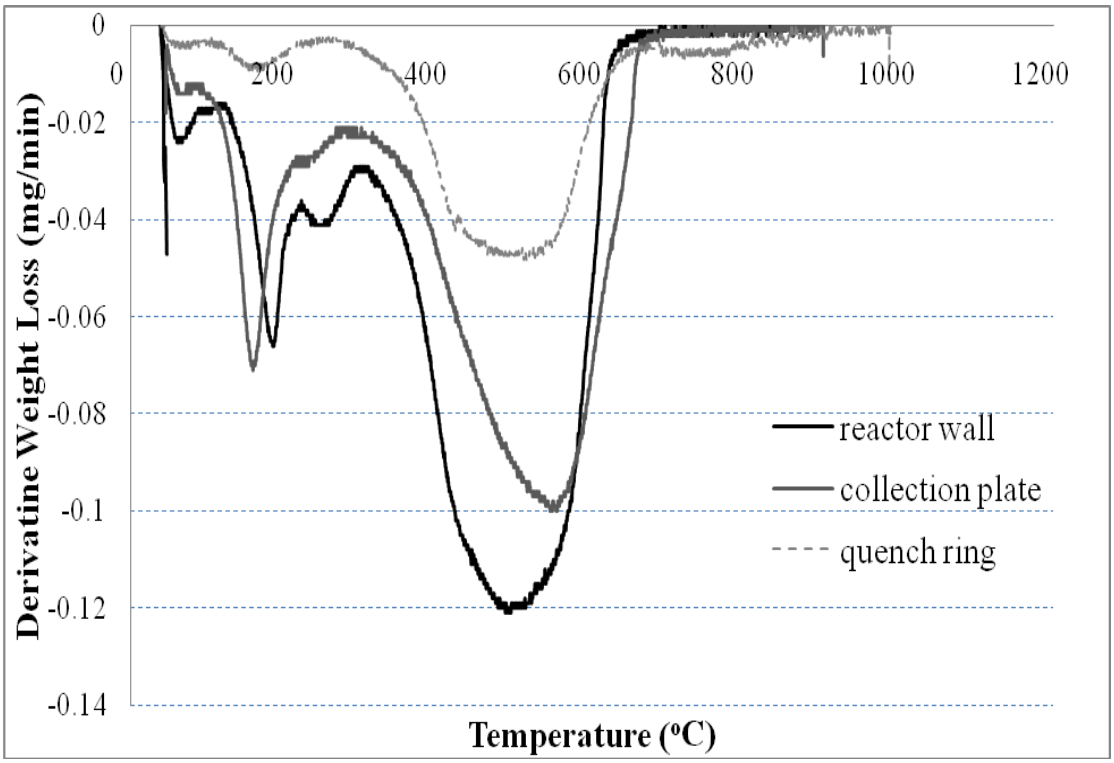

Figure 5.3 Derivative of the TGA results for DC-torch plasma produced CB samples collected from quench ring, reactor wall and collection plate

It can be observed that the samples collected from the reactor wall and from the collection plate present a strong peak around 200°C indicating the presence of higher amounts of volatile organic compounds when compared with the sample collected from the quench ring. This is in accordance with the results from Raman

Spectroscopy and with the modeling results presented by Guo [Guo, 2009]. The quench ring samples originate from a small backflow of the main plasma jet around the upstream inner edges of the quench ring structure; these powders are expected to have a much shorter residence times in the low temperature zones enabling the presence of VOCs.

XRD tests were performed to characterize the morphology of the CB powders. A characteristic XRD diffraction pattern of CB powder collected from the quench ring is presented in Figure 5.4a. The diffraction pattern shows a number of diffraction lines, only one of which, near 2θ angle of 23^o is characteristic of graphite materials (see Figure 3.12, Chapter 3 for natural graphite XRD diffraction pattern). A number of other diffraction lines are present near 2θ angles of 33^o, 37^o, 43^o, 47^o, 56^o and 58^o. These diffraction lines are produced from contaminants present in the samples and coming from the electrode material. Figure 5.5a presents the diffraction pattern of a CB sample collected from the reactor wall. The diffraction lines near 2θ angles of 23^o, 43^o, 72^o and 88^o are characteristic of natural graphite, however the diffraction lines near 2θ Θ angles of 48^o and 93^o are characteristic of other materials present in the sample as contaminants coming from the plasma torch electrode erosion. These contaminant materials were identified for the two types of CB samples analyzed (CB powders collected from the quench ring and reactor wall). In the case of the CB collected from the quench ring, the diffraction lines present in the spectra are characteristic of tungsten (W), α-iron (α-Fe), Fe_3C and WC, as shown in figure 5.4b. In the DC torch both the anode and cathode are made of tungsten (as described in Chapter 4) and tungsten carbide particles are formed during the experimental run, as observed by Harbec [Harbec, 2011]. The eroded material combines with the carbon present in the gas stream to form the carbide. The presence of iron is a confirmation that material is eroded from the quench ring, too. For the case of the carbon black powders collected from the reactor wall, the identified diffraction lines (see Figure 5.5b; diffraction lines present a small shift) correspond to W, WC and Fe_3C.

The SEM images (Figure 5.6) show carbon powders collected from the quench ring. The powders show large spherules of typically 25-50 μm, with strong agglomeration of smaller particles (500 nm to 1 μm in diameter) forming the spherules. A second agglomeration occurs between the spherules themselves leading to large agglomerates with irregular shapes. Also observed was the presence of few carbon nano-tubes (CNT's) or carbon nano-fibers in the samples (Figure 5.7). In fact we have in the torch nozzle conditions that were shown by Harbec (2005) to generate carbon nanotubes using the same plasma torch and experimental setup as for the present study. According to Harbec (2005, 2011) the plasma arc erodes the tungsten electrodes and generates tungsten vapor upstream of the torch nozzle. This generates tungsten nanoparticles in the cold gas injection section of the nozzle, these being transported to the nozzle walls by thermophoresis effect from the existing strong temperature gradients in this zone. Carbon vapor is injected and transported throughout the nozzle. A fraction of this carbon vapor nucleates on the cold walls into carbon nanoparticles. Another fraction diffuses to the tungsten nanoparticles and form nanoparticles of tungsten carbide. Upon cooling, the excess of carbon from these tungsten carbide nanoparticles is segregated to their surface where it graphitizes and forms CNT's.

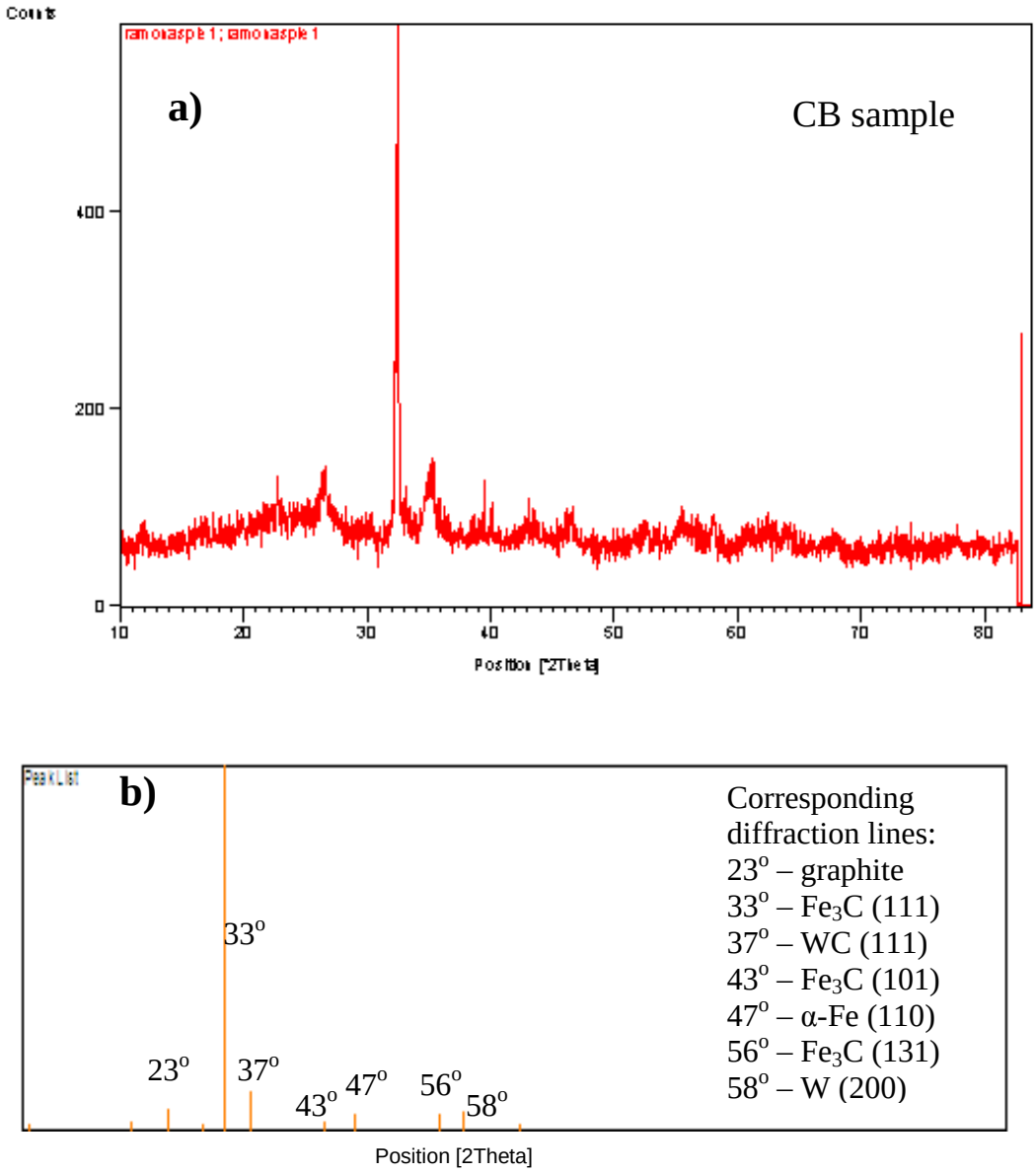

Figure 5.4 a) XRD spectra of DC-torch produced CB powders collected from quench ring; b) identification of XRD diffraction line

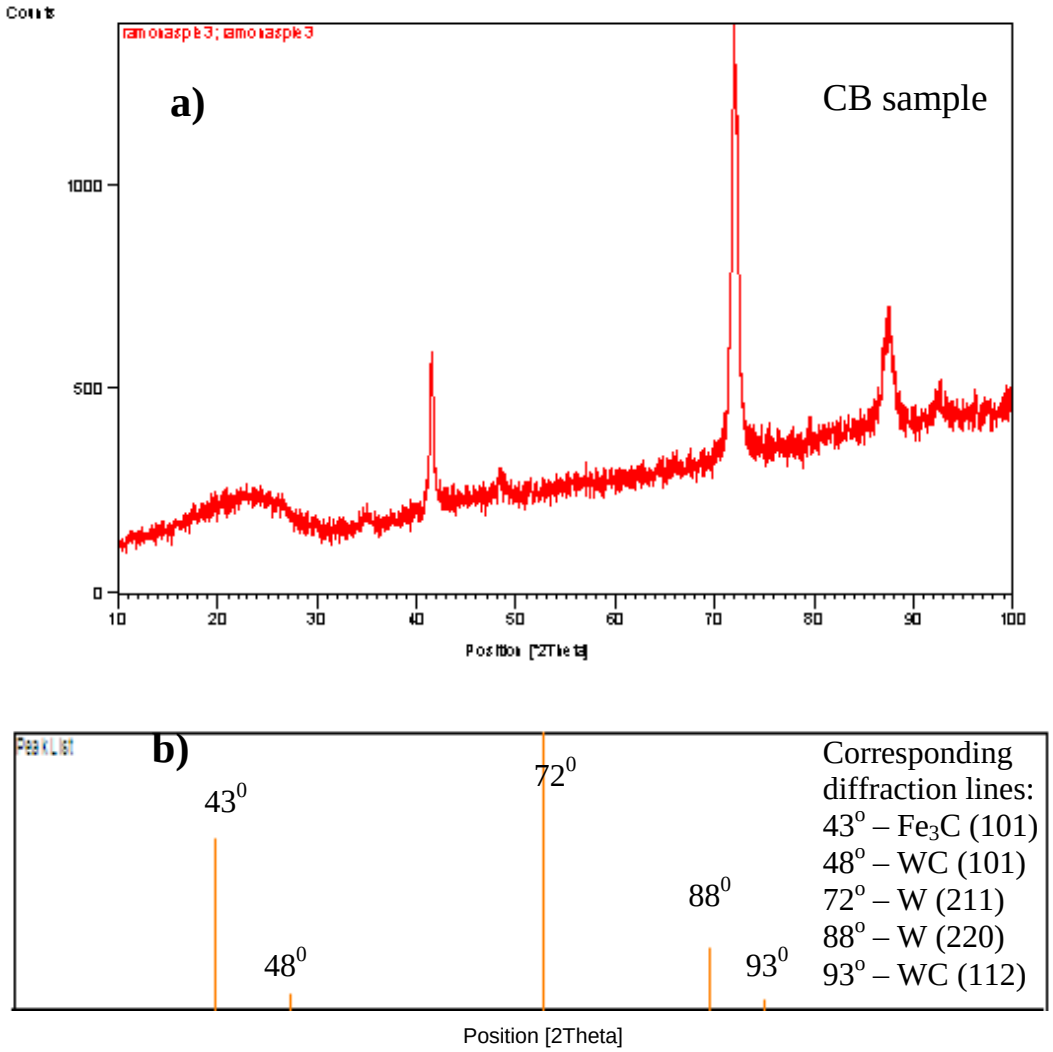

Figure 5.5 a) XRD spectra of DC produced CB powders collected from reactor wall; b) identification of XRD diffraction lines

A fraction of tungsten nanoparticles are transported to the quench ring, where they form CNT's in a similar way as the ones formed in the torch nozzle.

A similar CNT formation and growth mechanism was also shown possible directly on the surface of the quench ring using iron vapors as a source for the catalyst nanoparticles. The quench ring faces the plasma jet leaving the torch nozzle. In a system where no external feed of iron is supplied to the plasma jet, iron can still be generated internally through the high temperature of the plasma jet melting and vaporizing iron metal from the surface of the stainless-steel

quench ring. Iron nanoparticles nucleate in the cooler areas of the water cooled quench ring surfaces typically in the small recirculation zone in the upstream region, forming CNTs [Dai, 2007]. Small quantities of carbon nanotubes or nanofibers are thus possible in the present experiments because of the erosion/ablation of some metallic surfaces. One should also note that the small recirculation zone on the upstream surface of the quench ring forms a specific carbon particle synthesis zone, these particles being analyzed independently.

Powders collected from the reactor wall show an aggregated structure (Figure 5.8a); closer examination (Figure 5.8b) shows almost spherical particles which form aggregates. It appears that these particles are the ones which condense on the cooled reactor walls as soon as they reach this area and they do not follow the gas recirculation path. As a result, the growth of these particles stops early, and these powders have a uniform morphology, with particles having small dimensions of less than 50 nm in diameter.

Changing the collection area of the carbon black powders to the movable disk, we observe a change towards a more compact structure (Figure 5.9a). These particles have dimension of more than 10 μm. They are probably formed of primary spherical particles that are combined with the organic compounds (formed as secondary product in the system) and grow into a bigger particle during the recirculation into the hot areas of the reactor. This was concluded due to the fact that these big CB particles present small spherules on their surface (as you can see in Figure 5.9b) similar to the ones collected from the reactor wall.

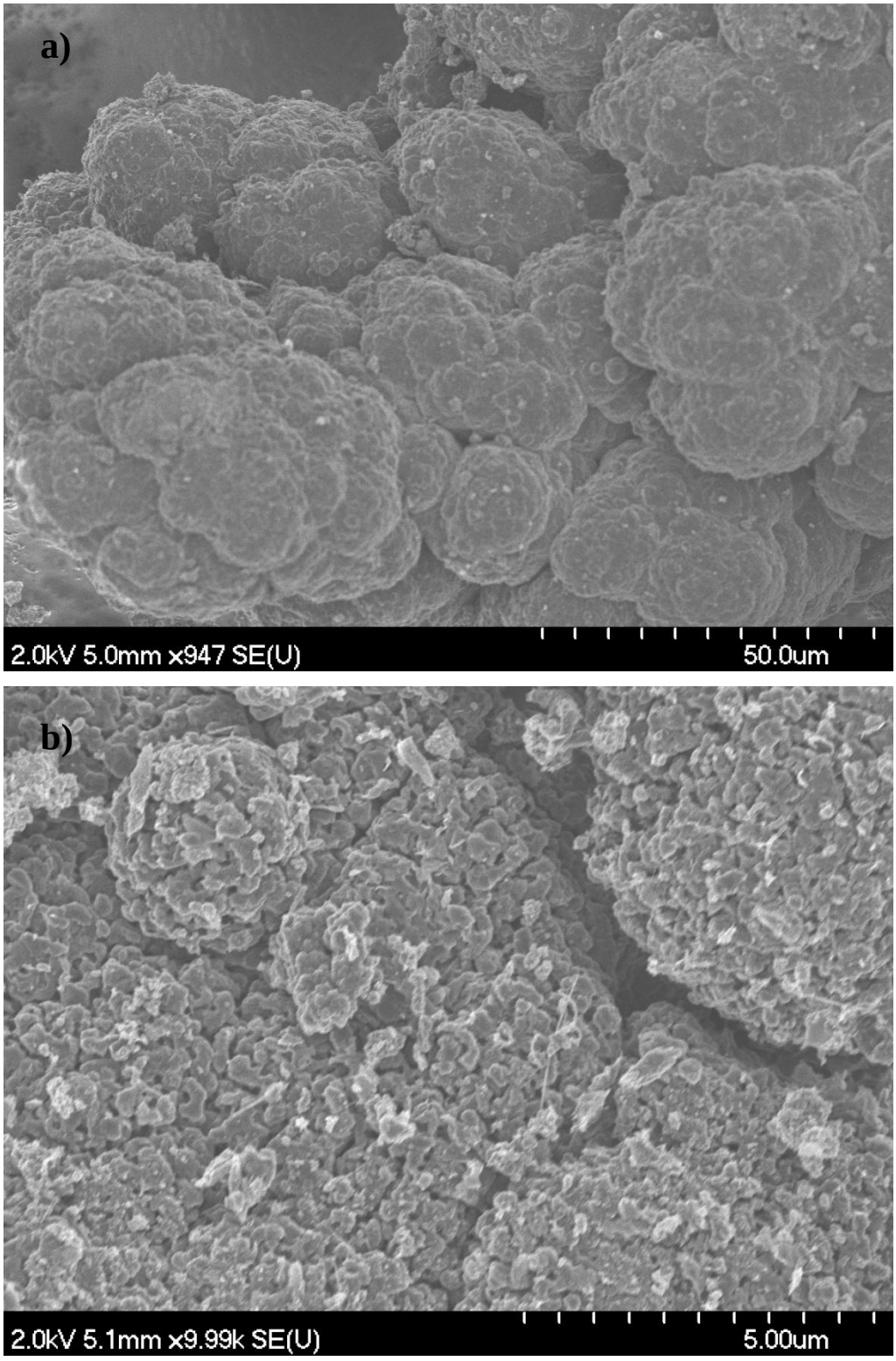

Figure 5.6 SEM image of the carbon solids collected in the DC reactor from torch nozzle internal surface at different magnifications: a) 50 µm scale bar; b) 5 µm scale bar

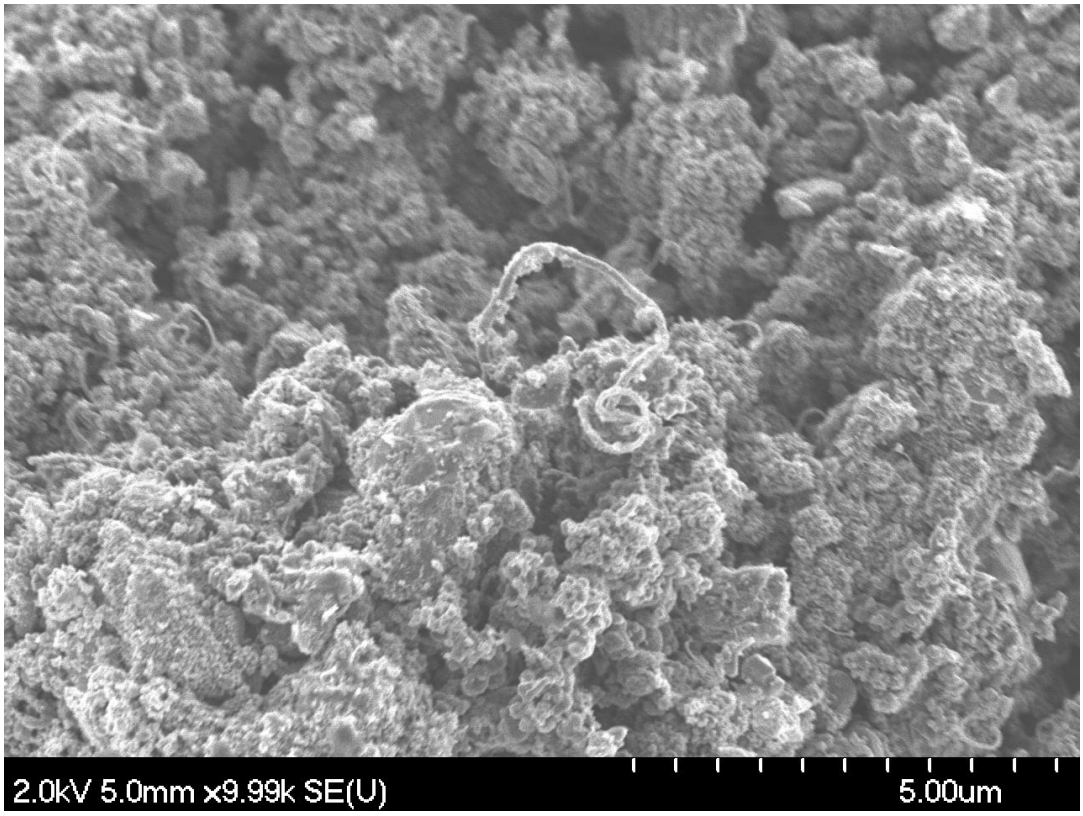

Figure 5.7 SEM image of DC produced carbon solids collected in the torch nozzle of the DC reactor showing the presence of a small quantity of either carbon nanotubes (CNT's) or carbon nanofibres

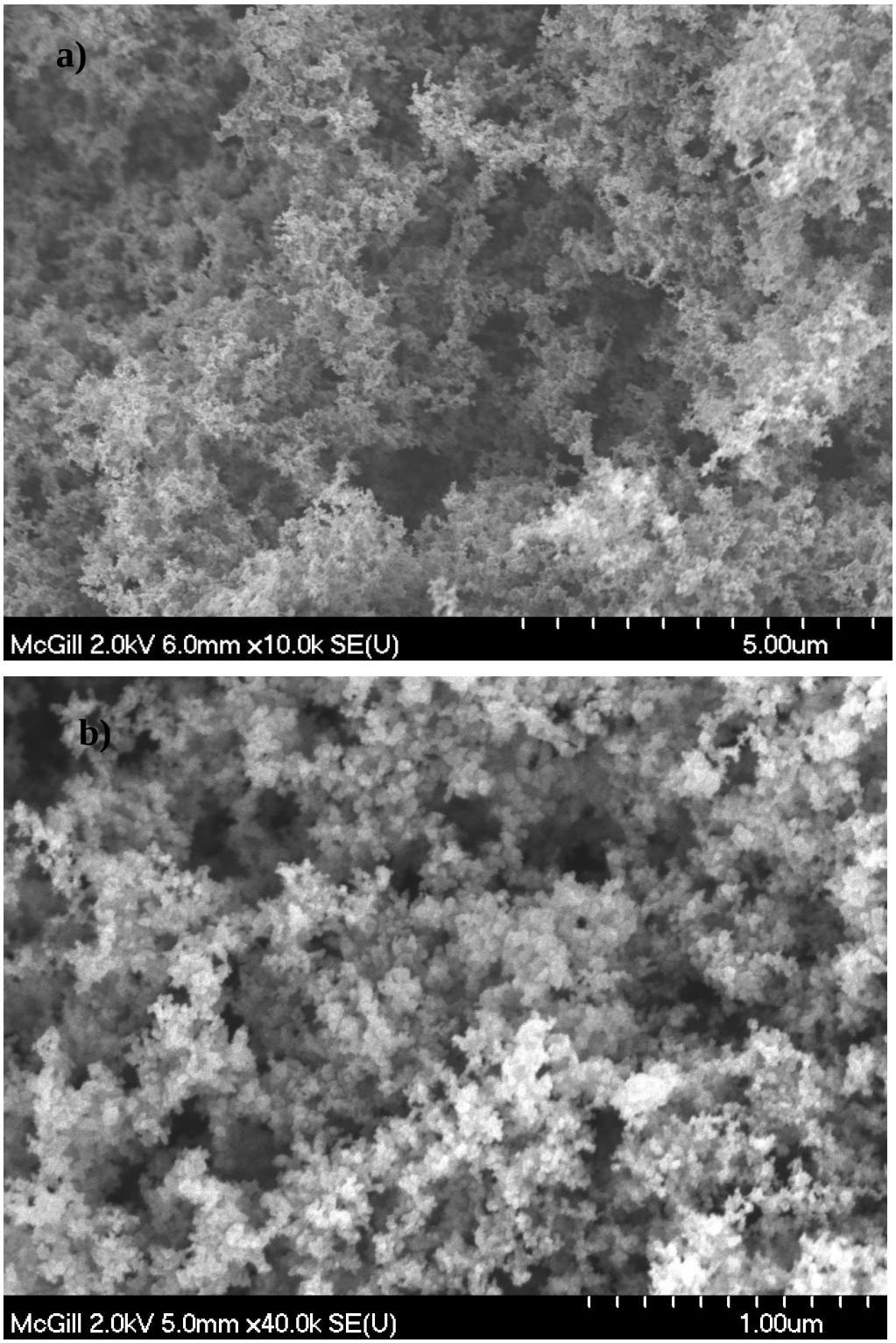

Figure 5.8 SEM image of carbon material collected from the DC reactor wall at: a) 5µm scale bar; b) 1µm scale bar

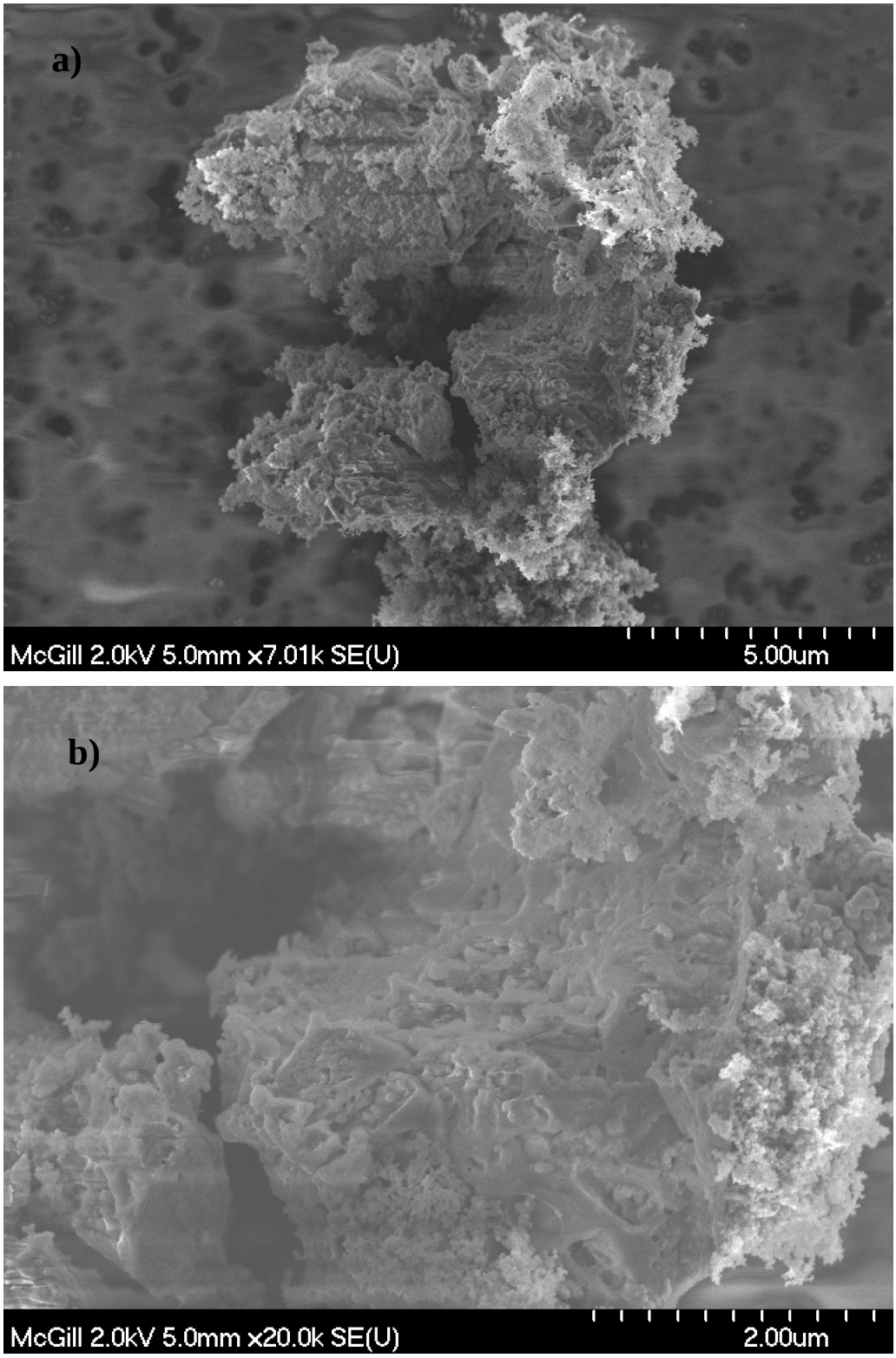

Figure 5.9 SEM image of the carbon material collected in the DC reactor on the movable disk at: a) 5µm scale bar; b) 2µm scale bar

Of all the various structures of the carbon powders collected from different parts of the DC system, the fine and well dispersed particles collected from the reactor walls present the morphology that is most suitable for the scope of the project. These powders were further characterized using TEM; a typical TEM micrograph of these powders is presented in Figure 5.10. The micrograph shows a crystalline structure, although more non organized areas are also present as seen in the bottom-right part of the image. These areas show small scale variations of the electron diffraction intensity. This indicates the presence of very small crystallites with no long range order (scale lengths smaller than about 5 nm). There are also areas where completely non organized structure can be observed as can be seen in Figure 5.11. This areas show an amorphous-like structure bridging the entire network of particles in a way opposite to the independent spherical agglomerated particles seen in Fig 5.8b. These structures are similar to the amorphous polymeric structures observed under electron microscopy.

These areas contain large amounts of the volatile organic compounds that were observed in the Raman spectroscopy measurements of Figure 5.1 indicating an important fluorescence background, and the TGA of Figure 5.3 showing a series of low temperature peaks of mass loss.

The presence of metallic impurities was also observed in the TEM images. As can be clearly seen in Figures 5.12a and 5.12b, important amounts of spherical metallic particles are present in the carbon powders. These particles have dimensions between 50 nm and 500 nm. The field showed in Figure 5.12a is not typical for the entire powder volume. Some contaminated areas, as the one presented here, were observed in the samples.

Using EDS, the metallic particles were identified as tungsten and iron particles. The EDS spectra of the carbon black samples collected from the quench ring (Figure 5.13a) show a series of small peaks characteristic of tungsten. The presence of tungsten on the quench ring confirms the transport of tungsten nanoparticles downstream of the torch nozzle to the quench ring. Furthermore, Figure 5.13b shows EDS spectra of carbon black samples collected from the

movable disk. These powders contain iron nanoparticles, which indicate that part of the iron eroded from the quench ring travel with the gas flow and is deposited downstream on the movable disk.

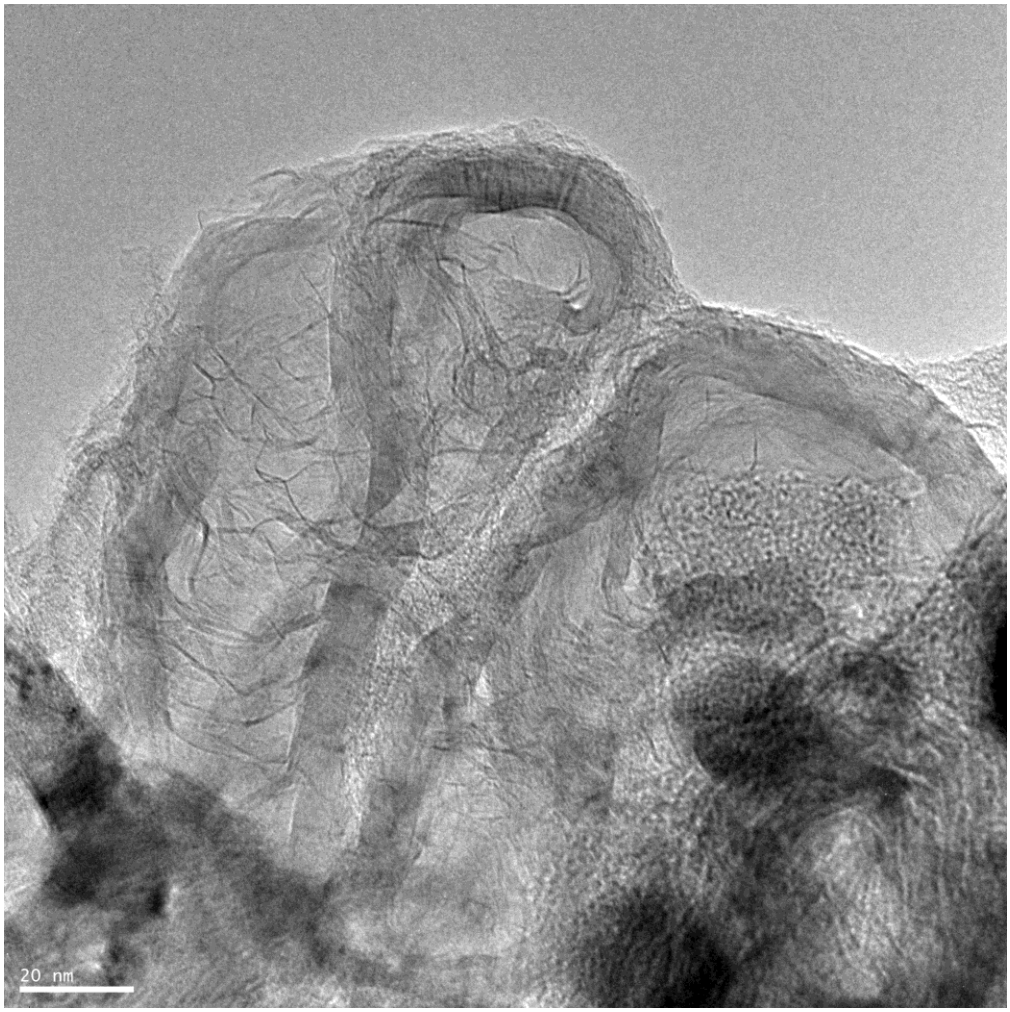

Figure 5.10 TEM image of carbon material collected from the DC reactor walls

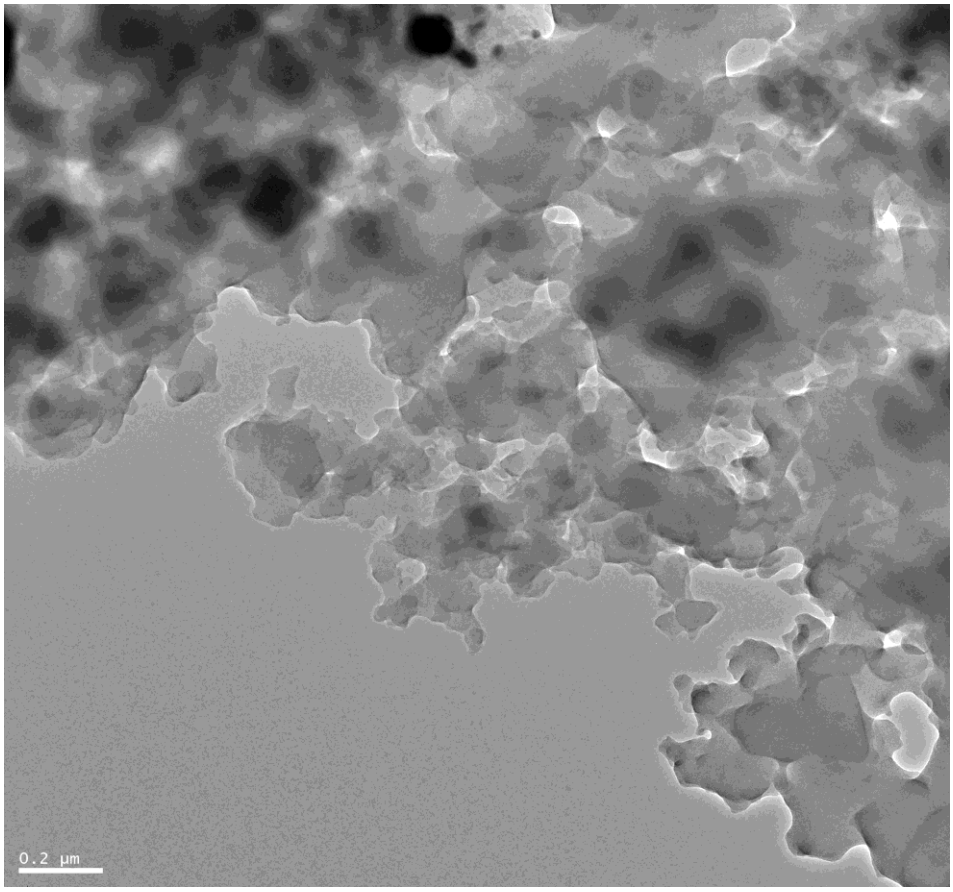

Figure 5.11 TEM image carbon material produced in the DC reactor and collected from the collection plate showing the presence of compounds with polymer-like amorphous structures

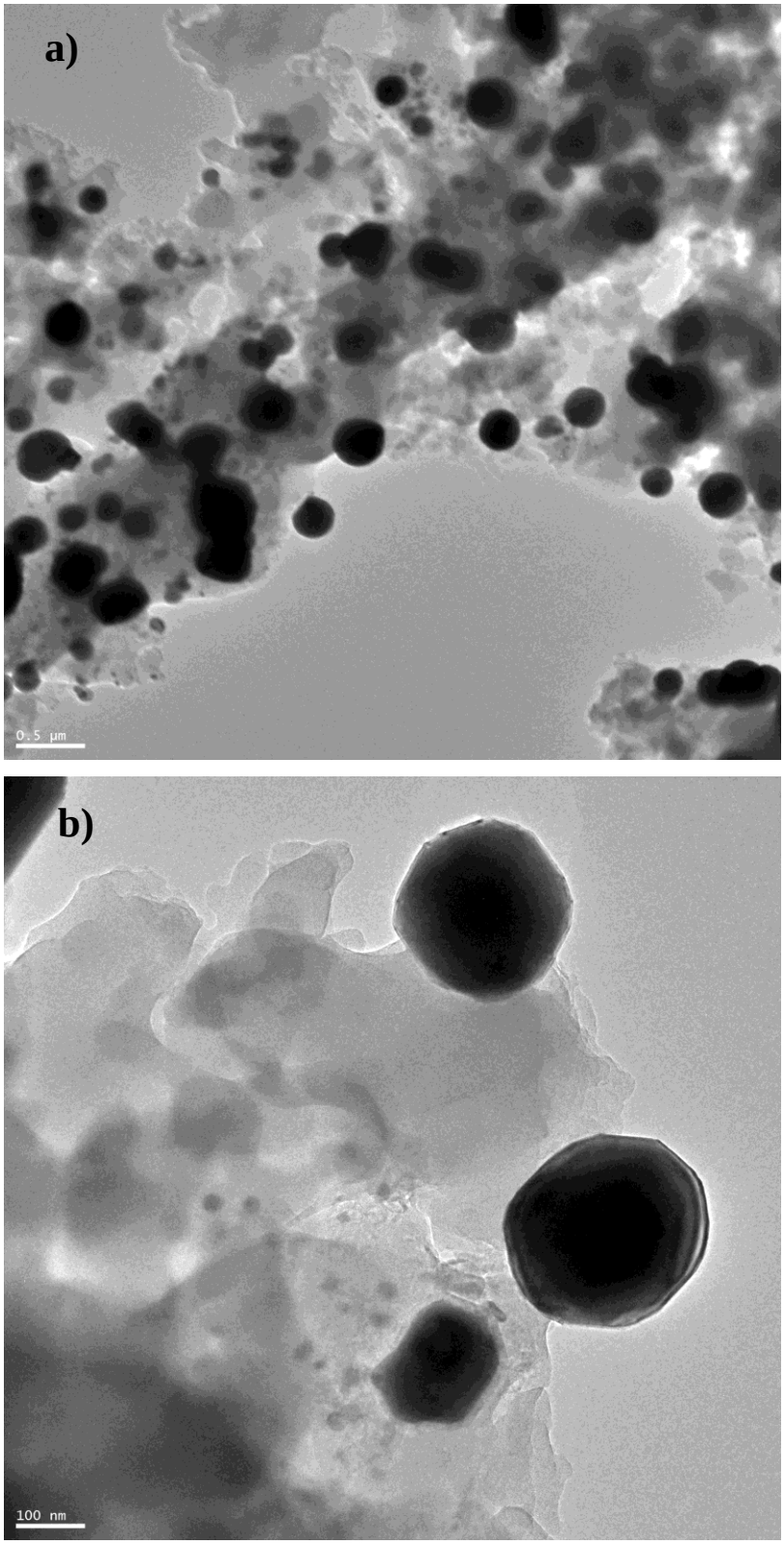

Figure 5.12 TEM image of the carbon material in the DC reactor showing metallic particle impurities: a) 500 nm scale bar; b) 100 nm scale bar

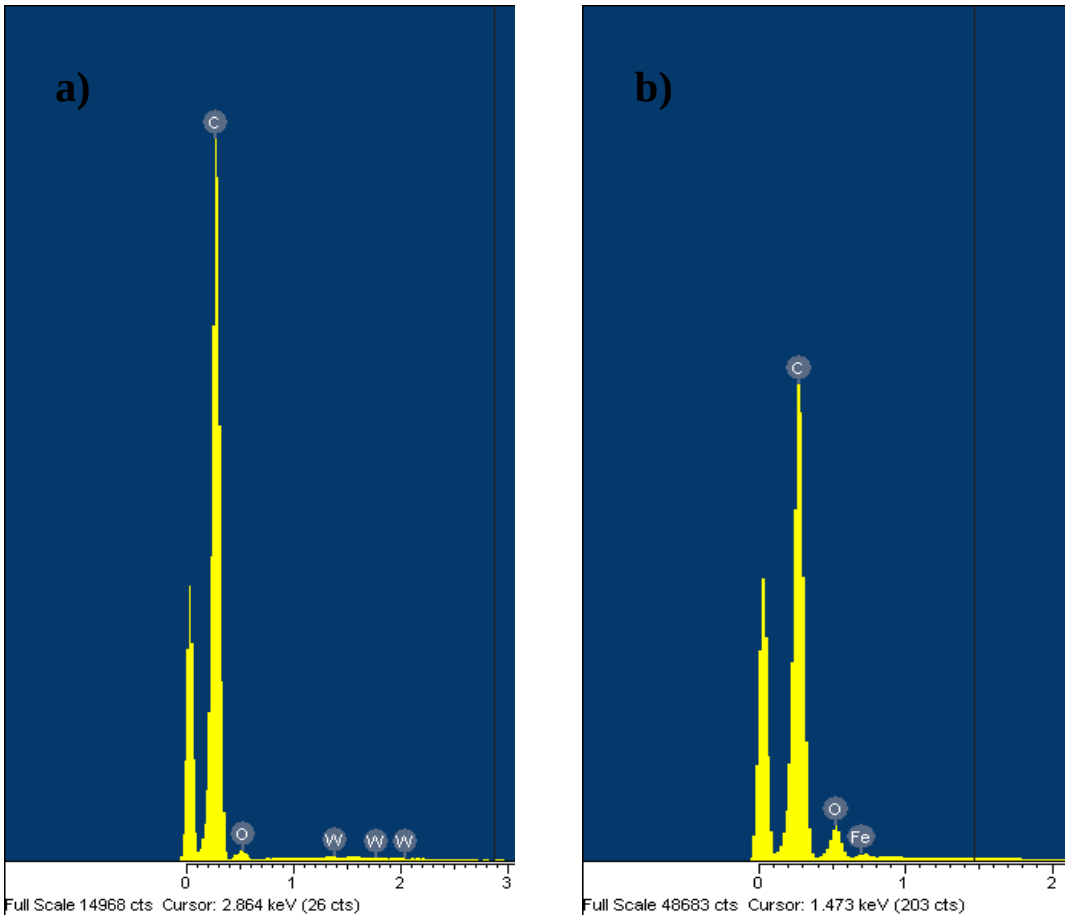

Figure 5.13 EDS spectra of carbon powders from the DC reactor identifying: a) tungsten particles identified in the carbon black sample collected from the quench ring; b) iron particles identified in carbon black sample collected from the movable disk

5.3 Discussion

The CB powders produced using the DC thermal system present different morphologies if collected from different parts of reactor: small dispersed particles for the samples collected from the reactor wall and big agglomerated particles if collected from the collection plate. This non-homogeneity in the particulate structures is related to the presence of flow recirculation loops in the system, generating various thermal history paths for the nucleation and agglomeration processes. These recirculation areas promote the formation of intermediate compounds, such as organic volatile compounds, which promote the

agglomeration of the spherical particles and change the properties of the final product. One important change is the decrease of the specific surface area values. A confirmation on the presence of organic compounds is presented in Chapter 9 using Raman Spectroscopy and TGA analysis.

The characterization of the CB powders produced in the DC reactor also showed the presence of large amounts of contaminants in the samples, generated by both the arc-based erosion of the torch electrodes and the quench ring ablation. Different materials (i.e. α-Fe, W, Fe_3C and WC) were identified by XRD analysis.

To be used as catalyst support material for PEM fuel cells applications, the CB powders need to contain nitrogen incorporated into a pyridinic bonding configuration on the edges of graphene crystallites, and an iron atom bonded to the nitrogen atoms, creating in this way the active centers of the catalyst (refer to Chapter 3, Figure 3.6 for the structure of the active site). The purity of the samples is a very important characteristic to avoid poisoning effects due to the presence of different contaminants in the catalyst, particularly metallic contaminants. These metallic particles can exchange electrons with the iron atoms present in the active site, thus decreasing the activity of the catalyst. Also, a high degree of crystallinity of the CB material is necessary to make available the graphitic edges for the formation of the active sites. The results indicated above show finally an important variability of the structures obtained in the reactor. There is also variability from run to run because of slight variations of the operating parameters, making difficult to predict the CB structure in the system. Reproducibility is a common problem in nanoparticle synthesis from thermal plasma systems, a problem which is expected to be strongly linked to the variability of the thermal history of the precursor species in a reactor. Plasma torch fluctuations, flow fields fluctuations and recirculations, and the very important gradients in the DC system generate important difficulties in the control of a stable nucleation field. For the above reasons of lack of uniformity and the fact the DC reactor-based nucleation implies a relatively large amount of metallic impurities, we believe the CB powders produced by DC thermal process cannot be used to generate the carbon support material for the catalyst structure

functionalization being seeked here. The electrodeless configuration of an ICP thermal plasma system is believed to provide a better alternative through the elimination of the contamination effects while simultaneously maintaining the high temperatures for good crystallization, and generating lower flow velocity fields for a better control of the nucleation process. The following chapters follow on this thermal plasma based CB nucleation and functionalization using the ICP thermal plasma source first in a reactor having the same geometry as the DC system in the present chapter.

Chapter 6 – Peer reviewed paper published in Plasma Chemistry and Plasma Processing Journal

Full reference: Pristavita, R., Mendoza-Gonzales, N.Y., Meunier, J.L., Berk, D., "Carbon Blacks Produced by Thermal Plasma: The Influence of the Reactor Geometry on the Product Morphology", Plasma Chem. Plasma Process., **30**, 267-279, 2010

This project started with the idea of nucleating CB powders having a certain degree of crystallinity and porosity by using and comparing two types of thermal plasma sources: a DC-torch system having very high quench rates and low residence times, and an ICP-torch system with smaller quench rates but longer residence times. The thermal plasma route was chosen here based on the high temperature of the process expected to enable the higher degree of crystallinity in the powders. At this stage of the project the experiments performed with the DC-torch system proved that the produced CB powders were not good candidates for the scope of this work aiming for a new catalysts support material in PEM fuel cell applications mainly because of the contamination due to electrode erosion, but also from the difficulties in controlling the nanoparticle morphologies.

The present chapter includes the experimental results on the CB production using an ICP thermal plasma system and two types of reactor geometries: a cylindrical shape reactor and a conical one. The experiments presented are first performed using an ICP system with a cylindrical reactor. The results present different CB morphologies generated in this reactor, and highlight the influence of recirculation areas in the system generating the various product structures.

Following the results presented by Castillo [12], a reactor having a conical expansion is considered as an alternative eliminating the recirculation flow fields. A modeling study is conducted to determine if this reactor geometry effectively minimizes the presence of recirculation areas in the present synthesis conditions, and generates a better control over the CB powder final morphology. Both the modeling and the experimental results are presented in this chapter.

An uniform specification of turbulent quantity based on the hydraulic diameter (m) and turbulent intensity (%) is specified in the present model when the flow enters the domain at the three inlets Q1, Q2 and Q3. The turbulent intensity is defined as the ratio of the root-mean-square of the velocity fluctuations, to the mean flow velocity. A turbulence intensity of 1% or less is generally considered low and turbulence intensities greater than 10% are considered high. The present case uses an arbitrary value of 1% which is characteristic for very low turbulent cases and considering that the plasma torch region is often considered as laminar flow.

The results indicate that not only a very good and highly reproducible process control is achieved in the new geometry, but also a pure and highly graphitized "carbon nano-flake" (CNF) structure is achieved, these CNF being in the shape of a stacking of between 6-16 atomic layers of graphene planar structures of typical planar size on the order of 50nmX100nm.

Carbon blacks produced by thermal plasma: The influence of the reactor geometry on the product morphology

Ramona Pristavita, Norma-Yadira Mendoza-Gonzalez, Jean-Luc Meunier and Dimitrios Berk

Abstract

Carbon black (CB) nanopowders were obtained by plasma decomposition of methane at various flow rates using inductively coupled thermal plasma (ICP) torch system of 35 kW. Nitrogen was also introduced in some experiments along with the methane. Using a cylindrical shape reactor, the obtained powders were composed mainly of spherical particles, nonuniform in terms of particles size with diameters between 30 nm and 150 nm. The shape and size of this reactor resulted in the presence of recirculation areas enabling the formation of large CB particles and other secondary volatile compounds. Changing the reactor to a conical geometry resulted in the production of CB powders showing a crystalline and flake-like morphology made of sheets having 6-16 graphitic planes. The conical shape avoids the presence of recirculation areas and promotes the formation of uniform powder morphology throughout the reactor.

Keywords: carbon black, carbon nano-flakes, thermal plasma, reactor geometry, ICP torch, PEM fuel cell catalyst

6.1 Introduction

There is presently an ongoing effort to develop and improve the performance of hydrogen fuel cells based on polymer electrolyte membrane (PEM), also called Proton Exchange Membrane fuel cells. The reactants in such a fuel cell are gaseous hydrogen and air. The hydrogen atoms are split into protons and electrons by a catalyst, and they pair up again on the other side of the membrane in the presence of air, forming water molecules. The PEM fuel cells represent a clean and efficient alternative energy source; however their production cost must be

reduced substantially to be economically viable. One possible way to reduce this cost is to develop an alternative low cost catalyst such as the non-noble catalysts [1]. The present catalyst material consists of carbon black (CB) powders on which platinum (Pt) particles are uniformly dispersed. The Pt particles act as catalyst helping the oxidation-reduction reactions taking place at the electrodes. While non-platinum catalysts still show lower activity and much lower durability than Pt, recent improvements in their beginning-of-life activity give increased hope for their eventual practicality. The non-noble catalysts materials consist also of CB powders on which active centers are formed. These active centers have a structure of metal-N_4 chelates. The metal atoms coordinated into the active site can be any transition metal atoms, but iron and cobalt are known to present the highest electrocatalytic activities. [2]

CB powders are composed of nearly round primary particles called nodules and have particle sizes between 10 nm and 300 nm. In fact, these primary particles are built using smaller building blocks presenting graphitic sheets typically having a random orientation. The primary particles fuse together and form aggregates. Strong electrical forces bond the aggregates and promote the formation of agglomerates [3]. CB, which is widely used in industry including in the energy and materials sectors, is produced at industrial scale using a furnace process or a thermal process. In recent years, new CB's powders were synthesized using plasma technology [4-6]. One of the advantages of such a technology is the possibility to use a variety of carbon sources in gaseous, liquid or solid state. The plasma process is also clean, it does not generate CO_2 and the resulting CB powders do not contain large amounts of impurities as those found in the flame processes.

In a thermal plasma system, the particle size and the number of nucleated particles are affected by two factors: the cooling rate at the location of the nucleation and the monomer concentration. High monomer concentration and low cooling rates favor the nucleation of larger and fewer particles [7, 8]. The properties of the product are also influenced by the local temperature: injection of carbon source in the arc zone (T~ 10000K for argon plasma) results in production

of a highly organized CB. The growth of the particles in a low temperature region of the reactor ($T<1600^0C$) will lead to an amorphous product with spherical particles [4]. The nature of the feedstock does not influence the size distribution of CB aggregated but an important role is played by the zone where the carbon source is injected [9].

The results presented in this communication are part of an overall work whose objective is to produce, using a plasma reactor, CB nanopowders having a high density of catalytic sites on the surface of the carbon particles which implies a high catalytic activity. The catalyst material needs to contain nitrogen atoms bonded to the graphitic support and iron atoms bounded to the nitrogen atoms, creating the active centers of the catalyst [10, 11]. In terms of chemical structure, the increase in the number of catalytic sites requires a crystalline nanostructure of the powders and an increase in the quantity of nitrogen incorporated in the nanostructure. CB was chosen because of its electrical conductivity, its high surface area and its ability to function in the highly acidic medium of the PEM fuel cells.

The size of the formed particles nucleating in a typical thermal plasma process is strongly influenced by the reactant concentration and the cooling rate [7]. The high temperature zone of thermal plasma often reaches above 10,000 K at the position of reactant injection. The carbon precursors are thus expected to be completely vaporized and largely dissociated in this injection region. Downstream of the plasma torch the gases are rapidly cooled and the chemical reactions generate condensable species. The very high quench rates ($10^5 – 10^7$ K/s) enable the formation of nano-scale particles; a homogeneous nucleation process is triggered which, in the presence of atomic C and the high temperatures still occurring downstream of this quench, may enhance the graphitization of the nanoparticles of carbon.

In this paper we present different types of CB powders obtained by plasma decomposition of methane at various flow rates using an inductively coupled thermal plasma (ICP) torch system. Two types of reactor geometries were modeled and tested, and a description of the influence of the flow and temperature

fields in these geometries on the final structural properties of the product is also discussed.

6.2 Experimental setup

CB nanopowders were obtained by plasma decomposition of a carbon-containing feedstock. The material was produced using a 35 kW inductively coupled thermal plasma (ICP) torch system using methane as the carbon precursor and various flow rates from 0.5 slpm to 6 slpm. The injection probe is inserted into the torch in axial position, the tip of the probe reaching the coil area of the torch body, below the first coil turn, allowing the injection of methane in the core of the plasma. In some experiments nitrogen is also introduced along with the carbon source using a flow of 0.1 slpm. The methane injection time varies between 5 and 32 minutes. In the experiments presented here, the reactor power is kept constant at about 10 kW plasma power (20 kW plate power) and the reactor pressure varies between 20.7 kPa and 89.6 kPa. The ICP torch can be attached to two different reactors, both water cooled and made of stainless-steel but having different geometries: a cylindrical reactor being 32 cm in diameter and 100 cm in length presented in Figure 6.1, and a conical reactor having 50 cm in length and an angle of expansion of 14^0 as presented in Figure 6.2 [12].

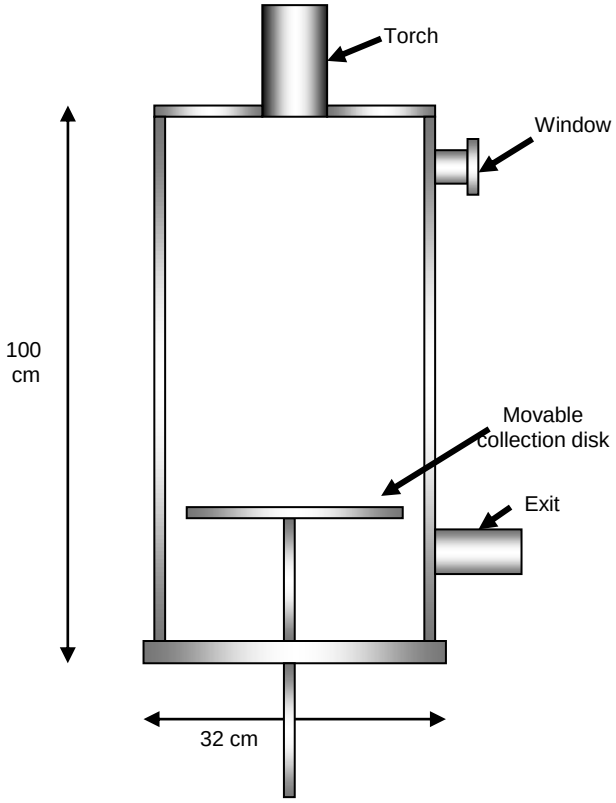

Figure 6.1 Diagram of cylindrical water cooled reactor

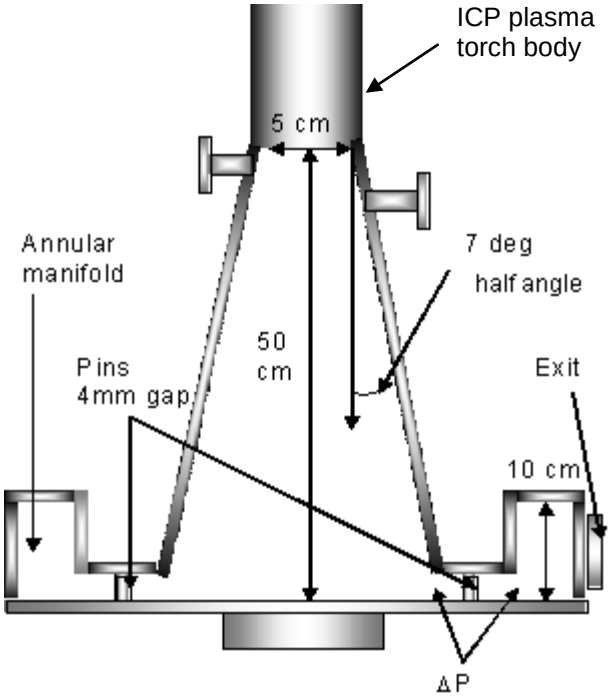

Figure 6.2 Diagram of conical water cooled reactor [12]

6.3 Results and discussions

6.3.1 Cylindrical reactor

The morphology of the particles obtained using the cylindrical reactor geometry (Figure 6.1) was analyzed using Scanning and Transmission Electron Microscopy (SEM and TEM). The particles show a spherical structure with diameter typically of the order of 30 nm (Figure 6.3a and Figure 6.4a) although bigger spherical particles up to 150 nm in diameter are also observed. Beside the presence of these bigger spherical particles, we also observe that particles collected from different positions within the reactor show differences in their structural properties. For example, the samples collected from the bottom of the reactor from the collection plate and from the lower part of the cylindrical reactor walls show particles having a spherical shape (Figure 6.3a), while the ones collected from the upper part of reactor walls show a bulk graphitic structure (Figure 6.3b). This is believed to be the result of geometry affecting the gas flow pattern and the thermal history of the particles. The sudden expansion of the gas at the top of the reactor causes the formation of recirculation areas in the reactor. In the recirculation areas, the growth history of the particles cannot be controlled. In particular, large residence times are expected in such flow patterns leading to a product having a large particles size distribution and different structural properties.

An increase of the carbon source flow rate modifies the CB structure from small, spherical particles forming aggregates and agglomerates to a columnar structure (Figure 6.3c and Figure 6.4b). The cooler recirculation areas present in the reactor result in the condensation of some of the species present in the gas stream, which eventually form secondary products. Using GC-MS on these samples, volatile organic compounds and a fraction of polycyclic aromatic hydrocarbons are observed to evolve during a thermal treatment up to 800 ºC. Increasing the carbon source flow rate from 1-2 slpm to 5-6 slpm generates more volatile compounds. These compounds act like a glue for the CB particles promoting the formation of columnar structures as seen in Figure 6.3c.

The small particle diameters obtained, starting at about 30 nm, are expected to lead to large specific surface areas. The specific surface area of the particles produced was measured using a BET technique. The values obtained for these powders were on the contrary very small, below 30 m^2/g. This indicated again that our samples contain a large fraction of contaminants which are possibly filling the pores and agglomerating the particles, resulting in a decrease of the specific surface area of the product.

The presence of these secondary products was confirmed by Raman Spectroscopy. The Raman spectra were obtained using an incident laser wavelength of 514 nm and a grating of 1800 lines/mm. All the spectra show distinct G and D bands characteristic of graphitic materials and a strong fluorescence background from the presence of volatile organic compounds in the sample. An increase of the carbon source flow rate during the production process led to an increase in the content of this volatile fraction. Also, the addition of 0.1 slpm of nitrogen to the methane flow during the production process was observed to increase the amount of contaminants produced (Figure 6.5).

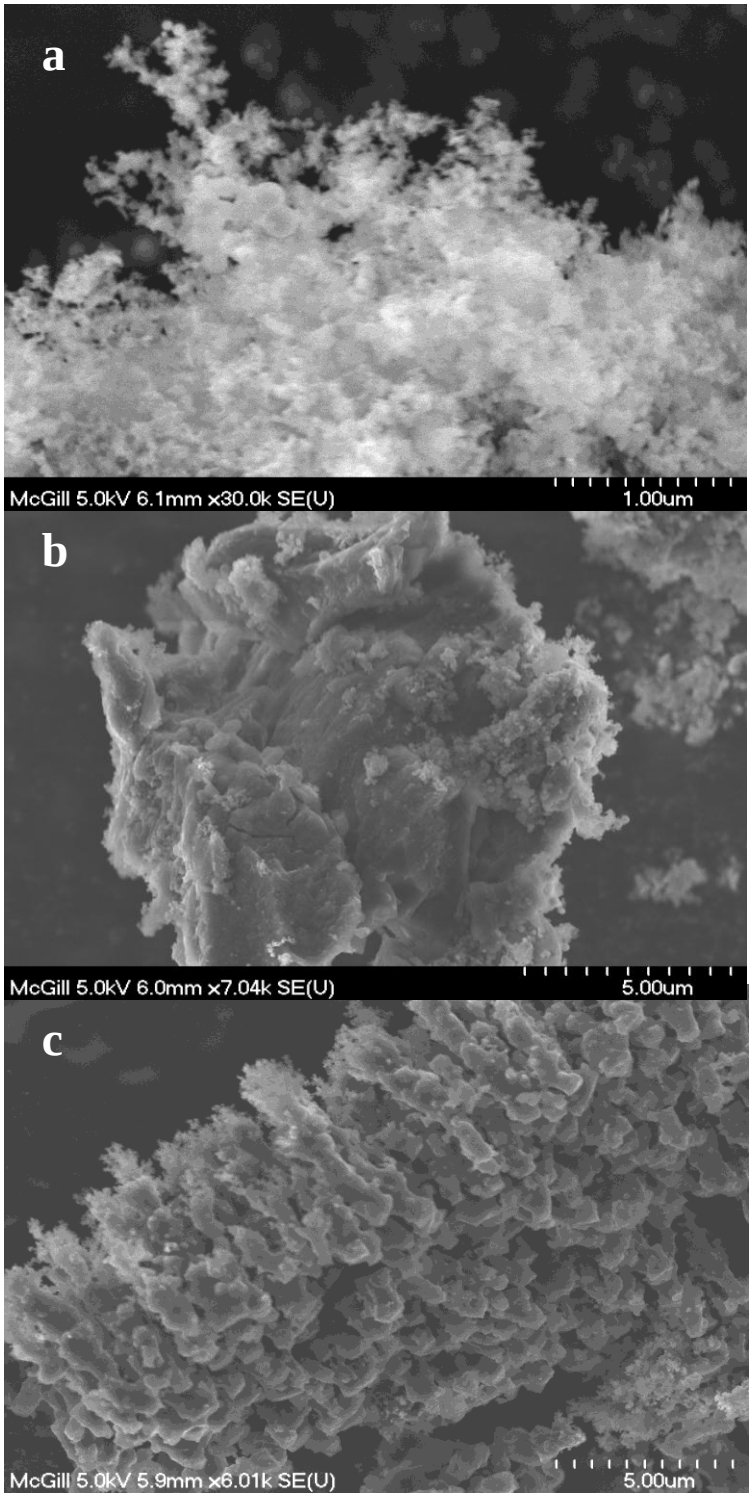

Figure 6.3 SEM images of CB samples produced using a methane flow rate of: a) 2 slpm and collected from the reactor bottom; b) 2 slpm and collected from upper part of reactor walls; c) 5 slpm and collected from reactor bottom

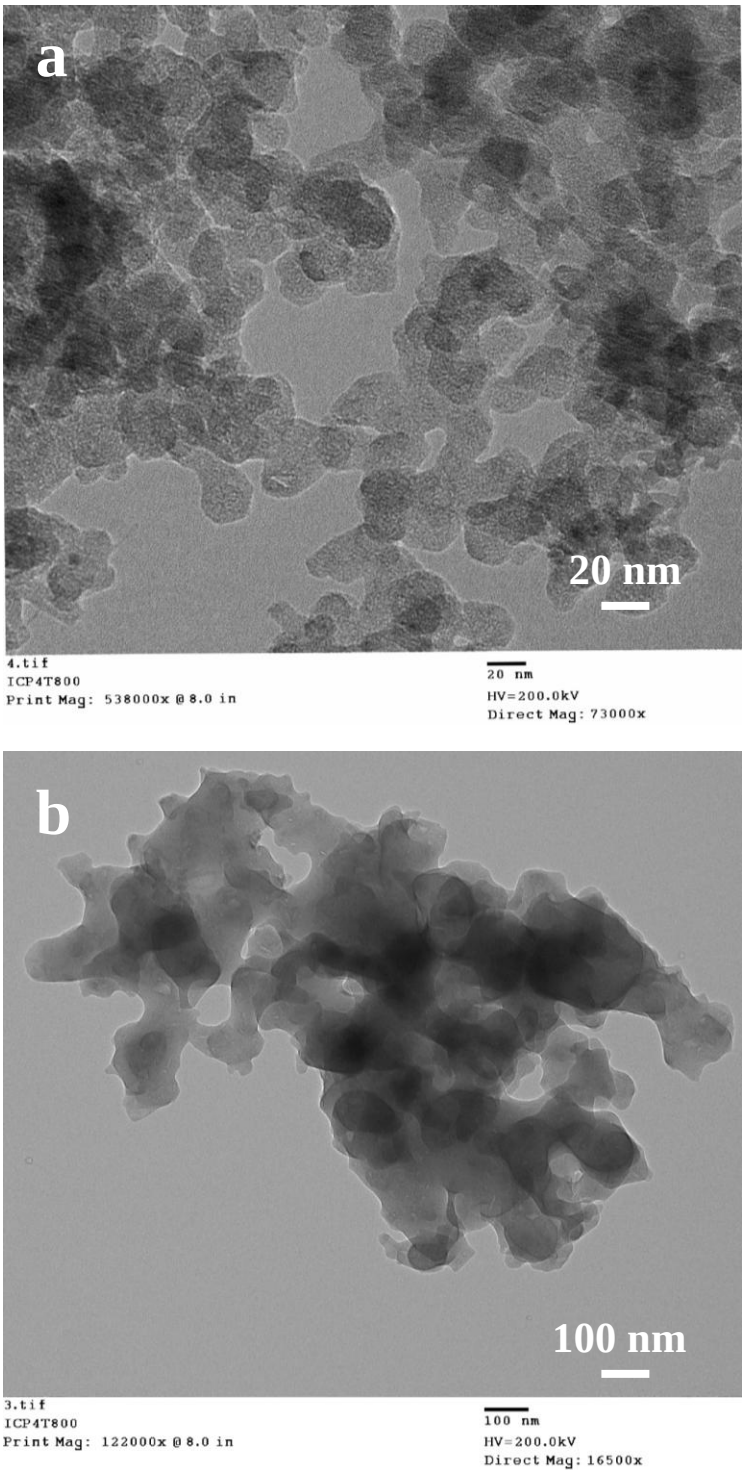

Figure 6.4 TEM images of CB samples produced using a methane flow rate of: a) 2 slpm and showing spherical particles; b) 5 slpm and showing columnar structure

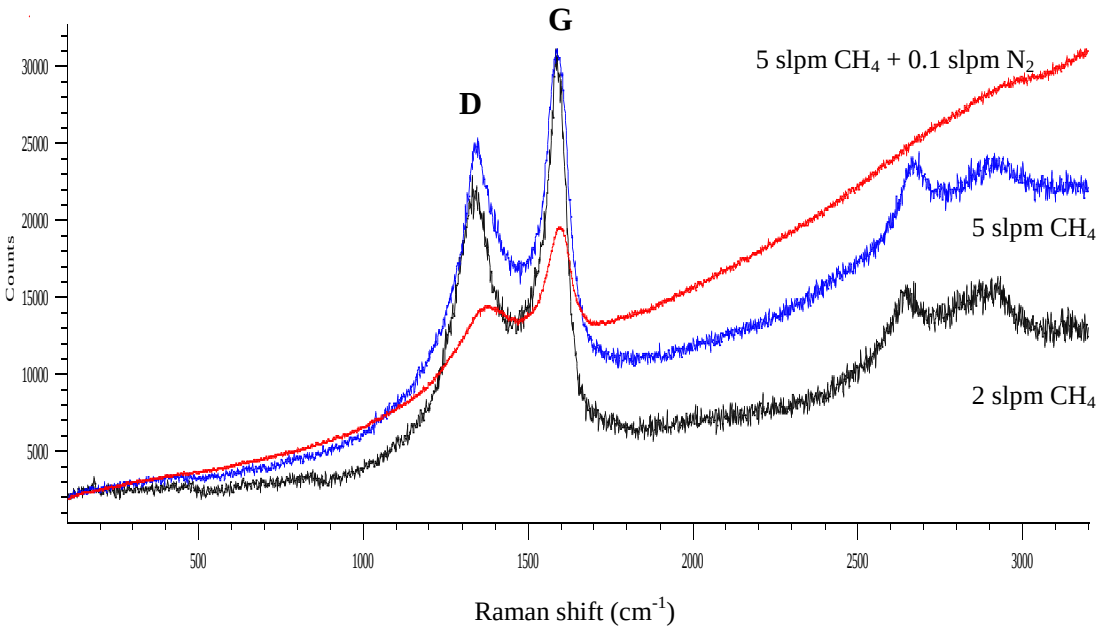

Figure 6.5 Raman spectra of CB samples at various flow rates presenting distinctive D and G primary bands and a fluorescence background

X-ray diffraction (XRD) patterns were recorded in order to determine the degree of crystallinity of the samples. These diffraction patterns show that the powders are essentially amorphous although the presence of two peaks characteristic of graphitic materials are observed at 2θ of 22^0 and 44^0 (Figure 6.6). This is indicative of CB primary particles being composed of small graphitic domains.

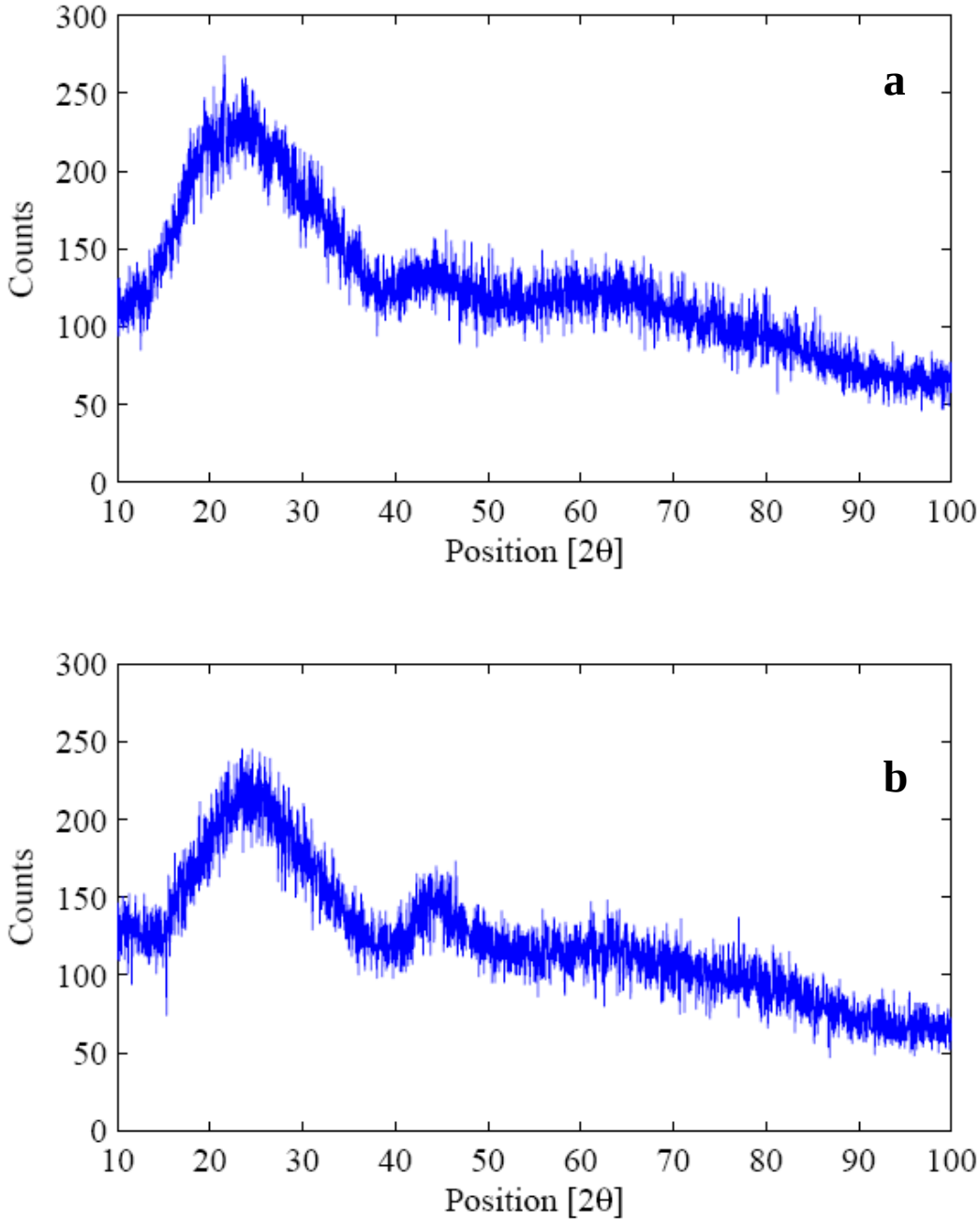

Figure 6.6 XRD diffraction patterns of CB samples produced using a methane flow rate of: a) 2 slpm; b) 5 slpm and showing an amorphous structure

6.3.2 Conical reactor

The cylindrical reactor geometry and the presence of recirculation zones were observed to influence strongly the structural properties of the product. The recirculation zones also affect the reproducibility of the results and strongly increase the variability of the micro-structures of the powders collected in different zones of the reactor. A reactor having a conical expansion with an angle of 14^0 (Figure 6.2) was used to eliminate the possibility of recirculation flows. Such geometry provides a gradual gas expansion from the torch to the reactor minimizing both recirculation areas and sudden quenching of the gas. A 4 mm annular gap between the conical section of the reactor and the bottom collection plate is used for the gas outlet. An annular manifold around this outlet collects the exit gases which exit through a single outlet in the manifold. A higher pressure drop is maintained across the annular gap in comparison to the pressure drop in the manifold, ensuring in this way a radial outlet flow pattern of the gases from the collection plate. This geometry also provides a symmetric flow pattern within the reactor chamber above the collection plate and stagnation point flow geometry on the plate itself [12].

The conical reactor geometry completely modified the structure of the CB powders produced at various pressures. At a low pressure of 20.7 kPa, the powders show predominantly an amorphous structure; however increasing the reactor pressure to 55.2 kPa and 89.6 kPa, a change to crystalline structures is observed.

The XRD patterns shown in Figure 6.7a and 6.7b are representative of powders obtained at low (20.7 kPa) and high pressures (55.2 kPa), respectively. Powders obtained at 20.7 kPa show an amorphous structure with no diffraction peaks associated to specific crystal planes while powders obtained at 55.2 kPa show a number of specific crystalline peaks. A comparison of this last diffraction pattern with that of natural graphite identifies the peaks corresponding to 2θ angles of 25^0, 42^0, 50^0, 72^0 and 88^0 to be characteristic of a graphitic structure.

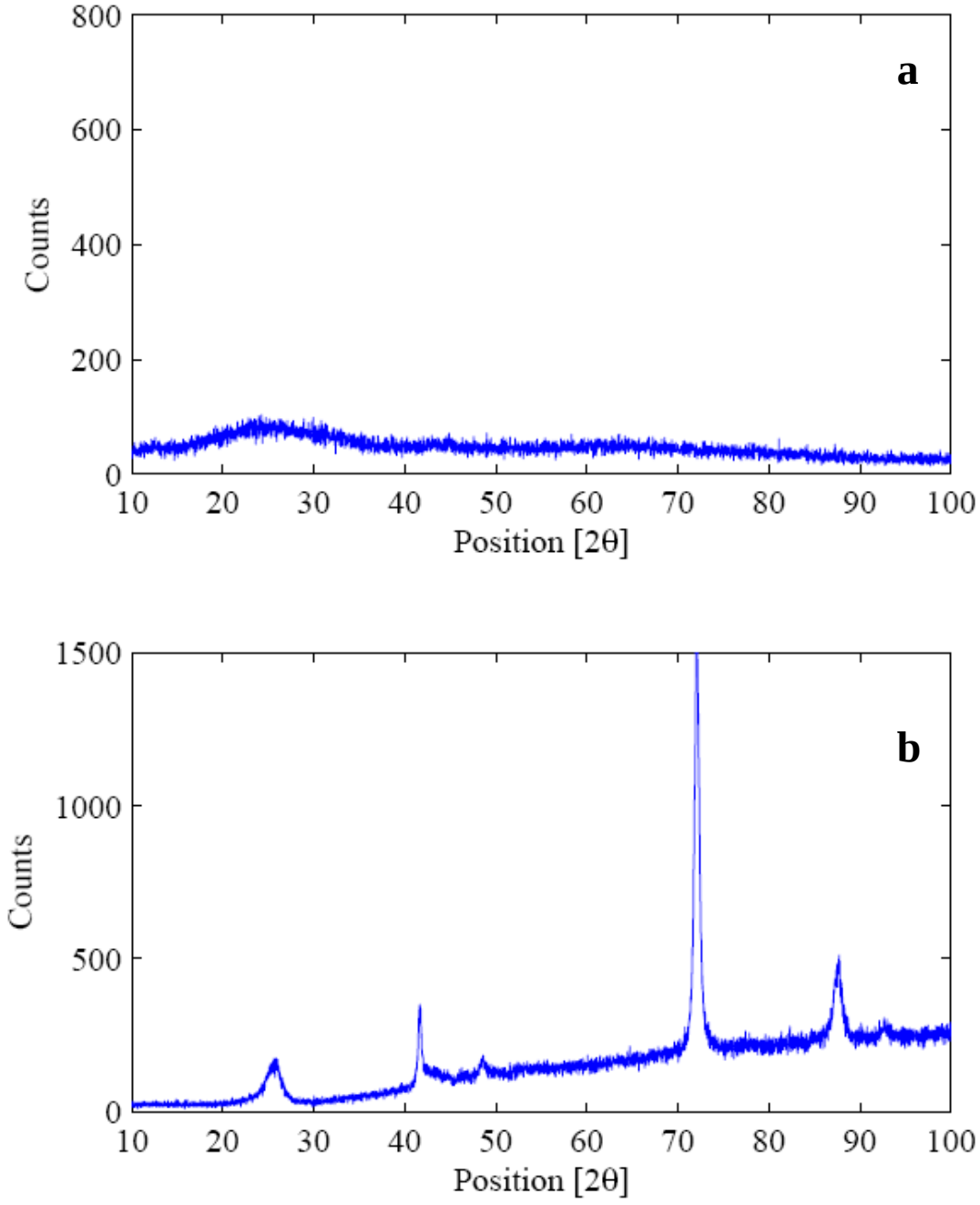

Figure 6.7 XRD diffraction patterns of powders obtained at: a) 20.7 kPa showing an amorphous structure and b) 55.2 kPa showing a crystalline structure

SEM and TEM images (Figures 6.8, 6.9 and 6.10) confirm these XRD results: an amorphous structure of the powders obtained at 20.7 kPa, and a crystalline structure of the powders obtained at 55.2 kPa and 89.6 kPa. Examination of the SEM image (Figure 6.8) and TEM images (Figure 6.10) shows that the crystalline particles obtained at higher pressures have a flake-like morphology, thereafter called "carbon nano-flakes", with dimensions of approximately 100 nm long, 50 nm wide and 5 nm thick. Close observation of the TEM micrograph show the graphitic planes in the cross section with a stacking of between 6 and 16 planes in the powders observed. Similar CB structures were previously produced by DC thermal plasma system [13] and non-thermal plasma process [14].

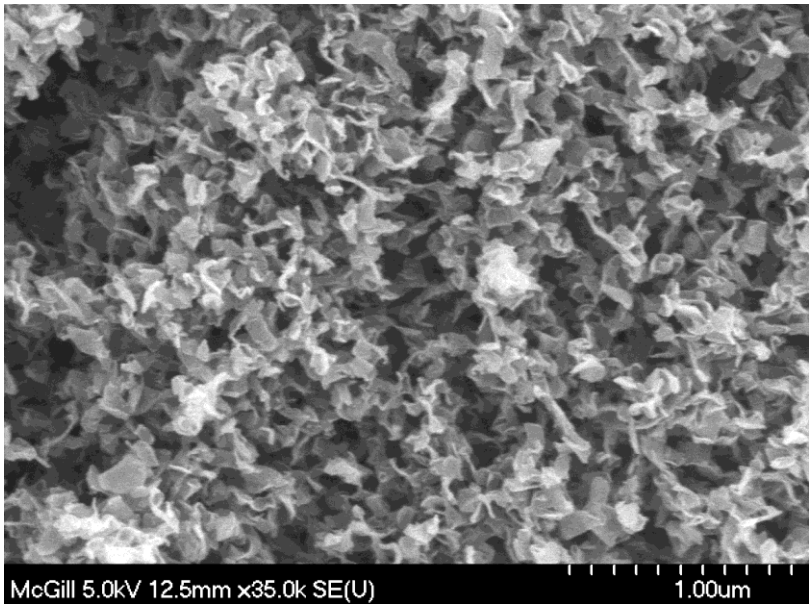

Figure 6.8 SEM image of CB powders obtained at 89.6 kPa showing carbon nano-flakes

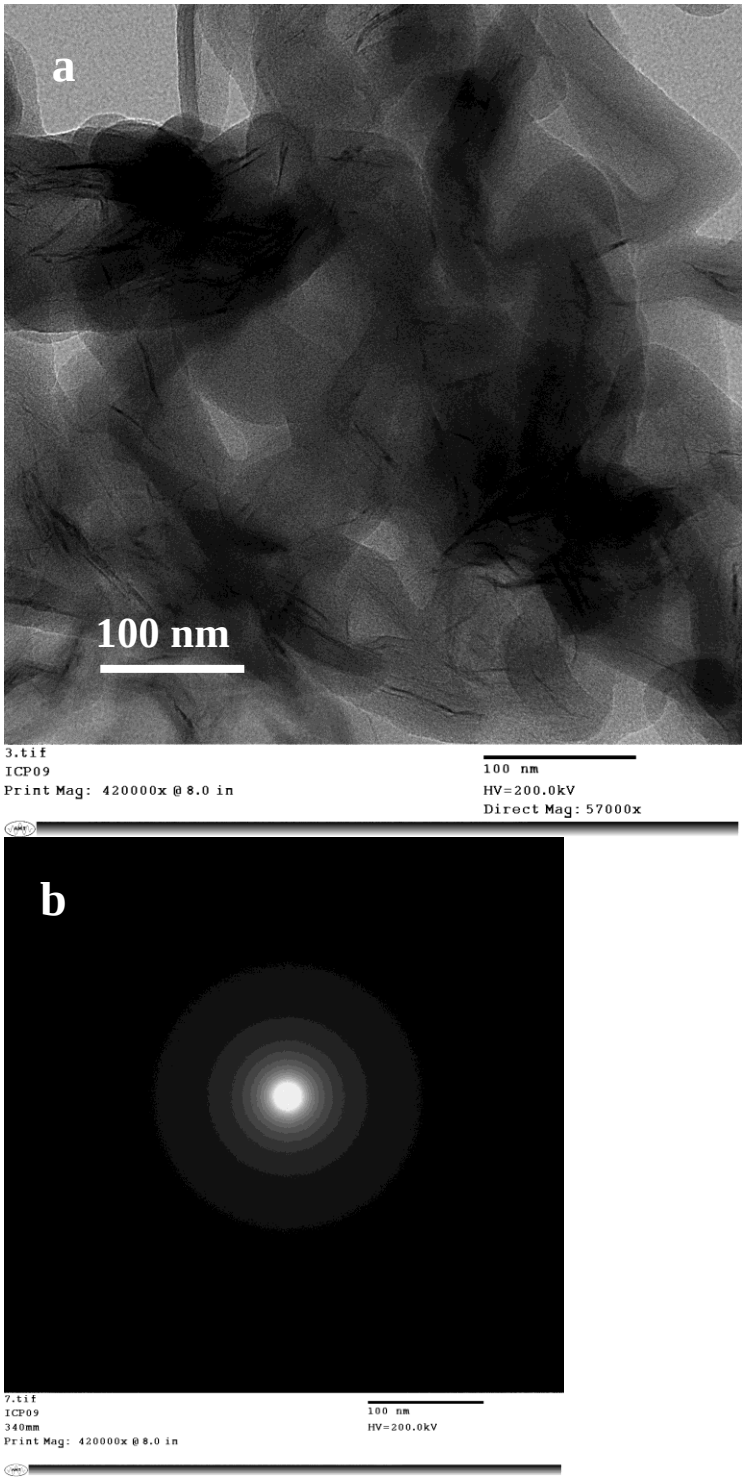

Figure 6.9 a) TEM image and b) electron diffraction pattern of CB obtained at 20.7 kPa indicating a microstructure dominantly amorphous

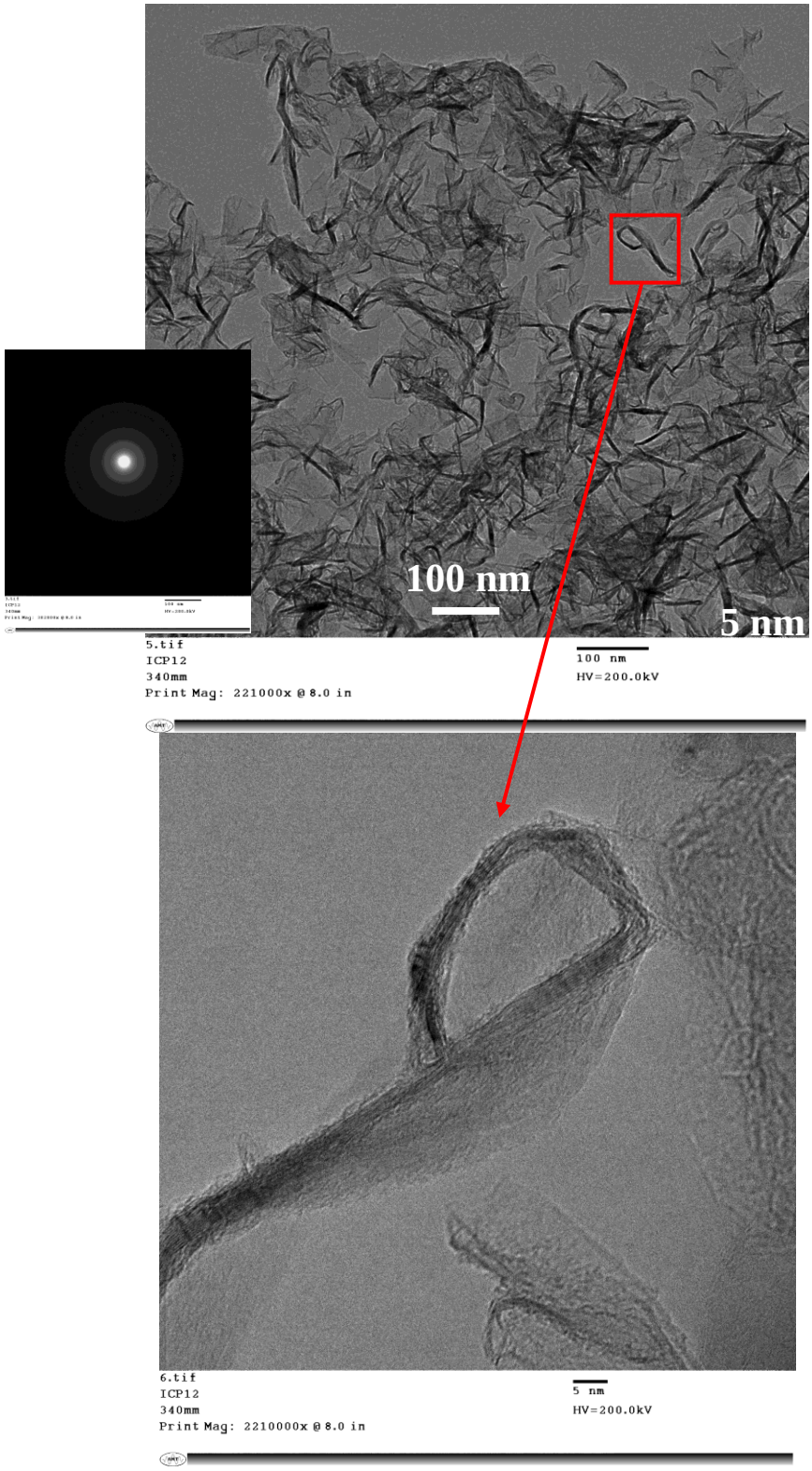

Figure 6.10 TEM images and diffraction pattern of CB obtained at 55.2 kPa indicating a crystalline structure

The BET tests results show that the surface areas of these powders vary between 119 and 345 m^2/g. The low values were obtained for the samples in which the presence of low amounts of organic volatile compounds was observed. It is believed that such organic compounds act as glue and agglomerate some of the carbon nano-flakes, filling the pores and resulting in a decreasing value of the specific surface area.

6.3.3 Comparison of the effect of cylindrical and conical geometries

Modeling of the flow and energy fields using the commercial code FLUENT 6.3 was performed in order to evaluate the occurrence and extent of the recirculation zones in the cylindrical reactor. The following assumptions were considered to solve the plasma flow model: two dimensional (2D) model with fully axisymmetric configuration, steady state flow neglecting gravity effects, turbulence effects included using the RNG k-epsilon model, argon plasma at local thermodynamic equilibrium (LTE), optically thin plasma and the use of a net emission coefficient. The solution for the electromagnetic fields for plasma generation was based on previous modeling studies [15]. Since our interest was to observe the velocity, temperature and recirculation patterns, the model was simplified to pure argon, implying that no carbon species were considered at this stage. The actual operating conditions were accounted in the model by specifying the following boundary conditions: Q_1 = 5 slpm, Q_2 =15 slpm, and Q_3 = 60 slpm which are the inlets flow rates for particle injection, central and sheath gas, respectively. The water cooled reactor walls were set to 300 K as in the experimental setup. The pressure of the reactor was considered at 20.7 kPa with 10 kW plasma power. Radial gradients at the torch outlet were assumed to be zero for all variables while the centerline condition were also set to zero radial gradients and radial velocity. Transport and thermodynamic properties of the plasma gas (e.g., density, viscosity, thermal conductivity, specific heat at constant pressure, and radiation losses) as a function of temperature were obtained from [16]. The underlying computational grid consisted of a total of 50,000 cells for the

conical reactor and 63,000 cells for the cylindrical reactor, thereby assuring that a high computational grid density and numerical accuracy were attained.

The results in Figure 6.11a present the stream-function lines clearly showing the formation of recirculation zones in the upper part of the cylindrical reactor, which is consistent with the powder morphology evolution with collecting position found experimentally. Figure 6.11b presents the gas temperature profile. In the core of the plasma the temperature reaches 10,420 K and it decreases to about 300 K towards the reactor walls.

The modeling results for the conical reactor (Figure 6.12a) present the stream-function lines showing that a uniform flow pattern is achieved using this reactor geometry. Modeling was performed using the same code and same modeling assumptions as for the cylindrical reactor. Figure 6.12b shows the temperature profile in the conical reactor. It can be observed that using the conical geometry the temperature gradients are smaller, which translates into longer residence times of particles in the hot area of the reactor. This promotes the formation of a crystalline structure of the product.

Recirculation areas were present in the cylindrical reactor, enabling the formation of large CB agglomerates and secondary volatile compounds collected on the walls close to the recirculating flow pattern. These volatile compounds act like glue filling the pores of the carbon black particles, decreasing the specific surface area of the powders obtained, and generating a columnar microstructure on the wall deposit. Using the conical reactor shape the presence of recirculation areas is avoided and enables a good control of the thermal history of the gas and solid particles in the reactor, promoting in this way the formation of uniform powder morphology throughout the reactor. Replicate experiments were made and proved the reproducibility of the experiments. Samples were collected from different parts of the reactor: upper and lower part of reactor wall and reactor bottom plate for each replicate experiment and analyzed using the same techniques presented above. The TEM and SEM results showed that these samples presented the same morphology. This reproducibility was also proved by the modeling study. Modeling the temperature/flow fields at 10 and 20 kW

plasma power for the two geometries indicated only small changes in these fields for the conical system, while important variations are observed in the cylindrical system. This agrees with the experimental results yielding very good reproducibility of the collected powder morphology with slightly varying conditions in the conical system, contrary to the difficulty of getting reproducible results in the cylindrical geometry.

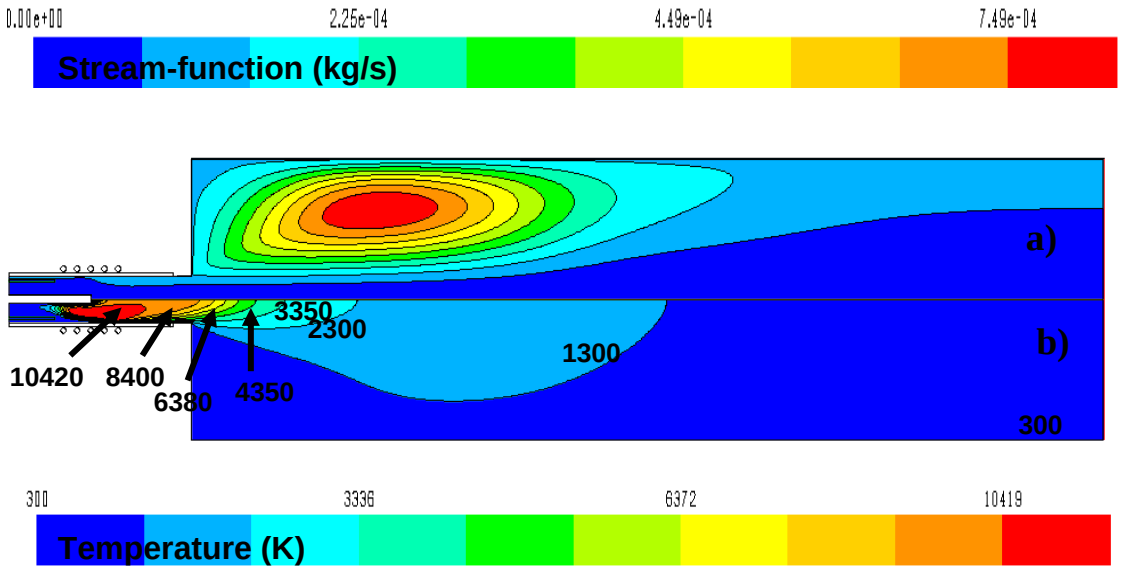

Figure 6.11 Distributions of: a) stream-function and b) temperature inside the cylindrical reactor from the 2D model, using typical plasma power of 10 kW and reactor pressure of 20.7 kPa

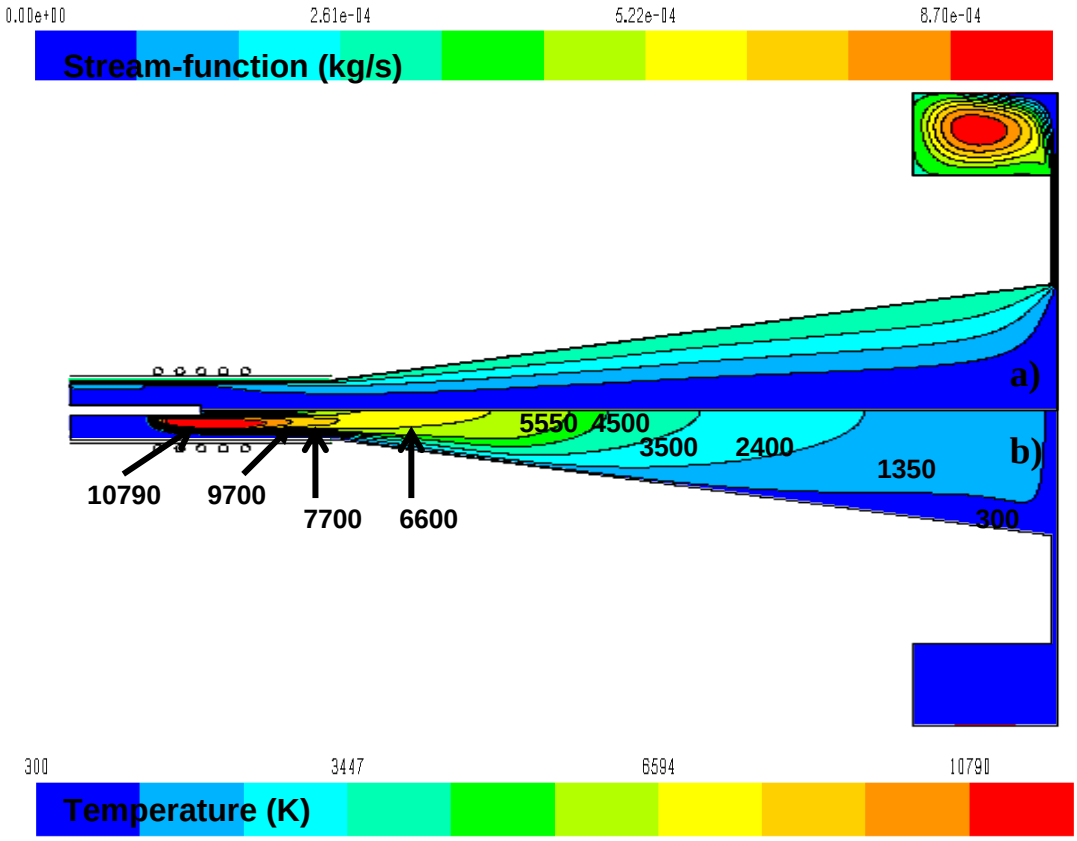

Figure 6.12 Distributions of: a) stream-function and b) temperature inside the conical reactor from the 2D model, using typical plasma power of 10 kW and reactor pressure of 20.7 kPa

The modeling results show that in the conical reactor the local Reynolds number based on local turbulent viscosity ratio is lower than 3000. This value is almost uniform on the conical part of the reactor, and it decreases close to the walls. In the case of the cylindrical reactor, the maximum value of the Reynolds number is located at the reactor center with a value of ~ 10,000 and it decreases towards the walls.

It was observed in the cylindrical reactor that increasing the carbon source flow rate changed the CB structure from small, round particles forming aggregates and agglomerates to columnar structures. This effect was accentuated when adding nitrogen along with the carbon source feed. It is believed that the formation of the

columnar structures is the result of the glue effect of the secondary volatile compounds forming along with the CB.

In the conical reactor the morphology of the product was affected by changing the experimental pressure: an amorphous powder structure was produced at low pressure (20.7 kPa), and crystalline powders were obtained at higher pressures (55.2 kPa and 89.6 kPa). General tendencies can be formulated for such behavior. Operating at low pressure generates larger temperature gradients and higher velocities. This results in particles spending less time in the high temperature areas of the reactor leading to the formation of an amorphous structure. By increasing the reactor pressure, the temperature gradients become smaller while velocities are decreasing; the particles in this case tend to spend more time in the high temperatures areas of the reactor leading to the formation of crystalline structures. Also, increasing the methane flow rate from 0.5 slpm to 5 slpm generated some volatile organic compounds along with the CB powders. The amount of these volatile compounds produced was low and it had no effect on the product final structural properties.

6.4 Conclusions

In the present paper two reactor geometries are presented for the production of CB in an ICP system. It is showed that the reactor geometry has a great influence on the product morphology. A uniform flow pattern and a good control of the thermal history of the gas and solid particles in the conical reactor promotes the formation of a product with an uniform morphology. The presence of the recirculation zones in the cylindrical reactor leads at the formation of products having different morphologies within the same experimental run but in different parts of the reactor. Also, long residence times of the particles in the colder recirculation zones induce the formation of volatile compounds which tend to glue the particles together and fill the pores, decreasing the specific surface area of the product. On the over hand, the good control of the thermal history made possible by the conical reactor enabled the formation of a new CB structure, the carbon nano-flakes.

References

[1] Charreteur, F., Jaouen, F., Ruggeri, S., Dodelet, J-P., "Fe/N/C non-precious catalysts for PEM fuel cells: influence of the structural parameters of pristine commercial carbon blacks on their activity for oxygen reduction", Electrochimica Acta, **53**, 2925-2938, 2007

[2] Lee, K., Zhan, L., Zhan, J., "PEM fuel Cell Electrocatalysts and Catalyst Layers: Fundamentals and Applications", Springer-Verlag London Limited, London 2008

[3] "Carbon Black User's Guide. Safety, Health, & Environmental Information", ICBA

[4] Fulcheri, L., Schwob, Y., Flamant, G., "Comparison Between New Carbon Nanostructured Produced by Plasma with Industrial Carbon Black Grades", J.Phys. III France, **7**, 491-503, 1997

[5] Juan L., Fangfang H., Yiwen L., Yongxiang Y., Xiaoyan D. and Liao X., "A New Grade Carbon Black Produced by Thermal Plasma Process", Plasma Science and Technology, 5, 1815-1819, 2003

[6] Kim, K.S., Seo, J.H., Nam, J.S., Ju, W.T., Hong, S.H., "Production of Hydrogen and Carbon Black by Methane Decomposition Using DC-RF Hybrid Thermal Plasmas", IEEE Transactions on Plasma Science, **33**, 813-823, 2005

[7] Girshick, S.L., Chiu, C.P., McMurry, P.H., "Modelling Particles Formation and Growth in a Plasma Synthesis Reactor", Plasma Chemistry and Plasma Processing, **8**, 145-157, 1988

[8] Girshick, S.L., Chiu, C.P., "Homogeneous Nucleation of Particles from the Vapor Phase in Thermal Plasma Synthesis", Plasma Chemistry and Plasma Processing, **9**, 355-369, 1989

[9] Fabry, F., Flamant, G., Fulcheri, L., "Carbon black processing by thermal plasma. Analysis of the particle formation mechanism.", Chemical Engineering Science, **56**, 2123-2132, 2001

[10] Médard, C., Lefevre, M., Dodelet, J-P., Jaouen, F., Lindbergh, G., "Oxygen reduction by Fe-based catalysts in PEM fuel cells conditions: Activity and

selectivity of the catalysts obtained with two Fe precursors and various carbon supports", Electrochimica Acta, **51**, 3202-3213, 2006

[11] Jaouen, F., Lefevre, M., Dodelet, J-P., Cai, M., "Heat-Treated Fe/N/C Catalysts for O_2 Electroreduction: Are Active Sites Hosted in Micropores?", J. Phys. Chem. B, **110**, 5553-5558, 2006

[12] Castillo, I., "Study of CeO_2 synthesis from liquid precursors in a RF-inductively coupled plasma reactor", Ph.D. Thesis, Chem. Eng. Department, McGill University, June 2007

[13] Li, N., Wang, Z., Zhao, K., Shi, Z., Gu, Z., Xu, S., „Large scale synthesis of N-doped multi-layered graphere sheets by arc-discharge method", Carbon, **48**, 255-259, 2009

[14] Moreno-Couranjou, M., Monthioux, M., Gonzalez-Aguilar, J., Fulcheri, L., "A non-thermal plasma process for the gas phase synthesis of carbon nanoparticles", Carbon, **47**, 2310-2321, 2009

[15] Mendoza-Gonzalez, N.Y., El Morsli, M., Proulx, P., "Production of Nanoparticles in Thermal Plasmas: A Model Including Evaporation, Nucleation, Coalescence and Fractal Aggregation", Journal of Thermal Spray Technology, **17**, No. 4, 533-550, 2008

[16] Boulos, M.I., Fauchais, P., Pfender E., "Thermal plasmas: fundamentals and applications", Plenum Press, **1**, 1994

Chapter 7 – Peer reviewed paper published in Plasma Chemistry and Plasma Processing Journal

Full reference: Pristavita, R., Meunier, J.L., Berk, D., "Carbon nano-flakes produced by an inductively coupled thermal plasma system for catalyst applications", Plasma Chem. Plasma Process., **31**, 393-403, 2011

The previous chapter (Chapters 6) presents the results obtained using the ICP thermal plasma system and two types of reactor geometries. It was showed that a cylindrical shape reactor did not produce a uniform CB powder morphology due to the presence of recirculation areas inside the reactor volume. Both the modeling work and the experimental results proved that by changing the reactor shape from a cylindrical to a conical geometry, a uniform flow pattern is achieved inside the reactor leading to a product having a uniform morphology throughout the entire reactor volume. The obtained CB product has nano-flake morphology and a high degree of crystallinity.

The present chapter presents the experimental results relating the observed carbon nano-flake (CNF) morphology to the conditions of production within the reactor. A consistency of the CNF purity and morphology under strongly varying reactor operating conditions is demonstrated, this being thereafter termed the "robustness: of the process. This robustness of the CNF production is demonstrated for methane flow rates of 0.5 slpm, 1slpm and 5slpm and reactor pressures values of 55.2 kPa and 89.6 kPa.

Keeping in mind the scope of the project, which is to produce a CB material suitable for PEM fuel cells applications, the flakes were functionalized directly within the synthesis reactor using nitrogen. The results on the CB nano-flakes nitrogen functionalization are also presented in this chapter. The addition of nitrogen into a pyridinic type structure is essential for the formation of the active sites of the catalyst. The amount of nitrogen we incorporated into the desired

pyridinic type structure is around 0.7 ± 0.3 at.%. It is important to mention that no iron was added to the catalyst support.

Regarding the characterization of the carbon nano-flakes, the dimensions of the particles were obtained from SEM images and using Raman Spectroscopy and not by using XRD diffraction patterns and applying the Scherrer formula. The reasoning behind this is linked to the uncertainty related to the shape of the particles. The shape factor in the Scherrer formula being essentially linked to spherical or ellipsoidal particles, this approach would be highly questionable for 2-D graphene structures having only ~6-16 atomic planes in thickness and up to 100 nm in planar dimension (as observed through HR-SEM). The Raman-based value of L_a and the high resolution SEM observation of the nano-flakes provide more information and less controversy than a calculation extrapolated using a badly defined shape factor.

Carbon nano-flakes produced by an inductively coupled thermal plasma system for catalyst applications

Ramona Pristavita, Jean-Luc Meunier and Dimitrios Berk

Abstract

Carbon material was produced using an inductively coupled thermal plasma (ICP) torch system of 35 kW and a conical shape reactor. The carbon nanopowders were obtained by plasma decomposition of methane at various flow rates and show a uniform microstructure throughout the reactor. The product has a crystalline graphitic structure, with a stacking of between 6 and 16 planes and a nano-flake morphology with particles dimensions of approximately 100 nm long, 50 nm wide and 5 nm thick. Nitrogen was also introduced in some synthesis experiments along with the methane precursor using flow rates of 0.1slpm and 0.2 slpm. The resulting product has the same structural properties and the nitrogen is incorporated into the graphitic structure through pyridinic type bonds.

7.1 Introduction

Carbon presents different allotropic forms such as diamond, graphite, carbon nanotube structures, fullerene family based solids, and amorphous carbon. The carbon atoms in graphite are organized in the form of layers of symmetrical hexagons, each of these layers being horizontally displaced relative to the next one. Starting with this perfect crystalline arrangement, degenerated structures can be constructed based on lower degrees of symmetry down to a completely amorphous structure. From the physical point of view, carbon black (CB) is an intermediate structural form between graphite and an amorphous structure [1].

Industrially, CB is produced using two main types of manufacturing processes: the furnace process and the thermal process. The furnace process uses heavy aromatic oils as feedstock and a closed reactor to atomize this feedstock. The reaction rate is controlled by steam or water spraying. The thermal process uses

natural gas as feedstock and a pair of furnaces that alternate approximately every five minutes between preheating and carbon black production[1]. More recently, plasma technologies have been used as a route for the synthesis of new CB structures [2-7]. One of the advantages of such a technology is the possibility to use a variety of carbon sources in gaseous, liquid or solid state. The plasma process is also clean, it does not generate CO_2 and the resulting CB powders do not contain large amounts of impurities as those found in the flame processes.

In a thermal plasma system, the particle size and the number of nucleated particles are affected by two factors: the cooling rate at the location of the nucleation and the monomer concentration. High monomer concentration and low cooling rates favor the nucleation of fewer particles having a larger particle size [3, 4]. The properties of the product are also influenced by the local temperature: injection of the carbon source in the arc zone (T~ 10,000 K for argon plasma) results in production of a highly organized CB. The growth of the particles in a low temperature region of the reactor (T<1,600 ^{0}C) will lead to an amorphous product with spherical particles [5]. The nature of the feedstock does not influence the size distribution of CB aggregated but an important role is played by the zone where the carbon source is injected [2].

CB is widely used in industry, including in the energy and transportation sectors for example as a catalyst support in the Polymer Electrolyte Membrane (PEM) fuel cell. A typical carbon black material used in PEM fuel cell studies is Vulcan XC72R produced by Cabot, although other carbons such as Black Pearls, Ketjen Black or Printex XE-2 produced by Degussa have also been used [8-11]. The PEM fuel cells are clean and efficient alternative energy sources; however their production cost must be reduced substantially in order for them to be economically viable. Of particular importance in the cost reduction is the development of an alternative, low cost catalyst. The catalyst material used presently consists of CB powder on which fine platinum (Pt) particles are uniformly dispersed. CB was chosen because of its electrical conductivity, its high

[1] Carbon Black User's Guide. Safety, Health, & Environmental Information. International carbon black association (ICBA) www.carbon-black.org

surface area and its ability to function in the highly acidic medium of the PEM fuel cells. Pt particles typically catalyze the oxidation reaction taking place at the anode and the reduction reaction taking place at the cathode. While non-platinum catalysts still show lower activity and much lower durability than Pt, recent improvements in their beginning-of-life activity give increased hope for their eventual practicality [12]. The non-noble catalysts materials consist also of CB powder which contains nitrogen atoms bonded to the graphitic support and iron atoms bounded to the nitrogen atoms, creating in this way the active Fe centers for catalysis [13]. These active centers have a structure of metal-N_4 chelates. The metal atoms coordinated into the active site can be any transition metal, but iron and cobalt are known to present the highest electrocatalytic activities [14].

The results presented in this communication are part of an overall work whose objective is to produce and control the morphology of CB nanopowders having a high density of catalytic sites on their surface leading to a high catalytic activity. The active centers are formed inside the pores of the material or on the edge of the graphene planes. Thus the degree of crystallinity of the produced material and its porosity are two of the most important properties of such a catalyst material [13, 11]. In terms of the chemical structure, the increase in the number of catalytic sites requires not only a crystalline nanostructure of the powders but also an increase in the quantity of nitrogen incorporated in the nanostructure.

In this paper we present carbon nano-powders having a crystalline flake-like morphology which is obtained by plasma decomposition of methane at various flow rates in the presence and absence of nitrogen using an inductively coupled thermal plasma (ICP) torch system.

7.2 Experimental

Carbon nanopowders were obtained by plasma decomposition of a carbon-containing feedstock. The material was produced using an inductively coupled thermal plasma (ICP) torch system of 35 kW using methane as a carbon precursor at various flow rates.

The induction plasma torch is a TEKNA PL-35 model, which is essentially composed of a copper coil of several turns wrapping a confinement tube inside which the induction plasma is generated. The plasma jet generated provides high temperatures (5,000 K to 10,000 K) and high enthalpies (10^3~10^5 kJ/kg), depending on the species present in the system[2]. The injection probe is inserted into the torch in the axial position, the tip of the probe reaching the coil area of the torch body below the first coil turn, allowing the injection of the carbon source in the core of the plasma. Three gas streams are necessary for the operation of the ICP torch: central, sheath and carrier gas. The gas used for each of these streams was argon.

The ICP torch is attached to a conical water cooled reactor having 50 cm in length and a full angle of expansion of 14^0 (7^0 half angle) as presented in Figure 7.1. Such geometry provides a gradual gas expansion from the torch to the reactor minimizing both recirculation areas and sudden quenching of the gas [15, 16]. A 4 mm annular gap between the conical section of the reactor and the bottom collection plate is used for the gas outlet. An annular manifold around this outlet collects the exit gases which exit through a single outlet in the manifold. A higher pressure drop is maintained across the annular gap in comparison to the pressure drop in the manifold, ensuring in this way a radial outlet flow pattern of the gases from the collection plate. This geometry also provides a symmetric flow pattern within the reactor chamber above the collection plate and a stagnation point flow geometry on the plate itself [15].

The methane was injected using flow rates of 0.5 slpm, 1 slpm and 5 slpm (measured at 294.5 K, 101.4 kPa). In some experiments nitrogen was also introduced along with the carbon source using flow rates of 0.1 slpm and 0.2 slpm. The methane injection time varies between 5 and 32 minutes. In the experiments presented here, the reactor power is kept constant at about 20 kW plate power and two reactor pressures were used: 55.2 kPa and 89.6 kPa.

[2] Induction Plasma Torch PL-35 & PL-50, Operation & Service Manual. Sherbrook: Tekna Plasma Systems, Inc; 2004.

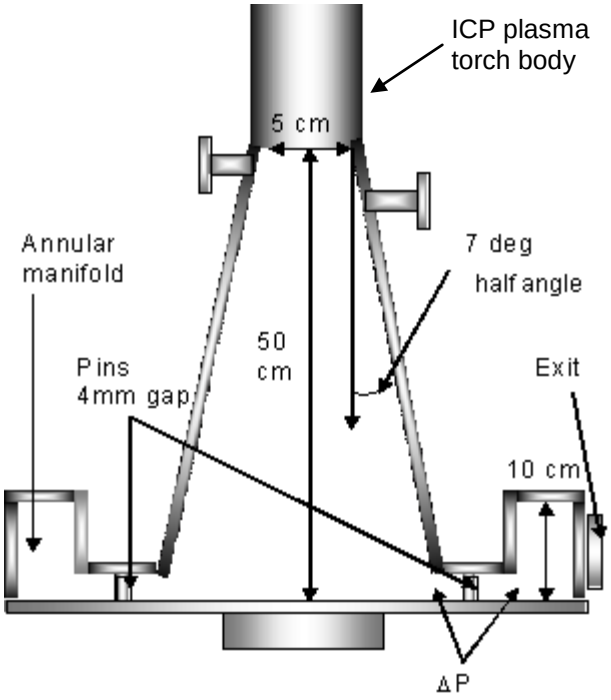

Figure 7.1 Diagram of conical water cooled reactor [12]

7.3 Results and discussions

7.3.1 Powders produced without nitrogen addition

The produced powders collected from different parts of the conical reactor show a uniform morphology [16], which was analyzed using scanning and transmission electron microscopy (SEM and TEM). The particles show a flake-like morphology (Figure 7.2a&b and Figure 7.3a&c) hereafter called "carbon nano-flakes", with typical dimensions of approximately 100 nm long, 50 nm wide and 5 nm thick. Close observation of the TEM micrograph (Figure 7.3b&d) show the graphitic planes in the cross section with a stacking of between 6 and 16 planes in the powders observed. Similar CB structures were previously produced by DC thermal plasma system [17] and a non-thermal plasma process [18].

The surface area of the powders as determined by the Brunauer Emmett Teller (BET) technique varied between 119 and 345 m^2/g. The lower values were obtained for the samples in which the presence of organic volatile compounds was observed. It is believed that such organic compounds act as a glue causing the

agglomeration of the carbon nano-flakes, and results in a decrease in the value of the specific surface area [16].

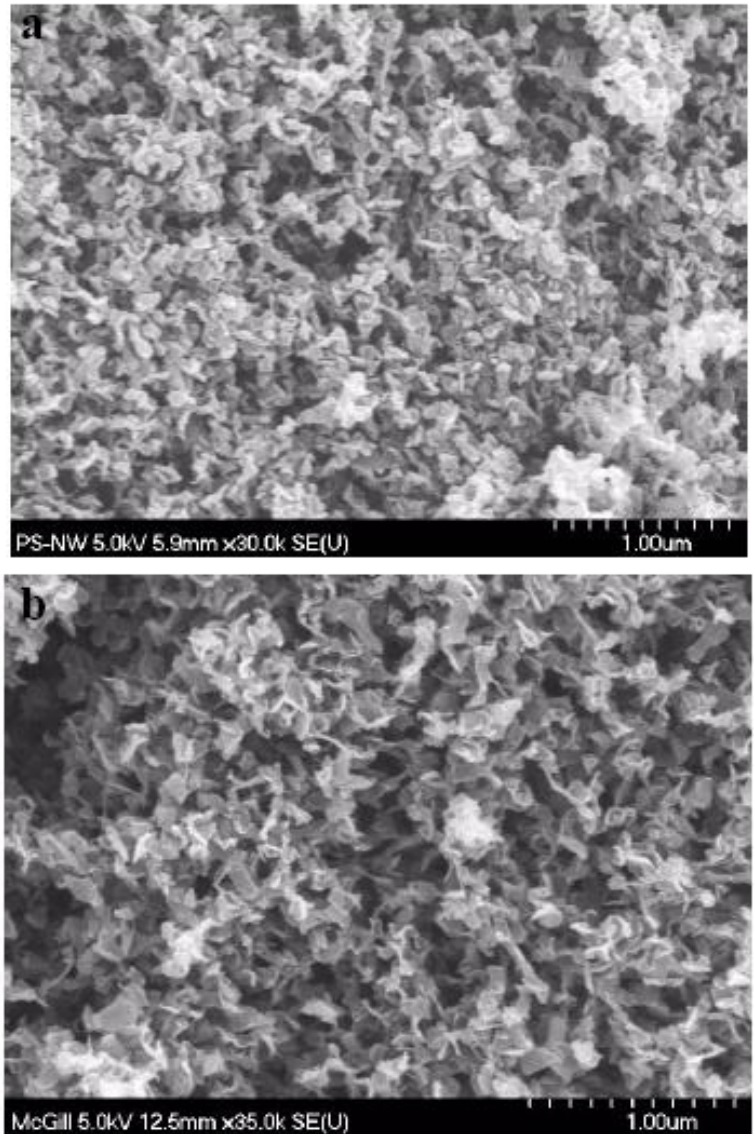

Figure 7.2 SEM image of carbon nano-flakes obtained at:
a) 55.2 kPa and b) 89.6 kPa

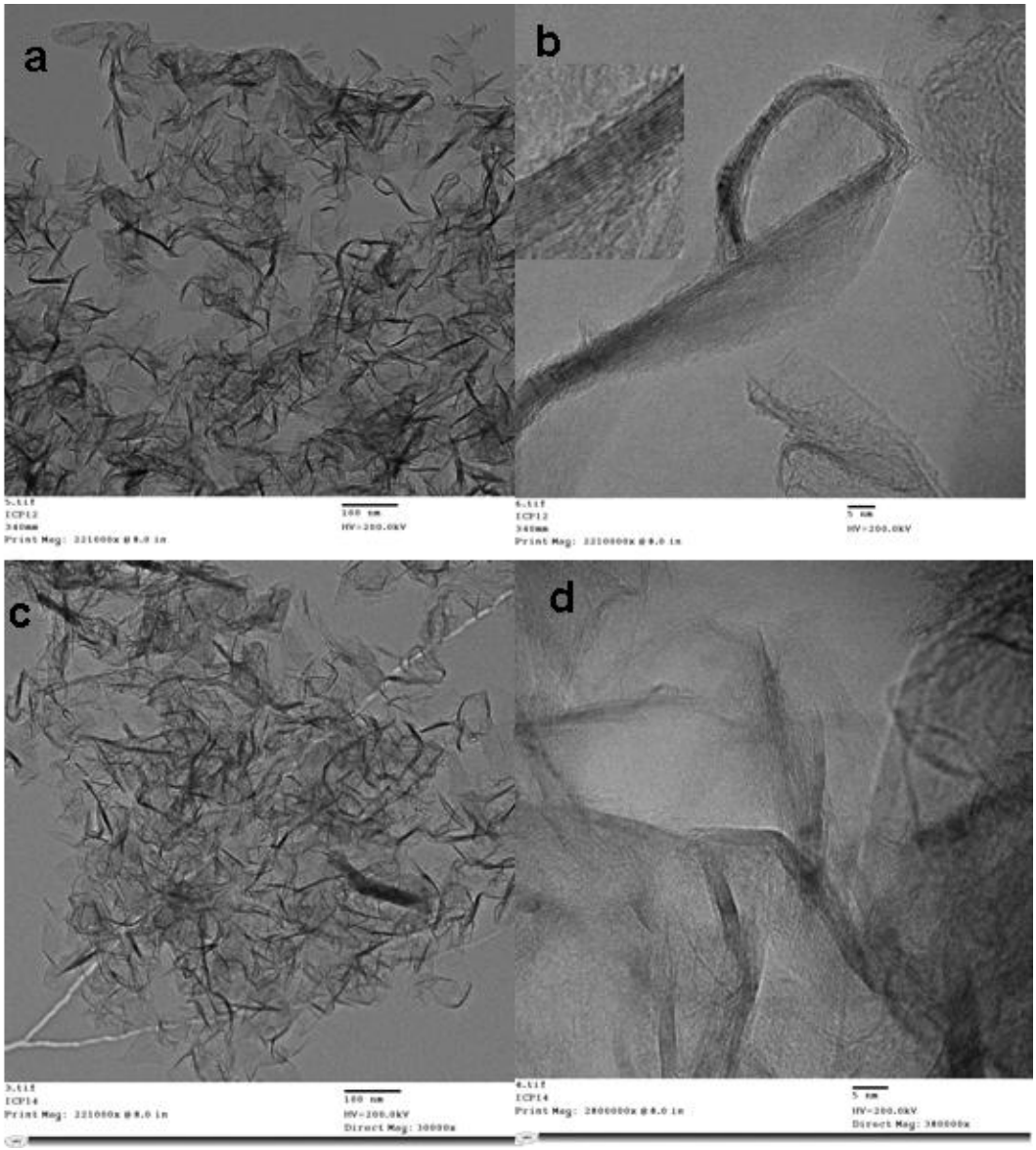

Figure 7.3 TEM images of carbon nano-flakes obtained at: a)& b) 55.2 kPa, c)& d) 89.6 kPa

Raman spectroscopy was used to assess the degree of crystallinity of the produced materials. The Raman spectra presented in Figure 7.4 were obtained using an incident laser wavelength of 514 nm and a grating of 1800 lines/mm. All the spectra show distinct G band at 1577cm^{-1} and a D band at 1345cm^{-1}, both being characteristic of graphitic materials, plus also the G$^{'}$ band at 2697cm^{-1}. Analysis of the Raman spectra of natural graphite reveals a sharp and intense G

band while the G' band is broader and less intense. The G' band changes in intensity and shape for carbon powders having a crystalline morphology composed of a small number of graphene layers (1 to 5 layers), becoming a single sharp and intense peak, more intense than the G band [19]. The powders produced in the present experiment show that the G' band is only slightly more intense than the G band. This seems to correlate with our powders being composed of graphene layers with a stacking of more than 5 layers.

The nano-flakes are composed of crystalline planes having an in-plane length (L_a) equal to 9.2 nm evaluated using the Raman-based method developed by Larouche and Stansfield [20]. This value is much higher than for other nanostructured carbon materials [20].

An assessment of the purity of the product can also be made from Raman spectra by using the relative ratios of the Raman peaks. The most suitable Raman ratio to use is the $I_{G'}/I_D$ ratio since the G' band results from a two-phonon process and its intensity decreases as the sample becomes less ordered because the impurities present in the sample does not allow the coupling effect necessary for the two-phonon process. By analyzing the Raman spectra obtained for the nano-flake powders, the calculated $I_{G'}/I_D$ ration is around 2.5, which corresponds to a fully crystalline sample [21].

The X-Ray Diffraction (XRD) pattern shown in Figure 7.5 is representative of powders obtained at 55.2 kPa and 89.6 kPa. All the diffraction patterns show a crystalline structure. Comparing this with the diffraction pattern of natural graphite, one identifies the peaks around 2θ angles of 25^0, 42^0, 72^0 and 88^0 to be characteristic of a graphitic structure. The peaks around 2θ angles of 25^0 and 88^0 are reflections of the 002 and 006 diffraction lines, which are an indication of the graphite layers structure of the nano-flakes. The peaks around 2θ angles of 42^0 and 72^0 are reflections of the 100 and 104 diffraction lines and are assigned to the hexagonal symmetry of the graphene plane [22].

The X-Ray Photoelectron Spectroscopy (XPS) results shown in Figure 7.6 reveal the presence of two characteristic peaks: one C1s (carbon) peak at 284.9 eV and an O1s (oxygen) peak at 532.6 eV. These results show a high purity of the

samples. The oxygen presence is due to exposure of samples to the ambient air. In these samples no nitrogen peak is observed as these experiments were performed without any addition of nitrogen to the plasma gas.

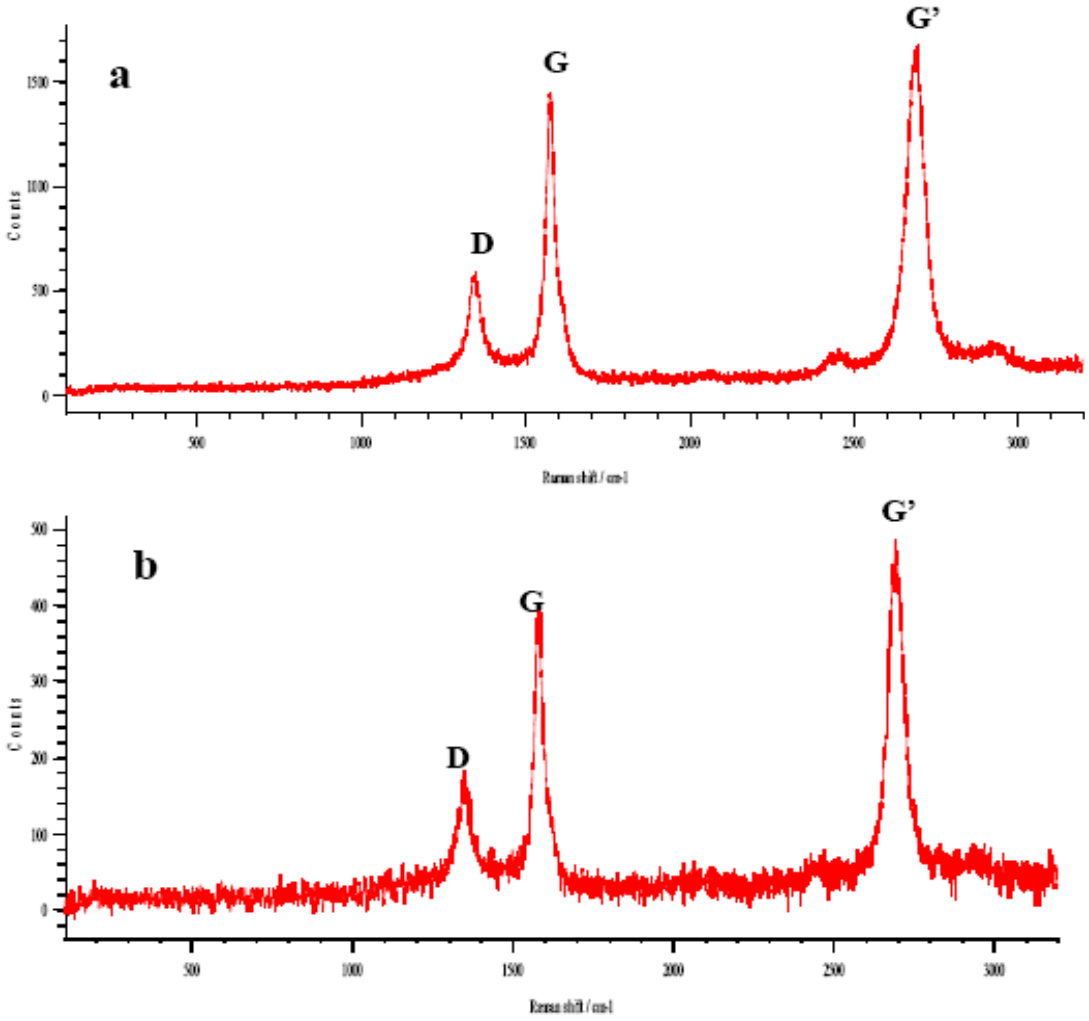

Figure 7.4 Raman spectra of carbon nano-flakes produced at: a) 55.2 kPa and b) 89.6 kPa showing distinctive D and G primary bands and G' secondary band

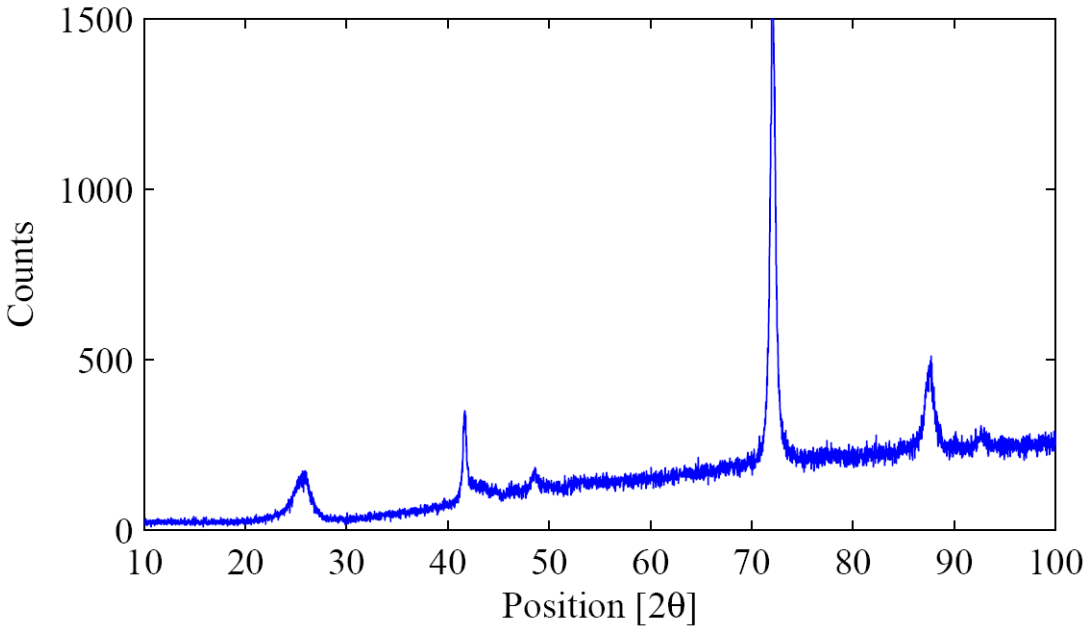

Figure 7.5 Typical XRD diffraction pattern of carbon nano-flakes showing a crystalline structure

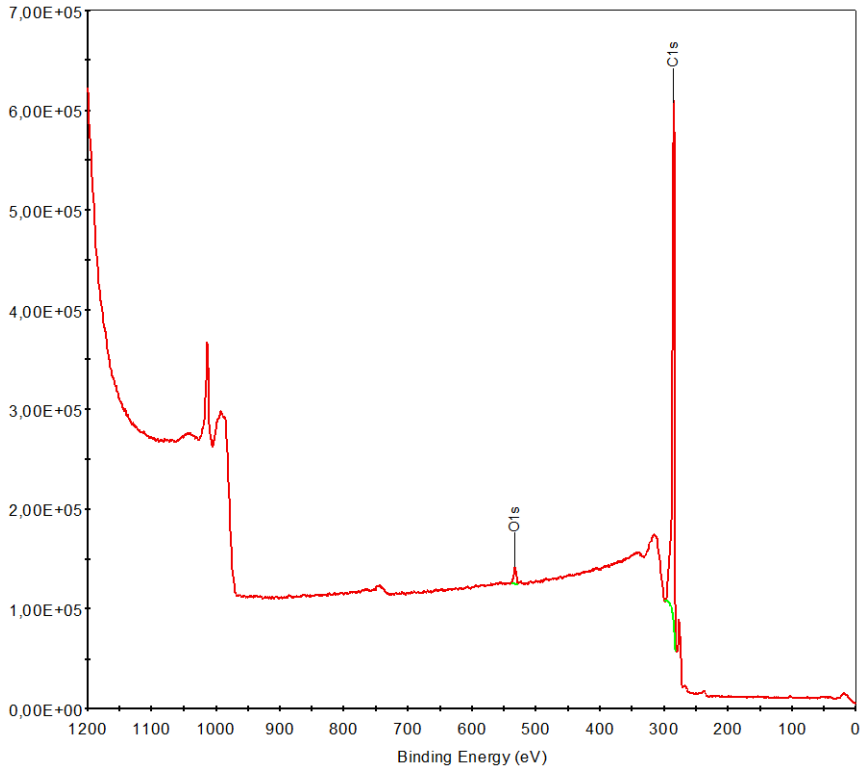

Figure 7.6 XPS spectrum of carbon-nano flakes produced without nitrogen addition

7.3.2 Powders produced with nitrogen addition

The TEM images shown in Figure 7.7a,c reveal the same flake-like morphology of particles as in the case of the material produced without nitrogen addition. Close examination of TEM images (Figure 7.7b,d) show a stacking with the same number of graphene planes (6 – 16) as in the case of powders produced without nitrogen addition. It can be concluded that the addition of nitrogen along with methane during the production process does not affect the morphology of the material.

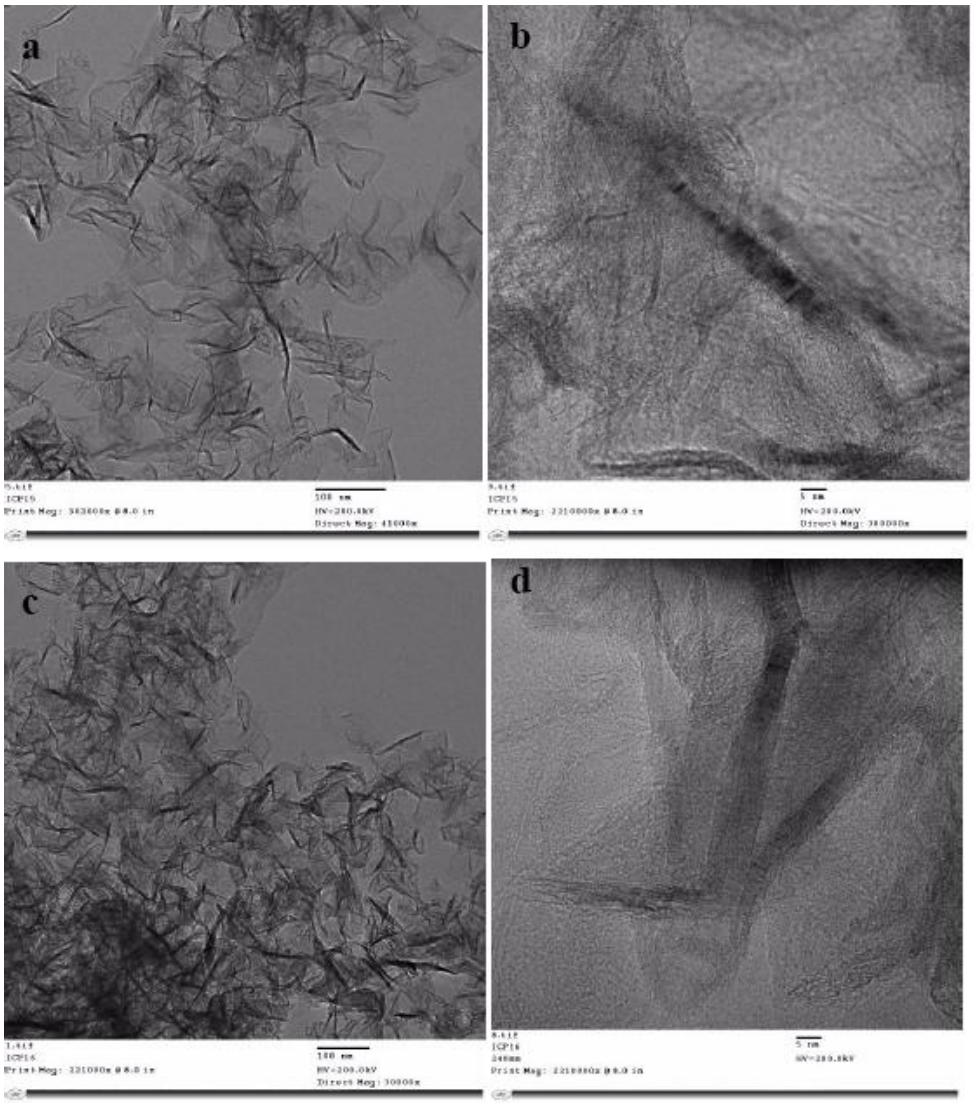

Figure 7.7 TEM images of carbon nano-flakes obtained at: a)& b) 55.2 kPa, c)& d) 89.6 kPa and with nitrogen addition

Raman spectroscopy was used again to asses the crystallinity of the samples produced with the addition of nitrogen. No change was observed in the shape of the Raman spectra of these samples if compared with the powders produced with no nitrogen addition (see Figure 7.4). We observe again the presence of the distinct G band at 1577cm^{-1}, D band at 1345cm^{-1} and G$^{'}$ band at 2697cm^{-1}, all characteristic of graphitic materials. This is again an indication that the nano-flake morphology of the powders was not affected by the addition of nitrogen.

The XPS spectrum presented in Figure 7.8 reveals the presence of the same two characteristic peaks observed in Figure 7.6: one C1s (carbon) peak at 284.6 eV and an O1s (oxygen) peak at 532.2 eV, but also observed is the presence of a small N1s (nitrogen) peak at 398.8 eV. These results show again a high purity of samples. High resolution analysis of the N1s peak presented in Figure 7.9 and the deconvolution of this peak shows that there are two types of N-bonding present: pyridinic type (peaks at 398.8 eV and 399.9 eV) and aliphatic type (peak at 410.1 eV)[3]. The amount of nitrogen incorporated into the desired pyridinic type structure is around 0.7 ± 0.3 at.%, however the total amount measured in the samples was up to 2 ± 1 at.%. The difference is nitrogen incorporated via the aliphatic type of N-bonding, most probably in a volatile organic compound. Further analysis on the solid carbon samples using thermal extraction techniques and GC-MS were made in various operating conditions of the reactor, these being presented in a separate publication. The main results for the samples produced using conditions of Figure 7.7 indicate again a high purity of the samples.

[3] National Institute of Standards and Technology (NIST), X-Ray Photoelectron Spectroscopy Database Version 3.5, www.nist.gov

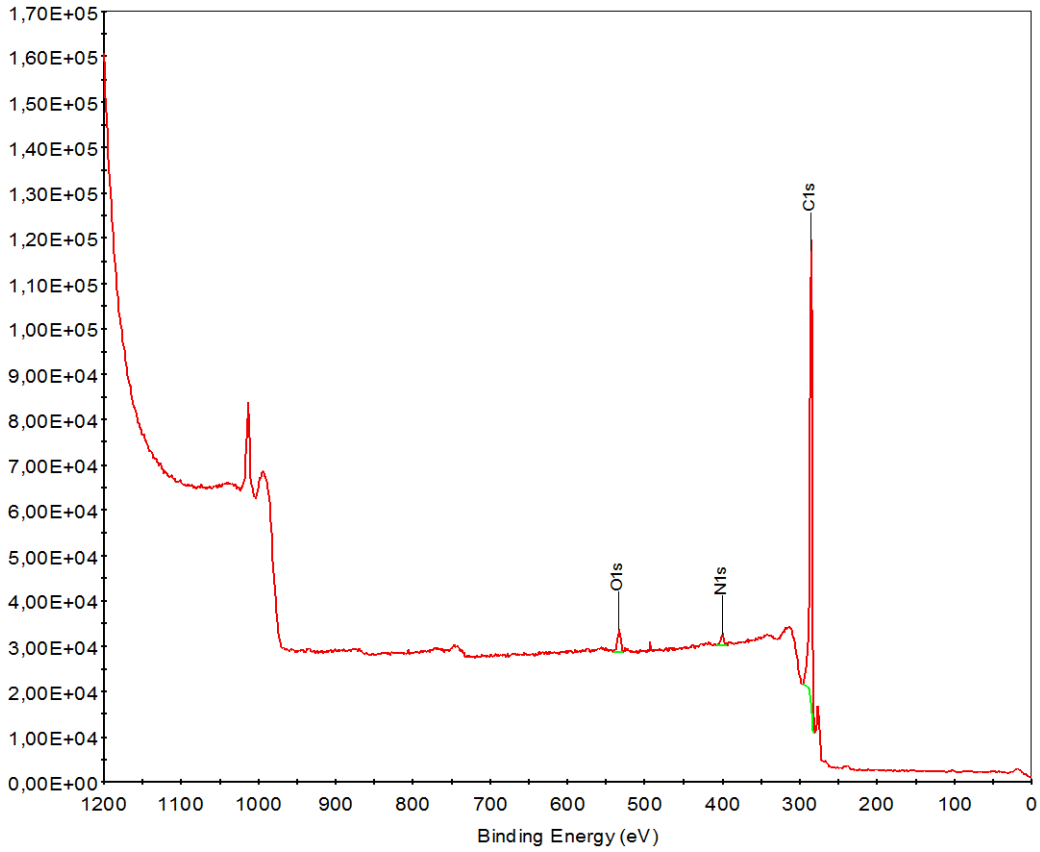

Figure 7.8 XPS spectrum of carbon-nano flakes produced with nitrogen addition

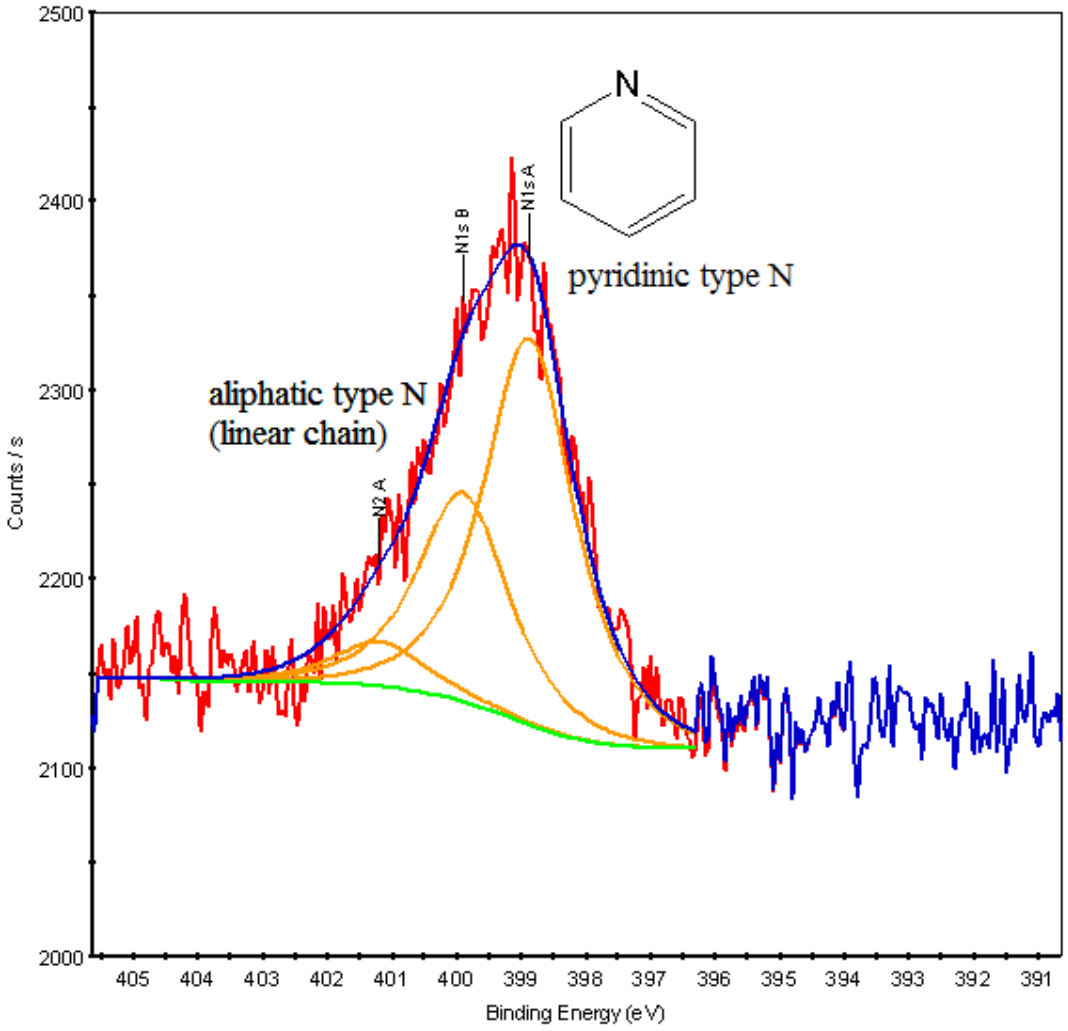

Figure 7.9 XPS high resolution nitrogen peak (red line represents recorded data; blue line is the summation of deconvoluted peaks) showing two types of N-bonding: pyridinic type (N1sA peaks at 398.87 eV and N1sB peak at 399. 90 eV) and aliphatic type (N2sA peak at 401.18 eV)

7.4 Conclusions

The present paper presents carbon nano-flakes produced using methane as a carbon precursor with or without the addition of nitrogen during the production process in an ICP thermal system. The uniform flow pattern achieved in the conical reactor enables a good control of the thermal history of the gas and solid particles in the conical reactor and promotes the formation of a clean product with a uniform morphology. It is showed that the addition of nitrogen did not affect the

morphology of the powders. Up to 1.98 at.% of nitrogen is incorporated in the crystalline carbon powders, from which about 0.69 at.% is in the form of a pyridinic type of N-bonding. Such type of bonding is desired for the creation of active sites in a catalyst material for PEM fuel cells.

Acknowledgments

The financial contributions of the Natural Sciences and Engineering Council of Canada, FQNRT and General Motors Canada are gratefully acknowledged.

References

[1] Donnet, J-P., Voet, A., "Carbon Black. Physics, Chemistry, and Elastomer Reinforcement", Marcel Dekker Inc., USA, 1976

[2] Fabry, F., Flamant, G., Fulcheri, L., "Carbon black processing by thermal plasma. Analysis of the particle formation mechanism.", Chemical Engineering Science, **56**, 2123-2132, 2001

[3] Girshick, S.L., Chiu, C.P., McMurry, P.H., "Modelling Particles Formation and Growth in a Plasma Synthesis Reactor", Plasma Chemistry and Plasma Processing, **8**, 145-157, 1988

[4] Girshick, S.L., Chiu, C.P., "Homogeneous Nucleation of Particles from the Vapor Phase in Thermal Plasma Synthesis", Plasma Chemistry and Plasma Processing, **9**, 355-369, 1989

[5] Fulcheri, L., Schwob, Y., Flamant, G., "Comparison Between New Carbon Nanostructured Produced by Plasma with Industrial Carbon Black Grades", J.Phys. III France, **7**, 491-503, 1997

[6] Juan L., Fangfang H., Yiwen L., Yongxiang Y., Xiaoyan D. and Liao X., "A New Grade Carbon Black Produced by Thermal Plasma Process", Plasma Science and Technology, **5**, 1815-1819, 2003

[7] Kim, K.S., Seo, J.H., Nam, J.S., Ju, W.T., Hong, S.H., "Production of Hydrogen and Carbon Black by Methane Decomposition Using DC-RF Hybrid Thermal Plasmas", IEEE Transactions on Plasma Science, **33**, 813-823, 2005

[8] Antolini, E., Salgado, J.R.C., Giz, M.J., Gonzales, E.R., "Effects of geometric and electronic factors on ORR activity of carbon supported Pt-Co electrocatalysts in PEM fuel cells", International Journal of hydrogen Energy, **30**, 1213-1220, 2005

[9] Litster, S., McLean, G., "PEM fuel cell electrodes", Journal of Power Sources, **130**, 61-76, 2004

[10] Barbir, F., "PEM Fuel Cells. Theory and Practice", Elsevier Inc., USA, 2005

[11] Médard, C., Lefevre, M., Dodelet, J-P., Jaouen, F., Lindbergh, G., "Oxygen reduction by Fe-based catalysts in PEM fuel cells conditions: Activity and selectivity of the catalysts obtained with two Fe precursors and various carbon supports", Electrochimica Acta, **51**, 3202-3213, 2006

[12] Lefevre, M., Dodelet, J.P., "O_2 Reduction in PEM Fuel Cells: Activity and Active Site Structural Information for Catalysts Obtained by the pyrolisis at high temperature of Fe precursosrs", J. Phys. Chem. B, **104**, 11238-11247, 2000

[13] Jaouen, F., Lefevre, M., Dodelet, J.P., Cai, M., " Heat – Treated Fe/N/C Catalysts for O_2 Electroreduction: Are Active Sites Hosted in Micropores?", J. Phys. Chem., **110**, 5553-5558, 2006

[14] Lee, K., Zhan, L., Zhan, J., "PEM fuel Cell Electrocatalysts and Catalyst Layers: Fundamentals and Applications", Springer-Verlag London Limited, London 2008

[15] Castillo, I.A., Munz, R.J., "New in-situ sampling and New in-situ sampling and analysis of the production of CeO_2 powders from liquid precursors using a novel wet collection system in a rf inductively coupled thermal plasma reactor. Part 1: Reactor system and sampling probe", Plasma Chem. Plasma Process., **27**, 737-759, 2007

[16] Pristavita, R., Mendoza-Gonzales, N.Y., Meunier, J.L., Berk, D., "Carbon Blacks Produced by Thermal Plasma: The Influence of the Reactor Geometry on the Product Morphology", Plasma Chem. Plasma Process., **30**, 267-279, 2010

[17] Li, N., Wang, Z., Zhao, K., Shi, Z., Gu, Z., Xu, S., „Large scale synthesis of N-doped multi-layered graphere sheets by arc-discharge method", Carbon, **48**, 255-259, 2009

[18] Moreno-Couranjou, M., Monthioux, M., Gonzalez-Aguilar, J., Fulcheri, L., "A non-thermal plasma process for the gas phase synthesis of carbon nanoparticles", Carbon, **47**, 2310-2321, 2009

[19] Ferrari, A.C., Meyer, J.C., Scardaci, V., Casiraghi, C., Lazzeri, M., Mauri, F., Jiand, D., Novoselov, K.S., Roth, S., Geim, A.K., "Raman Spectrum of Graphene and Graphene Layers", Phisical Review Letters, **97**, 187401, 2006

[20] Larouche, N., Stansfield, B.L., "Classifying nanostructured carbons using graphitic indices derived from Raman spectra", Carbon, **48,** 620, 2010

[21] DiLeo, R., Landi, B.L., Raffaelle, R.P., "Purity assessment of multiwalled carbon nanotubes by Raman spectroscopy", Journal of Applied Physics**, 101,** 064307, 2007

[22] Inagaki, M., "New Carbons. Control of Structure and Functions", Elsevier Science Ltd., UK, 2000

Chapter 8 – Peer reviewed paper submitted to Plasma Chemistry and Plasma Processing Journal

Previous chapter (Chapter 7) presents the experimental results relating the production of carbon nano-flake morphology to the conditions of production within the conical shape reactor. The robustness of the carbon nano-flakes production process is demonstrated under varying conditions: methane flow rates of a0.5 slpm, 1slpm and 5slpm and reactor pressures values of 55.2 kPa and 89.6 kPa.

The present chapter includes the results of a modeling work showing that the reactor geometry used in this study enables a uniform flow and temperature evolution within the reactor volume. Three pressure cases of 20.7 kPa, 55.2 kPa and 101.3 kPa and two plasma powers cases of 10 kW and 20 kW were studied. It is demonstrated that a better and more robust process control is achieved with this reactor shape under varying operating conditions allowing the system operation in a wide range of reactor pressures without affecting the particles morphology. The nucleation temperature and quench rate values evaluated in the model provide conditions to explain the graphitic structure of the nano-flakes.

Carbon Nanoparticles Production by Inductively Coupled Thermal Plasmas: Controlling the Thermal History of Particle Nucleation

Ramona Pristavita, Norma-Yadira Mendoza-Gonzalez, Jean-Luc Meunier and Dimitrios Berk

Abstract

The process control for reproducibility, uniformity, and achievement of desired structures for carbon black generated in thermal plasma devices is studied in this paper through modeling, and correlated with experimental results. A numerical simulation of the flow and energy fields, stream function lines and the quench rates of the plasma gas in a conical shape reactor at different pressures was made. An argon plasma is used with highly diluted methane (0.6-7%) as the carbon precursor. The quench rates were studied in order to observe the flow development and hence the thermal history of particle nucleation. Three pressure cases of 20.7 kPa, 55.2 kPa and 101.3 kPa and two plasma powers cases of 10 kW and 20 kW were studied. The modeling results enabled carbon nanoflakes production in the experimental tests performed on an ICP thermal plasma system. Results indicate a robust process control enabling very little particle morphology variation over this wide range of reactor pressure values and varying plasma power, and a very high reproducibility of the particle morphologies obtained.

Keywords: carbon black, conical reactor, CFD modeling, quench rates, stream function, nucleation, carbon nanoflakes, carbon nanoparticles.

8.1 Introduction

Carbon black (CB) is elemental carbon in the form of colloidal particles that are produced by the incomplete combustion or thermal decomposition of solid, liquid or gaseous hydrocarbons under controlled conditions. Two main types of manufacturing processes are known based on the feedstock and type of heat treatment: the heavy oil based process, also called “furnace” process, and the

natural gas based process, also called “thermal” process. The current world CB production is estimated at more than 8 million tons per year. More than 95% of the total CB production comes from the “furnace” process [1]. The disadvantages of these processes are the incomplete combustion of the carbon precursor and limited reaction temperatures, these being a function of the carbon source/air ratio. Also, both processes emit large amounts of polluting gases, such as CO, CO_2, SO_2 and NO_x.

In recent years, new CB powders were synthesized using plasma technology. Some of the advantages of such a technology are the possibility to use a variety of carbon sources in gaseous, liquid or solid state, and the ability to work at different pressures without affecting too much the energy input. The plasma process is also clean, it does not generate CO_2 and the resulting CB powders do not contain large amounts of impurities as those found in the flame processes. Plasma based processes enable an electrical control of the temperature and a relatively independent supply of carbon. This decoupling of the carbon material production from the energy requirements leads to a better control of the temperature and velocity profiles, and of the residence times in the synthesis reactor. The possibility of a finer control of the energy and fluid fields now provides ways to tailor and control the nanostructure of the carbon black particles towards specific needs and applications not accessible using the conventional heavy oil or natural gas processes.

Girshick *et al* [2, 3] conducted a general modeling investigation on the physical requirements for homogeneous nucleation of particles from the vapor phase of some arbitrary material in a thermal plasma reactor. They reported the three main routes for the conversion from the gas phase to a condensed phase: homogeneous nucleation, condensation on an existing particle and heterogeneous nucleation at a particle surface. The homogeneous nucleation is favored by high temperature chemistry and rapid cooling.

Fabry *et al* [4] developed a 100 kW 3-phase AC plasma torch with an open circuit voltage of 760 V, a maximum current of 266 A and a frequency of 50 Hz. Using Transmission Electron Microscopy (TEM) to analyze the product, they also

observed the presence of three families of carbon black. The first one was composed of particles with a high degree of organization and poorly aggregated molecules. The second family was composed of nearly spherical amorphous particles, which indicated a formation mechanism at low temperatures. The last family looked like aggregated acetylene black, suggesting a formation at high temperature.

Juan *et al* [5] showed a new route to produce carbon black in which natural gas was cracked in the absence of oxygen using electric energy supply given by a plasma jet. The obtained carbon black particles had a narrow size distribution, a small average diameter (38 nm) and a highly branched aggregate structure.

A DC-RF hybrid thermal plasma reactor was developed by Kim *et al* [6]. The carbon source was methane. The produced carbon black presented a large surface area and also a high degree of crystallization.

In 2009, a non-thermal plasma reactor was used by Moreno-Couranjou *et al* [1] for the continuous gas phase synthesis of carbon nanoparticles at atmospheric pressure. A large range of carbon morphologies were synthesized, including concentric texture nanocarbons similar to furnace-type CB, acetylene-type CB, carbon shells filled with metal, "crumpled paper sheet" isotropic texture nanoparticles and carbon rods.

More recently, graphene flake structures were produced by Levchenko *et al* in a high-current arc discharge setup [7]. A Y-Ni catalyst powder was used in their work to promote the growth of the 2-D flake structure. The estimated size of these flakes was approximately 500 – 2500 nm, typically with up to 10 graphene layers. The product purity varies within the reactor volume. CNTs and soot material were also produced, indicating that the control of the nucleation process is still lacking.

The energy sector constitutes one domain of application where very specific structural requirements of the CB nanoparticles are needed. Our previous work concentrated on creating clean, homogeneous, strongly graphitized CB particles on which a specific nitrogen and iron chemical functionalization is attached. The target objective for these structures being to replace platinum by non-noble and

atomically dispersed catalytic sites in polymer electrolyte membrane (PEM) fuel cells [8, 12]. The results rapidly showed that the plasma reactor design was a key point in controlling the energy/flow fields and the resulting particle structure [8]. A reactor geometry enabling a control of these fields also provided the means to transform the spherical CB nanostructure into a flake-like structure consisting of a stacking of around 6-16 graphene layers, thereafter called carbon nanoflakes (CNF). A closer analysis of these structures indicated the very high crystallinity of the material generated, the elimination of the impurity by-products such as volatile organic compounds (VOCs), and the inclusion of the nitrogen functionalization into pyridinic sites as needed for the non-noble catalyst application [12]. These results are essentially linked to the control of the particle nucleation process now achievable in the thermal plasma reactor. Experimental *in situ* measurements in thermal plasma reactors used for particle synthesis are unfortunately very difficult or impossible to implement. Modeling is used in the present paper to provide some understanding of this energy/fluid/nucleation fields control generating a clean CNF product as observed experimentally. It is also providing some understanding on the reasons behind the "robustness" of this plasma reactor design in achieving a consistent product even under strongly varying process parameters.

8.2 Plasma Model

The model presented in this study is applied to a 35 kW inductively coupled thermal plasma (ICP) torch system. The plasma gas used is Argon. The Argon flow rates for the axial probe injection, central and sheath gas are Q_1 = 5 slpm, Q_2 =15 slpm, and Q_3 = 60 slpm, respectively. The plasma gas used is Argon. The Argon flow rates for the axial probe injection, central and sheath gas, respectively are Q_1 = 5 slpm, Q_2 =15 slpm, and Q_3 = 60 slpm. The CB powders were produced using methane as the carbon precursor and various flow rates from 0.5 slpm to 6 slpm. The methane is injected axially in the core of the plasma and the reactor power is kept constant at about 10 kW plasma power while the reactor pressure varies between 20.7 kPa and 101.3 kPa. The ICP torch is attached to conical

reactor having 50 cm in length and an angle of expansion of 14^o as can be seen in Figure 8.1. Such geometry provides a gradual gas expansion from the torch and into the reactor minimizing both recirculation areas and sudden quenching of the gas. A 4 mm annular gap between the conical section of the reactor and the bottom collection plate is used for the gas outlet. An annular manifold around this outlet collects the exit gases which exit through a single outlet in the manifold. A higher pressure drop is maintained across the annular gap in comparison to the pressure drop in the manifold, ensuring in this way a highly symmetric radial outlet flow pattern of the gases from the collection plate. This geometry also provides a symmetric flow pattern within the reactor chamber above the collection plate and a stagnation point flow geometry on the plate itself [9, 12].

The following assumptions were made in solving the plasma flow model: a two dimensional (2D) model with fully axisymmetric configuration is used with axial coordinate z and radial coordinate r, and the reactor dimensions specified in Figure 8.1; steady state flow neglecting gravity effects; turbulence effects are included using the Renormalization Group (RNG) k-epsilon model; an argon plasma is used at local thermodynamic equilibrium (LTE); the plasma is optically thin and a net emission coefficient is used. The RNG k-epsilon model is a renormalization of the Navier-Stokes equation to account for the effects of smaller scales of motion. The solution of the electromagnetic fields for the plasma generation was based on previous modeling studies [10]. The actual operating conditions were accounted in the model by specifying the following boundary conditions for the inlet flow rates for the axial probe injection, central and sheath gas, respectively: Q_1 = 5 slpm, Q_2 =15 slpm, and Q_3 = 60 slpm. The water cooled reactor walls were set to 300 K as in the experimental setup. Axial gradients at the reactor outlet were assumed to be zero for all variables while the centerline condition was set to zero radial gradients and zero radial velocity. Transport and thermodynamic properties of the plasma gas (e.g., density, viscosity, thermal conductivity, specific heat at constant pressure, and radiation losses) as a function of temperature were obtained from Boulos et al. [11]. The underlying computational grid consisted of a total of 63 000 - 1 mm quadrilateral cells,

thereby assuring that a high computational grid density and numerical accuracy were attained.

The preceding assumptions lead to the simplification of the conservation equations for momentum and energy equations. The resulting elliptical partial differential (EPD) equations are solved using the sequential solver of the CFD finite-volumes commercial code FLUENT 6.3.

Continuity: $$\frac{\partial(\rho u)}{\partial z}+\frac{1}{r}\frac{\partial(\rho r v)}{\partial r}=0 \tag{8.1}$$

Momentum: $$\rho u\frac{\partial u}{\partial z}+\rho v\frac{\partial u}{\partial r}=-\frac{\partial p}{\partial z}+2\frac{\partial}{\partial z}\left(\mu\frac{\partial u}{\partial z}\right)+\frac{1}{r}\frac{\partial}{\partial r}\left[\mu r\left(\frac{\partial u}{\partial r}+\frac{\partial v}{\partial z}\right)\right]+F_z+F_{zb} \tag{8.2}$$

$$\rho u\frac{\partial v}{\partial z}+\rho v\frac{\partial v}{\partial r}=-\frac{\partial p}{\partial r}+\frac{\partial}{\partial z}\left[\mu\left(\frac{\partial v}{\partial z}+\frac{\partial u}{\partial r}\right)\right]+\frac{2}{r}\frac{\partial}{\partial r}\left[\mu r\frac{\partial v}{\partial r}\right]+F_r+F_{rb} \tag{8.3}$$

Energy: $$\rho u\frac{\partial h}{\partial z}+\rho v\frac{\partial h}{\partial r}=\frac{\partial}{\partial z}\left(\frac{\lambda}{Cp}\frac{\partial h}{\partial z}\right)+\frac{1}{r}\frac{\partial}{\partial r}\left[r\frac{\lambda}{Cp}\frac{\partial u}{\partial r}\right]+P-R-P_{loss} \tag{8.4}$$

In the above equations *u* and *v* are the axial and radial velocity components, ρ,μ, λ, and *Cp* are the density, viscosity, thermal conductivity, and specific heat at constant pressure, respectively. Variable *h* is the enthalpy, *p* is the pressure and *P* and *R* are the Ohmic heating power and the volumetric radiation heat losses, respectively. F_{rb} and F_{zb} are artificial source terms used to freeze the flow outside the plasma torch, a method not very elegant but efficient to fix flow conditions where it is not of interest, while solving some of the equations (electromagnetic) in the same region. The parameter $\mu_{eff}=\mu_l/\mu_t$ is the effective viscosity, which is the combination of molecular μ_l and turbulent μ_t viscosities.

The Lorentz forces and Ohmic heating power are expressed as:

$$Fr = \frac{1}{2}\mu_0 \sigma Re(E_\theta H_z^*) \tag{8.5}$$

$$Fz = -\frac{1}{2}\mu_0 \sigma Re(E_\theta H_r^*) \tag{8.6}$$

$$P = \frac{1}{2}\mu_0 \sigma Re(E_\theta E_\theta^*) \tag{8.7}$$

where μ_0 is the magnetic permeability of free space, σ is the electric conductivity, and Re denotes the real part of a complex number. The superscript * denotes the conjugate.

The electromagnetic fields can be obtained by the following relations after solving the vector potential equations:

$$E_\theta = -i\omega A_\theta \tag{8.8}$$

$$\mu_0 H_z = \frac{1}{r}\frac{\partial(rA_\theta)}{\partial r} \tag{8.9}$$

$$\mu_0 H_r = -\frac{\partial(A_\theta)}{\partial r} \tag{8.10}$$

where ω is the angle frequency and A_θ is the tangential component of the vector potential, which can be calculated as:

$$\nabla^2 A_\theta - (A_\theta / r^2) = -\mu_0 (J_{coil} + J_{ind}) \tag{8.11}$$

In the above equation J_{coil} is the current density induced by the oscillating voltage applied to the two ends of the coil and J_{ind} is the current density developed in the plasma and the coil by the induced electric field.

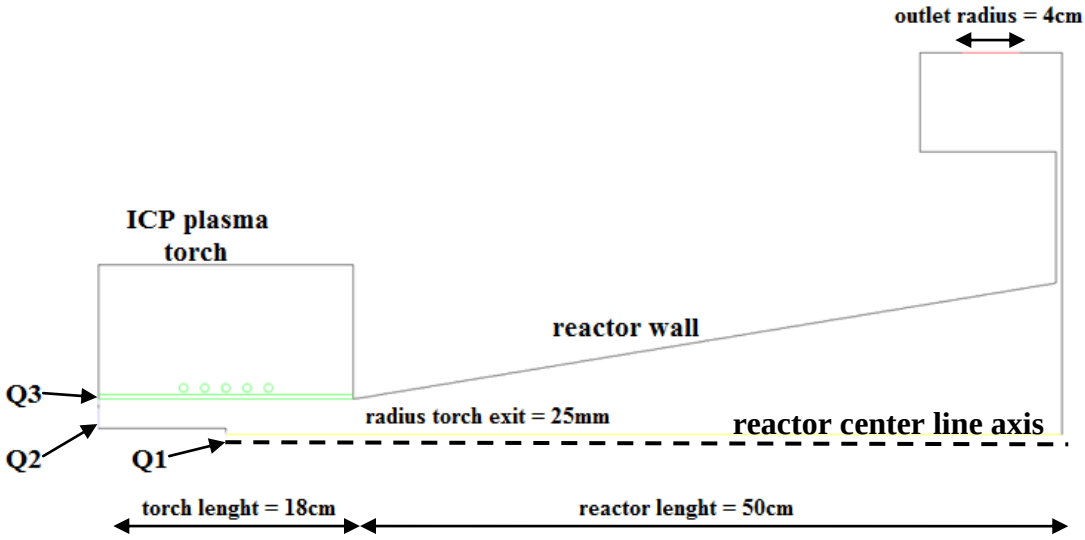

Figure 8.1 Axisymmetrical geometry of the conical reactor (not to scale)

8.3 Modeling results

The results of the computational fluid dynamics (CFD) modeling are presented in two parts. The first part presents a comparison of different operational cases, demonstrating that the carbon nano-flakes production process using the ICP thermal plasma system and the conical shape reactor is a robust process in terms of maintaining a relatively constant and uniform product structure under varying process parameters. Two values of plasma power of 10 kW and 20 kW were considered, and three reactor pressures: 20.7 kPa, 55.2 kPa and 101.3 kPa. The second part is devoted to the understanding of carbon nanoflakes formation by analyzing the fluid flow thermal history.

8.3.1 Comparison of temperature and velocity results for the three pressure cases

Figure 8.2 shows the temperature and velocity fields for the three reactor pressure cases and plasma power of 10 kW. A maximal temperature above 10000 K is achieved in the plasma zone. Temperatures around 8500 K are observed at the end of the torch outlet and decrease upon entering the reactor zone because of the geometry expansion and cooled walls. The temperature field differences

among the three reactor pressure cases at a plasma power of 10 kW is small; these can be better observed in the axial profile of Figure 8.3a. Figure 8.3a shows these axial temperature profiles are quite similar for the three pressures, with a small influence of the reactor pressure on temperature values observed in the lower half of the reactor zone. We can also observe a small temperature decrease with increasing reactor pressure. For the case of 20 kW plasma power we observe a similar trend in the temperature profiles. It can be seen from Figure 3a that pressure changes in such a synthesis reactor does not lead to important changes in the thermal fields and thermal history of the flow and expected nucleation processes. Comparing the two plasma power cases, we observe that an increase of the plasma power from 10 to 20 kW generates slightly increasing temperatures at the beginning of the reactor zone (z=0.18 m), these high axial temperature values are then pushed further downstream into the reactor. Of particular importance for carbon is the temperature range between 5000 and 3000 K which corresponds to particle nucleation as discussed in the next section. It is interesting to note from Figure 8.3a that the axial gradients of temperature in this range are practically the same for the three pressures, and still relatively similar for the two power cases. This behavior tends to indicate that for a given set of torch power/pressure operating parameters in the ranges used for Figure 8.3a, fluctuations in these parameters should not induce important modifications on the thermal fields for carbon particle nucleation.

The velocity fields for the case of plasma power of 10 kW presented in Figure 8.2 show flow velocities increasing in the plasma torch section and then decreasing drastically in the reactor. The axial velocity profiles can be seen in Figure 8.3b. The difference observed between the three pressure cases is more important than for the temperature fields. The highest velocities observed are of the order of 95 m/s, 40 m/s and 25 m/s for reactor pressures of 20.7 kPa, 55.2 kPa and 101.3 kPa respectively, for the case of plasma power of 10 kW. A reduction of the velocities with increasing pressure translates into a longer residence time of the particles in the hot areas of the reactor where nucleation is expected to occur

(typically in the 3000 - 5000 K zone as discussed in the next section). It was however demonstrated experimentally that this difference did not have a significant effect on the carbon powders morphology [8, 12]. When plasma power is increased to 20 kW a similar trend in the velocity profiles is observed, with higher velocities values, around 115 m/s, 50 m/s and 30 m/s for reactor pressures of 20.7 kPa, 55.2 kPa and 101.3 kPa respectively.

8.3.2 Understanding the carbon nano-flakes formation

Besides the energy (temperature) and flow fields, an understanding of the nanoparticle nucleation process requires the additional knowledge of the stream lines, quench rates and particle residence times. These parameters collectively characterize the thermal history of the flow and hence the nanoparticles formation.

Figure 8.4 presents the stream function lines in kg/s indicating the flow patterns in the reactor at 55.2 kPa and 10 kW. One main characteristic of the present conical geometry is a very uniform flow pattern in the reactor itself, and very importantly the complete absence of recirculation zones. Three streamlines were selected as being characteristic of the flow conditions: 1.0×10^{-4} kg/s close to the centerline, 2.0×10^{-4} kg/s, and 3.0×10^{-4} kg/s close to the wall.

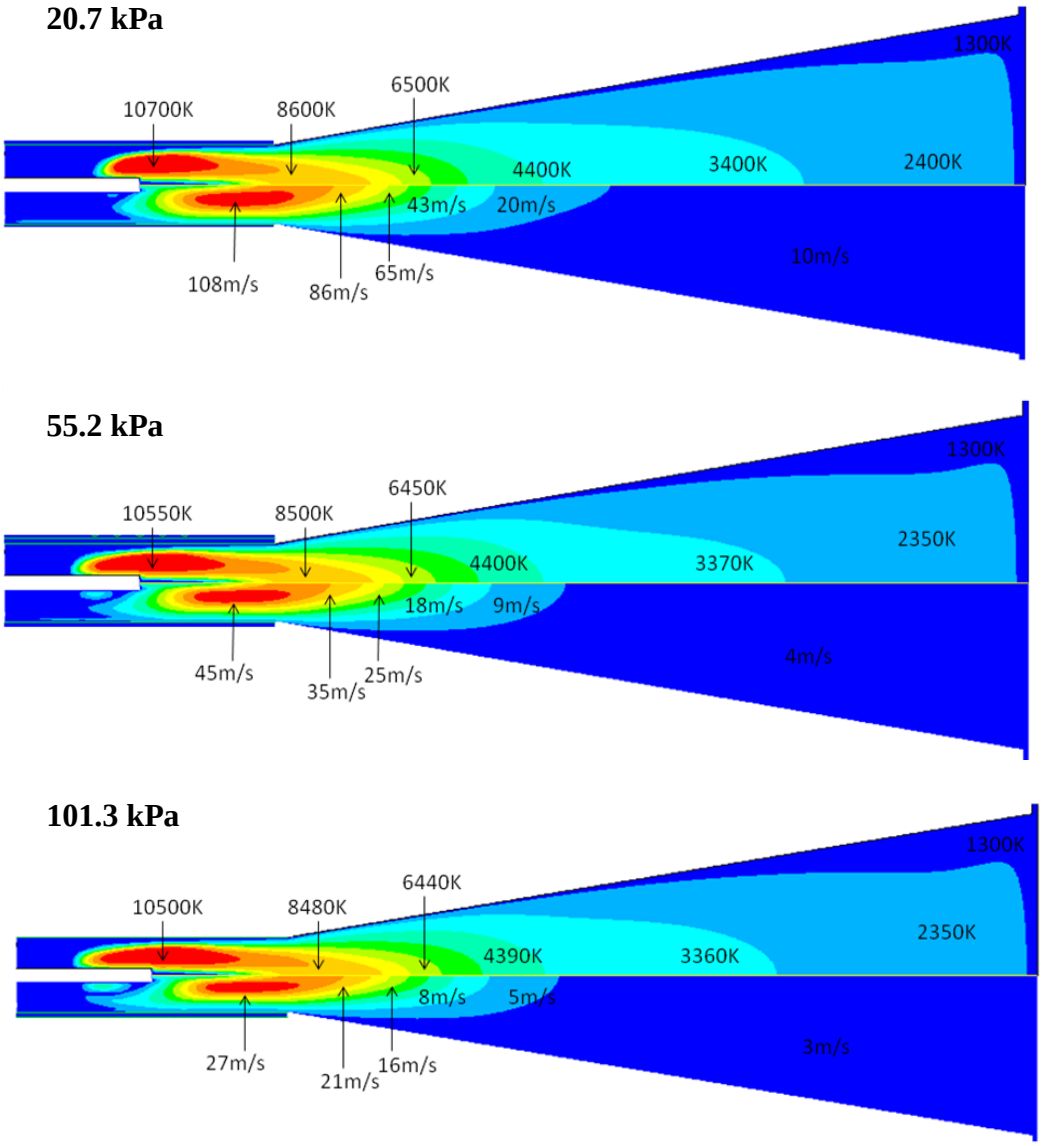

Figure 8.2 Temperature (upper half) and velocity (lower half) profiles for the three reactor pressure cases: 20.7 kPa, 55.2 kPa and 101.3 kPa and plasma power of 10 kW

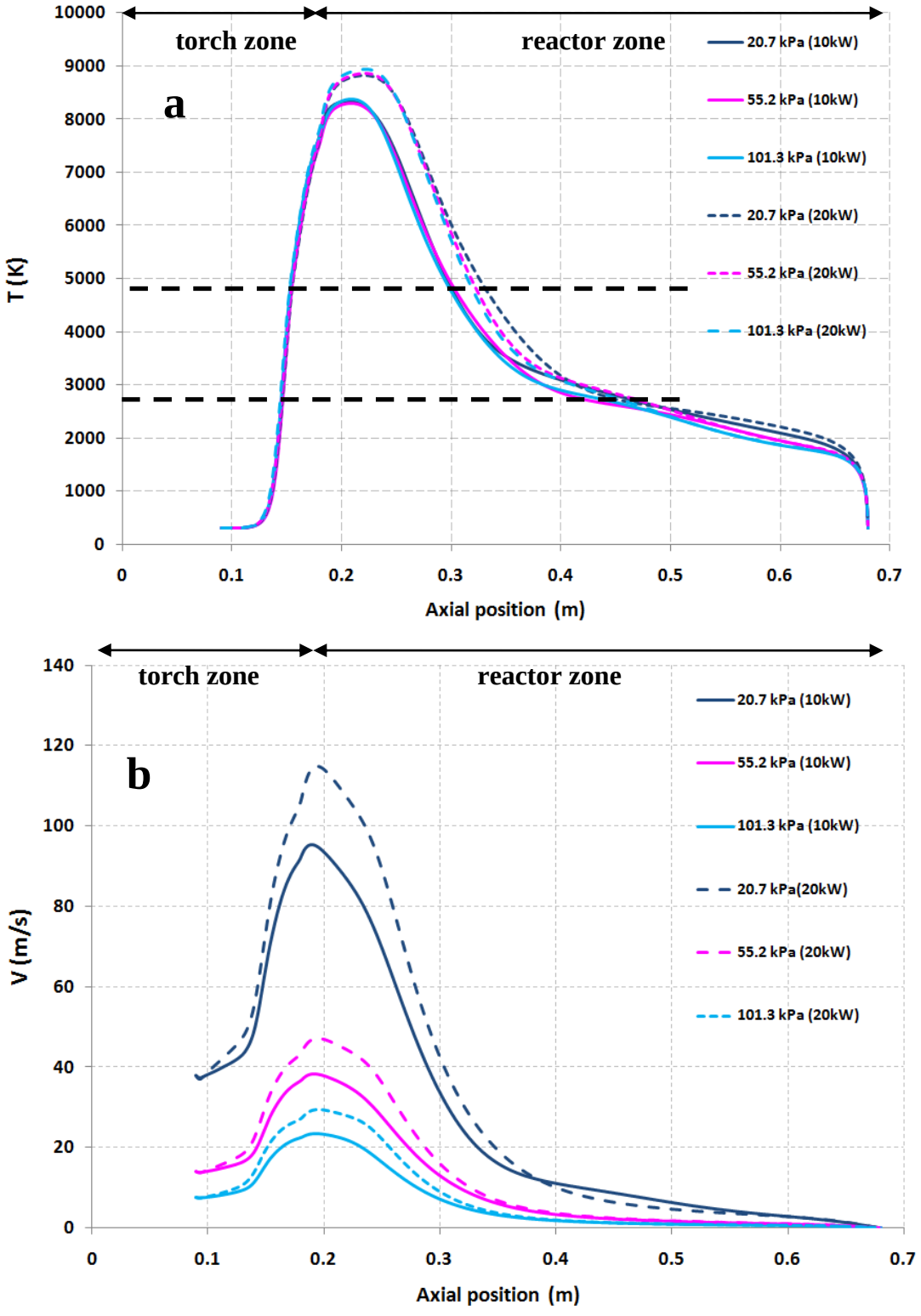

Figure 8.3 a) Temperature and b) velocity profiles along the reactor axis for three reactor pressure cases (20.7 kPa, 55.2 kPa and 101.3 kPa) and two plasma powers (10 kW and 20 kW)

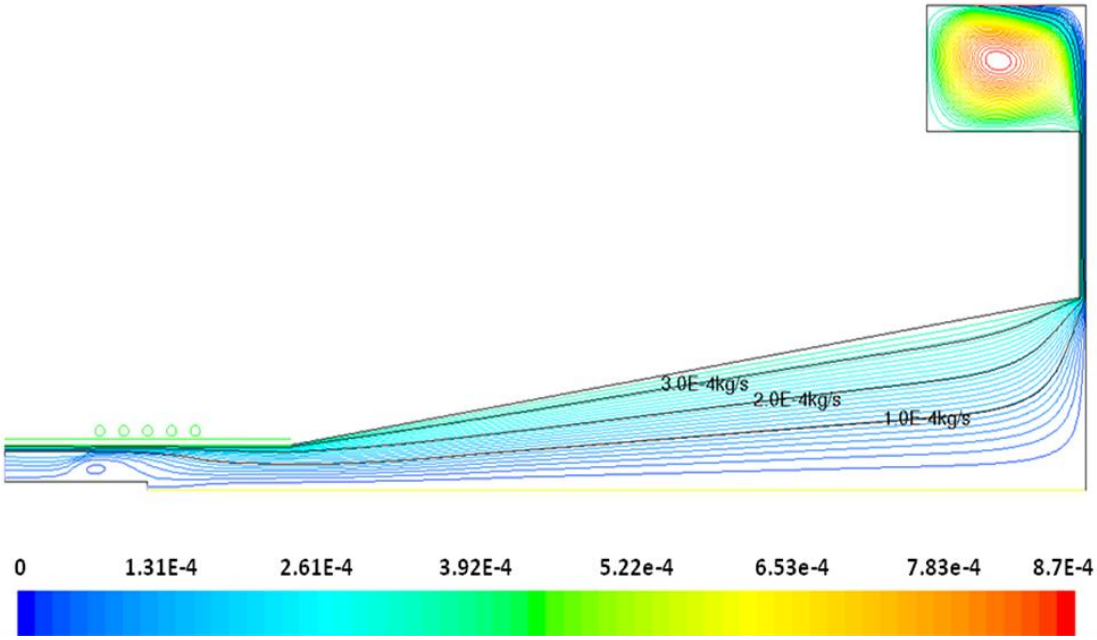

Figure 8.4 Streamlines in kg/ for the case of a reactor pressure value of 55.2 kPa and plasma power of 10 kW. Three specific streamlines corresponding to $1.0x10^{-4}$ kg/s, $2.0x10^{-4}$ kg/s and $3.0x10^{-4}$ kg/s kg/s are highlighted.

Equilibrium thermodynamic calculations presented in Figure 8.5 allow some evaluation of the nucleation temperature range expected for solid carbon species to form in the system, this range being roughly between 3000 and 5000 K as indicated earlier. These thermodynamic calculations were made using a molar ratio Ar/CH_4 of 80/1 (80 slpm Ar and 1 slpm CH_4). It is to be noted that no methane flow was considered in the numerical model calculations presented in sections 8.2 and 8.3.1, only an Ar flow was used. The methane flow rate used in the experiments is however a very small fraction of the argon flow used, and no major differences are expected in the temperature and flow fields.

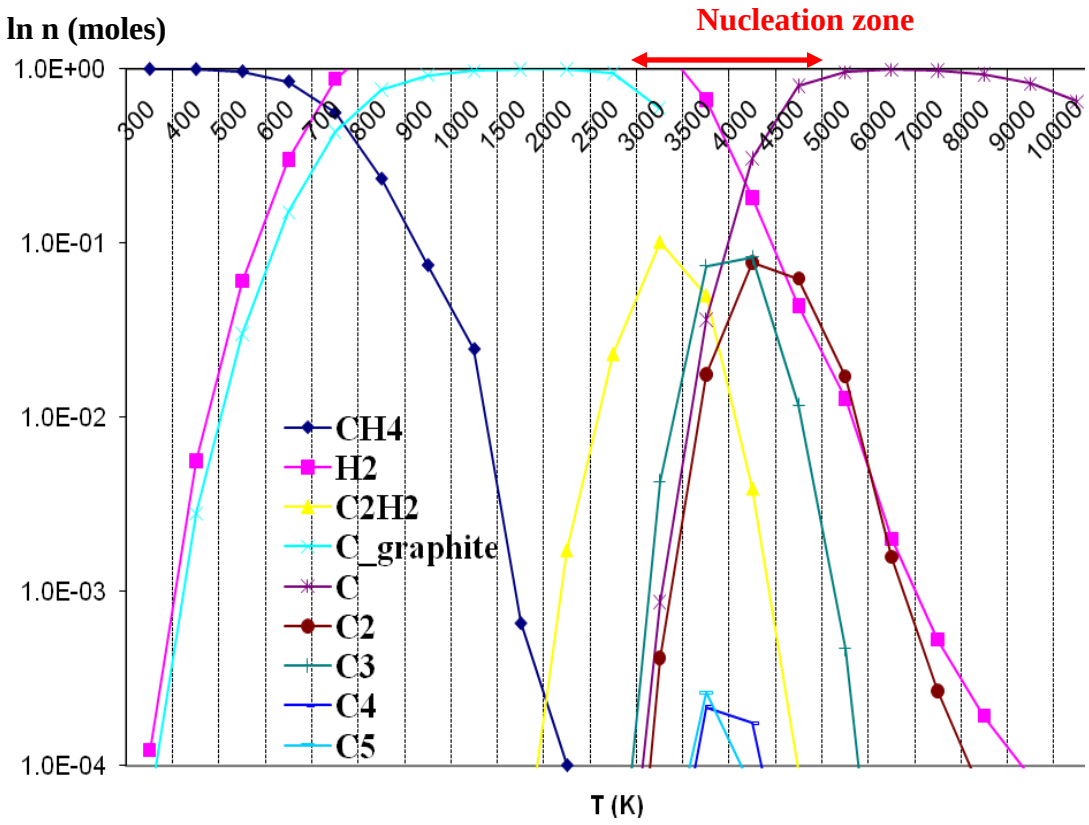

Figure 8.5 Equilibrium thermodynamic calculations for the Ar + CH_4 system (80/1 molar ratio). The range of temperatures leading to solid carbon is broadly indicated as the "nucleation zone".

Figure 8.6 shows the specific nucleation temperature fields for the three reactor pressures at a plasma power of 10 kW. One can see that the position, shape and extent of the nucleation zone do not vary much for the three cases. The carbon structures generated in the experimental test reactor under the various conditions presented in Figure 8.6 all showed identical and spatially uniform morphologies in the shape of graphene flakes, thereafter called carbon nanoflakes (CNF), as shown on Figure 8.7 [12]. Uniformity of this morphology was observed throughout the various collection zones such as the conical wall and the end plate of the reactor. These results indicate that the small difference in the width of the modeled nucleation zone does not have a great impact on the carbon nanoflakes morphology.

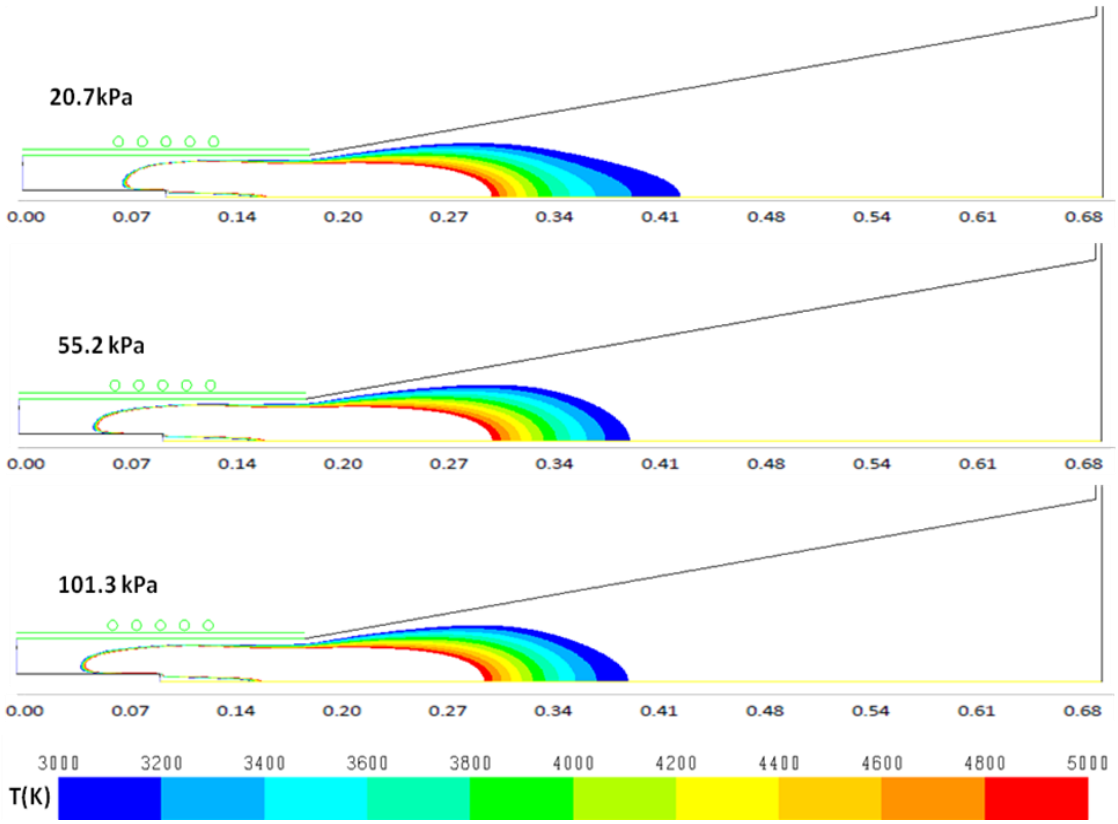

Figure 8.6 Temperature fields between 3000 and 5000 K, corresponding roughly to the carbon particle nucleation range for the three following cases of reactor pressures: a) 20.7 kPa, b) 55.2 kPa, and c) 101.3 kPa and 10 kw plasma power.

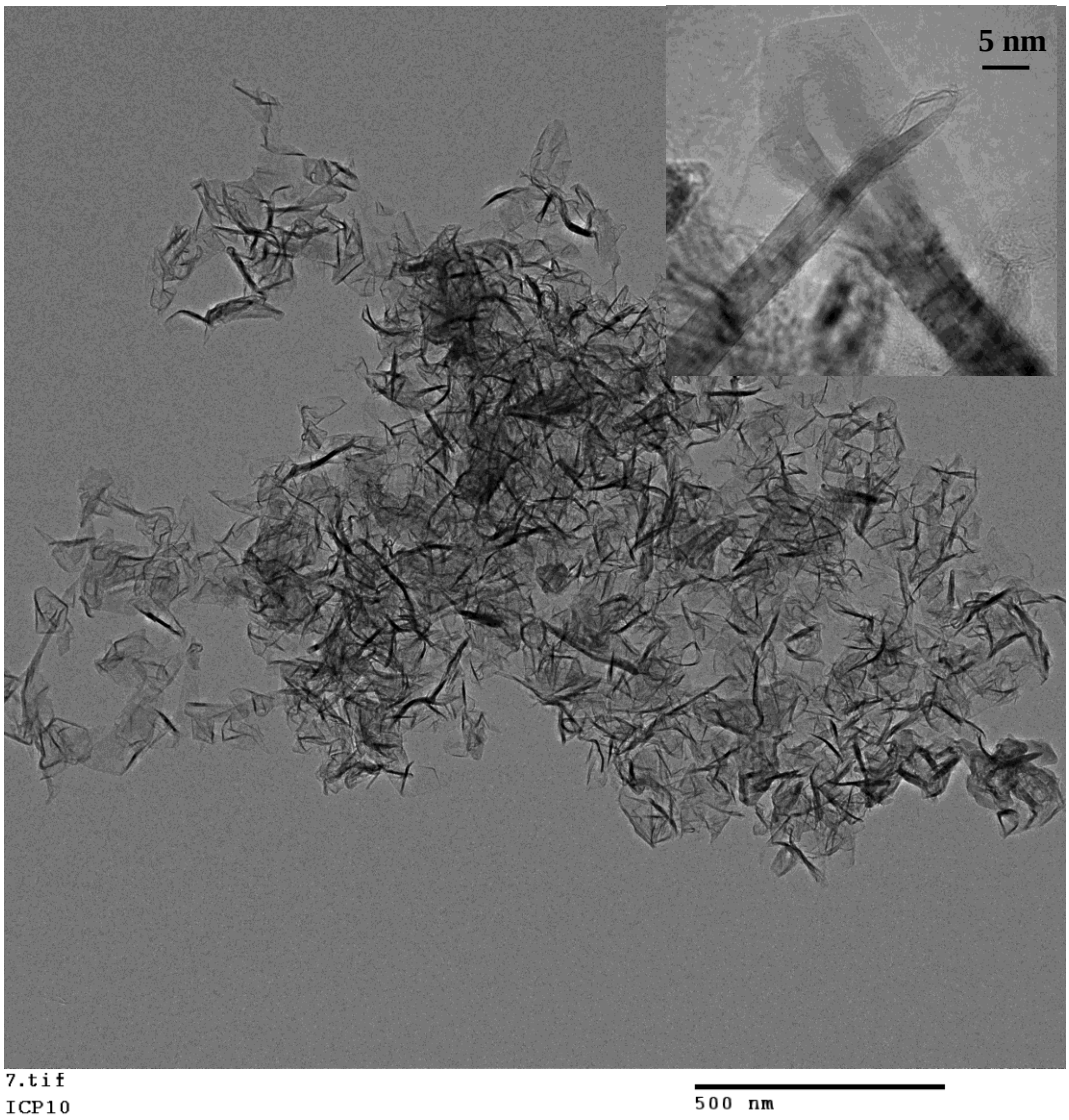

Figure 8.7 TEM images of carbon nano-flakes obtained at reactor pressure of 101.3 kPa and plasma power of 10 kW

The following section focuses on the case of a reactor pressure value of 55.2 kPa as being representative for the generation of a uniform morphology of the carbon nanoflakes. Figure 8.8 presents the temperature profiles following the central axis as well as the three specific stream lines indicated in Figure 8.4. One can see higher temperatures along the centerline and decreasing towards the reactor wall. The temperature gradients observed in the first half of the reactor will enhance the particle nucleation when temperature falls below 5000 K. The

particle nucleation will mainly occur along the axis and streamlines of $1.0x10^{-4}$ kg/s and $2.0x10^{-4}$ kg/s as seen from the 5000-3000 K zone, and is unlikely to occur close to the reactor walls where temperatures are too low.

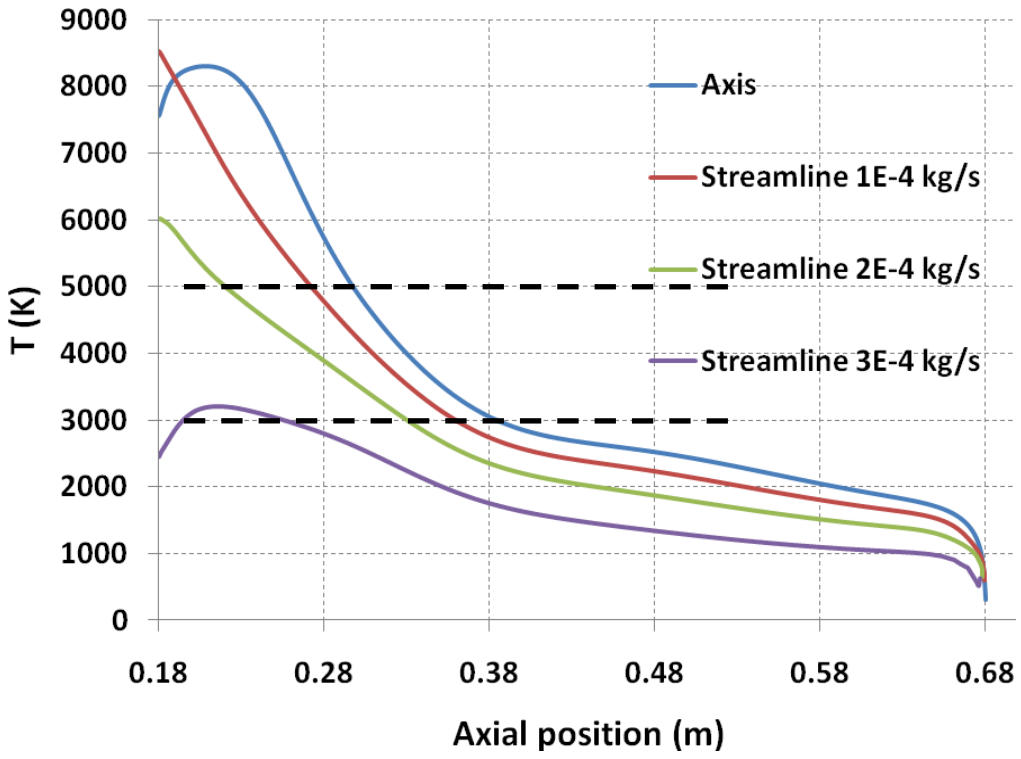

Figure 8.8 Temperature evolution along the axis and three stream flow lines of $1.0x10^{-4}$kg/s, $2.0x10^{-4}$kg/s and $3.0x10^{-4}$kg/s for a reactor pressure of 55.2 kPa.

Figure 8.9 presents the residence time of the fluid in a given calculation cell element of the computational grid, each cell having relatively uniform axial lengths of 1 mm. The figure also provides the two isotherms corresponding to the nucleation zone for the case of a reactor pressure of 55.2 kPa. The residence time/cell values are typically below 50 ms. The total residence time of a fluid element in the nucleation zone can now be obtained by integrating the residence time/cell along a stream line between the boundaries of the nucleation zone. Figure 8.10a shows this integral of the flow residence time/cell along the reactor

axis and specified streamlines for a reactor pressure of 55.2 kPa in the carbon nucleation temperature range (3000 K - 5000 K).

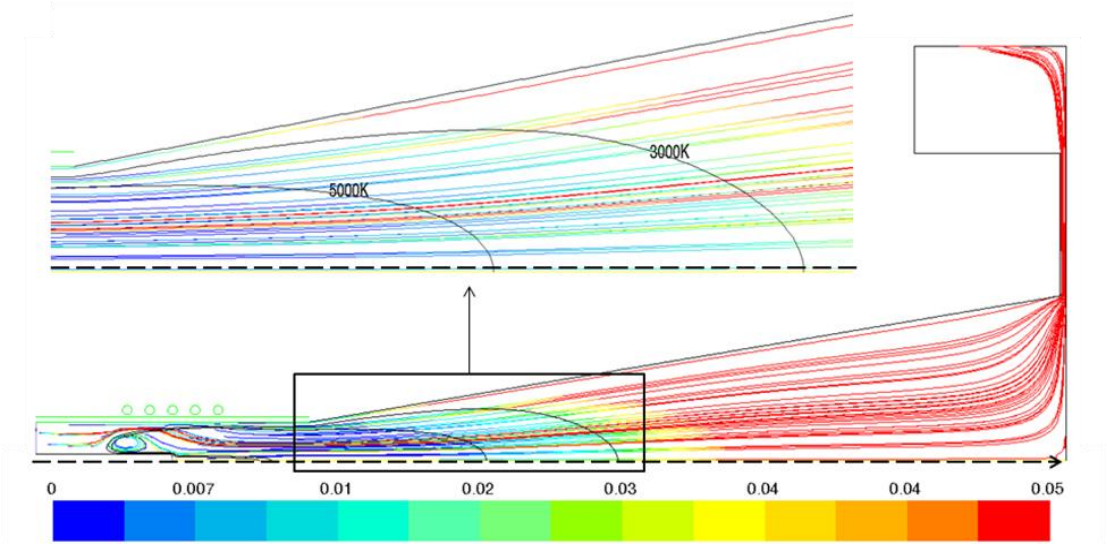

Figure 8.9 Residence time/cell [s] of the fluid along streamlines, with isotherms of the nucleation zone for the case of a reactor pressure of 55.2 kPa.

Figure 8.10b presents the streamlines used for the calculations. Note that the present model does not consider the kinetics of the particle nucleation process and growth. We can however assume that the nucleated particles follow the flow, and their residence time for growth should correlate well to the flow residence time since practically no more carbon is available for growth below 3000 K. Figure 8.7 is also indicating that the primary nanoflake structures are well isolated structures not formed through particle-particle collisions and agglomeration; agglomeration essentially occurs upon collection, and the resulting powder remains very light in nature and easily dispersed. Figure 8.10 indicates that residence time in the growth zone is essentially constant and increases only slightly as the radial position gets close to the 7^{th} streamline, and then decreases towards the reactor wall. Total residence time values in the growth zone are well below 0.1 second, and the maximum residence time variation observed in the reactor is below 10 ms. One should note this last value indicates an extremely narrow fluctuation range in the particle nucleation history when compared to typical reactors having non-

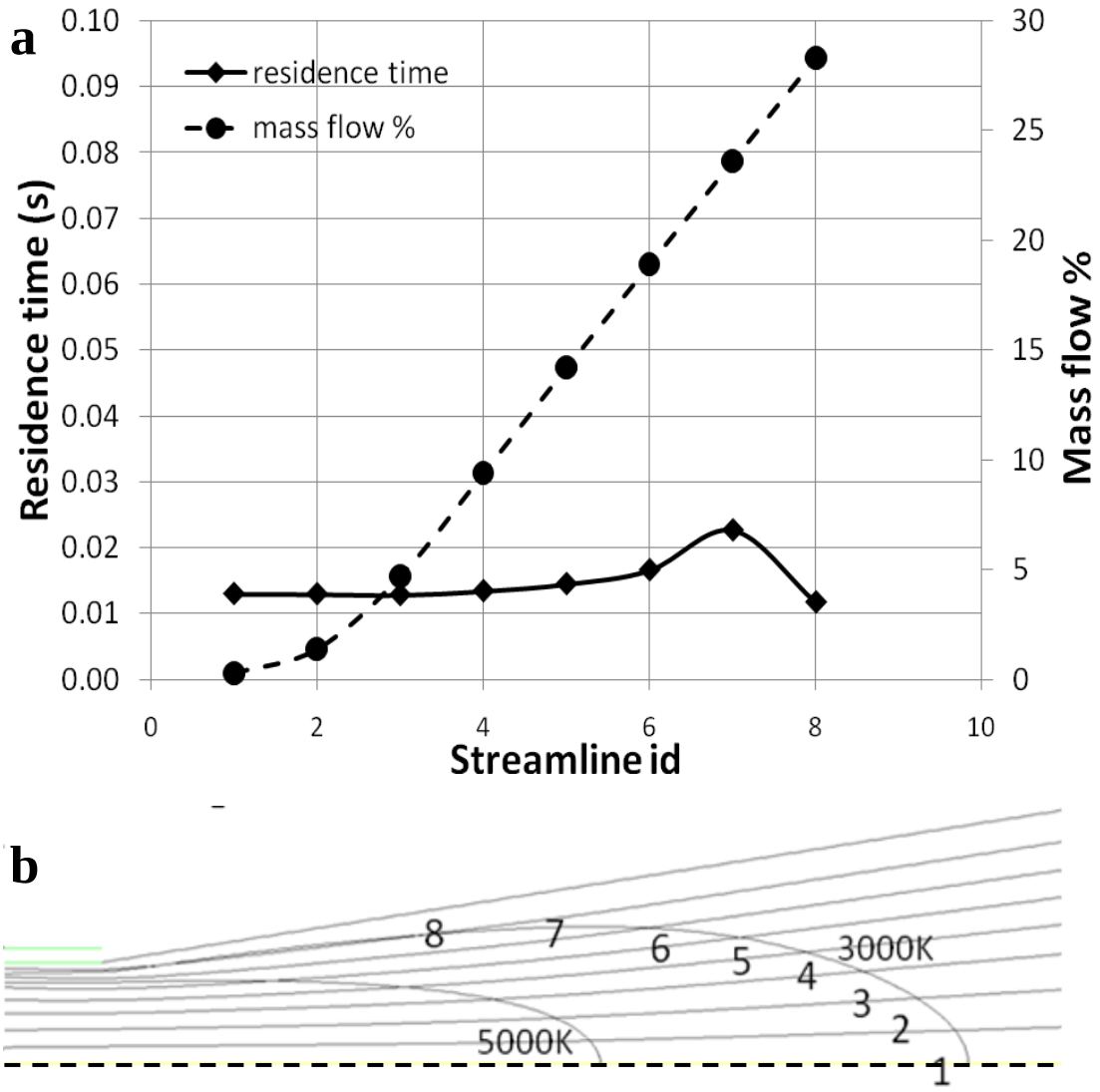

Figure 8.10 a) Total residence time in the carbon nucleation temperature range (3000 K - 5000 K) along specific streamlines, over for the case of a reactor pressure of 55.2 kPa; b) Identification of the streamlines used: 1 – reactor axis, 2 – 1.5×10^{-5} kg/s, 3 – 5.0×10^{-5} kg/s, 4 – 1.0×10^{-4} kg/s, 5 – 1.5×10^{-4} kg/s, 6 – 2.0×10^{-4} kg/s, 7 – 2.5×10^{-4} kg/s and 8 – 3.0×10^{-4} kg/s.

uniform flow patterns and some recirculation zones; one may expect for example in recirculation zones to see residence times that are at least 2-3 orders of magnitude larger. The experimental results showing uniformity in the morphology of the product within the entire reactor volume effectively correlates with this

narrow residence time variation. On Figure 8.10 is also presented the mass flow percentage for each streamline. The mass of gas along the streamlines increases from 0.3% on the reactor axis to close to 30% close to the reactor walls. This indicates that the majority of the carbon particles nucleated will be present in the gas stream close to the reactor walls, and these will effectively nucleate with an even narrower profile of residence time distribution.

Table 8.1 presents the quench rates in K/s units along the axis and the seven streamlines of Figure 10 for the case of reactor pressure of 55.2 kPa and 10 kW plasma power. The axial extension of the streamlines is roughly limited to the region corresponding to the nucleation zone (5000-3000 K) as shown in Figure 8.3a. Quenching rates around 10^5 K/s are observed throughout this zone for all stream lines. Again, a very narrow quench rate profile is observed in this reactor, highlighting the uniformity of the particle morphology being expected. This correlates well with the high uniformity of the carbon nano-flakes collected on the side walls and end plate following experimental runs, together with a high reproducibility of the achieved morphology over a series of experiments.

Table 8.1 Quench rates (K/s) following the stream lines for the case of reactor pressure of 55.2 kPa and 10 kW plasma power

Id number	Mass flow rate (kg/s)	Quench Rate (K/s)	Δz(m)
1	**3.2×10^{-6}**	**1.54×10^{5}**	**0.085**
2	**1.5×10^{-5}**	**1.54×10^{5}**	**0.085**
3	**5.0×10^{-5}**	**1.56×10^{5}**	**0.084**
4	**1.0×10^{-4}**	**1.49×10^{5}**	**0.087**
5	**1.5×10^{-4}**	**1.38×10^{5}**	**0.094**
6	**2.0×10^{-4}**	**1.21×10^{5}**	**0.108**
7	**2.5×10^{-4}**	**6.58×10^{4}**	**0.128**
8	**3.0×10^{-4}**	**1.71×10^{5}**	**0.061**

The existence of high quench rates promotes the production of fine particles as already reported in other works [13, 14] related to the synthesis of carbon nano-flakes. Based on TEM observations, the carbon nano-flakes show planar

structures that are typically longer in one direction. Image analysis reveal typical sheet morphologies having between 6-16 graphitic planes, with particles dimensions of approximately 100 nm ± 20 nm long, 50 nm ± 10 nm wide and around 5 nm thick (refer to Figure 8.7 for nano-flakes morphology). Particles size measurements were also made using a Mastersizer 2000 from Malvern Instruments (see Figure 8.11). These measurements are based on light scattered by spherical particles and use Mie theory to compute the particles size distribution. The result is a distribution of diameters based on spherical particles, a sphere being described by a single number. Since the carbon nanoparticles are far from being spherical, this method is actually measuring an equivalent spherical particles size by fitting the scattering data to a size distribution [15]. The surface area moment mean D[3,2], or Sauter Mean Diameter (SMD), is the most used in applications where the surface area is important (i.e. catalysis). If we consider three particles with different dimensions, the surface area moment mean can be calculated using the formula: $D[3,2] = (a^3+b^3+c^3)/(a^2+b^2+c^2)$, where a, b and c are the equivalent sphere diameters for the measured particles. Highlighting this theoretical aspect and analyzing the distribution curve, we can report a mean particles size of about 160 nm. This value fits quite well with the nanoflakes in-plane length values recorded from the TEM observations.

The number of graphitic layers is probably determined during the nucleation stage. The high temperature values in the nucleation region promote the initial critical nuclei formation and most probably sets the early crystal structure, hence the size of the critical nuclei is expected to set some number of graphitic planes. New carbon atoms arriving will show high in-plane mobility to reach the edges which are stable attachment sites, and low out of plane mobility to form new planes. So the growth, once the initial nuclei are formed, goes towards extending the lateral sizes, with each direction having specific interaction energies. Moving away from the nucleation zone, the particles enter the growth zone. Here the growth of particles is influenced by the residence time. The differential growth of particles in specific directions (length of particles seen higher than the width of particles) is probably the result of the presence of two types of edges in the

graphene sheets: “zig-zag’ edges and “armchair” edges as presented in Figure 8.12. We assume that the growth is favorized along one crystallographic orientation of the graphene crystal.

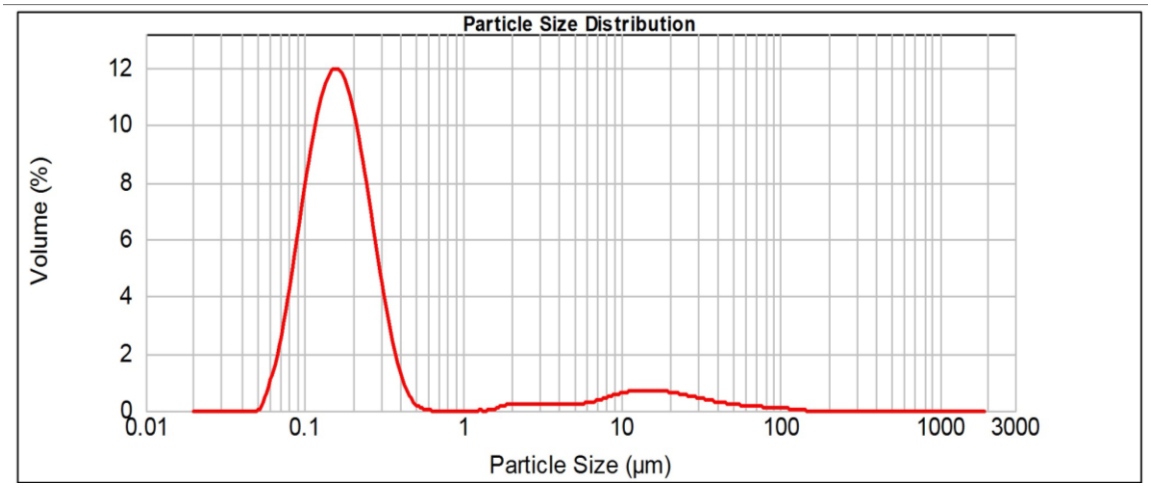

Figure 8.11 Carbon nano-flake particles size distribution as evaluated by a light scattering technique assuming a spherical particle morphology.

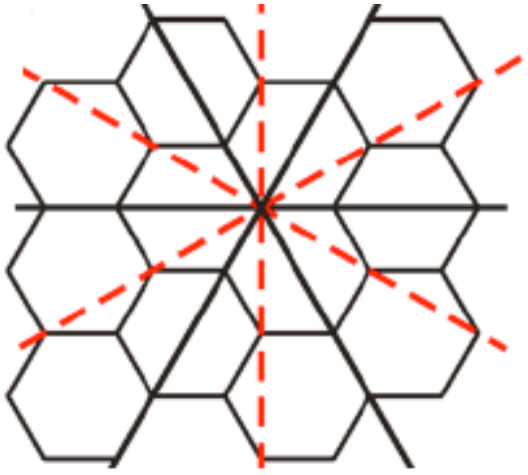

Figure 8.12 Sketch of the honey-comb crystal geometry within the graphene plane. Two distinct crystallographic orientations of the graphene crystal are possible: armchair (solid lines) and zigzag (dashed lines) [16]

4. Conclusions

The present modeling work shows that the reactor geometry used in this study enables a uniform flow and temperature evolution within the reactor volume. A better and more robust process control is achieved under varying operating conditions allowing the system operation in a wide range of reactor pressures without affecting the particles morphology generated with this highly diluted methane in argon system. The high nucleation temperature and quench rate values evaluated in the model provide conditions for the formation of nanoparticle nuclei having a small number of graphitic planar structures. The short enough residence times help to maintain the planar structures within the 100 nm scale.

A very important aspect highlighted by the modeling results and demonstrated experimentally is that plasma power and pressure fluctuations do not affect the product uniformity; no important changes were observed in the temperature profiles and nucleation history upon varying the plasma power from 10 kW to 20 kW and pressures between 20.7 and 101.3 kPa.

Acknowledgments

The financial contributions of the Natural Sciences and Engineering Council of Canada, FQNRT are gratefully acknowledged.

References

[1] Moreno-Couranjou, M., Monthioux, M., Gonzalez-Aguilar, J., Fulcheri, L., “A non-thermal plasma process for the gas phase synthesis of carbon nanoparticles”, Carbon, **47**, 2310-2321, 2009

[2] Girshick, S.L., Chiu, C.P., McMurry, P.H., “Modelling Particles Formation and Growth in a Plasma Synthesis Reactor”, Plasma Chemistry and Plasma Processing, **8**, 145-157, 1988

[3] Girshick, S.L., Chiu, C.P., “Homogeneous Nucleation of Particles from the Vapor Phase in Thermal Plasma Synthesis”, Plasma Chemistry and Plasma Processing, **9**, 355-369, 1989

[4] Fabry, F., Flamant, G., Fulcheri, L., “Carbon black processing by thermal plasma. Analysis of the particle formation mechanism.”, Chemical Engineering Science, **56**, 2123-2132, 2001

[5] Juan L., Fangfang H., Yiwen L., Yongxiang Y., Xiaoyan D. and Liao X., “A New Grade Carbon Black Produced by Thermal Plasma Process”, Plasma Science and Technology, **5**, 1815-1819, 2003

[6] Kim, K.S., Seo, J.H., Nam, J.S., Ju, W.T., Hong, S.H., “Production of Hydrogen and Carbon Black by Methane Decomposition Using DC-RF Hybrid Thermal Plasmas”, IEEE Transactions on Plasma Science, **33**, 813-823, 2005

[7] Levchenko I, Volotskova O, Shashurin A, Raitses Y, Ostrikov K, Keidar M, The large-scale production of graphene flakes using magnetically-enhanced arc discharge between carbon electrodes, Carbon, **48**, 4570-4574, 2010

[8] Pristavita, R., Mendoza-Gonzales, N.Y., Meunier, J.L., Berk, D., “Carbon Blacks Produced by Thermal Plasma: The Influence of the Reactor Geometry on the Product Morphology”, Plasma Chem. Plasma Process., **30**, 267-279, 2010

[9] Castillo, I.A., Munz, R.J., “New in-situ sampling and New in-situ sampling and analysis of the production of CeO_2 powders from liquid precursors using a novel wet collection system in a rf inductively coupled thermal plasma reactor. Part 1: Reactor system and sampling probe”, Plasma Chem. Plasma Process., **27**, 737-759, 2007

[10] Mendoza-Gonzalez, N.Y., El Morsli, M., Proulx, P., "Production of Nanoparticles in Thermal Plasmas: A Model Including Evaporation, Nucleation, Coalescence and Fractal Aggregation", Journal of Thermal Spray Technology,**17**, No. 4, 533-550, 2008

[11] Boulos, M.I., Fauchais, P., Pfender E., "Thermal plasmas: fundamentals and applications", Plenum Press, **1**, 1994

[12] Pristavita, R., Meunier, J.L., Berk, D., “Carbon nano-flakes produced by an inductively coupled thermal plasma system for catalyst applications”, Plasma Chem. Plasma Process., **31**, 393-403, 2011

[13] Harbec, D., "Producing carbon nanotubes using the technology of DC thermal plasma torch", PhD Thesis, McGill University, Chemical Engineering Department, Montreal, Canada, 2005

[14] Larouche, F., Smiljanic, O., Sun, X.S., Stansfield, B.L., "Solutal Bénard-Marangoni instability as a growth mechanism for single-walled carbon nanotubes", Carbon, **43**, 986-993, 2005

[15] Thiele, E.S., French, R.H., "Light-Scattering Properties of Representative, Morphological Rutile Titania Particles Studied Using a finite-Element Method", Journal of Ceram. Soc., **81** [3], 469-479, 1998

[16] Neubeck, S., You, Y.M., Ni, Z.H., Blake, P., Geim, A.K., Novoselev, K.S., "Direct determination of the crystallographic orientation of grapheme edges by atomic resolution imaging", Applied Physics Letters, **97**, 053110, 2010

Chapter 9 – Peer reviewed paper submitted to Plasma Chemistry and Plasma Processing Journal

During the time of this project, two thermal plasma systems (a DC system and an ICP system) were used to produce carbon blacks having a certain degree of crystallinity and certain porosity. These characteristics of the carbon powders were dictated by the intended application requiring some specific functionalization of local graphene-like structures for catalysts applications in PEM fuel cells.

Both systems presented recirculation areas related to the geometry of the reactors and the presence of large radial flow velocity gradients generated by the thermal plasma streams. This leads to products having nonuniform morphologies in the reactors and difficult reproducibility from test to test. Important amounts of organic contaminants are also formed in both systems. These organic contaminants are binding with the CB particles during the production process, promoting the formation of particle agglomeration and columnar structures. They effectively act as glue for the CB particles, which leads to a decrease of the surface area of the final product.

It was demonstrated that by changing the ICP reactor design from a cylindrical to a conical geometry, the control of the flow dynamics enables to minimize the formation of recirculation areas in the system. Such a control leads to a product containing no organic contaminants or an insignificant amount of such compounds.

Since these organic compounds were produced in a large fraction of the experimental runs in both systems, a thermal treatment was developed to allow extraction and analysis of these contaminants. The results of this analysis are presented in this chapter.

Volatile compounds present in carbon blacks produced by thermal plasmas

Ramona Pristavita, Ranjan Roy, Blain Moran, Jean-Luc Meunier and Dimitrios Berk

Abstract

Carbon black nanopowders were produced using two thermal plasma processes based on DC, respectively ICP plasma torches. Although the produced particles were in the nanometer size range, the values obtained for the surface area of the particles using a Brunauer Emmett Teller technique were very small. This indicated the presence of contaminants in the experimental powders, as confirmed by Raman spectroscopy and Thermogravimetric Analysis. A thermal treatment process was developed in order to extract these volatile compounds, which were then identified using a Gas Chromatography - Mass Spectrometry method. The experimental powders were analyzed using Scanning and Transmission Electron Microscopy, X-Ray Diffraction and Raman Spectroscopy before and after the thermal treatment in order to determine the effect of the heat treatment on the powder structural properties.

Keywords: nanostructure, carbon black, catalyst support, adsorption, chromatography, thermal plasma

9.1 Introduction

Carbon black (CB) is a carbon material composed of nearly round primary particles called nodules presenting graphitic sheets as building blocks. The primary particles fuse together and form aggregates. Strong electrical forces bond the aggregates and promote the formation of agglomerates [1]. CB is widely used in industry including in the energy and materials sectors. It is produced at industrial scale using thermal processes. Recently new types of carbon black powders were synthesized using plasma technologies [2-7]. One of the advantages of using such technology is the possibility to use many different carbon sources in

gaseous, liquid or solid state. Independent of the production process used, it was observed that nearly all types of carbon blacks contained a certain fraction of volatile organic compounds, such as polycyclic aromatic hydrocarbons (PAH) [8-11]. These volatile organic compounds are known as very toxic airborne pollutants due to their carcinogenic and mutagenic properties [12, 13]. They are extracted from the carbon black materials using different methods (e.g shaking or ultrasonic extraction). These techniques work well when dealing with carbon blacks having a large particle size. In the case of materials with a small particle size, such as nano-carbon blacks produced using plasma technology, strong adsorption of these volatile organic compounds into the carbon matrix prevents their extraction using conventional methodology. For these materials more robust extraction methods such as Soxhlet extractions, Supercritical Fluid extractions and Accelerated Solvent extractions are used [10]. All these methods are solvent based, which means they use a solvent or mixture of solvents for the extraction of the volatile fractions.

In the present study CB nanopowders were produced by thermal plasma and the obtained powders were characterized using different analytical techniques. Since the presence of volatile organic compounds (VOC's) in the samples was observed, a thermal treatment was developed in order to separate these compounds from the carbon black experimental powders, to collect and identify the specific compounds. We choose a thermal treatment because it does not involve any chemicals, thus avoiding any changes in the chemical composition of the CB powders. The VOC's were collected on silica gel which was further used for the identification of these compounds. Gas Chromatography - Mass Spectrometry (GC-MS) was used as an analytical tool for the identification of the low boiling points volatile compounds ($T_b < 300^oC$), the maximum temperature of the detection column in the apparatus being 300^oC. For the high boiling point volatile compounds ($T_b > 300^oC$) soxhlet extraction was performed and the extract was analyzed using GC-MS.

9.2 Experimental equipment and methodology

9.2.1 Carbon black production

CB nanopowders were obtained by plasma decomposition of a carbon-containing feedstock. The material was produced using two different plasma systems which give different production conditions: a non-transferred DC thermal plasma torch with a nominal power of 100 kW and about 120 g/hour production rates, and an inductively coupled plasma (ICP) torch with a nominal power of 35 kW and production rates of about 60 g/hour.

During the CB production using the DC system, the carbon source used was benzene which was injected directly in the torch nozzle for rapid dissociation. The benzene was vaporized and heated up to 300^{o}C prior to injection. The benzene flow rates were 10 smlpm and 15 smlpm and the carbon source injection time varied between 3 and 12 minutes. The plasma-forming gas used was argon introduced through a vortex generator placed between the torch electrodes. A flow of 20 slpm hydrogen was also introduced in the torch nozzle along with benzene to prevent the formation of carbon black and the blocking of the nozzle. The reactor pressure was kept constant at about 26 kPa following an initial vacuum purging, and the power used in this study was fixed at 20 kW for the argon plasma gas. The reactor is a cylindrical water-cooled reactor made of stainless steel. The internal diameter of the reactor is 40 cm and the length of the reactor is 100 cm.

In the ICP torch system methane was used as carbon precursors at various flow rates. The methane was injected axially in the core of the hot plasma using low (0.5 slpm, 1 slmp and 2 slpm) or high flow rates (5 slpm and 6 slpm). The methane injection time varied between 8 and 30 minutes. The reactor pressure varied between 20.7 kPa and 89.6 kPa and the power was kept constant at about 10 kW plate power. The ICP torch was attached first to a cylindrical water cooled reactor (32 cm in diameter and 100 cm in length). The reactor geometry was later changed to a second conical reactor having 50 cm in length and an angle of expansion of 14^{o} [14, 15].

In both DC and ICP systems, nitrogen was also introduced in some experiments along with the carbon source during the production of the powders, using flow

rates of 0.1 slpm and 0.2 slpm. The objective for the nitrogen addition is to achieve a functionalization showing nitrogen atoms on pyridinic sites of the graphene structures for catalytic applications.

9.2.2 Heat treatment system

The experimental equipment for the heat treatment of the CB powders is presented schematically in Figure 9.1. The system is composed of a tube furnace, a quartz reactor, a quartz boat and the collection tube. Quartz was chosen because the furnace is heated to a maximum temperature of 800°C. The sample was placed in a quartz boat placed inside the quartz tube reactor. The volatile fraction was collected in the collection tube, where it was adsorbed on silica gel. The collection tube was immersed in an ice bath to promote the condensation of the volatile organic compounds and their adsorption on the silica gel. The carrier gas used was Ar, and a thermocouple was mounted on the exit line to record the temperature of the exit gases.

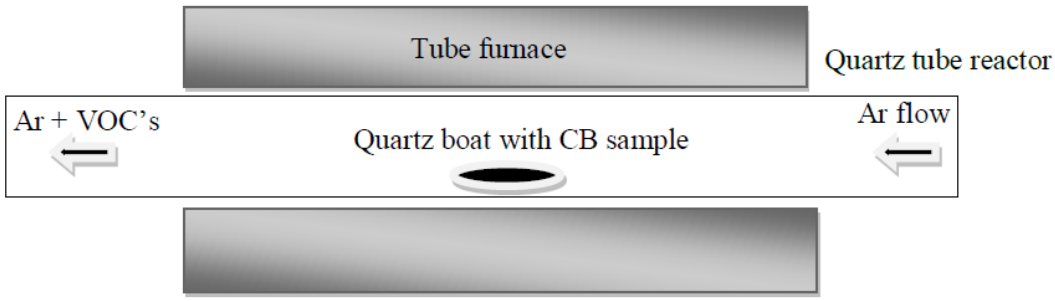

Figure 9.1 Schematic diagram of tube furnace system for the heat treatment of the samples obtained in the plasma devices

The CB samples were heated by the tube furnace using a heating rate of 10^{o}C/min and a constant flow of argon gas was used to carry any VOC's to the collection tube. Argon was used as a carrier gas at atmospheric pressure. The system was always purged with argon for 10 minutes before heating the sample to remove any oxygen. A constant flowrate of 600 smlpm of argon was used for each sample based on preliminary tests indicating that flowrates above 700

mL/min are blowing the CB sample out of the quartz boat, and flowrates less than 600 mL/min allow the volatilized compounds to condense on the quartz tube walls before reaching the collection tube. After adsorption of the VOC's, the silica gel was transferred from the collection tube into head space vials.

Please refer to Appendixes IV for operation procedure for the thermal treatment setup.

9.2.3 Sample preparation, analysis and identification of volatile organic compounds

The head space vials containing the VOC's adsorbed on silica gel were placed on a Gerstal Multipurpose Sampler where they were incubated for 35 minutes at 200^{o}C to allow the desorption of the VOC's into the vials. Then, samples of 1000 µL were analysed by GC-MS. The analyses were performed with a Thermo Scientific Trace Gas Chromatograph Ultra coupled to an External Ion Trap Mass Spectrometer (ITQ 1100). The GC is equipped with a Restek Rtxi-5ms column with a length of 30 m, film thickness 25 µm and an internal diameter of 0.25 mm. The GC was programmed in the following manner: the split/splitless injector was set to 225^{o}C with a split flow of 200 mlpm and a split ratio of 1:200, the helium flow was maintained at 1 mlpm; the oven was set at 75^{o}C for 0.5 minutes and ramped up to 300^{o}C using a heating rate of 15^{o}C/min. The GC to MS transfer line was maintained at 250^{o}C. The MS was set up in the following manner: the ion source temperature was fixed at 200^{o}C, the damping gas flow used was 0.3 mlpm. The scan mode was 10-400 amu using positive ion mode. Four separate scans were performed for each sample to optimize the results: 1) A full mass scan from 10-600 amu; 2) A segmented scan excluding the mass of silica gel; 3) Single Ion Monitoring Scan based on the potential aromatic masses; 4) a MsN (Multiple Fragmentation of Parent Ions in External Ion Trap) scan based on Scan 2 to confirm the aromatic structure of each peak found in the Total Ion Chromatograph (TIC).

After the analysis of VOC's having a low boiling point (T_b<300^{o}C), soxtherm extractions were performed on the silica gel samples. The samples were mixed

with a 50% acetone, 50% hexane solvent mixture. The extractions were performed using a 2000 automatic Soxtherm from SCP Science Gerhardt. The program used included a maximum treatment temperature of 300^{o}C and an extraction temperature of 150^{o}C. The boiling time was 2 hours and 15 minutes and the extraction time was 1 hour and 15 minutes. Three cycles of 20 minutes each were performed for the reduction of the solvent with a reduction pulse of 3 seconds.

The remaining solvent containing the extracted VOC's was placed into head space vials and the samples were analyzed using GC-MS using the method described above.

9.3 Results and discussion

9.3.1 Characterization of CB powders

The Scanning Electron Microscopy (SEM) images in Figure 9.2 present different types of CB powders produced with the DC and ICP systems using different experimental conditions. We can observe that the structural properties of the samples varies with the carbon flow rate used and the type and geometry of reactor used. By increasing the benzene flow rate in the DC system from 10 slpm to 15 slpm, the particles changed in morphology and size, as can be seen in Figures 2a and 2b. By increasing the methane flow rate in the ICP cylindrical reactor system from 1 to 5 slpm, the structure of the particles change from round spherical particles, having particles size between 30 nm and 150 nm forming a grape-like agglomerate, to a columnar structure (Figures 2c, d) . The formation of the columnar structure is due to the cooler recirculation areas present in the reactors resulting in the condensation of some of the species present in the gas stream which eventually form secondary products. Increasing the carbon source flow rate from 1-2 slpm to 5-6 slpm generates more VOC's. These compounds act like a glue for the CB particles promoting the formation of columnar structures as seen in Figure 2d [15].

The small particle diameters obtained of about 30 nm were expected to lead to large specific surface areas. The specific surface area of the particles produced

was measured using a Brunauer Emmett Teller (BET) technique. The values obtained for these powders were on the contrary much smaller than expected, below 30 m^2/g. This indicated that these samples contain a large fraction of VOC's which are agglomerating the particles, resulting in a decrease of the specific surface area of the product.

Changing the geometry of the ICP reactor to a conical expansion eliminating the recirculation zones [16], carbon nanoflake-like structures were obtained (Figures 9.2e, f). In this case, only a small amount of VOC's was observed for methane flow rate increasing above 5slpm.

The presence of these secondary products was confirmed by Raman Spectroscopy. The Raman spectra were obtained using an incident laser wavelength of 514 nm and a grating of 1800 lpmm. All the spectra show the distinct G and D bands which are characteristic of graphitic materials, superposed on a fluorescence background that is particularly visible for Raman shifts above 1600 cm^{-1} (Figure 9.3). This was indicative of the presence in the sample of a significant fraction of VOC's. It was observed that by increasing the carbon source flow rate, the amount of contaminants in the experimental powder was also increased. Also, the presence of nitrogen in the system was observed to increase the amount of the contaminants produced. After a heat treatment up to 800^oC, the Raman spectra of the samples showed an important decrease in the fluorescence background resulting from the elimination of the volatile compounds from the experimental powders as seen in Figure 9.3. We also observe that the heat treatment did not affect greatly the position of the D and G primary and secondary bands. Only a small shift of the bands towards the left side of the spectrum was observed. We also observe an increase in the intensity of the G band which is an indication of an increase in the degree of crystallinity of the sample, which was expected since graphitization of carbon blacks at high temperatures is a well-known phenomena.

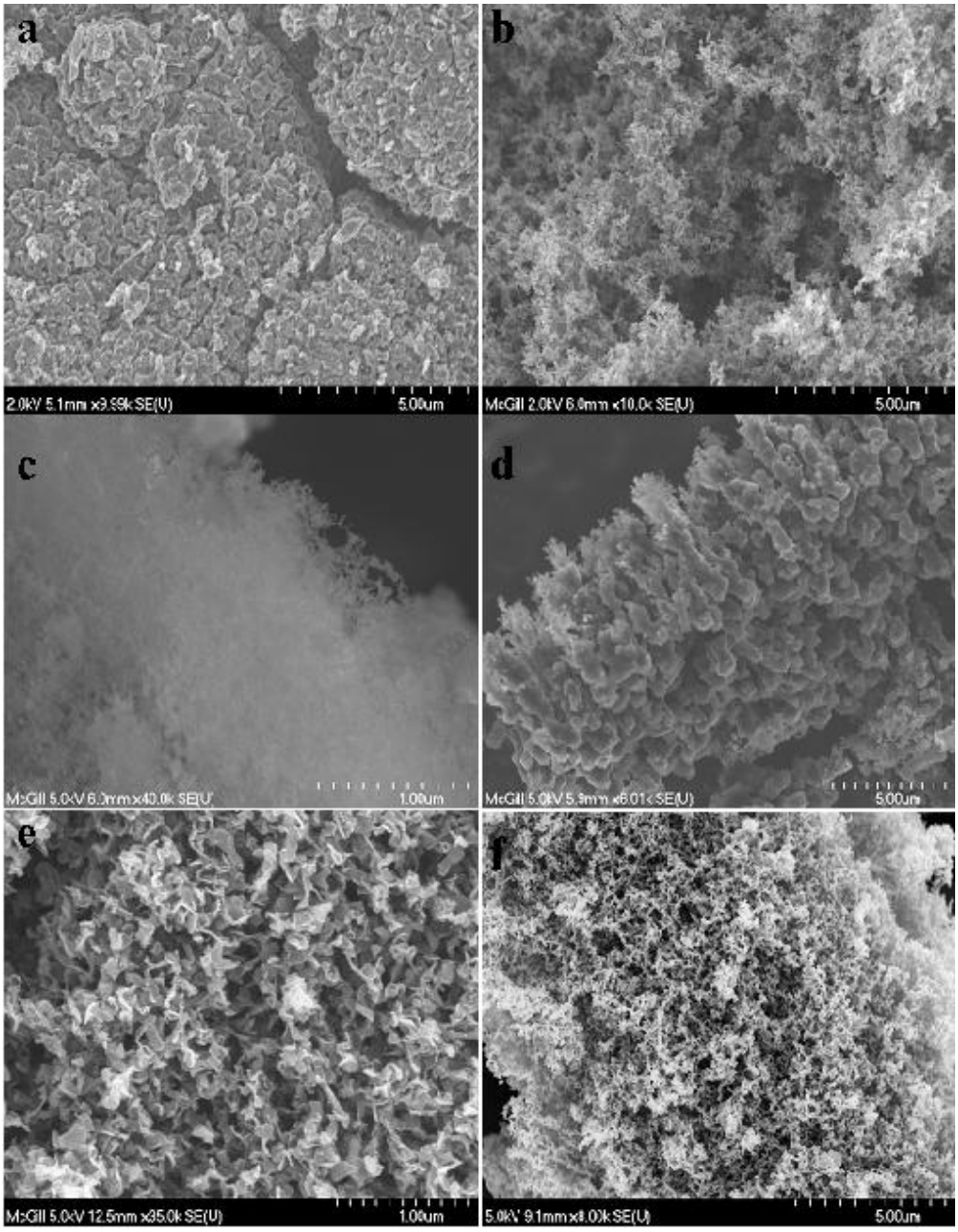

Figure 9.2 SEM image of CB samples produced using: a) DC system, 10 smlpm benzene, with nitrogen addition; b) DC system, 15 smlpm benzene; c) ICP system, 1 slpm methane, cylindrical reactor; d) ICP system, 5 slpm methane, cylindrical reactor; e) ICP system, 0.5 slpm methane, conical reactor; f) ICP system,1 slpm methane, conical reactor, with nitrogen addition. High resolution SEM observation of the structures in (e) and (f) show the crystalline graphene nano-flake structure with 6-16 graphene layers and 50-100 nm planar length scales [see 16]

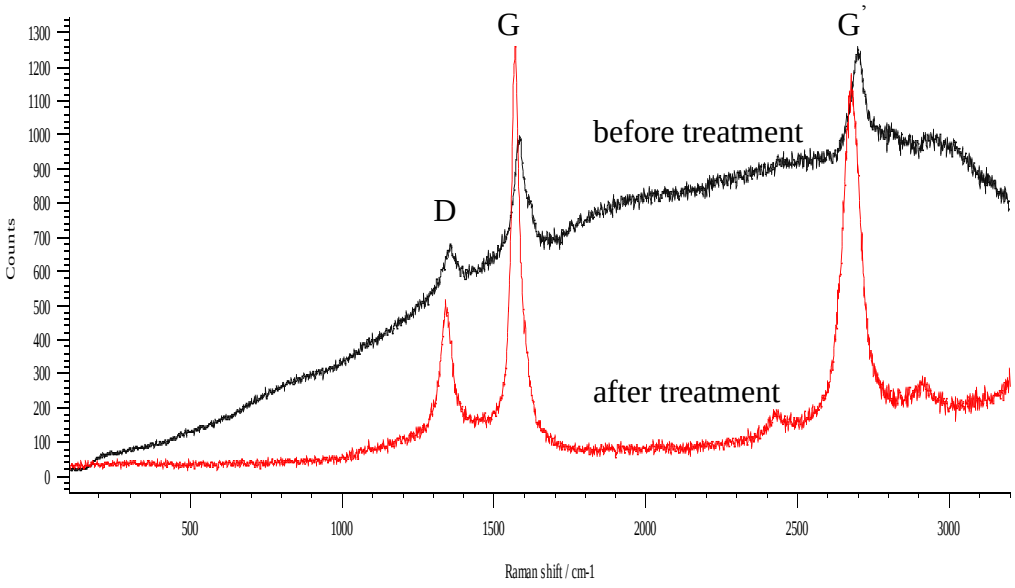

Figure 9.3 Raman spectra of CB samples produced using the ICP system and a methane flow of 1 slpm, before and after the thermal treatment

Thermogravimetric Analysis (TGA) of the samples was performed in an argon atmosphere using a heating rate of 10^{o}C/min up to a temperature of 800^{o}C. The heat treatment of carbon material in an inert atmosphere in the absence of oxygen does not result in carbon mass loss. The mass losses recorded in our experiments are due to the removal of contaminants from the sample. Figure 9.4 shows TGA graphs for 3 representative samples produced using the two types of plasma systems: the DC system and ICP system with two reactor geometries (cylindrical and conical).

Mass losses between 5.18% and 41.69% were recorded for treatments up to 800^{o}C. It was observed that the carbon blacks produced using the DC system had the greatest mass losses, so these samples contained the largest amounts of volatile compounds. According to Guo [17] during the operation of the DC plasma system, the core of the high velocity/high temperature viscous plasma jet leaving the nozzle is confined and does not mix with the surrounding environment until it hits the collection plate, forming recirculation loops. Because of the much low temperatures prevailing in this recirculation zone, some gaseous species

present in the stream may form secondary compounds which are mixed with the CB particles. The smallest mass loses were recorded for the case of the carbon blacks produced with the ICP system and a conical shape reactor. This system was designed to eliminate the recirculation areas and avoid the colder regions in the reactor. This provided a clear and predictable thermal history of the reactants and particles in the reactor, with all the species present in the gas stream undergoing the complete sequential process of nucleation, growth of carbon black particles, and collection.

We can observe also that the mass loss occurs in the range 200ºC - 500ºC. We separated the analyzed products into two groups based on the treatment temperature required in the analysis: low boiling point VOC's and high boiling point VOC's.

In the XRD diffraction patterns two peaks characteristic of graphitic materials were observed: one at the 2θ angle of 22^{o} and the second one around 44^{o}. An increase in the intensity of the second peak (Figure 9.5) was observed after the thermal treatment up to 800^{o}C, which indicated a small increase in the degree of graphitization of the thermally treated experimental powder.

The same change in the structure of the sample, after the heat treatment, was observed using Transmission Electron Microscopy (TEM). Figure 9.6 presents the same experimental CB powder, produced using the ICP system with the cylindrical reactor before and after the heat treatment. The powder showed an amorphous structure and a columnar shape of the particles as can be seen in Figure 9.6a. After heating the sample up to 800^{o}C the structure changed from completely amorphous to a more graphitized structure, and from columnar particles shape to bulky particles with more isotropic shapes. Also, the diffraction patterns (Figure 9.6, right side) of the samples showed the transition from the amorphous to a crystalline structure.

Specific surface area measurements using BET technique were performed before and after the thermal treatment of the carbon black samples. Carbon blacks produced with the DC system showed specific surface area values between 11.1 m^2/g and 30.2 m^2/g as produced. After the thermal treatment the values changed to around 55.6 m^2/g. For the samples produced using the ICP system and the cylindrical shape reactor, the specific surface area values changed from about 125 m^2/g before the thermal treatment to around 156.3 m^2/g after thermal treatment. With the conical shape reactor the powders specific surface area values stayed at about the same value: 348 m^2/g.

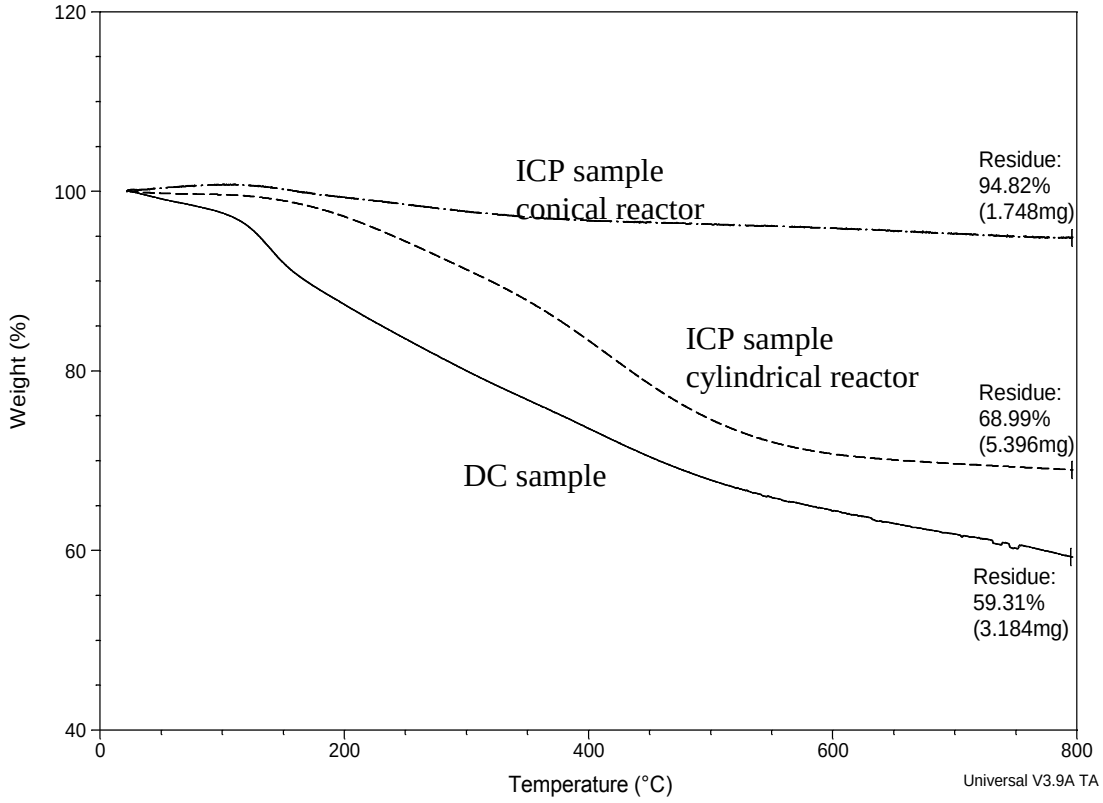

Figure 9.4 TGA mass loss in argon atmosphere of different CB materials produced using the DC and the ICP systems

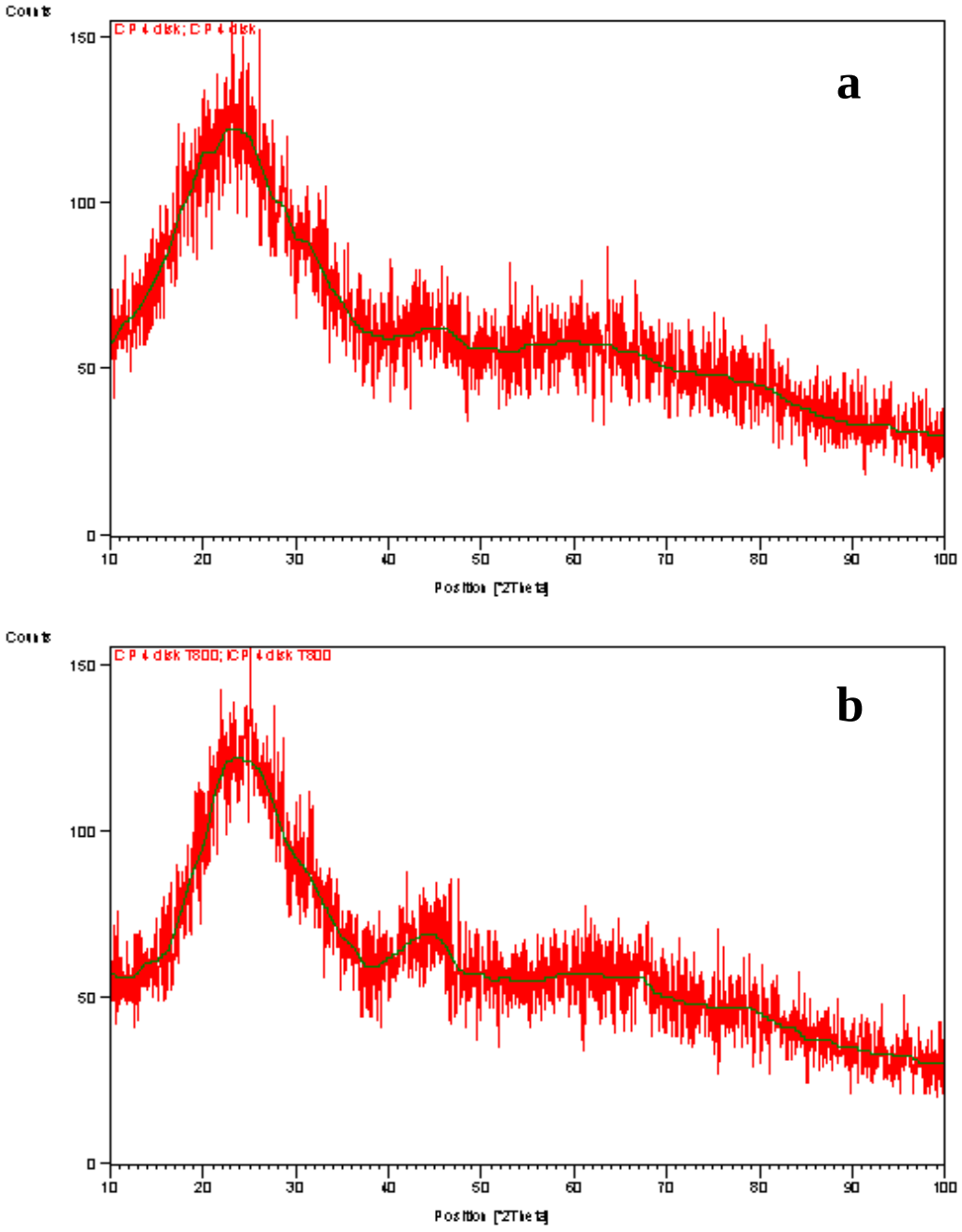

Figure 9.5 Diffraction patterns of a) untreated and b) treated experimental powder produced using the ICP reactor and a methane flow of 6 slpm. The broad peak at angle 2θ=22° corresponds to graphitic structure

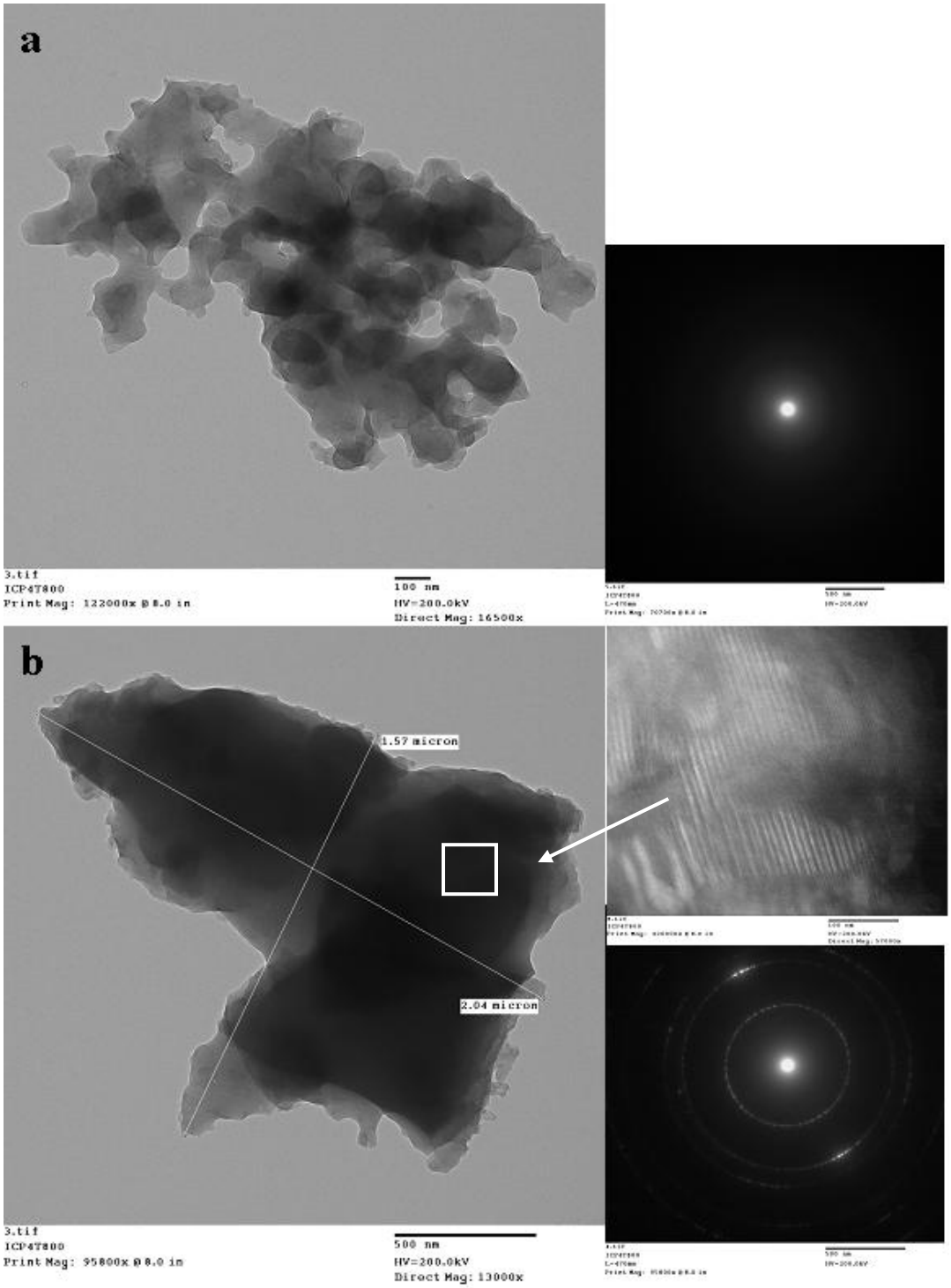

Figure 9.6 TEM images and diffraction patterns of CB powder produced using the ICP reactor and a methane flow of 6 slpm. a) untreated sample showing an amorphous structure and b) treated sample showing a crystalline structure

9.3.2 Identification of VOC's

The tube furnace experiments and the TGA analysis showed similar mass losses occurring after heating the CB samples up to 800ºC. Treatments up 200^{o}C, 600^{o}C and 800^{o}C were also performed separately and the fractions collected were analyzed using GC-MS.

The GC-MS results show the presence in the CB samples of low boiling point VOC's. The DC samples contained the highest amounts of organic compounds and it was observed that the majority of these compounds were in the form of aromatic compounds (compounds containing one or more benzene rings). For the samples produced using the ICP reactor a close correlation was observed between the amount of organic compounds present in the CB samples and the collection position within the cylindrical reactor. The samples collected from the upper part of the reactor where the presence of recirculation areas was observed and modeled contained a higher concentration of VOC's. Also, some long chain hydrocarbons containing nitrogen were observed in the samples when nitrogen was introduced in the system along with the methane during production. Few VOC's were present in the carbon nano-flakes samples produced using the ICP system with the conical shape reactor and methane flow rates above 5 slpm, while no VOC's were observed at lower flow rates.

Figure 9.7 presents Total Ion Chromatogram (TIC) and Mass/Charge ratio profiles for the analysis of CB samples produced using the DC reactor. Table 9.1 lists the high probability compounds identified in the samples. Some of these compounds contain oxygen, which can be explained by the exposure of the CB samples to the air during the collection step after the synthesis experiment.

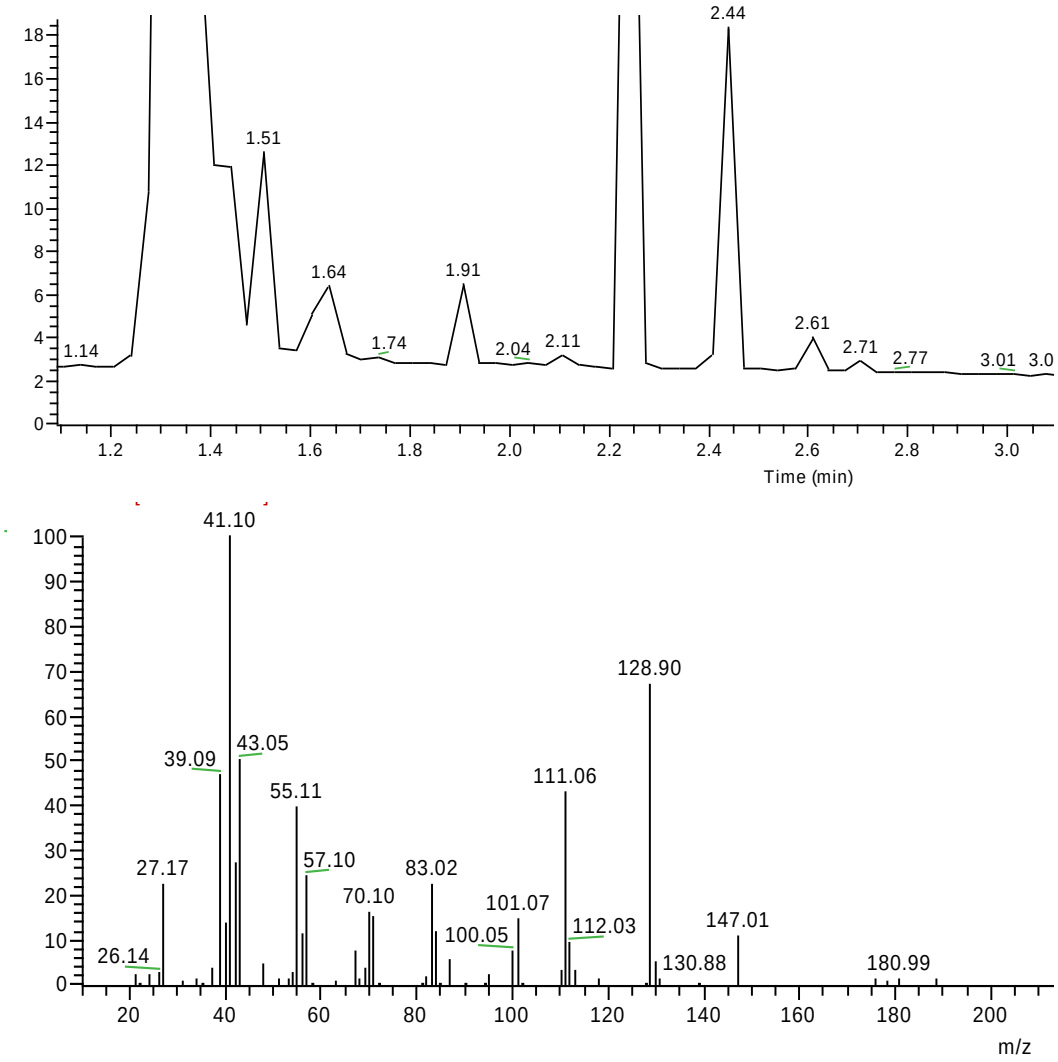

Figure 9.7 Example of TIC (top) and Mass/Charge ratio (bottom) profiles from the CB samples produced using the DC system

Table 9.1 Compounds identified in the CB samples by GC-MS in positive electron ionization mode with confirmation using secondary fragmentation.

Compound Name	Retention time (min)	Probability on the compound
Ethylbenzene	2.61	> 80%
3-Hydroxy-3,5-dimethyl-2-hexanone	2.23	> 80%
2-Pentanone-4-hydroxy-4-methyl	2.22	> 80%
Xylene	3.36 2.60	> 80%
Iso-Butyl Tiglate	2.22	> 50%
Oxalic acid, allyl methyl ester	1.41	> 50%
2,3,5,8-Trimethyldecane	7.71	> 50%

The GC-MS results showed that two types of compounds were identified as present in the carbon black samples: organic compounds containing one aromatic ring and linear or ramified chain hydrocarbons. All the identified compounds have boiling points below 200^{o}C. The fact that not all of these compounds were extracted from carbon black samples during the thermal treatment up to 200^{o}C, while some were extracted at temperatures between 600^{o}C and 800^{o}C, indicate that these compounds interact very strongly with the carbon matrix. The need of a high extraction temperature indicates these compounds are probably trapped in the porosity of the carbon powder, leading to longer treatment times and higher temperatures being necessary for their extraction.

Such organic structures are formed at low temperatures, probably below 300^{o}C, in comparison to the very high temperatures occurring in the plasma regions responsible for the carbon particle nucleation that are well above 2000^{o}C. The fact that these contaminants are generated along with the carbon structures in

the reactors is an indication of the existence of zones having temperatures that are well below the normal carbon particle nucleation temperatures, together with the long residence times necessary for the transport and growth of these species in the porous structures. This correlates well with experimental observations and the modeling results [15, 16] showing the presence of recirculation areas in the two plasma reactors.

9.4 Conclusions

During the production of carbon black using DC and ICP plasma systems, volatile compounds are produced along with the experimental powder. By increasing the carbon source flow rate, the amount of these contaminants in the experimental powder was also increased. These volatile contaminants were acting as a "glue" for the agglomeration of the carbon black particles. This leads to a significant decrease in the observed values of the specific surface area of the particles. Using a thermal treatment process the volatile compounds were extracted from the experimental powders and their chemical composition was identified, the low and high boiling points compounds being primarily identified using GC-MS method. An increase in the degree of graphitization of experimental powders was observed after treatment up to 800^{o}C.

Acknowledgments

The financial contributions of the Natural Sciences and Engineering Council of Canada, and FQNRT are gratefully acknowledged.

References

1. "Carbon Black User's Guide. Safety, Health, & Environmental Information", ICBA

2. Fabry, F., Flamant, G., Fulcheri, L., "Carbon black processing by thermal plasma. Analysis of the particle formation mechanism.", Chemical Engineering Science, **56**, 2123-2132, 2001

3. Fulcheri, L., Schwob, Y., Flamant, G., “Comparison Between New Carbon Nanostructured Produced by Plasma with Industrial Carbon Black Grades”, J.Phys. III France, **7**, 491-503, 1997

4. Juan. L. Fangfang, H., Yiwen, L., Yongxiang, Y., Xiaoyan, D., Liao, X., “A New Grade Carbon Black Produced by Thermal Plasma Process”, Plasma Science and Technology, **5**, 1815-1819, 2003

5. Kim, K.S., Seo, J.H., Nam, J.S., Ju, W.T., Hong, S.H., “Production of Hydrogen and Carbon Black by Methane Decomposition Using DC-RF Hybrid Thermal Plasmas”, IEEE Transactions on Plasma Science, **33**, 813-823, 2005

6. Moreno-Couranjou, M., Monthioux, M., Gonzalez-Aguilar, J., Fulcheri, L., “A non-thermal plasma process for the gas phase synthesis of carbon nanoparticles”, Carbon, **47**, 2310-2321, 2009

7. Li, N., Wang, Z., Zhao, K., Shi, Z., Gu, Z., Xu, S., “Large scale synthesis of N-doped multi-layered graphere sheets by arc-discharge method”, Carbon, **48**, 255-259, 2009

8. Diaz, E., Ordonez, S., Vega, A., “Adsorption of volatile organic compounds onto carbon nanotubes, carbon nanofibers, and high-surface-area graphites”, Elsevier, **305**, 7-16, 2007

9. Tsai, P.J., Shieh, H.Y., Hsieh, L.T., Lee, W.J., “The fate of PAHs in the carbon black manufacturing process”, Atmospheric Environment, **35**, 3495-3501, 2001

10. Jonker, M.T.O., Koelmans, A.A., “Extraction of Polycyclic Aromatic Hydrocarbons from Soot and Sediment: Solvent Evaluation and Implications for Sorption Mechanism”, Environ. Sci. Technol., **36**, 4107-7113, 2002

11. Akhter, M.S., Chughtai, A.R., Smith, D.M., “The Structure of Hexane Soot II: Extraction Studies”, Applied Spectroscopy, **39**, 154-167, 1985

12. Howard, J.B., Longwell, J.P., Marr, J.A., Pope, C.J., “Effect of PAH isomerizations on mutagenicity of combustion products”, Combustion and Flame, **101**, 262-270, 1995

13. Levendis, Y.A., Atal, A., Carlson, J.B., “On the correlation of CO and PAH emissions from the combustion of pulverized coal and waste tires”, Environ. Sci. Technol., **32**, 3767-3777, 1998

14. Castillo, I., "Study of CeO_2 synthesis from liquid precursors in a RF-inductively coupled plasma reactor", Ph.D. Thesis, Chem. Eng. Department, McGill University, June 2007

15. Pristavita R, Mendoza-Gonzales NY, Meunier JL, Berk D., "Carbon Blacks Produced by Thermal Plasma: The Influence of the Reactor Geometry on the Product Morphology", Plasma Chem. Plasma Process, **30**, 267-279, 2010

16. Pristavita, R., Meunier, J.L., Berk, D., "Carbon nano-flakes produced by an inductively coupled thermal plasma system for catalyst applications", Plasma Chem. Plasma Process., **31**, 393-403, 2011

17. Guo, Liping, "Modeling of a supersonic DC plasma torch in CNT production", Ph.D. Thesis, Chem. Eng. Department, McGill University, September 2009

Chapter 10 – Discussion

10.1 CB production using the DC thermal plasma system

The CB powders produced with this system showed mainly an amorphous structure and non-uniform particle morphologies when collected from three different parts of the reactor (quench ring, reactor wall and collection plate). This difference in the morphology is explained by the presence of recirculation areas induced by the geometry of the reactor, the very high velocity of the viscous plasma jet and the presence of the collection plate. The plasma jet leaving the nozzle is confined and does not mix with the surrounding environment until it hits the collection plate, forming the recirculation loops [Guo, 2009]. The residence time of particles in these recirculation volumes is longer than the residence time of the particles in other parts of the reactor. Because of the low temperatures prevailing in these recirculation zones, some gaseous species present in the stream form secondary compounds which are mixed with the CB particles and trigger an agglomeration process.

XPS analysis shows the presence of contaminants in the CB samples. In the case of the CB collected from the quench ring, materials like W, α-Fe, WC and Fe_3C are present. These materials are formed during the experiment from the combination of the material eroded from electrodes, both the anode and the cathode being made of tungsten, the stainless-steel quench ring ablation and from the carbon species present in the gas stream. For the case of the CB powders collected from the reactor wall, similar contaminants (i.e. W, WC and Fe_3C) are present in the samples.

The nonuniformity and the low purity of the CB samples produced with the DC thermal plasma system eliminates the possibility of using these materials as catalyst support materials for PEM fuel cells application. As the results on the two ICP reactors indicate, the problem of lack of uniformity and reproducibility in the powder structures could be solved in the DC reactor by changing the geometry of the reactor body through a better control of the flow patterns. For example, a tubular reactor having the same inlet diameter as the DC torch exit and a

controlled expansion over a longer reactor length would minimize the recirculation zones. Adjusting the geometry through modeling of the flow fields can be made in a way similar to the ICP system. This however would not eliminate the contamination problem, this problem being a very important aspect in this project.

10.2 CB production using the ICP thermal plasma system

In order to eliminate the contamination problems and to allow a better control over the nucleation process and the crystallization, the CB powder generation was studied using the electrode less ICP thermal plasma system which is characterized by larger plasma volumes, lower flow velocities and longer residence times in the hot plasma zones. The experiments were first done using a standard cylindrical geometry of the reactor. The obtained powders were composed mainly of spherical particles, non-uniform in terms of particles size with diameters ranging between 30 nm and 150 nm. We also observed that particles collected on different positions of the reactor walls show differences in their structural properties. For example, the samples collected from the bottom of the reactor on the collection plate and on the lower part of the cylindrical reactor walls show particles that are spherical, while the ones collected on the upper part of the reactor walls show a bulk graphitic structure. This is the result of the reactor geometry affecting the gas flow patterns and the thermal history of the particles nucleation and growth. Although flow velocities are lower in the ICP reactor compared to the DC system, similar phenomena are observed in the cylindrical reactor geometry: strong radial gradients in flow velocity and high viscosity of the flow are responsible for the presence of the recirculation zones in the reactor. In these zones, the growth history of the particles cannot be controlled. In such flow patterns long residence times can be expected, as well as a large variability of these residence times and thermal history, leading to a product having a wider particles size distribution and different structural properties.

An increase of the carbon source flow rate modifies the CB structure from small, spherical particles forming aggregates and agglomerates to columnar

structures. The recirculation volumes present in the reactor are cooler zones enabling the early condensation of carbon species present in the gas stream and the formation of secondary volatile compounds. These secondary products act as glue for the spherical CB particles, sticking them together and promoting the formation of the columnar structures.

The change in reactor geometry followed an objective to control better the thermal history of the particle nucleation and growth process. Following the change to a conical geometry that is tuned to the ICP energy/flow fields eliminating turbulence and recirculation zones, the CB powders produced showed very uniform particle morphologies within the reactor, as evaluated from the electron microscopy observation. The product has a crystalline and flake-like morphology, TEM observations showing planar structures that are typically longer in one direction. Image analysis reveal typical sheet morphologies having between 6-16 graphitic planes, with particles dimensions of approximately 100 nm ± 10 nm long, 50 nm ± 10 nm wide and around 5 nm thick (roughly between 2 to slightly above 5 nm depending of the number of graphene planes and based on an interplanar distance of 0.334 nm for the graphite structure). These powders have a very specific structure in comparison to the CB particles family, the well graphitized flake-like morphology was named carbon nano-flakes (CNF). The better control of the nucleation and growth history in the conical reactor avoiding the presence of recirculation volumes was showed to promote the formation of a uniform CNF morphology throughout the reactor.

10.3 CB nitrogen functionalization in the ICP system

After obtaining the CNF material which presents the crystalline morphology suitable for the use of these powders as a Fe-based catalyst support material, a nitrogen functionalization of CB powders was achieved using the ICP thermal plasma system. Nitrogen was introduced during the synthesis experiments along with the methane precursor using flow rates of 0.1 slpm and 0.2 slpm of nitrogen. The resulting product was showed to have the same structural properties in terms of crystallinity, particle dimensions and uniformity of the CNF samples as the

material produced without nitrogen addition. Furthermore, XPS showed the nitrogen is getting in part incorporated into the graphitic structure through pyridinic bonds, which is the type of bonding desired for the formation of the active sites of the catalyst material. As a reminder, these active sites are formed when iron atoms are coordinated to a group of nitrogen atoms on pyridinic sites of graphitic plane porosity.

10.4 Study of the thermal history of the particles formation

A numerical simulation of the velocity and temperature fields, stream function lines, and quench rates of the plasma gas at different pressures in the conical geometry was made. This mathematical model was first developed to evaluate the gas flow patterns and the occurrence and extent of the recirculation zones in both the cylindrical and conical reactors. The two reactor geometries were compared and the results highlight a uniform flow pattern with no recirculation volumes achieved in the conical reactor. On the other hand, the cylindrical geometry shows clearly the formation of recirculation zones in the upper part of the reactor body, which is consistent with the powder morphology evolution with collecting position found experimentally. The quench rates were studied also in the ICP system in order to evaluate the influence of different experimental pressures on the carbon nano-flake morphology. The present geometry enables a uniform flow and temperature evolution and much better and robust process control under varying operating conditions allowing the system to operate in a wide range of reactor pressures without affecting the particles morphology.

10.5 Extraction and identification of volatile organic contaminants

During the production of carbon black using both DC and ICP plasma systems, volatile compounds were produced along with the experimental powders as observed from the BET measurements, Raman Spectroscopy and Thermogravimetric Analysis. By increasing the carbon source flow rate during the production process, the amount of these contaminants in the experimental

powder was also increased. These volatile contaminants act as a "glue" and promote the agglomeration of the CB particles. This leads to a significant decrease in the observed values of the specific surface area of the particles.

Using a thermal treatment process, the volatile compounds were extracted from the experimental powders and their chemical composition was identified, the low and high boiling points compounds being primarily identified using a GC-MS method. Organic compounds such as ethyl benzene, 3-hydroy-3,5-dimehtly-2-hexanone, 2-pentanone-4hydroxyl-4methyl, xylene, iso-butyl tiglate, oxalic acid, allyl hexyl ester and 2,3,5,8-teremethyldecane were present in the CB samples.

The CB powders were analyzed using Scanning and Transmission Electron Microscopy, X-Ray Diffraction and Raman Spectroscopy before and after the thermal treatment in order to determine the effect of the heat treatment on the powder structural properties. An increase in the degree of graphitization of CB powders was observed after treatment up to 800^{o}C.

10.6 Activity and stability of the catalyst prepared using carbon nano-flakes sample

This project is in collaboration with Professors Dodelet and Stansfield teams working at INRS-EMT Varennes. The team of Prof. Dodelet has a long experience in the field of non-noble catalyst development for PEM fuel cells application. They published a series of brake-through results indicating the suitability of these catalysts for this type of applications.

A catalyst was prepared at INRS-EMT using the CNF source material by adding the iron using the method developed by their laboratory. This method consists in a two step thermal treatment of a mixture of CB material, iron acetate and phenantroline (phenatroline/CB powder ratio = 3, i.e. 750 mg phenantroline/250 mg CB powder). Iron acetate is used as the iron source (~32 mg iron acetate which is equivalent of 1% Fe loading) and the phenantroline acting as a filler in the pores of the CB support material. This mixture is ball milled for 3 hours at 400 rpm. After this, two pyrolysis are performed: the first pyrolysis in argon at 1050^{o}C for 60 minutes, and the second pyrolysis in an ammonia (NH_3) atmosphere at

950^{o}C for 20 minutes [Dodelet, 2006]. The second pyrolysis is performed in an ammonia atmosphere because ammonia etches the surface of the CB creating pores where active sites are formed. By increasing the number of active sites present in the catalyst, the activity of the catalyst is also increased.

Figure 10.1 presents a comparison of the activity of the catalyst prepared using the CNF powders (labeled "ICP15" on the figure) with the activity of the Pt-based catalyst and N-Fe-functionalized catalysts prepared at INRS Varennes (labeled "our best" in the figure) using a non-plasma technique. The test was performed in a PEM fuel cell set-up. The results show that the catalyst prepared using a CNF powder has a lower activity compared to the Pt-based catalyst and the catalysts prepared by the INRS-EMT team. We believe this is mainly the result of the lower amount of nitrogen functionalization in the CNF samples. It is also important to consider the fact that during the two-pyrolysis used in the catalyst preparation, the flake morphology of the material is modified by the high temperature treatment. At such elevated temperatures, the flakes are expected to sinter and form graphitic blocks, thus decreasing the number of edges available for the formation of the active centers of the catalyst.

More important than the activity level, which could be improved with increasing amount of nitrogen functionalization, are the stability tests in the fuel cell environment. Stability is the major problem at present for this type of non-noble catalyst structure, the long time availability of the catalyst sites being strongly affected by the corrosion phenomena in the acidic environment of the cell, and possible poisoning of the catalyst sites from the by-products of the various reactions taking place. The tests performed on the CNF samples show a surprisingly good stability of the catalyst for the total 12 hours of test duration in a PEM fuel cell environment (Figure 10.2). This result is in strong contrast with all the other N-Fe-based catalysts degrading rapidly in the first 10 hours. Such a behavior is in agreement with the fact that catalyst stability increases with the degree of crystallinity of the support material, which is extremely high for the CNF compared to the other CB tested and as you can see in Figure 10.3. The carbon nano-flake sample is labeled "ICP10" in the graphic.

The stability test was performed in cycles of 4 hours duration each, and an increase in the activity of the catalyst was observed at the beginning of each testing cycle. This is probably due to the chemical processes and a rearrangement of the atoms, with possible formation of new active sites, taking place during the testing of the catalyst.

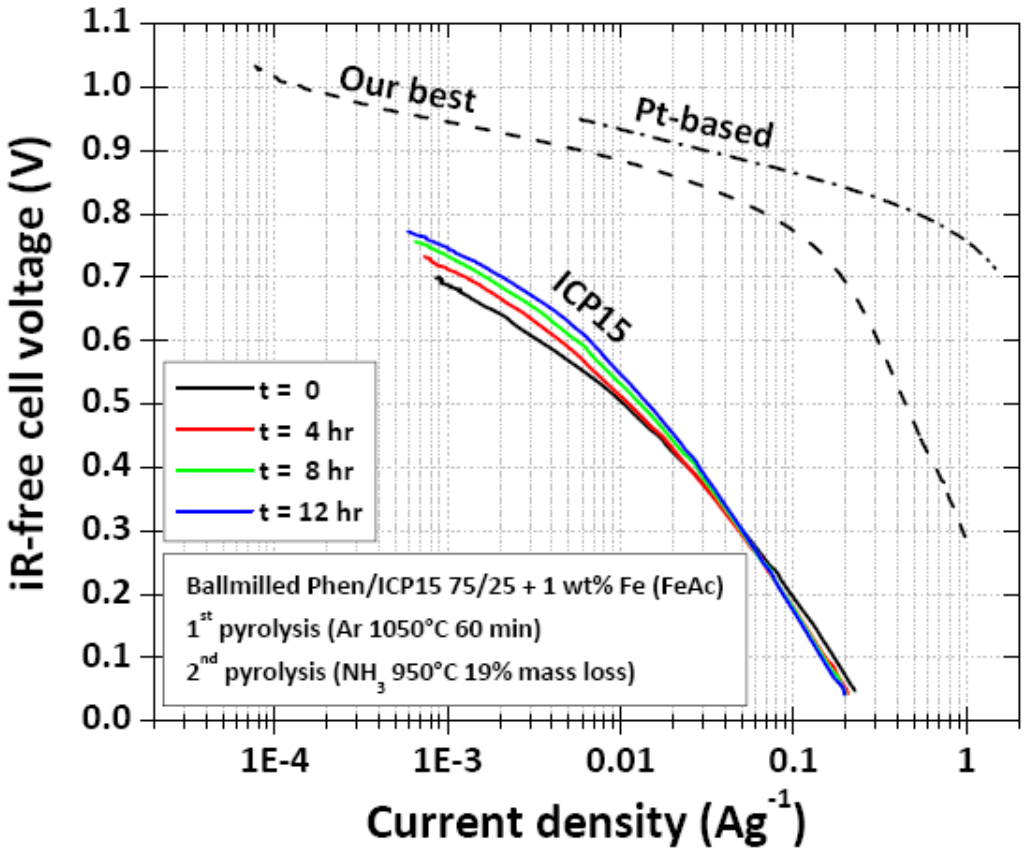

Figure 10.1 Comparison of the activity of the catalyst prepared using the CNF powders (labeled "ICP15") generated in the present project, with the activity of Pt-based catalyst and similar N-Fe-functionalized catalysts prepared by non-plasma techniques at INRS Varennes (labeled "our best")

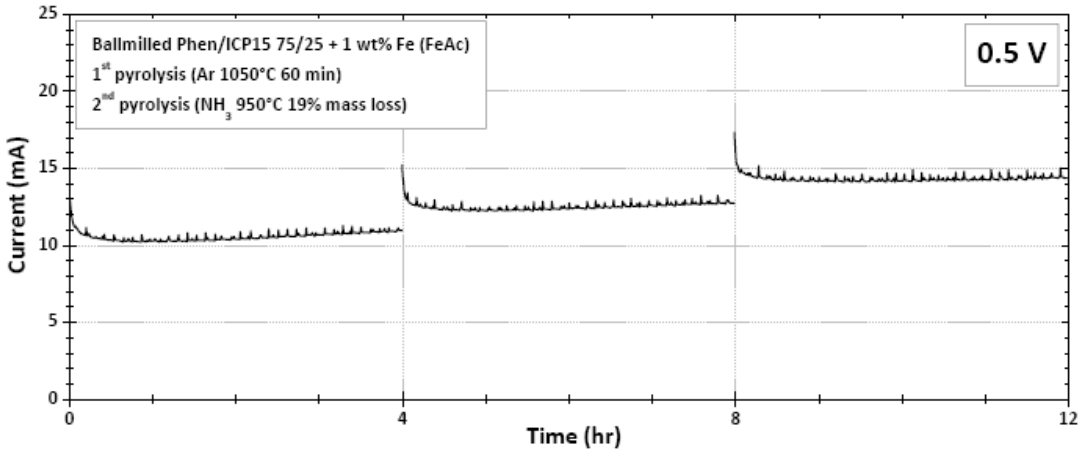

Figure 10.2 Stability test results for the catalyst prepared using CNF samples

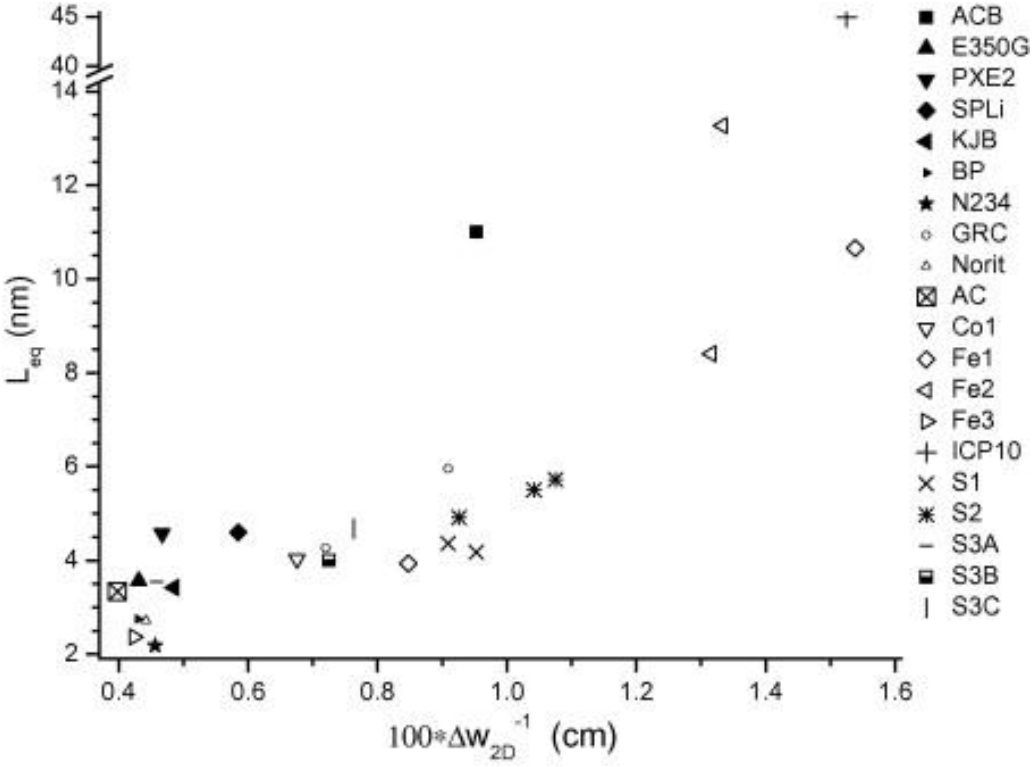

Figure 10.3 Classification of NCs using L_{eq} as a function of Δw_{2D}^{-1} [Larouche, 2010]

10.7 Other possible applications of carbon nano-flakes

The target application for the carbon nanostructures in this project is to be used as a catalyst material support in PEM fuel cells mainly for automotive applications. Although we are still very far from reaching the proper conditions, other possible applications for this type of fuel cells include consumer electronics (i.e. cell phones, laptops, camcorders, radios), portable and stationary powers supplies. Additional examples are given below, the specific interest for CNF being their high crystallinity enabling better transport properties and possible better resistance to corrosion in electrolytic applications.

Carbon-based materials have other possible applications in batteries, for example as electrodes. In a lithium-ion battery, the negative electrode is entirely made up of carbon and the positive electrode is a mixture of lithiated metal oxide mixed with a carbon material. This carbon, which is mainly graphite, is added to improve the electronic conductivity of the electrode [Kinoshita, 2001].

Carbon materials with high surface area and good electrical conductance are used as electrical double layer capacitors [Yoshida *et al*, 1987]. These "supercapacitors" use the interface generated between two different phases, a solid and a liquid electrode, generating an electric double layer in the very thin liquid electrolyte layer being formed. The highest the surface area of the electrodes, the higher is the amount of electric charges aligned in the double layers on both electrodes [Inagaki, 2000]. Double layer capacitors are used for back-up sources of memory in computers, together with solar batteries to increase the stability of the discharge voltage and the life [Inagaki, 2000]. Such supercapacitors are also expected to be important as power sources complementing the energy source supplied by the battery in electric transportation applications.

Carbon also plays a major role in the industrial electrochemical production of many chemical materials, such as: chlorine, aluminum metal and organic chemicals. Carbon is formed into solid structures that serve as the electrode sites where electrochemical reactions occur and products are formed. These carbon electrodes are formed by molding mixtures of graphite powder and pitch into

solid pieces and then heating to high temperatures. The graphite electrodes are a big improvement in performance and life over the amorphous carbons because they are capable of sustaining higher currents to increase production rates; they are more corrosion resistant and thermal-shock resistant [Kinoshita, 2001].

A very interesting application of carbon materials is their use as adsorbent for heavy oils from contaminated waters. For this application exfoliated graphite is used. The exfoliated graphite is obtained at industrial scale by heating up natural graphite to 1000^{o}C with sulfuric acid [Kinoshita, 2001]. Carbon nano-flakes are good candidates for this type of application because of the production method based on a plasma process, which is a clean method and does not involve the use of corrosive and toxic chemicals such as acids.

Chapter 11 – Original contributions and recommendations for future work

11.1 Original contributions

The most relevant original contributions of this work are:

- The generation and optimization, by ICP plasma decomposition of methane, of a CB nanostructure for non noble catalyst synthesis leading to a high degree of crystallinity and porosity of the particular CNF structure being formed.

- The incorporation of nitrogen into this CNF structure via in situ functionalization, creating the desired pyridinic C-N bonds as a base structure for the atomic level dispersion of non-noble metal catalysts and their application as Pt replacement.

- A better understanding of the control processes leading to reproducibility and uniformity of size and morphology in thermal plasma-based carbon nanoparticle generation. In particular, the importance of a reactor design enabling a good control over the energy and fluid fields for the generation of a relatively uniform thermal history of nanoparticle nucleation, growth and collection throughout the reactor was demonstrated. A correlation is made between the different synthesis parameters, the reactor design and the carbon nanoparticle structural and chemical properties in such a high temperature process.

11.2 Recommendations for future work

The recommendations for future work are mainly experimental, with one modeling aspect to be further studied.

1. During the production and in-situ nitrogen functionalization of carbon nano-flakes (CNF), only 0.7 at.% nitrogen is added to the graphitic structure. Even if the amount of nitrogen added in the system during the

production process is doubled (from 0.1 slpm to 0.2 slpm) the amount of nitrogen incorporated into the desired pyridinic structure is the same. We conclude that there is a limitation in the system which does not allow the incorporation of a higher amount of nitrogen into the CNFs. This is probably due to the fact that the maximum ionization temperature of nitrogen is around 10 000 K. This is the temperature at which the maximum number of N ions (N^+ and N_2^+) is obtained [Boulos, 1994]. The temperature range where the carbon particles are nucleated is between 3000 and 5000 K (see Appendixes V – Fact Sage calculations results). In this temperature range only a very small fraction of nitrogen ions are available for the functionalization of the carbon material. Other methods of nitrogen functionalization should be studied, keeping in mind the need of a clean and easy way to produce this material. One route would be to use another nitrogen precursor showing a lower ionization temperature. Another possible approach could be the production of the CNF using the same method, followed by a nitrogen treatment of the powders in the same experimental system but employing different experimental conditions: lower power and lower reactor pressure to allow the presence of exited species in the jet afterglow. Alternatively, another possibility of adding more nitrogen into the CNF structure could be to use a cold plasma system (non-equilibrium plasama), where the material is not exposed to high temperatures, but nitrogen species are created due to the non-equilibrium effects in the plasma.

2. Different methods to add iron and form the active sites should also be studied. The method developed at INRS-EMT Varennes is not suitable for the CNF morphology. During the two pyrolysis (up to 950 ^oC and 1050 ^oC), the nano-flake morphology is being destroyed. The particles change in morphology, the flakes fusing together and forming bigger particles. This is most probably resulting in a substantial reduction of the number of graphitic edges available for the formation of active sites, translating into a low activity of the catalyst as seen in Figure 10.2. Other methods to add

iron can be a cold plasma treatment or a chemical treatment. Ferrocene can be used in both cases as an iron source. Other organic compounds containing iron or having a chelates structure could also be used.

3. The testing of the catalyst material in the fuel cell environment includes the formation of an ink, which is applied to a carbon cloth to create the electrode to be used for the test. A direct way to create the electrodes can be to deposit the CB onto the carbon cloth *in situ* in the reactor. The carbon cloth can be attached directly to the collection plate inside the reactor before the production experiment, this cloth serving as a support of the CNF in the following treatment steps: N-functionalization if not simultaneous to the CNF synthesis, Fe-functionalization, Nafion impregnation. This would solve many problems related to nanoparticle handling and agglomeration, homogeneity of the catalyst coating, and morphology transformations in the various *ex situ* processes

4. Since the activity tests revealed an increase in the catalyst performance after each testing cycle, a study of the evolution of the catalyst material should be done. The catalyst should be characterized before and after each test to determine if changes occur in the number of nitrogen and iron atoms coordinated into the active sites. Another important aspect rising from this work should be addresses: could in-plane porosity help to generate more sites instead of relying only on edge effects? Are we finally forming in-plane porosity during fuel cell operation, which porosity eventually capturing any available N and Fe not fixed in other active sites?

5. Regarding the modeling work, a particle nucleation model should be implemented. Such models have been developed before and are presented in the literature but for spherical particles only. We see from this work that the growth of particles is favored along specific directions (in-plane of the graphene structure, and along one planar length of the carbon nano-flakes). The interesting shape of the carbon nano-flakes material raises questions regarding the anisotropic nucleation process.

References

1. Austin, A.E., "Proc. 3rd Conf. on Carbon", 389, 1958

2. Alexakis, T., "Production of fullerenes via the thermal plasma dissociation of tetrachloroethylene (C2Cl4)", PhD Thesis, CRTP, McGill University, Montreal, Canada, 1997

3. Atwood, J.L., Davies, J.E.D., Macnicol, D.D., Vogtle, F., "Comprehensive Supramolecular Chemistry", Volume 1 "Functional analogues of the Oxygen Binding and Activating Heme", Elsevier Science Inc., USA, 1996

4. Barbir, F., "PEM Fuel Cells", Elsevier Academic Press, USA, 2005

5. Boulos, M. I., Fauchais, P., Pfender, E., "Thermal plasmas. Fundamentals and Applications" Vol. 1, Plenum (1994)

6. Boulos, M. I., "Thermal plasma processing", IEEE Transactions on Plasma Science, **19**(6), 1078, (1991)

7. Castillo, I., "Study of CeO_2 synthesis from liquid precursors in a RF-inductively coupled plasma reactor", PhD Thesis, McGill University, Chemical Engineering Department, Montreal, Canada, 2007

8. Costamagna, P., Srinivasan, S., "Quantum jumps in the PEMFC science and technology from the 1960s to the year 2000. Part II. Engineering, technology development and application aspects", Journal of Power Sources, **102**, 253-269, 2001

9. Darmstadt, H., Roy, C., "Surface spectroscopic study of basic sites on carbon black", Carbon, **41**, 2653-2689, 2003

10. DiLeo, R., Landi, B.L., Raffaelle, R.P., "Purity assessment of multiwalled carbon nanotubes by Raman spectroscopy", Journal of Applied Physics, **101**, 064307, 2007

11. Donnet, J-P., Voet, A., "Carbon Black. Physics, Chemistry, and Elastomer Reinforcement", Marcel Dekker Inc., USA, 1976

12. Fabry, F., Flamant, G., Fulcheri, L., "Carbon black processing by thermal plasma. Analysis of the particle formation mechanism.", Chemical Engineering Science, **56**, 2123-2132, 2001

13. Ferrari, A.C., Meyer, J.C., Scardaci, V., Casiraghi, C., Lazzeri, M., Mauri, F., Jiand, D., Novoselov, K.S., Roth, S., Geim, A.K., "Raman Spectrum of Graphene and Graphene Layers", Phisical Review Letters, **97**, 187401, 2006

14. Fulcheri, L., Schwob, Y., Flamant, G., "Comparison Between New Carbon Nanostructured Produced by Plasma with Industrial Carbon Black Grades", J.Phys. III France, **7**, 491-503, 1997

15. Gasteiger, H.A., "Activity benchmarks and requirements for pt, pt-alloy, and non-Pt oxygen reduction catalysts for PEMFCs", Applied Catalysis B: Environmental, **56**, 9-35, 2005

16. Gauvin, R., "A Review of Transmission Electron Microscopy for the Characterization of Materials", Material Characterization and Optical Probe Techniques, vol. CR69, 1997

17. Girshick, S.L., Chiu, C.P., McMurry, P.H., "Modelling Particles Formation and Growth in a Plasma Synthesis Reactor", Plasma Chemistry and Plasma Processing, **8**, 145-157, 1988

18. Girshick, S.L., Chiu, C.P., "Homogeneous Nucleation of Particles from the Vapor Phase in Thermal Plasma Synthesis", Plasma Chemistry and Plasma Processing, **9**, 355-369, 1989

19. Gold, D., Bonet, C., Chauvin, G., Mathieu, A.C., Geirnaert, G., Millet, J., "A 100 kW three phase AC plasma furnace for spheroidisation of aluminium silicate particles.", Plasma Chemistry and Plasma Processing, **1**(2), 161-177, 1981

20. Gonzalez-Aguilar, J., Moreno, M., Fulcheri, L., "Carbon nanostructures production by gas-phase plasma processes at atmospheric pressure", J.Phys. D: Appl. Phys., **40**, 2361-2374, 2007

21. Guo, L., "Modeling of a supersonic DC plasma torch in CNT production", PhD Thesis, McGill University, Chemical Engineering Department, Montreal, Canada, 2009

22. Gupta, S., Tryk, D., Aldred, W., Yeager, E., "Heat-treated polyacrylonitrile-based catalysts for oxygen electroreduction", J. Appl. Electrochem., **19**, 19-27, 1989

23. Dai, G.P., Meunier, J-L., "Large-scale continuous synthesis of high purity carbon nanotubes in a dc thermal plasma torch reactor", Proc. 18th Int. Symp. on Plasma Chemistry, Kyoto (Japan), 2007

24. Harbec, D., "Producing carbon nanotubes using the technology of DC thermal plasma torch", PhD Thesis, McGill University, Chemical Engineering Department, Montreal, Canada, 2005

25. Harbec, D., Meunier, J.L., Guo, L., Jureidini, J., "A parametric study of carbon nanotubes production from tetrachloroethylene using a supersonic thermal plasma jet", Carbon, **45**, 2054-2064, 2007

26. Harbec, D., Meunier, J.L., Guo, L., Gauvin, R., El Mallah, N., "Carbon nanotubes from the dissociation of C2Cl4 using a dc thermal plasma torch", J. Phys. D: Appl. Phys., **37**, 2121-2126, 2004

27. Inagaki, M., "New Carbons. Control of Structure and Functions", Elsevier Science Ltd., UK, 2000

28. Jager, C., Henning, Th., Schlogl, R., Spillecke, O., "Spectral properties of carbon black", Journal of Non-Crystalline Solids, **258**, 161-179, 1999

29. James, D. Brian, "Cost Estimation for Direct H_2 PEM Fuel Cell System for Automotive Applications", Directed Technologies Inc., 2010

30. Jaouen, F., Lefevre, M., Dodelet, J-P., Cai, M., "Heat-Treated Fe/N/C Catalysts for O_2 Electroreduction: Are Active Sites Hosted in Micropores?", J. Phys. Chem. B, **110**, 5553-5558, 2006

31. Jasinsky, R., "A New Fuel Cell Cathode Catalyst", Nature, **201**, 1212, 1964

32. Jawhari, T., Roid, A., Casado, J., "Raman Spectrosopic Characterization of Some Commercially Available Carbon Black Materials", Carbon, **33**, 1561-1565, 1995

33. Juan, L. and all, "A New Grade Carbon Black Produced by Thermal Plasma Process", Plasma Science and Technology, **5**, 1815-1819, 2003

34. Kim, K.S., Seo, J.H., Nam, J.S., Ju, W.T., Hong, S.H., "Production of Hydrogen and Carbon Black by Methane Decomposition Using DC-RF Hybrid Thermal Plasmas", IEEE Transactions on Plasma Science, **33**, 813-823, 2005

35. Kinoshita, K., "Electrochemical uses of carbon", Electrochemistry Encyclopedia, Berkeley, USA, January 2001

36. Larouche, N., Stansfield, B.L., "Classifying nanostructured carbons using graphitic indices derived from Raman spectra", Carbon, **48,** 620, 2010

37. Levchenko, I., Volotskova, O., Shashurin, A., Raitses, Y., Ostrikov, K., Keidar, M., "The large-scale production of grapheme flakes using magnetically-enhanced arc discharge between carbon electrodes", Carbon, **48**, 4556-4577, 2010

38. Lefevre, M., Dodelet, J.P., Bertrand, P., "Molecular Oxygen Reduction in PEM fuel Cells: Evidence for the Simultaneous Presence of Two Active Sites in Fe-Based Catalysts", J. Phys. Chem. B, **106**, 8705-8713, 2002

39. Loretto, M. H., "Electron Beam Analysis of Materials", Chapman and Hall, 1984

40. Moreno-Couranjou, M., Monthioux, M., Gonzalez-Aguilar, J. and Fulcheri, L. "A non-thermal plasma process for the gas phase synthesis of carbon nanoparticles", Carbon, **47**, 2310, 2009

41. Médard, C., Lefevre, M., Dodelet, J-P., Jaouen, F., Lindbergh, G., "Oxygen reduction by Fe-based catalysts in PEM fuel cells conditions: Activity and selectivity of the catalysts obtained with two Fe precursors and various carbon supports", Electrochimica Acta, **51**, 3202-3213, 2006

42. O'Hayre, R., Cha, S-W., Colella, W., Prinz, F.B., "Fuell Cell Fundamentals", John Wiley & Sons Inc., USA, 2006

43. Pels, J.R., Kapteijn, F., Moulijn, J.A., Zhu, Q., Thomas, K.M., "Evolution of nitrogen functionalities in carbonaceous materials during pyrolysis", Carbon, **33**, 1641-1653, 1995

44. Probst, N., Grivei, E., Fabry, F., "Quality and Performance of Carbon Black from Plasma Process ", Rubber Chemistry and Technology, **75**, 891-905, 2002

45. Rao, C.V., Reddy, A.L.M., Ishikawa, Y., Ajayan, P.M., "Synthesis and electrocatalytic oxygen reduction activity of grapheme-supported Pt_3Co and Pt_3Cr alloy nanoparticles", Carbon, **49**, 931-936, 2011

46. Smith, J.M., "Chemical Engineering Kinetics", McGraw Hill, 3rd Edition, 1981

47. Vielstich, W., Arnold, L., Gasteiger, H.A., “Handbook of Fuel Cells”, Volume 1 “Fundamentals and Survey of Systems”, John Wiley & Sons Inc., USA, 2003.

48. Vielstich, W., Lamm, A., Gasteiger, H., “Handbook of fuel Cells. Fundamentals, Technoly and Applications”, Wiley, USA 2004

49. Wasel, W., Kuwana, K., Saito, K., “Soot Activation Energy for a Xylene-Fueled CVD Reactor”, **5**, A15, 2007

50. Williams, D.B., Carter, C.B., “Transmission Electron Microscopy”, Vol. I to IV, Plenum Press, New York, 1996

51. Zagal, J.H., Bedioui, F., Dodelet, J.P., “N4-Macrocyclic Metal Complexes”, Springer, New York, 2006

52. Zhong, H., Zhang, H., Liu, G., Liang, Y., Hu, J., Yi, B., “A novel non-noble electrocatalyst for the PEM fuel cell based on molybdenum nitride”, Electrochemistry Communications, **8**, 707-712, 2006

53. Yeager, E., “Electrocatalysis for O_2 reduction”, Electrochim. Acta, **29**, 1527-1537, 1989

54. “Carbon Black User’s Guide. Safety, Health, & Environmental Information”, ICBA

55. “Induction Plasma Torch PL-35 & PL-50, Operation & Service Manual”, Tekna Plasma Systems, Inc., Sherbrooke, 2004

56. http://srdata.nist.gov/xps/Default/aspx

Appendixes I – Carbon black structures

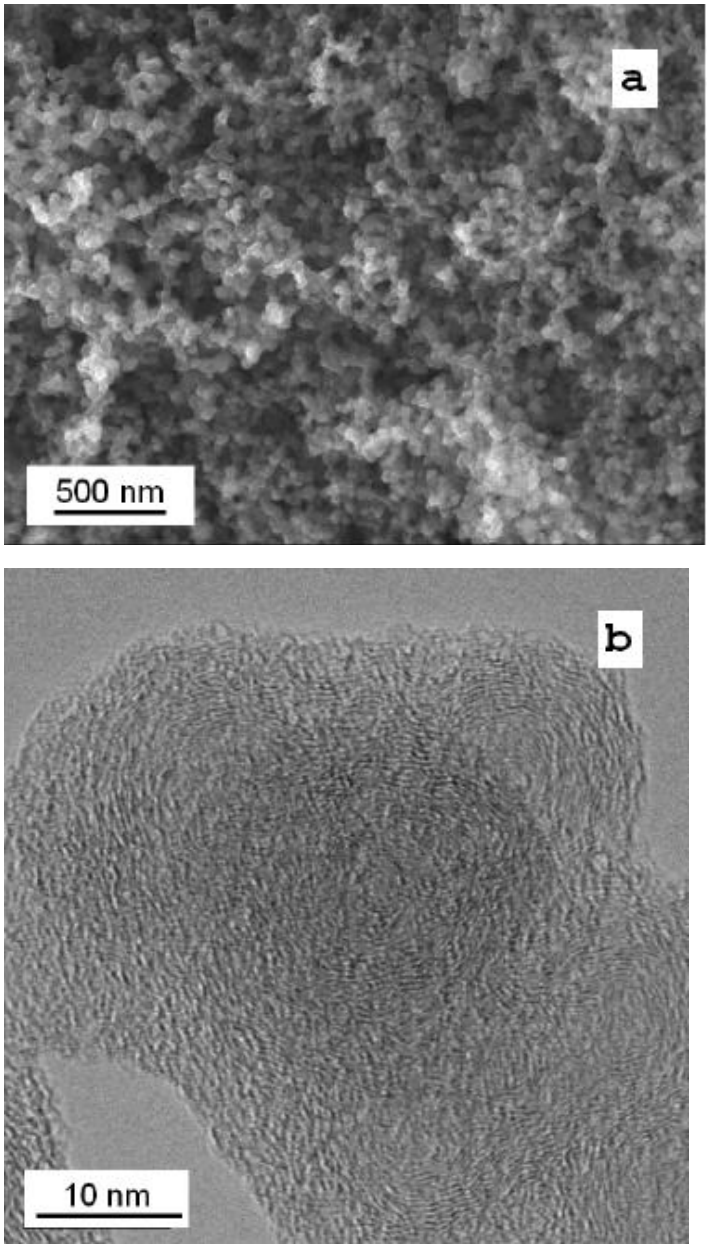

Furnace-like CB [Gonzalez-Aguilar et al, 2007]

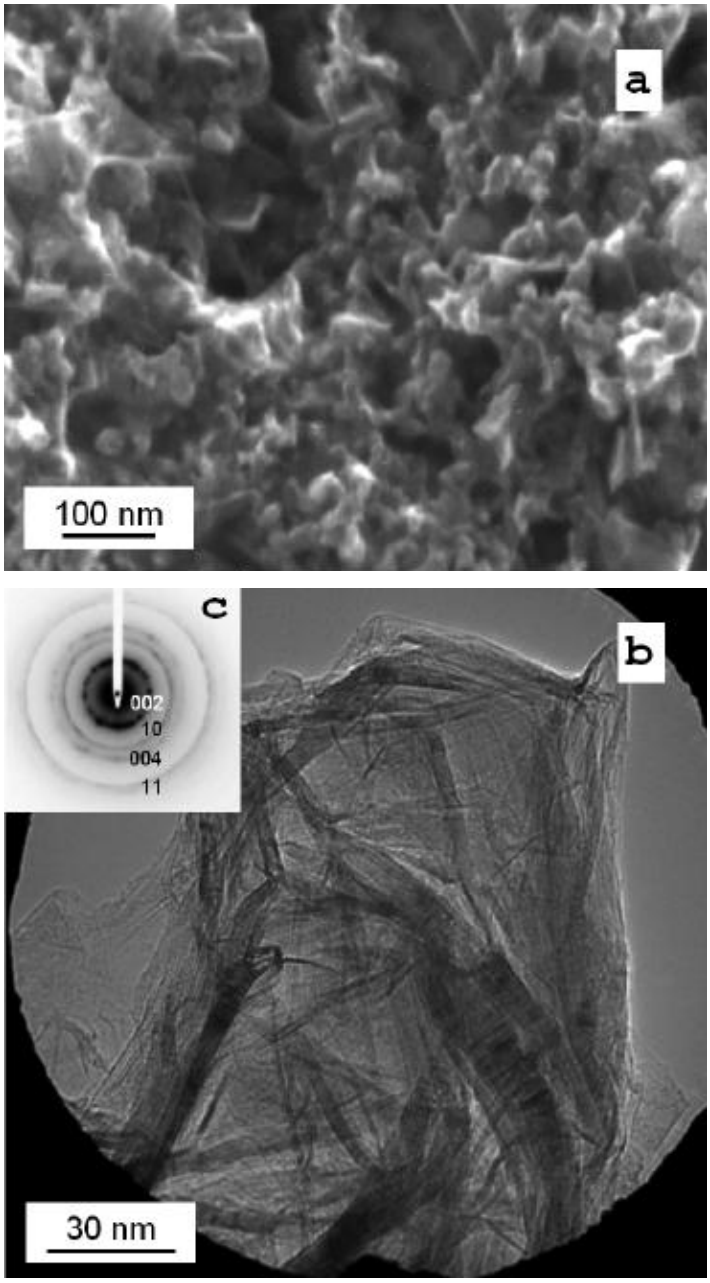

Crumbled paper sheets-like CB [Gonzalez-Aguilar et al, 2007]

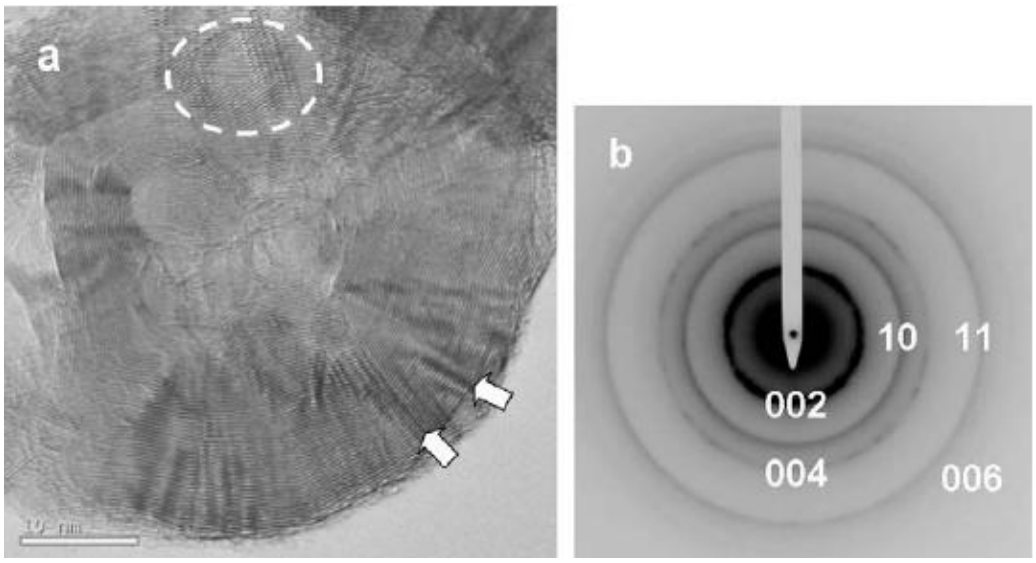

Acetylene type CB [Moreno-Couranjou et al, 2009]

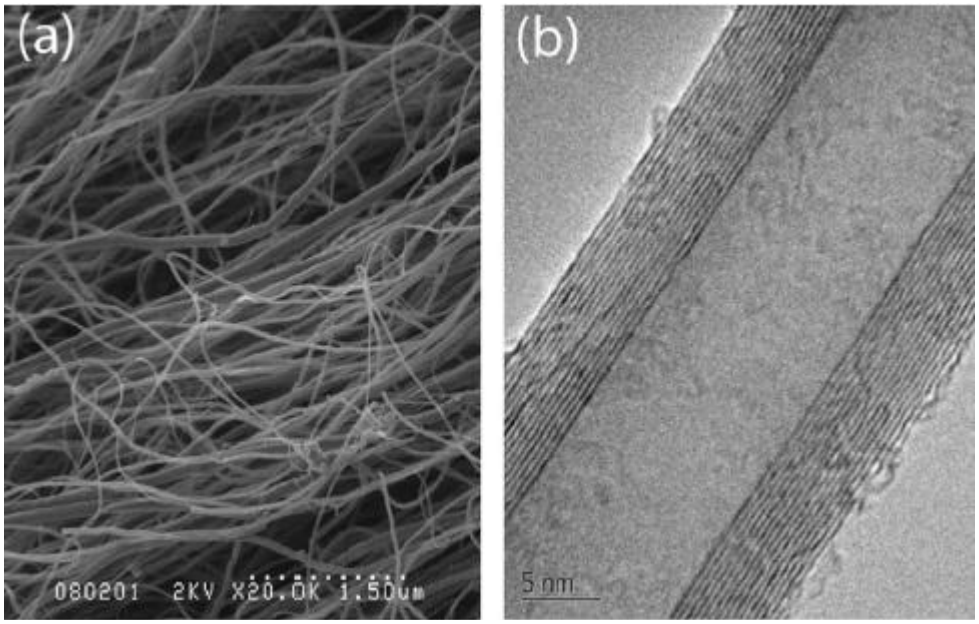

Carbon nano-tubes [DiLeo et al, 2007]

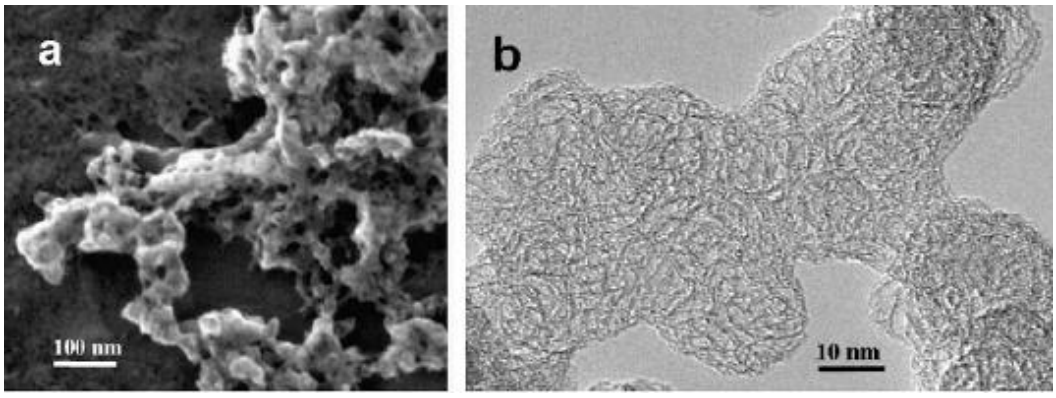

Carbon nanoparticles with microporous structure [Moreno-Couranjou et al, 2009]

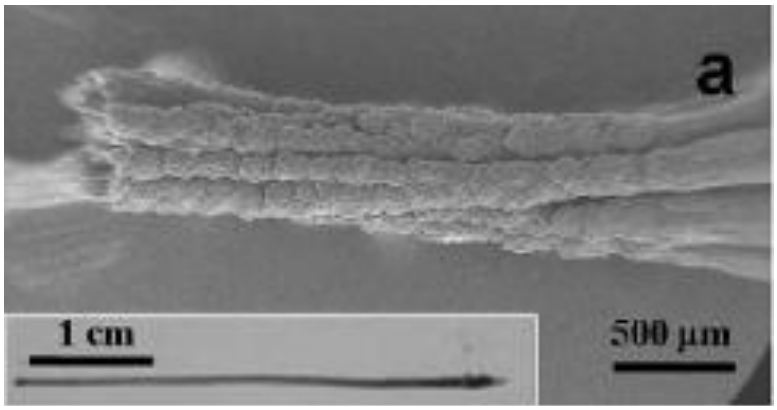

Carbon rods [Moreno-Couranjou et al, 2009]

Appendixes II – Fact Sage calculations

Ar + CH_4 system

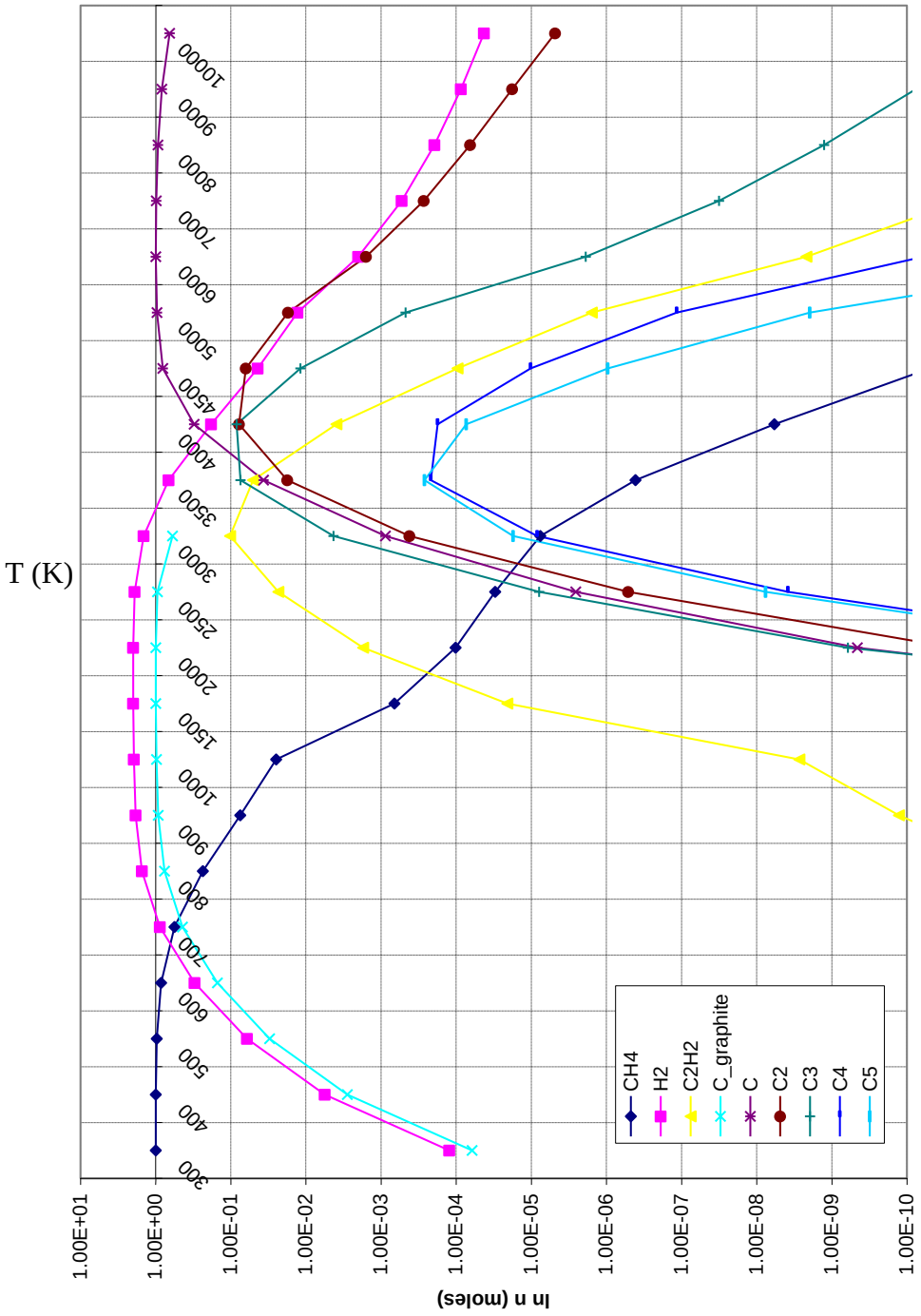

Ar + CH_4 + N_2 system